Dottorato – Scienze della Terra e del Mare
Scienze della Terra e del Mare
Settore Scientifico Disciplinare GEO/08

New insights of the volcanic gas signature of the Central American Volcanic Arc

IL DOTTORE

Battaglia Angelo

IL COORDINATORE

Prof. Alessandro Aiuppa

IL TUTOR

Prof. Alessandro Aiuppa

CO-TUTOR

Prof. Maarten de Moor

CICLO XXXI
ANNO CONSEGUIMENTO TITOLO 2019

Summary

Summary 2
Abstract 5
1 Central American Volcanic Arc 7
1.1 Introduction 7
1.2 Geological, tectonic and structural setting of CAVA 10
1.3 Volcanologic and geochemical setting 14
1.4 Volcanic gases 17
1.5 Helium isotopes 19
2 Methodology 21
2.1 Volcanic Gases 21
2.1.1 Electrochemical sensors 21
2.1.2 Spectroscopic sensors 25
2.1.3 Multi-GAS 25
2.1.4 Calibration 27
2.1.5 Processing Multi-GAS data 29
2.2 UV Camera 29
2.2.1 Data processing with Vulcamera 31
2.3 Rocks 32
2.3.1 Noble gases in fluid Inclusions 33
2.3.2 Major and trace elements 34
3 Overview of the presented resulted and structure of the dissertation 35
4 The magmatic gas signature of Pacaya volcano 37
4.1 Abstract 37
4.2 Introduction 38
4.3 Geological, volcanological and geochemical background 40
4.3.1 CAVA and Guatemala 40
4.3.2 Pacaya volcano 42
4.4 Materials and Methods 43
4.4.1 Multi-GAS 43
4.4.2 UV camera 43
4.4.3 Direct sampling 44
4.4.4 Chemistry of rocks and olivine crystals 44
4.4.5 Noble gas isotopes in fluid inclusions 45
4.5 Results 46
4.5.1 Plume composition and SO_2 fluxes 46
4.5.2 Chemical and carbon isotope composition of fumarole gases 49
4.5.3 Chemistry of whole rocks and olivine crystals 51
4.5.4 Noble gases in fluid inclusions 52
4.6 Discussion 56
4.6.1 The chemical signature of magmatic gases at Pacaya 56
4.6.2 Constraints on the magmatic source 59

4.6.3 C and He isotopes 60
4.6.4 Volatile fluxes 65
4.6.5 Implications for the volcanic CO_2 output in Guatemala 66
4.7 Conclusions 67
4.7.1 Acknowledgements 68
4.8 Tables 70
4.9 Supplementary Tables 75
5 Tracking Formation of a Lava Lake From Ground and Space: Masaya Volcano (Nicaragua), 2014–2017 87
5.1 Abstract 87
5.2 Introduction 88
5.3 Materials and methods 90
5.3.1 Masaya Volcano 90
5.3.2 Gas measurements 91
5.3.3 Space-based thermal data 94
5.4 Results 95
5.5 Discussion 99
5.5.1 A CO_2-rich gas 100
5.5.2 Measured vs. modeled gas compositions 100
5.5.3 A deep trigger? 106
5.5.4 Formation of the lava lake 109
5.5.5 Comparison with other lava lakes 112
5.6 Conclusions 113
5.7 Acknowledgements 114
5.8 Supplementary Table 115
6 Insights into the mechanisms of phreatic eruptions from continuous high frequency volcanic gas monitoring: Rincón de la Vieja volcano, Costa Rica 118
6.1 Abstract 118
6.2 Introduction 119
6.3 Rincón de la Vieja volcano 120
6.4 Materials and methods 123
6.5 Results 127
6.6 Discussion 130
6.6.1 Rincón de la Vieja gas signature: magmatic or hydrothermal? 134
6.6.2 The role of the sublimnic hydrothermal system 137
6.6.3 The eruption trigger 139
6.6.4 Implications for monitoring of active crater lakes 141
6.5.5 Conclusion 142
6.7 Acknowledgements 143
6.8 Tables 143

7 Along arc variation 148
7.1 El Salvador segment 150
7.2 Santa Ana volcano 151
7.3 Ilopango volcano 152
7.4 San Miguel volcano 153
7.5 Results 154
7.6 Discussion 159
8 Conclusion 161
9 Reference list 164
10 Acnowledgements 191

Abstract

Volcanic gas emissions carry crucial information on pre- and syn-eruptive processes, and on behaviour of active volcanic systems. Gas variations arise from replenishment of magma storage zones with mafic magma, from magma ascent and evolution, and from interaction with hydrothermal systems and volcanic lakes. As such, volcanic gases represent "open windows" into genesis and release of volatiles from the Earth's interior. Volcanic emission measurements allow understanding subsurface magmatic and hydrothermal processes, and contribute to eruption forecasting. Carbon dioxide and sulfur gas represent the most abundant and studied gas species. In particular, CO_2, due his fast exsolution during magma decompression, represents an important parameter for volcanic hazard assessment. In addition, due to his greenhouse effect, quantification of CO_2 budget from natural emissions at global scale represents a key scientific challenge. Indeed, active volcanic systems are able to release considerable quantities of gas. Volcanic arcs, in particular, release large amounts of CO_2 due to carbon recycling from subducted sediments and crust, and due to fluid addition from the mantle wedge. Understanding and modelling these processes allow forecasting volcanic eruptions, quantifying the volcanos' total volatile budgets, and contributing to climate change modelling.

In the past years, the scientific community has made efforts in order to discriminate the role and contribution of subducted slab sediments and altered oceanic crust on the geochemistry of magmas in volcanic arcs worldwide. New geochemical tracers and isotopes, in tandem with other volcanological data, has allowed characterizing the mantle source. In spite of the efforts made, many active volcanic systems are still poorly studied and monitored, and an improved knowledge on dynamics of volcanic degassing and in global gas budgets are needed, with particular attention to carbon dioxide. Technological progress has brought significant advances in geochemistry. Unlike the past, new instrument allow to continuously monitoring volcanic gas, reducing drastically the risks for the operators.

In this study (chapter 4, 5, 6), I took advantage of the recent advent of new techniques such as the *Multi-GAS* (Multi-component gas analyser system) and the *Ultraviolet dual camera* instruments. The *Multi-GAS* can perform gas measurements in a fully automatic way, while *UV cameras* allow measuring SO_2 fluxes with high spatial/temporal resolution. Combining gas chemical composition (*Multi-GAS*) with SO_2 flux (*UV dual camera*), it is possible to estimate the gas fluxes of other gas species.

My PhD focused on characterizing gas compositions and fluxes from three most active volcanoes in the Central America Volcanic Arc (CAVA): Pacaya

(Guatemala), Masaya (Nicaragua), and Rincón de la Vieja (Costa Rica). At Pacaya (Guatemala), I used a multi-disciplinary approach, combining geochemistry of gas and rocks, in the attempt to gain insights into the magmatic gas signature, on the volatile budget, and for characterizing the mantle source. Plume compositional data suggest Pacaya exhibits a H_2O-poor (for an arc volcano) composition (80.5 mol. %), with a characteristic magmatic CO_2/S_t ratio of ~1.0 to 1.5. Both the H_2O-poor and low CO_2/S_t ratio composition concur to suggest a limited slab-fluid contribution (at least compared to other volcanoes/arc segments; *Aiuppa et al.*, 2017), and a dominant mantle-wedge derivation of the emitted volatiles. The $^3He/^4He$ ratios measured in fluid inclusions hosted in olivines (Ra) are the highest values in CAVA volcanism. This strongly supports that the mantle source beneath Pacaya lacks of any contamination of radiogenic ^4He from the slab or the crust.

At Rincón de la Vieja (Costa Rica), I combined gas geochemistry with volcano seismicity in order to derive constraints on the triggers of phreatic/phreatomagmatic explosions. For the first time, the composition of the gas released during discrete phreatic events (confirmed seismically) was resolved using Multi-GAS. The results demonstrate chemically distinct gas compositions during quiescent degassing versus explosive eruptive degassing. These results confirm (*Christenson and Tassi*, 2015) that the complex interplay between rising magmatic gases and sublimnic hydrothermal systems likely play a decisive role as eruption triggers.

On Masaya (Nicaragua), I combined ground-based gas measurements and space-based thermal data in order to evaluate changes in gas composition associated with resumption of lava lake activity in 2015, and to derive novel information on the driving magmatic processes. Our results show that appearance of the lava lake in December 2015 was anticipated in mid- to late-November by a noticeable volcanic gas plume compositional change toward more CO_2-rich compositions, and by a sizeable CO_2 flux increase. Moreover, in view of the paucity of helium isotopes data for the northern part of CAVA, I collected rock samples on Pacaya and in 3 volcanoes in El Salvador (Santa Ana, San Miguel and Ilopango volcanic systems) to performe noble gas isotopes measurements in fluid inclusions. The data obtained here refine previous results obtained for the CAVA arc and suggest that $^3He/^4He$ along CAVA shows a regional trend as observed for other geochemical tracers (e.g., Ba/La, C/S, see chapter 7).

The general of this work is to expand gas knowledge on poorly studied volcanic systems, improve the geochemical database of Central America, and contribute to a better understanding of magmatic and geochemical processes in convergent margins.

Chapter 1

1 Central American Volcanic Arc

1.1 Introduction

Volcanoes are significant sources of major gases such as H_2O, SO_2, CO_2, H_2S, HCl and HF into the atmosphere. In particular, subduction at active margins plays an important role in the exchange of volatiles between superficial reservoirs and the Earth's interior, because magmas originating from the mantle wedge in volcanic arcs have higher volatiles concentrations than magmas derived from mid-ocean ridges (*Marty et al. 1989; Giggenbach, 1992a; Giggenbach, 1996*). Gas abundances in magmas and exsolved gas reflect volatile contributions from the slab, from depleted vs. undepleted mantle, crustal assimilation (e.g., de-carbonation and dehydration of crustal rocks) and magma differentiation in the crust. Evaluating gas composition, and quantifying the budget of volatile fluxes, can allow forecasting volcanic eruptions and better understanding the natural forcing on climate.

In this context, the Central America Volcanic Arc (CAVA) is a perfect natural laboratory because it offers the possibility to investigate the relationships between variations in geological, structural and physical features and geochemistry of magma, rocks and fluids in volcanic and hydrothermal manifestations. CAVA can be divided into eight segments. The segmentation is reflected in differences in the strikes and position of volcanic lineaments (*Carr 1984; Carr et al. 2003*), in volcanic activity, in the volume distribution of volcanic centers, and in large geochemical variations that occur in both lavas (*Carr et al. 1990; Morris et al. 1990*) and gas *(Fischer et al. 2002*).

After water vapour, carbon dioxide and sulfur dioxide (SO_2) represent the most prevalent gas species emitted from most volcanoes. Quiescent and active plume CO_2 degassing from open-conduit volcanoes makes an important contribution to earth degassing. Current estimates of volcanic carbon emissions in volcanic plumes are poorly constrained due to a lack of direct measurements, even if observations have increased in number recently (*Brantley and Koepenick 1995; Burton et al. 2013*). SO_2 is the only gas commonly measured remotely, due to its optical proprieties (relatively strong absorption band in the ultraviolet) and very low concentration in the atmosphere. Most of SO_2 flux measurements worldwide have been obtained using the COSPEC and DOAS techniques. Volcanic plume SO_2 budgets cover at least 13 CAVA volcanoes (*Aiuppa et al., 2014, Andres and Kasgnoc 1998; Rodrıguez et al. 2004; Delmelle et al. 1999; Duffell et al. 2001; Duffell*

et al. 2003; McGonigle et al. 2002; McGonigle et al. 2004; Zimmer et al. 2004 Mather et al. 2006), but uncertainties on the total arc budget remain due to incomplete and sparse information. Volcanic gas CO_2/S_t ratio information is only available for some segments of the arc (eg. Nicaragua and Costa Rica, *Robidoux et al. 2017, Aiuppa et al. 2018; Aiuppa et al. 2014, de Moor et al. 2016*), while data for the northern part of the arc are missing (e.g. Guatemala and El Salvador segments).

Recently, new geochemical tools have been developed in order to improve accuracy and quality of gas measurements. The advent of ultraviolet dual camera systems (*Burton 2006; Bluth et al., 2007*) has paved the way to SO_2 flux measurements of improved spatial and temporal resolution. The Multi-component gas analyser system (Multi-GAS) (*Aiuppa et al.* 2005*; Shinohara*, 2005) allows measuring volcanic gas composition (CO_2, SO_2, H_2S, H_2O, H_2) with high temporal resolution in a fully automatic way. Combining results from both instruments, CO_2, H_2O, H_2 fluxes can now be obtained. A central objective of the present PhD dissertation is to use these novel techniques to characterize gas signature and fluxes at three of the most active volcanoes in the central-northern part of CAVA, including the poorly monitored Rincón de la Vieja volcanic system in Costa Rica.

Great efforts have recently been made to better understand the gas origin and cyclying in convergent margin environments. In particular, in order to discriminate the roles of various components of the subduction factory (subducted slab, sediments and altered oceanic crust, mantle wedge) in controlling the volatile geochemistry of arc magmas. In the specific CAVA case, general consensus has been reached that slab-derived fluids play the most significant role in the generation of Nicaraguan magma, while the slab input decreases in El Salvador and Guatemala and Costa Rica. These variations in slab flux create along-arc variations in trace elements ratios in magmas (e.g., Ba/La, U/Th, U/La) and in gas chemical (C/S ratios) and isotopic (N, Cl, He and C) signatures. Noble gases are especially relevant tracers of the origin of arc fluids. Several helium isotopes dataset of fumaroles and geothermal manifestations exist for CAVA (*Leeuw et al. 2007; Snyder et al. 2003; Snyder et al. 2001; Elkins et al. 2006; Shaw et al. 2003; Poreda and Craig, 1989*). These studies have shown that helium degassed throughout the CAVA arc is a mixture of mantle He with lower $^3He/^4He$ ratio He produced by radiogenic helium additions in the crust and from the slab (^4He from U and Th decay). Lower $^3He/^4He$ ratio are typically restricted to regions behind the volcanic front and only in some parts of the volcanic arc. In contrast, studies investigating the helium isotope variations in fluid inclusions (FIs) hosted in olivine and pyroxene crystals from tephra and lavas are more limited in

number (*Fisher et al. 2010; Shaw et al. 2006; Fisher et al. 2005; Di Piazza et al. 2015; Poreda and Craig, 1989*). These minerals can trap mantle volatiles as fluid or melt inclusions during crystallization within a magma chamber. As showed in most of CAVA volcanoes analyzed so far (*Fischer et al.* 2005*; Shaw et al.* 2006*; Di Piazza et al.* 2015*; Robidoux et al.* 2017), the $^{3}He/^{4}He$ ratios in olivine-hosted fluid inclusions are typically higher than in (or at the upper range of) volcanic gases from the same volcanic system (*Robidoux et al., 2016*). Thus, FIs provide more reliable indications on magmatic He signature, because contamination by shallow fluids or air are systematically less significant. Data on helium ratios from FIs are missing or incomplete for the northwest part of CAVA (e.g. Guatemala and El Salvador), and refining/expanding this dataset is a key topic of the present dissertation. Work performed at Pacaya volcano in Guatemala is presented in chapter 4, while work carried out in El Salvador is presented in the last chapter of this Thesis.

1.2 Geological, tectonic and structural setting of CAVA

The Central American Volcanic Arc (CAVA) represents a chain of volcanoes extending for more than 1200 km along the Pacific coast, from the Guatemalan-Mexican border to western Panama. This volcanic arc is the result of subduction of the Cocos plate beneath the Carribean plate (fig.1.1). The direction of convergence of these two plates is N25-30°E (*Protti et al. 1995*). Several differences exist in physical parameters along CAVA arc. The convergence rate between the Cocos and Caribbean plates gradually increases toward the southeast, from 7 to 9 cm/yr. (*DeMets, 2001*). The subducting lithosphere is divided into two segments by the Cocos Ridge offshore of southern Costa Rica. The north-western segment is made of older and colder Cocos materials subducting at a relatively steep angle beneath Guatemala (55°) and El Salvador and Nicaragua (61°- 65°), and at relatively shallower dips (35° - 65°) below Costa Rica (*Syracuse and Abers 2006, Shaw et al., 2003*). In addition, the age of the subducting Cocos lithosphere exhibits differences between the south-easternmost segment in central Costa Rica (17 to 25 Ma) and other parts of the subduction zone (about 26 Ma). Crustal thickness decreases from Guatemala (50-40 km) to Nicaragua (30 km), increases across Costa Rica and western Panama, and then again thins in central Panama (*Carr 1984; Case et al., 1990*) (fig.1.2).

To the NW, the Motagua - Polochic transform fault system, cutting across Guatemala, separates the Caribbean (Chortis block) and North American plates (fig. 1.1). This is the beginning of the CAVA arc. The Chortis block extends from the sinistral Motagua-Polochic-Faults in Guatemala (NW) to the territory of Nicaragua and represents the continental basement (granitic and metamorphic) (*Heydolph et al., 2012*), while the Chorotega block constitutes the Costa Rica basement and was formed during the Mesozoic and Cenozoic as a thickened oceanic crust (*MacKenzie et al., 2008*). Analysis of sediments on the subducting Cocos Plate adjacent to the Middle American Trench (from the Deep Sea Drilling Program, DSDP, and the Ocean Drilling Program, ODP) showed the presence of a ~400 m of sedimentary column. The upper portion (~200 m) consists of Quaternary to upper Miocene hemipelagic diatomaceous mud and middle Miocene brown abyssal clays, while the lower part consists principally of the middle-lower Miocene chalky carbonate (*Patino et al., 2000*).

Two major types of structures exist in Central America: those transverse to the volcanic chain and those parallel to the chain. The major transverse structures are alignments of volcanic centers (usually strike about N-S) and faults usually strike N30E or N-S, (*Stoiber and Carr 1973*).

The parallel structures are normal faults in all CAVA segments except in west and central Guatemala. The strike of these structures changes markedly at the

end of boundary regions (e.g. east Guatemala - El Salvador, El Salvador - west Nicaragua, west Nicaragua - east Nicaragua and Costa Rica). From central Guatemala to western Nicaragua, boundary regions are characterized by intense normal faulting (*Stoiber and Carr 1973*) where sometimes there are basaltic cinder cone as in the Ipala graben area in southeast Guatemala. The Middle America trench, the surficial expression of subduction process, represents a main parallel structure present throughout CAVA. Other important parallel structures are the El Salvador fault Zone (ESFZ, also called Jalpatagua Fault Zone, JFZ) and the Nicaragua depression, a complex array of dextral strike-slip faults with dominant E-W strike and a right-lateral kinematic (fig.1.1).

The Guatemala segment is characterized by intense extensional stress with crustal thinning, graben formation and crustal pull apart structures. Extensional stress is generated by counterclockwise block rotation as result of the rotation of upper crustal blocks in northern Central America.

These complex tectonic settings generate four different morpho-tectonic segments in Guatemala (fig.1.1; *Burkart & Self, 1985*) with different extensional regimes. Except for zone I (NW), virtually unaffected by Neogene extensional tectonics, zone II and zone III resulted in large volcanic rock productivity with the Atitlan and Amatitlan caldera complex respectively. Zone III is a basin-and-range style structure and the principal movement is eastward, while zone IV is characterized by arc-parallel pull apart-basins. In southern Guatemala, E-W crustal extension (as evidenced by the existence of a series of N-S trending grabens; *Burkart & Self, 1985*) and right-lateral strike-slip movements in the Jalpatagua Fault Zone (JFZ), are observed. The transition zone between morpho-tectonic segments from Guatemala to El Salvador are characterized by pull-apart structures.

In El Salvador, three sets of faults exist that strike northwest, north-northeast and east. Here, the volcanic arc extends along El Salvador fault zone (ESFZ) a large structure (> 100 km) oriented NW-SE with right-lateral and oblique-slip movements. This extensional regime is associated with intense seismic activity, quaternary deformation, and large volume silicic calderas. In addition, it is the source of destructive earthquakes along the volcanic arc (*Martínez-Díaz et al., 2004*). The Gulf of Fonseca separating El Salvador and western Nicaragua.

In Nicaragua, unlike in other CAVA segments, convergence azimuth is 15° oblique relative to the trench (*Barckhausen et al. 2001*). Nicaragua represents the southern part of the Chortis block, the granitic and metamorphic continental basement (*Frischbutter 2002*). In this region, the crust beneath the volcanic arc is thin (24 ± 2.5 km – 31.6 ± 6.5), while the thickest crust lies in the Nicaraguan back arc (43 ± 2.5 km) and beneath Costa Rica arc (37.9 ± 5.2 km; *Mackenzie et al., 2008*). As in El Salvador, the large NW-SE transverse

extensional structures form the Nicaragua depression. Large part of this depression is occupied by the Managua Lake, the ignimbrite plateau of Tipitapa, and the Nicaragua Lake (*Hradecký et al., 2007*). In Nicaragua, NE striking faults dominate the forearc and arc (*Carr, 1976*), while in El Salvador, Guatemala, and Costa Rica, there is more evidence of NW striking right-lateral faults (*Carr, 1976; Marshall et al., 2000*). These NW striking faults are thought to be associated with segment breaks along the Central American volcanic arc (*Stoiber and Carr, 1973; Carr, 1976*).

Costa Rica is located at the southern terminus of the collisional zone between Cocos and Carribean plates. The direction of convergence of these two plates is N25-30°E (*Protti et al., 1995*) with a relatively shallower dips. The interaction of these plates with the Nazca plate and with the Panama block creates a complicated tectonic setting. Nazca and Cocos plates are divided from the preexistent *Farallon* plate broken along a preexisting fracture zone in equatorial region at ~ 27 Ma (*Barckhausen et al., 2001*). Off the coast of Costa Rica, the Cocos Ridge separates Cocos and Nazca plates. The Cocos ridge, parallel to the recent motion of the underlying Cocos Plate, extends more than 1000 km from the "Cocos-Nazca Spreading center" (CNS; also known as Galapagos Spreading Center), directly north of the Galapagos Platform to the trench off the coast of Costa Rica (*Werner et al., 2003*). Ridge subduction causes a wide gap (175-km) in the volcanic chain and a segmentation of the Benioff zone (*Protti et al., 1995*). Part of the Cocos plate generated in the East Pacific Rise subducts under Nicaragua and northern Costa Rica while Cocos plate generated at the Galapagos Spreading Center subducts under central and southern Costa Rica and produce ocean-island-basalt (OIB)-type volcanism in this region. South of the border between Costa Rica and Panama is a right lateral transform fault called "Panama Fracture zone" (*Protti et al., 1995*).

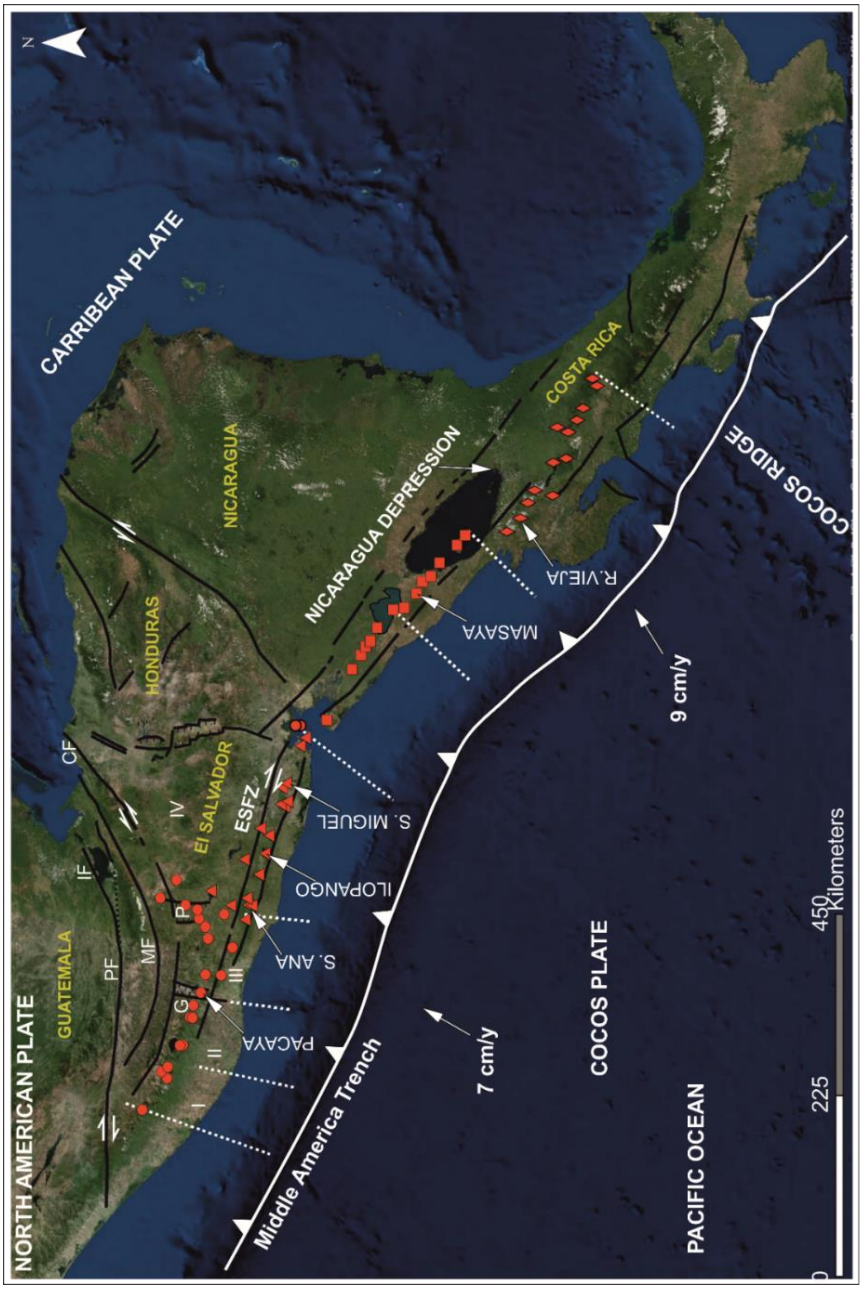

Figure 1.1 Morphotectonic sketch of Central America, showing principal tettonic linements and location of the active volcanic systems discussed in the text. Satellite image from Google Earth. Red symbols indicate the volcanic front. Circles: Guatemalan volcanoes; triangles: El Salvador volcanoes; squares: Nicaraguan volcanoes; rhombus: Costa Rica volcanoes. Symbols I, II, III, IV identify the morphotectonic zones described in Burkart et al., (1985). P= Ipala graben; G= Guatemala graben; ESFZ= El Salvador fault zone also called Jalpatagua fault zone. White dotted lines represent the eigh segments of the arc (Carr 1984). Convergence rate (7 to 9 cm/yr from DeMets, 2001).

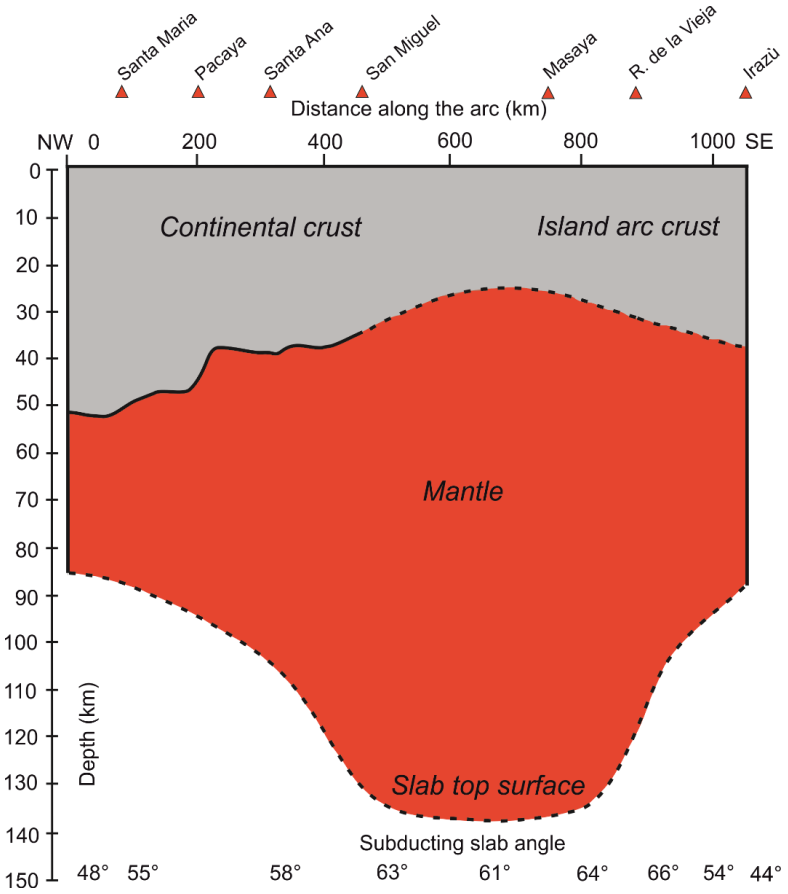

Figure 1.2 Along- arc profile below CAVA. Modified from Wehrman et al. (2011). The profile is extending ~1000 km, illustrating the variations in the depth to the surface of the subducting slab, crustal thickness, mantle wedge thickness and composition of the overlying crust. Slab depth and Guatemalan crustal thickness are from Syracuse and Abers (2006); crustal thicknesses of Nicaragua and Costa Rica are from MacKenzie et al. (2008).

1.3 Volcanologic and geochemical setting

This study is focalized on three of the most active volcanoes of the Central American Volcanic Arc (CAVA) from Guatemala to Costa Rica. Tectonic and structural settings in CAVA are responsible for magma genesis,

geochemical variations, volcanic and hydrothermal manifestations and gas composition.

As in other arc settings, these subduction-related volcanic centers can be divided in volcanic front (VF) centers and the behind the volcanic front (BVF) (*Carr 1984*) up to 350 km from the Middle America trench. In addition, a second line of volcanoes exists of calc-alkaline affinity. Here, lavas have different geochemistry, with an intermediate slab input (e.g. Ba/La) between the volcanic front and the BVF (*Patino et al., 1997; Carr et al., 2003*). The volcanic front is aligned along the active margin, and is composed of ~40 clusters formed by many quaternary composite volcanoes, calderas and small cinder cones with very different morphology that trend parallel to the strike of the subducting Cocos plate. The BVF volcanism mainly lies east of the volcanic front in Honduras, Nicaragua and Costa Rica (*Patino et al., 2000*) and principally consists of small cinder cones. Volcanism in this region is related to crustal extension and decompression melting due to interaction between the North American and Caribbean Plates (*Walker et al., 2000, Snyder et al., 2001*).

The Central American volcanic front can be divided into eight segments based on differences in strikes and position of volcanic lineaments in the volcanic chain, evidenced by the discontinuity in the deep seismic zone (fig.1.1, *Carr 1984; Carr et al., 2003*). The segmentation is reflected in different geochemical signatures and in the volume distribution of volcanic centers. Segmentation is also highlighted by differences in the volcanic eruption types (*Stoiber and Carr 1973*), including solfataric activity in central Guatemala with frequently nuees ardentes, strong historically explosive activity in El Salvador and Nicaragua with voluminous lava flows, and ash eruptions with little to no at in Costa Rican volcanoes.

From North to South, Santiaguito-Santa Maria, Fuego and Pacaya volcanic systems represent the most active volcanoes in Guatemala. Extensional stress favorites a high volume of erupted magma, as evidenced at Atitlan and Amatitlan caldera complexes. This extensional regime, as in other areas of the world, explains the presence of bimodal (basaltic- Rhyolitic) volcanism in Guatemala (*Burkart et al., 1985*).

The Santiaguito-Santa Maria complex has been erupting a high-Na, calc-alcaline dacite since it began to grow in 1922 (*Rose 1987b*). Fuego erupts high-Al olivine basalts and has frequent explosive eruptions. Pacaya formed on the south side of the 100 Km^2 Amatitlan caldera. It is located at the southeast end of the central Guatemala segment, adjacent to Agua and Fuego volcanoes. It has erupted high-Al olivine basalt (*Eggers 1971; Wunderman and Rose 1984*). Some Pacaya products have characteristics between the low-Ti volcanic front and the high-Ti back-arc. The relation between tectonic and volcanism in southern Guatemala is discussed in chapter 4.

The volcanic arc extends along the El Salvador Fault Zone (ESFZ), and it is associated with extensional deformation and large volume silicic calderas and abundant production of ryolites. Nine large volcanic centers exist. From North to South, Santa Ana-Izalco complex, Ilopango caldera, San Vincente, San Salvador, and San Miguel volcanoes are the major volcanic systems that generated several eruptions in the past (see chapter 7). The eruptive products of Santa Ana are olivine basalts and basaltic andesite, andesites typical for a calcalkaline series. Some lava flows show more silicic composition: andesite to dacite and trachyandesite (*Carr and Pointer, 1981; Carr et al., 1990*). Ilopango caldera erupts andesitic-dacitic lavas. A large eruption in the A.D 429 produced the Terra Blanca Joven (TBJ) tephra, a vast and extensive volcanic deposit. The last vigorous eruption in the 1879–1880 has formed the Cerros Quemados domes in the center of the lake. This dome contains mafic enclaves that suggest a mafic magma trigger for the eruption (*Richer 2004*). Analysis of these mafic inclusions are discussed in the chapter 7.
In Nicaraguan, the volcanic front extends to south in the regional graben (Nicaraguan Depression). Cerro Negro, Neyapa, Momotombo, San Cristobal, Masaya and Conception are the most important volcanic systems in Nicaragua. Volcanic rocks in Nicaragua are generally classified as basalts, basaltic andesite and andesites (*Saginor et al., 2011*) with tholeiitic affinity (*Pearce 1999*).
Subduction generated two distinct volcanic arcs in Costa Rica: the "Cordellera Central" (Poás, Barva, Irazù and Turrialba volcanoes) and the "Cordillera de Guanacaste" (Orosí-Cacao, Rincón de la Vieja-Santa María, Miravalles and Tenorio-Montezuma volcanoes). Costa Rica is distinct from the rest of Central America because of an ocean-island basalt (OIB) character of the lavas (*Leeman et al., 1994*). Geochemically, these basalts are similar to those erupted by the Galapagos hot spot (*Carr et al., 2003*).

In the past decades, many authors have addressed the issue of understanding the large geochemical variations along the arc. These variations reflect the interaction between changing physical parameters and the contribution of various source (hemipelagic sediments, carbonates, slab components and mantle wedge). The Central American magmas have geochemical characteristics that reflect involvement of two distinctly different sediments at the top of the Cocos plate (*Patino et al 2000*). These sedimentary deposits include both hemipelagic (upper part ~200 m) and carbonate (lower part ~200 m) successions, while the basal section of the Cocos Plate consists of MORB/altered MORB and has not been directly characterized (*Carr et al., 2003*). As shown in figure 1.3, the Ba/La ratio exhibits very little variations in the sediments section. This Ba/La sedimentary ratio is much higher than the MORB, and so it represents a suitable tracer of the sedimentary slab input.

The U/Th ratio exhibits large variations, and is statistically indistinguishable between the two sediment sections (*Carr et al., 2003*), thus yielding a less clear view on slab processes (relative to Ba/La); other tracers, such as U/La, are tracers of the carbonates, while U/La (similar in MORB and carbonates) is a good tracer of the hemipelagic section.
These and other geochemical tracers, including gas compositions (C/S ratio) and N, Cl, He and C gas isotopes (*Fischer et al., 2002; Shaw et al., 2003; Leeuw et al., 2007; Barnes et al., 2009; Aiuppa et al., 2014; Di Piazza et al., 2015; Robidoux et al., 2017*), indicate mantle-like signatures in the northernmost (Guatemala and El Salvador) and southernmost (Costa Rica) ends of the front. In contrast, slab fluid contribution, and sediment - and/or serpentinite-derived signature, is observed in Nicaragua. Details of geophysical-geochemical variations along CAVA are discussed in chapter 7.

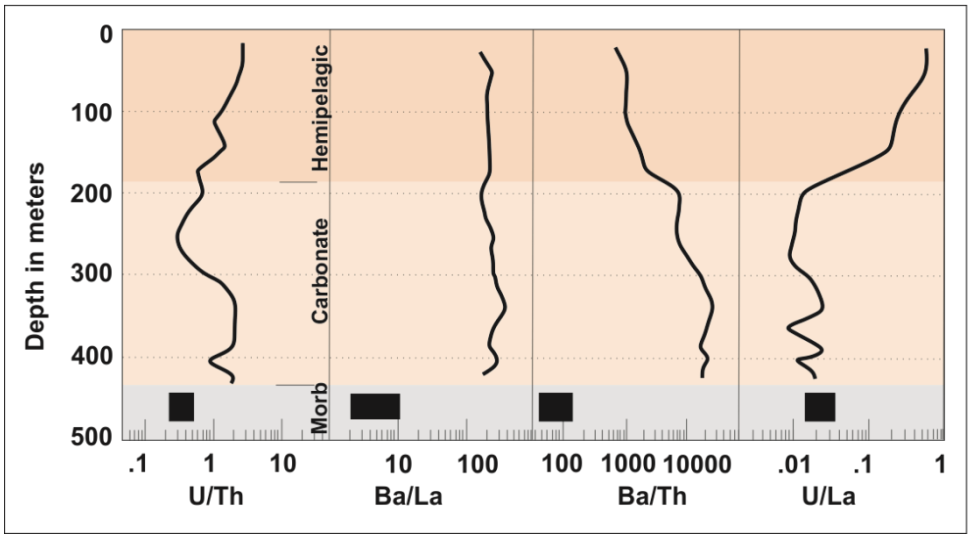

Figura 1.3 Geochemestry of DSDP 495 section. Black squares are EMORB and NMORB from McDonough (1989). Modified from Carr et al., 2003

1.4 **Volcanic gases**

Magma degassing is one of the most fundamental processes of volcanism and its effects are responsible for the dynamics of eruptions and the evolution of magmas in the crust.Volcanoes are significant sources of major gases such as H_2O, SO_2, CO_2, H_2S, HCl, and HF into the atmosphere. In particular, magmas originating from the sub-arc mantle have higher volatile concentrations and higher relative abundances of H_2O, CO_2 and N_2 than magmas derived from mid-ocean ridges (*Marty et al., 1989; Giggenbach, 1992a; Giggenbach, 1996*). Measurement of volcanic emissions (crater plumes, fumaroles, diffuse soil degassing) improve our understanding of subsurface magmatic and hydrothermal conditions, and contribute to eruption forecasting. Indeed, the chemical composition and abundance of gas species reflect the chemical

composition of magmas and the relative roles of key processes, such as the respective contributions of slab, depleted vs. undepleted mantle, crustal assimilation, (e.g., de-carbonation and dehydration of crustal rocks), differentiation of magma in the crust and interaction with hydrothermal aquifers in the shallow levels. The exsolution of magmatic gas is the driving force of volcanic eruptions.

Volcanic CO_2 and SO_2 have received primary attention in this work because they allow tracking deep magmatic processes, and monitoring active volcanoes due its different solubility and behaviour in the magma phase. Indeed, during magma ascent, the solubility of volatiles decreases and gases separate from the magma at different pressure (depth).
In the recent past, the development of remote techniques has allowed to make estimates of global volcanic emissions.
Quiescent and active plume CO_2 degassing from open-conduit volcanoes is an important contribution to earth degassing. Current estimates of volcanic carbon emissions from global subaerial volcanism are poorly constrained due to a lack of direct measurements. *Burton et al., 2013* recently calculated that subaerial volcanism produces ~100-500 Mt/yr of CO_2 worldwide and there is still no clear characterization of its origin and exchange process in the subduction zone environment (*Dasgupta et al. 2013; Manning, 2014*). In the Central America volcanic arc, as in the most volcanic region, many efforts have been made in order to expand and refine volcanic gas datasets, but this is still far from being complete (*Andres and Kasgnoc, 1998; Burton et al., 2000; Williams-Jones et al., 2003; Shaw et al., 2003–2006; Rodriguez et al., 2004; Zimmer et al., 2004; Mather et al., 2006; Witt et al., 2008; Hilton et al., 2010; GVP, 2011; Conde et al. 2013; Conde et al. 2014; Aiuppa et al., 2014*).
After water vapour and carbon dioxide, sulfur dioxide (SO_2) represents the most prevalent gas species emitted from most volcanoes. Also, due to its optical proprieties (relatively strong absorption band in the ultraviolet) and very low concentration in the atmosphere, SO_2 is the only gas which is commonly measured remotely. In the past, most of SO_2 flux measurements have been obtained with COSPEC and DOAS instruments. Recently, ultraviolet dual camera have increasingly been used, thanks to their increased spatial and temporal resolution. Otherwise, direct (remote) quantification of CO_2 flux is difficult due to elevated background in atmosphere. The determination of the CO_2 flux thus relies on combining measurement of the gas CO_2/SO_2 ratio and the SO_2 flux (or other technique as He/CO_2 ratio).
Many authors have contributed to constraining the SO_2 budget along CAVA (*Aiuppa et al., 2014*; *Andres and Kasgnoc 1998; Rodrıguez et al. 2004; Delmelle et al. 1999; Duffell et al. 2001; Duffell et al. 2003; McGonigle et*

al. 2002; McGonigle et al. 2004; Zimmer et al. 2004; Mather et al., 2006). In Central America, the actual reported SO_2 flux data cover at least 13 active volcanoes between Guatemala and Costa Rica. *Mather et al.,* (2006) summarized these results and estimated a total arc SO_2 flux of 4320 T/d. Overall, the range of measured fluxes from single volcanoes is large, from 30 to 1,540 T/d of SO_2, and as for CO_2 depends largely on the specific degassing system of each volcano (*Mather et al., 2006; Shinohara et al., 2013a*). *Aiuppa et al.,* (2014) estimated the total SO_2 flux for the Nicaraguan and Costa Rican segments as 2890 T/d. CAVA is composed of □40 clusters formed by many quaternary composite volcanoes and so current estimates of volcanic emissions in subaerial volcanic plumes are not well constrained due to a lack of measurements.

During this PhD, work has been done to improve our current knowledge on CO_2/SO_2 signature and gas fluxes from some previously poorly studied active CAVA volcanoes.

1.5 Helium isotopes

Six noble gases exist in nature: helium (He), neon (Ne), argon (Ar), krypton (Kr), xenon (Xe), and the radioactive radon (Rn). They are monatomic gases and their outer shells of electrons are full. This is a unique characteristic among the elements and it means that they are chemical inert elements. This feature implies that their composition have not been modified by chemical and/or biological reactions during Earth's history providing an exceptional tool to investigate the origin of volatile on the Earth. During mantle melting, noble gases enter in the melt phase, as well as other incompatible elements. Being volatile elements, noble gases are then exsolved from ascending magma upon decompression, and are ultimately released by magmatic systems. Each noble gas has different radiogenic and non radiogenic isotopes. Helium has only two stable isotopes: ^4He and ^3He. ^4He represent the 99.99% of terrestrial helium. It has radiogenic origin and derives from decay of U and Th in rocks. ^3He is considered primordial and represents a very small portion of helium (0.00015%). The main source of ^3He is degassing of the Earth interior. The distinctive abundance of helium isotopes in different Earth's reservoirs allow identifying the magmatic sources and deep processes. Helium isotopic ratios are expressed as R/Ra, in which R is $^3He/^4He$ of the sample while Ra is the atmospheric $^3He/^4He$ ratio (1.39*10-6). Helium ratio signatures of MORB and OIB basalts have been constrained from more than 30 years of helium analyses. MORBs worldwide have 8±1 R/Ra (*Graham, 2002*), while OIB basalts span from 5 to 50 R/Ra. The large dispersion in OIB basalts has been attributed to a deeper and variably degassed source, as well as by variable extent of recycling of crustal materials with high $U/^3He$ (*Moreira 2013*).

The $^{3}He/^{4}He$ ratio may be modified by deep processes and by secondary shallow processes (e.g. crustal slab-derived fluids contamination, radiogenic He addition in magma chambers) as shown in figure 1.4.

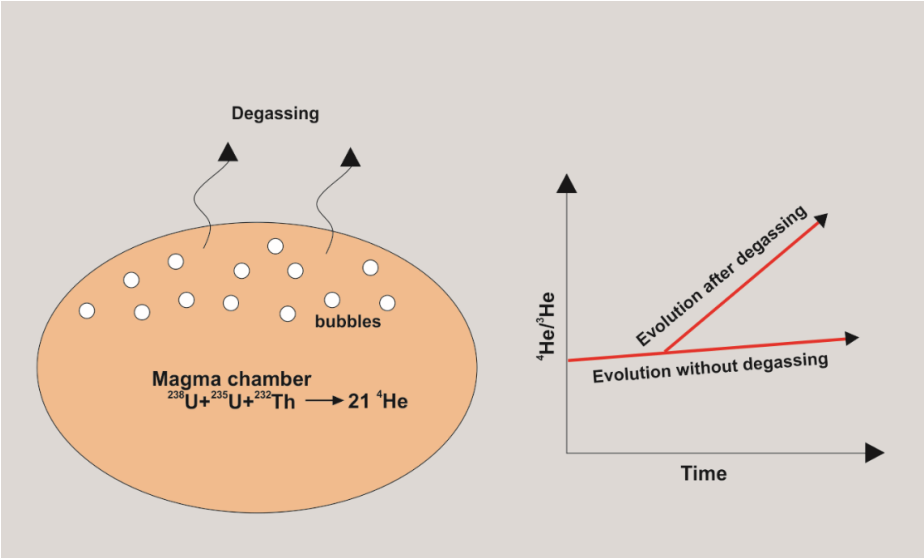

Figure 1.4 Cartoon showing how degassing can influence the helium isotopic ratio modified from Moreira 2013. When CO_2 is oversaturated in magma, it forms bubbles that can be degassed from the magmatic chamber. Helium has low solubility in magmas similar to CO_2 and will enter in the gas phase. The degassed magma has a high ($U+Th/^{3}He$ ratio).

Frequently, noble gases are studied in fumaroles and geothermal fluids (*Hilton et al., 2002; Sano and Fischer, 2013, Oppenheimer et al., 2014; and references therein*). The limits of these studies are the possible atmospheric and/or crustal contamination occurring at shallow levels, after magmatic degassing. Often, a $^{3}He/^{4}He$ ratio wide range is measured in superficial gas manifestations that may not well reflect the composition of the magmatic source. In contrast, fluid inclusions (FIs) hosted in mafic crystals (olivine and pyroxene) preserve the composition of the deep condition and provide to a more representative view of the deep source (*Rizzo et al., 2015; Robidoux et al., 2017; Battaglia et al., 2018; Boudoire et al., 2018* and references therein). Fluid inclusions are a common feature of minerals. When a crystal grows in the presence of a fluid phase, some of the fluid can be trapped as imperfections in the growing crystal to form fluid inclusions (*Roedder, 1958, 1963; Deines, 2002* and references therein). The trapped fluid may be liquid, vapor, or supercritical fluid, and its composition is domainated by water and CO_2. The common size of natural fluid inclusions is a few millimeters but there is no limit in size (*Bodnar 2003*). This fluid (generally gas) trapped in FI(s) represent an early stage of degassing, especially in olivine crystals that crystallize early from basaltic melts and then preserve the deeper magmatic conditions (e.g., *Boudoire et al., 2018* and references therein).

Chapter 2

2 Methodology

This section reviews the methodologies and techniques that have been used to reach the research goals discussed in the previous chapters.

2.1 Volcanic Gases

In the past decade, with the progress of technology, new instrumental geochemical tools have been developed in order to improve the temporal resolution of gas measurement, and to decrease risk for operators in volcanology discipline. The Multi-gas technique, first introduced in *Aiuppa 2005* and *Shionara 2005*, consists in a fully automatic instrument to measure gas concentrations in volcanic plumes and fumaroles using a combination of electrochemical sensors, IR spectrometers and other electronic devices.

2.1.1 Electrochemical sensors

A gas sensor is a device that detects the presence of a gas in the atmosphere and generates an electronic signal directly proportional to the gas concentration. Gas sensors can be classified according to the operational mechanism. The majority of the sensors used for detecting volcanic gases are infrared and electrochemical. The first electrochemical sensors, built in the 1950, were used to measure oxygen concentration in air, and subsequently to detect toxic gases in industrial and working environment. The sensors differ according to their use and they can have differ sensibility, accuracy and life time. As for other scientific instruments, their operation is based on measurement of an electrical signal whose amplitude is directly proportional to concentration of the target gas in air.

Generally speaking, an electrochemical sensor (fig. 2.1) is made up of a small cell in which noble metal electrodes are immersed in an electrolyte. The three electrodes have different functions:

- A measuring electrode (working electrode or anode), which creates a current by means of redox reaction with the gas to be measured.
- A counter electrode (or cathode), together with the measuring electrode completes the circuit by reducing a chemical species (normally oxygen), or oxidizing it.
- A reference electrode, present in most modern sensors and whose function will be described below.

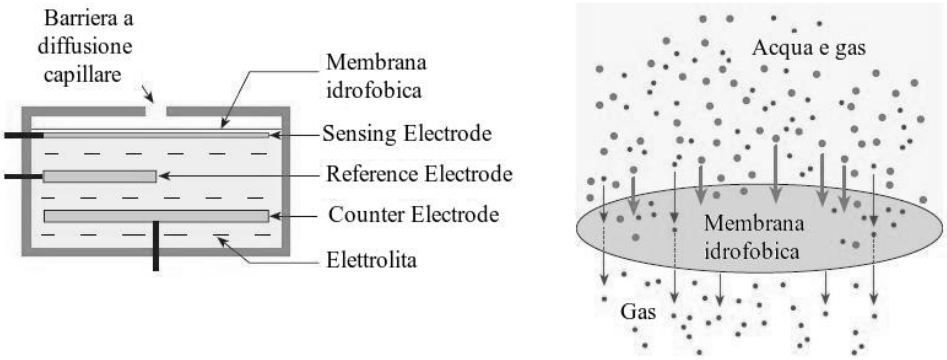

Figure 2.1 Electrochemical sensor scheme.

The sensor is equipped with a capillary opening through which the gas cab pass through. The gas then spreads through a hydrophobic membrane, reaching the electrodes.

A reagent gas passing through the sensor membrane undergoes oxidation or reduction which reacting contact with the electrodes. The materials making up the electrodes are chosen depending on the species to be detected, owing to its catalyzing role for a specific redox reaction.

For example, carbon monoxide, a reduced gas, is oxidized turning the measuring electrode into a cathode. The reactions that involve carbon monoxide in the different electrodes are as follows:

$2CO + 2H_2O \Rightarrow 2CO_2 + 4\,H^+ + 4e^-$	Measuring electrode	2.1
$O_2 + 4H^+ + 4e^- \Rightarrow 2H_2O$	Counter electrode	2.2
$2CO + O_2 \Rightarrow 2CO_2$	Reaction	2.3

By connecting a resistor between the measuring electrode and the counter electrode, a measurable current will be generate permeating quantitative determination of the gas concentration. For this reason, two-electrode electrochemical sensors are also referred as amperometric. The most modern sensors require a supply current because they have a third electrode, called reference electrode, used to maintain a slight steady and constant voltage with the measuring electrode (biasing). The biasing is used to eliminate interference due to reactions that take place on the counter electrode, influencing the sensitivity of the sensor. In fact the potential of this electrode tends to vary and sometimes increases if the concentration of the gas increases. The electrochemical sensors with this type of circuit is called potentiostatic. A constant gas influx is guarantee from a pump. The position of the pump with respect to the sensor must be such as to avoid the conditions of gas over-pressure. This latter would lead to the reaction of a greater quantity of gas with the electrodes, falsifying the measurement.

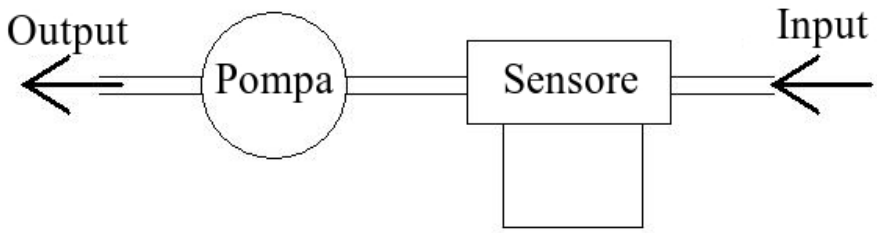

Figure 2.2 Scheme of a pump with respect to sensors.

Electrochemical sensors have the advantage of good linearity, sensitivity and accuracy, but are afftected by dependence on environmental parameters: temperature, relative humidity, pressure and oxygen concentration in the air. The operating temperature range in modern sensors is from 0 °C to + 30°C. At high temperatures, the redox reactions occurring on the electrodes can be facilitated and the sensor could over-estimate the real gas concentrations. At low temperatures, instead, the reactions can slow down causing an opposite effect. The temperature effect is typically 0.5% to 1.0% per degree centigrade, depending on the manufacturer and type of sensor.
Pressure dose not directly influence the efficiency of electrochemical sensors. However, it may happen that excessively high pressures push in the sensor a greater quantity of gas that, reacting with the electrodes, does increase the concentration detected. This effect rapidly cancels out when the pressure falls within the operating range.
Two other important parameters that may condition the lifetime of sensors and signal accuracy are humidity and presence/absence of oxygen. Electrochemical sensors made up of an electrolyte can be damaged from long exposures to environments with high or low relative humidity values (Rh <15% or Rh> 90%) that cause variations of the volume of water present inside the cell. An increase in volume of water may cause, for example, a rupture of the hydrophobic membrane, while a decrease can lead to phenomena of crystallization of the electrolyte. In some cases, the sensors can work in environments with high concentrations of reactant gases and low concentrations of oxygen. A long exposure to these environmental conditions can shorten the lifetime of the sensor, and therefore prevent its correct operation.
All components of an electrochemical sensor are chosen in such a way as to make it more sensitive to the gas it needs to detect. Despite this, other gases tend however to interfer with the measurement. The degree of interference for each gas is specified in the sensor data sheet, but has to be verified/estimated using standard gases in the laboratory. The sensor response to the interfering

gas tends to be linear, so the interference factor is easily calculable for each couple of gas (e.g. SO_2-H_2S and H_2-CO).

CiTiceL electrochemical sensors

This sensor brand is used in all the Multi-GAS made at UniPa (*Aiuppa, 2015*). The following sensors were used aboard of the Multi-GAS used in the present study (Table 2.1).

Table 2.1

Sensor	Gas	Range (ppmv)	Resolution (ppmv)	Temperature range (°C)	Accuracy
TD2F-1A	SO_2	0 - 200	0.5	-20 +50	2% of signal
TC4-1A	H_2S	0 - 50	0.25	-20 +50	1% of signal
T3HYT	H_2	0 - 200	2	-20 +50	2% of signal

For their calibration they are used two gases: CO_2 for zero concentration and two standards: SO_2 100.7 ppmv e H_2S 38 ppmv. The choice of using only two points to construct a straight line calibration is possible thanks to the good linearity of the response of the two sensors to the gases to be measured (figure 2.3 and figure 2.6). Accuracy is guaranteed as 2% and 1% of signal for SO_2 and H_2S respectively. The error associated with each Multi-gas derived ratio is $\leq \pm 15\%$ for H_2S/SO_2. Interference of SO_2 gas on the H_2S sensor (15 – 20 %) was determined during calibration procedure and corrected with the Ratiocalc software.

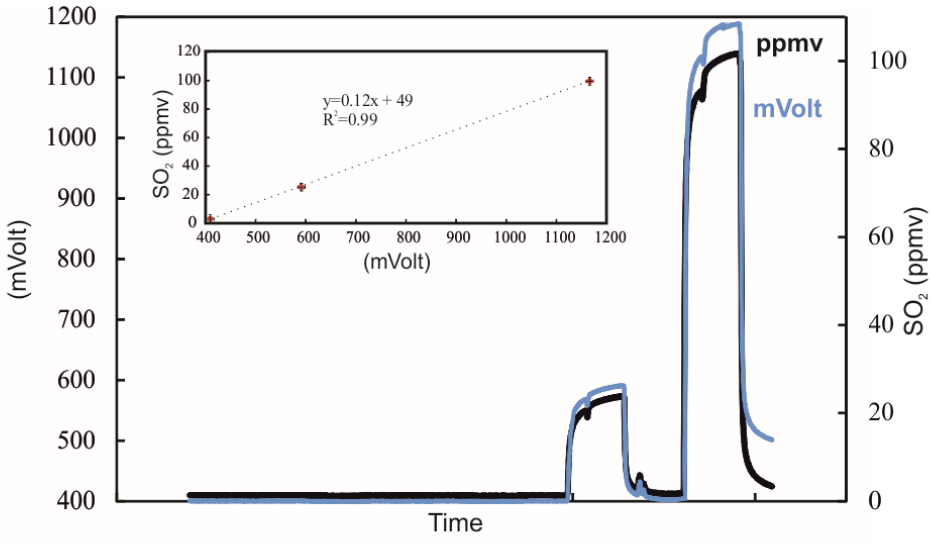

Figure 2.3 Experimental curve of SO_2 calibration with two standards: 25 and 100.7 ppmv respectively.

2.1.2 **Spectroscopic sensors**

Carbon dioxide absorbs energy in the infrared portion of the electromagnetic spectrum. Absorption occurs at frequencies corresponding to the frequency resonance of the bonds between the atoms of the molecule. The greater the amount of CO_2 molecules in the air, the higher its concentration, and the greater the absorption of energy in the spectrum. In the most common spectroscopic sensors for CO_2 detection, the source of infrared radiation is a hot tungsten filament. The light emitted passes through two filters to redefine the spectrum of radiation. A first filter allows passage of only the desired frequencies absorbed by the CO_2, while the second filter transmits light at a frequency not absorbed by CO_2. So, in the absence of CO_2, the intensity of the two radiations reaching the two photomultipliers are maximum and equal; as the CO_2 concentration increases, the intensities of the two light beams will differ by a quantity proportional to the gas concentration. The ratio between these two intensities is converted into a relationship between two electrical signals that automatically compensates for any oscillations of the intensity of the source radiation.
The spectroscopic sensor on board of Multi-GAS instrument is a GASCARD NG made from Edinburgh sensor brand.

Table 2.2

Sensor	Gas	Range (ppmv)	Resolution (ppmv)	Temperature range (°C)	Accuracy
GASCARD NG	CO_2	0-3000	0.5	0 - 45	± 2% of range

The Gascard CO_2 sensor has no interference with any gas, and its calibration is more stable than for electrochemical sensors. Calibration is obtained by exposing the sensor to a series of gas standards of known gas concentration (figure 2.6) and adjusting the ZERO and SPAN of the sensor accordingly. Accuracy of spectrometer is guaranteed as ± 2% of range (60 ppmv). The error associated with each Multi-GAS derived ratio is $\leq \pm 20\%$ for CO_2/SO_2.

2.1.3 **Multi-GAS**

In a Multi-GAS, the three sensors described in the previous paragraphs are assembled inside of a waterproof case of size 30 x 20 x 15 cm together with one pump (flux, 1.2 liters per minute, lpm), two electronic boards (input and data logger) and one internal battery as power supply. The Campbell CR6 data logger we use in the present Multi-GAS configuration can receive the output voltages of the sensors and convert them digitally, using a 16 bit A /

D converter. Data are sampled at 0.5 to 1 hz and stored in a micro SD card. The CR6 data logger allows direct connection to Ethernet with 10/100 Ethernet RJ-45 or Ethernet over USB, and allows to manage parameters of the instrument via software. Knowing relative humidity and temperature in volcanic gases H_2O concentration can be calculated. Alternatively it can be measured directly with infrared sensors (Licor Li-840A). Relative humidity and temperature of gas are measured with a thermo-igrometer (Galltec sensor, measuring range, 0 – 100 % Rh, accuracy, ± 2%) and water concentration in volcanic gas is obtained using the equation (2.4) suggested by *Buck (1981)*:

$$H_2O[ppm] = 6.1121 * (1.0007 + 3.46 * P^{-6}) * e^{\frac{17.502*T}{240.97+T}} * Rh * 10^4 P^{-1}$$
(eq. 2.4)

A GPS and a Wi-Fi modem allow complete management of the instrument. The on-board Wi-Fi modem also allows connection with smartphone or tablet application for a real time monitoring and full control of the instrument. GPS module allows georeferencing measurements.
The Multi-GAS can work in different modes: *permanent station, semi-permanent station* and *mobile* mode. In *permanent station* mode, the instrument is installed on an active crater, powered by external batteries and solar panels. In this configuration, the instrument is programmed to work in fully automated way to perform several measurement cycles per day. Thanks to the reduced consumption, the instrument has a great autonomy in any weather conditions. The data can be transferred via radio link or internet connection and can be processed in real time. In *semi-permanent* mode, a light, basic version of instrument (with reduced powering, size and weight) is temporarily installed in a remote volcano for a short period (measurement intervals of a few weeks or months). In a *mobile* mode, the Multi-GAS is used in a field survey around a crater rim or fumarolic field. A silicone tube about 2 meters long allows capturing gas at a height of about 30 cm from the ground. The GPS module saves spatial coordinates in order to map the lateral chemical heterogeneity of the target system.
During this work, the Multi-GAS instrument was installed at Pacaya (Guatemala), Rincón de la Vieja (Costa Rica) volcanoes in a fully automated *semi-permanent* configuration, and as a permanent station at Masaya (Nicaragua). During field trips at Santa Ana volcano (El Salvador), it was used as a *mobile* station.

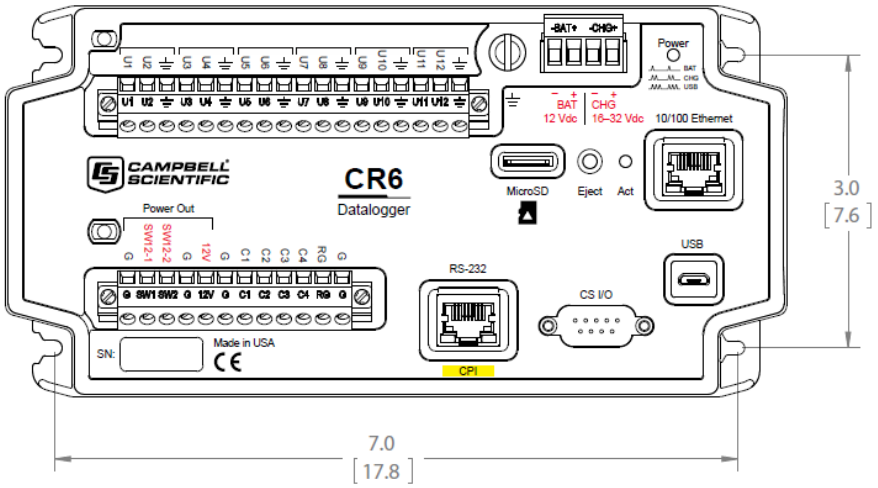

Figure 2.4 Campbell scientific CR6 data logger.

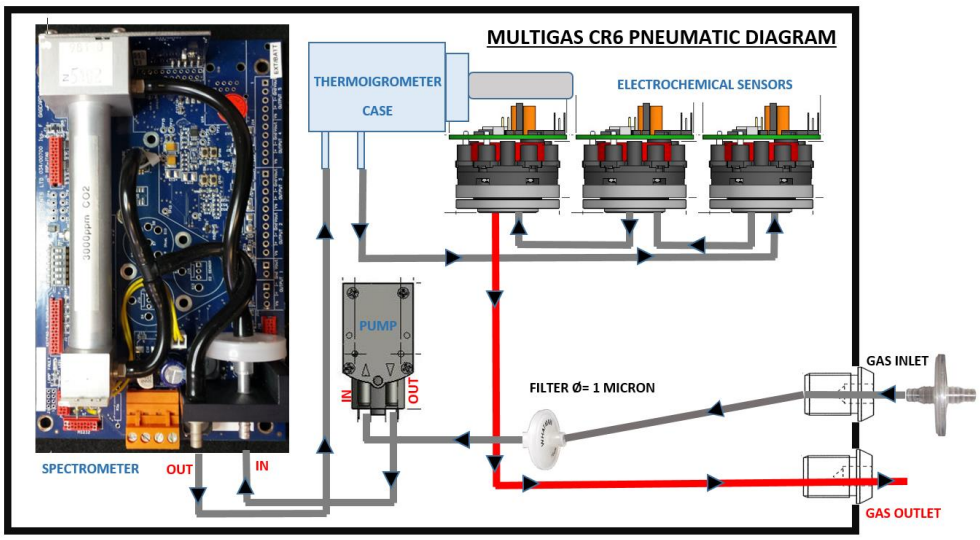

Figure 2.5 Multi-GAS Scheme and components

2.1.4 **Calibration**

Calibration of gas sensors is performed by actively pumping a gas standard at constant and low flow (0.2-2 lpm) into the sensor kit. Two-point calibrations are sufficient to calibrate both electrochemical and infrared sensors that respond linearly to gas abundances within their specified gas range. Sensor calibration consists in then commonly accomplished using two standards: one for zero (commonly air) and one for the full scale of the sensor. In fact, multiple gas standards can be used to check linearity and sensors' precision and accuracy. The gas standard is flown into the Multi-GAS from a 5 L tedlar bag. The constant gas flux is controlled by the pump placed at the end of the circuit. Silicone tubes of variable diameter are used for the various connections.

Before a reliable concentration value can be read, it is appropriate to run the system with the standard gas for a certain period, so to remove air contamination and bring the sensor into normal operation (warmup). At this point, the operator will be able to check the calibration status of the sensor and make the necessary adjustments, if needed. The calibration can be performed by operating the sensor system and cards with two methods: electronic or software. As anticipated in the previous paragraphs, the electronic boards of the sensors have trimmer, zero and span that allow to adjust the output voltage in response to the different gas concentration values to be detected: this allows us to make a first calibration on the sensors called characterization. At the end of first calibration step with a gas standard, by connecting the Multi-GAS to a computer or with a micro SD, we can access to the data using the *Ratiocalc* software (*Tamburello 2015*). This allows processing the data to adjust a series of parameters that define the concentration values, minimum and maximum, associated to the respective output voltage produced by sensors. Ratiocalc has a tool for sensor calibration analysis, and calculation of best-fit lines. Figure 2.6 show the experimental calibration curves for SO_2 and H_2S electrochemical sensors. The electric outputs of these sensors (mVolt) are finally converted into counts with an A/D converter, and the output saved into a data logger file.

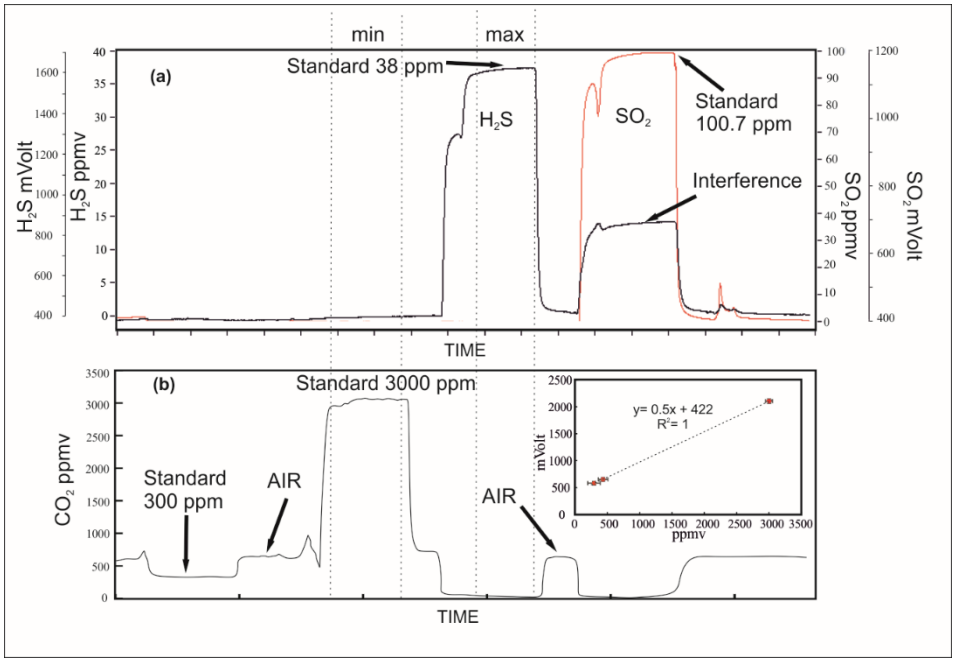

Figure 2.6 Figure show a calibration sequence. (a) Experimental curve of calibration of SO_2 and H_2S electrochemical sensors. (b) Experimental curve of calibration of CO_2 with two standard. Standard CO_2 gas (without sulphur species) has used as zero for SO_2 and H_2S gases.

2.1.5 **Processing Multi-GAS data**

Multi-GAS data are processed with Ratiocalc software (*Tamburello 2015*). The installer and manual are downloadable from: https:// sites.google.com/site/giancarlotamburello/volcanology/ratiocalc.

This software allows to menage volcanic gas concentration data, ratios calculation, cross–sensitivities between gases and sensors, and H_2O calculation. Ratiocalc can calculate ratios with two different methods best-fit regression (*Aiuppa et al., 2005*) and point to point ratio (*Tamburello 2015*).

Multi-GAS data are used to derive gas concentrations in a volcanic plume and/or fumarolic plume, and to derive CO_2/SO_2, SO_2/H_2S and H_2O/H_2 molar ratios by taking the gradient of the best-fit regression lines in appropriate scatter plots. To explore the time-variability of gas compositions, a number of such scatter plots are sequentially created by Ratiocalc (*Tamburello 2015*), each from data acquired during individual time windows of a few minutes. Measurement intervals were considered null (e.g., no ratio is calculated) when CO_2 and SO_2 concentrations are below fixed threshold values (e.g., $SO_2 < 1$ ppmv) or the $R^2 < 0.6$. Interference between electrochemical sensors can be calculated and corrected in the full dataset, using results of the calibration (Fig. 2.6). An integrate map module in ratiocalc software allows to explore data spatially when the Multi-GAS is used in a *mobile* mode in order to investigate different gas manifestations and create a map of the gas concetrations. Ratiocalc allows exporting processed data, scatter plots and figures.

2.2 **UV Camera**

A dual UV camera system employs two digital cameras, each of model JAI CM 140 GR, with 10-bit digitization and 1392×1040 pixels. These cameras mount CCD sensors sensible to UV light. The cameras are equipped with Uka Optics quartz lenses with a focal lens of 9 - 12 mm, and a field of view of 37° to 45°. These quartz lenses do not affect the investigated wavelength, the focus is manual and the iris ranges from 2.8-16. An Edmund Optics pass-band filter (cantered at either 310 nm or 330 nm) is placed on the back of each lens (see below).

The camera operates on the principle of contrasting the brightness of the pixels in the presence/absence of SO_2 absorption when measuring back-scattered sunlight (skylight). This is achieved using two Edmund Optics pass-band filters placed between the lenses and the CCD of the two simultaneously operating cameras. The use of the two filter method (*Kantzas et al. 2010*), with simultaneous image acquisition from two cameras, allows compensating for aerosol attenuation/backscattering, while minimizing any temporal mismatch associated with filter changes on a single camera system (*Mori and*

Burton, 2006; Bluth et al., 2006). It also allows increasing sampling rate up to 2 synchronous images every 2 seconds taken from two cameras (*Kantzas et al. 2010*).
In the dual camera system, a first filter, named as α, transmits light at 310 nm, strongly affected by the presence of SO_2. The second filter, β, mounted on the second co-aligned camera, transmits light at 330 nm that is not absorbed by SO_2. Sulphur dioxide absorption ends at ~320 nm (*Vandaele et al., 1994*) (fig. 2.7), and filters α and β operate in the range 300-320 nm and 320-340 nm respectively. A qualitative measure of absorbance A can therefore be obtained per camera pixel, following eq. 2.4:

$$A = -\log_{10}\left[\frac{\left(\frac{IP_{310}}{IB_{310}}\right)}{\left(\frac{IP_{330}}{IB_{330}}\right)}\right] - A_0 \qquad \text{(eq. 2.4)}$$

where A is the absorbance, I^{310} and I^{330} are the pixel intensities associated with cameras mounting the 310 or 330 nm filter, while A_0 is the absorbance level associated with clear background sky sub-area of the image that is assumed to be unaffected by SO_2 absorption.

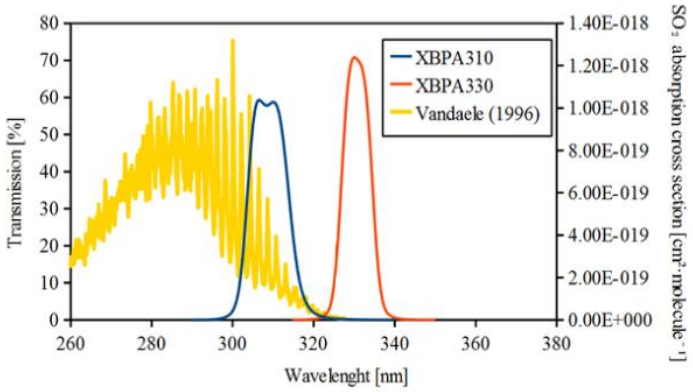

Figure 2.7 Vandaele SO_2 cross section and the two pass-band filter range.

Absorbance (eq. 2.4) is then converted in SO_2 column density integrating data from a co-located ultraviolet spectrometer, pointing to a known sub-area within the camera field of view. This allows us to obtain in real-time the proportionality ratio (slope and intercept of the calibration curve) between absorbance and SO_2 column densities, using the method described in *Lubcke et al.* (2013).
The use of the UV spectrometer allows to quantitatively measuring the full UV spectrum discriminating the different bandwidth contributions. This allows us to fit the theoretical SO_2 absorption cross-section (*Vandaele et al.*,

1994) with the differential absorption between two consecutive spectra, which are acquired at 5 seconds steps. The Ocean-Optic USB2000+ Spectrometer in use has a Sony ILX511B Linear Silicon CCD Array Detector at 2048 pixels on-board, with a Wavelength Response of 200-1100 nm and a dynamic range of 8.5 x 108 and a SNR of 250:1 at full signal. Calibrated SO_2 column densities over the entire images are then obtained by integrating images achieved by the UV-camera with information achieved by the spectrometer.

The final derived SO_2 column density image is used for obtaining a profile orthogonal to the plume direction. The integrated profile (integrated column amount or ICA) is then multiplied by the plume transport speed to calculate a SO_2 flux.

2.2.1 **Data processing with Vulcamera**

The two co-aligned cameras capture sequential image of a volcanic plume, with an acquisition rate of ~1 Hz and are able to resolve up to ~5 m. The collected data are post-processed using the Vulcamera software (*Tamburello et al., 2011*), following the methodology of *Kantzas et al. (2010).*

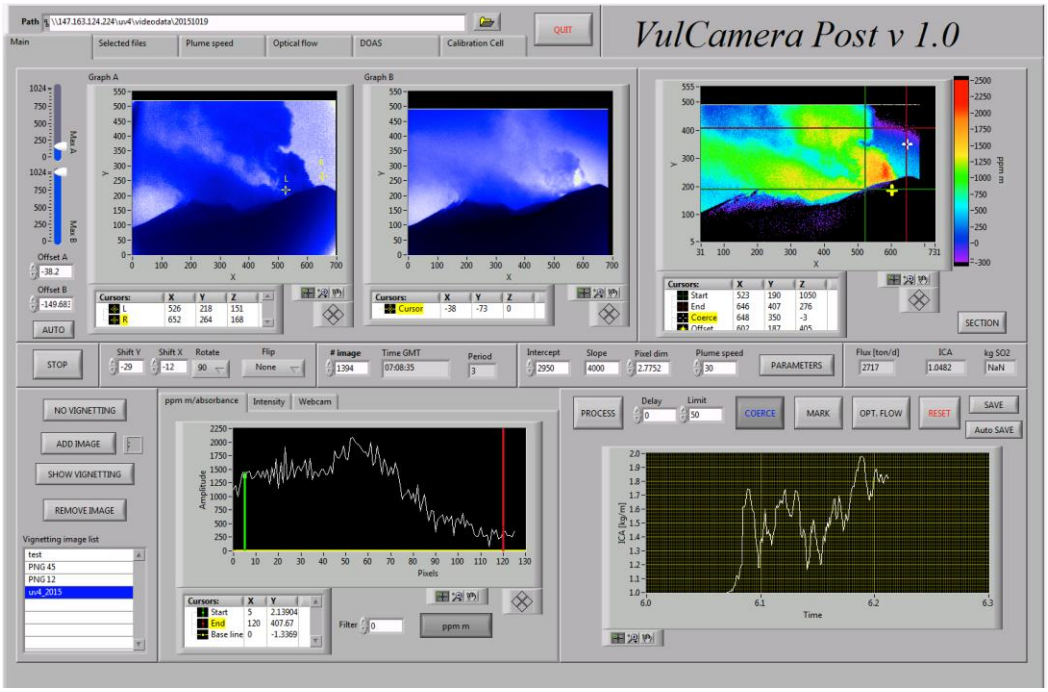

Figure 2.8 The main frame of Vulcamera Software. On the top are displayed the two pass-band filtered uv images and the absorbance images. On the bottom there are the ICA time series graph, on the right, and the pixel vs amplitude graph on the left

Vulcamera is a stand-alone software with a user-friendly user interface for performing exploratory analysis on UV image dataset. The main panel of Vulcamera (Figure 2.8) displays the raw 310 and 330 nm filtered images in

blue colour scale, called "Graph A" and "Graph B" respectively. A SO_2 column density (SCD) image is simultaneously calculated and displayed using the entered intercept and slope parameters. A SCD profile is obtained by selecting its initial and final positions in the "Graph A".

The Integrated Column Amount (ICA) is calculated from the bottom left graph by integrating the white curve within the green, red and yellow lines. The background offset is selected with the white cursor in the SCD pseudo-colour graph, and automatically subtracted. A first order correction of the dilution effect is performed by subtracting an average UV intensity measured on a dark background framed (e.g. a portion of the image targeting a volcanic rock surface), assuming a negligible UV reflectivity and therefore a dominant contribution from scattering effects. The dark background is selected with the yellow cursor in the SCD graph.

If the raw images exhibit an intense darkening at the edges (especially if the passband filters are placed in front the lenses), Vulcamera allows to correct it with a correction mask calculated from an image of a homogeneous clear sky as background.

Plume transport speed can be calculated in Vulcamera following two methods: cross correlation between ICA time series, and optical flow algorithms. The former consists in calculating two distinct ICA time series from two parallel plume profiles separated by a certain distance (dx), that will exhibit a time shift (dt) as a function of the plume speed. The shift is due to the time required for a puff of gas to travel from the first to the second profile. The cross-correlation function will find an average time shift in an interval of time, and plume speed is calculated as dx/dt.

Optical flow algorithms have been extensively documented (*Peters et al., 2015*) as accurate methods for calculating speed vectors of trackable features of a volcanic plume (e.g. gas puff edges). The algorithms analyze the apparent motion of image objects between two consecutive frames under the assumptions that the pixel intensities of an object do not change significantly between consecutive frames, and that the neighbouring pixels have similar motion. Vulcamera allows using two different optical flows algorithms: Lucas Kanade and Horn and Shunck (*Bruhn et al., 2005*). These optical flow algorithms work by selecting a region in the SCD image within the red and green cursors. A dedicated front panel allows to change the optical flow parameters. A plot with speed vectors allows selecting the best algorithm and setting, and applying different filters (smoothing and direction) in order to reduce errors in the plume velocity calculation.

2.3 **Rocks**

I selected the most representative samples of the recently history of Pacaya volcano following *Matias et al.,* (2012). Rocks from El Salvador are collected

on Ilopango, Santa Ana and San Miguel volcanic systems. Ilopango sample derived from the dacitc Isla quemada dome at the center of the lake forming during the last vigorous eruption in the 1879–1880. Both Santa Ana and San Miguel samples were collected into the active craters. The entire procedure of sample preparation of whole rocks and olivines crystals was performed at INGV Palermo laboratories. Rock samples were mechanically fragmented using a crusher. The crushed samples were then sieved in order to select size fractions within the range of 0.5, 1 and 2 mm. The two fractions 0.5 and 1 mm were used for noble gases measurement. The small fraction (< 0.5 mm) was used for major and trace elements analysis.

2.3.1 **Noble gases in fluid Inclusions**

Analyses of He, Ne, and Ar concentrations and isotope ratios from FI were performed at the laboratory of INGV, Sezione di Palermo. The procedure of sample preparation and analysis is described in *Di Piazza et al.* (2015), *Rizzo et al. (2015), Robidoux et al.* (2017), and *Battaglia et al*. (2018). Olivine crystals were separated from the glass in the two fractions (0.5 and 1 mm) by using a heavy liquid (Na polytungstate) and then carefully handpicked under a binocular microscope; crystals with glassy and/or altered surfaces were discarded. The selected crystals were cleaned ultrasonically with successive treatments in diluted acid (6.5% HNO_3) and deionized water. Aliquots of 0.5 - to 1 g were analysed by single-step crushing in replicate measurements for elemental and isotope composition of helium, neon, and argon in fluid inclusions hosted in olivine crystals. A sieved aliquot of mineral was inserted into a stainless-steel bowl, and placed in a crusher capable of loading up to six samples simultaneously. The system was heated under pumping conditions for 48–72 h at 130 °C in order to reach an ultrahigh vacuum (1029 mbar). Samples were then crushed at room temperature (22 °C), and the gas released by the opening of fluid inclusions was purified in a stainless-steel preparation line in order to remove all species in the gas mixture other than noble gases. He, Ne, and Ar were cryogenically separated and introduced into mass spectrometers. Helium isotopes (^{3}He and ^{4}He) and ^{20}Ne were measured separately by two different split-flight-tube mass spectrometers (Helix SFT-Thermo). The ^{3}He/^{4}He ratios were corrected for atmospheric contamination based on the measured ^{4}He/^{20}Ne ratio (e.g., *Sano and Wakita*, 1985) and are expressed as Rc/Ra values. Argon isotopes (^{36}Ar, ^{38}Ar, and ^{40}Ar) were analysed by a multicollector mass spectrometer (GVI Argus) with an analytical uncertainty of ≤0.9%. The uncertainty in the measured amounts of He, Ne, and Ar elements was <5%. Typical blanks for He, Ne, and Ar were $<10^{-14}$, $<10^{-16}$ and $<10^{-14}$ mol, respectively, and were at least 1-2 orders of magnitude lower than values measured in the samples.

Figure 2.9 a) Mechanical separation of mafic inclusion in dacite rock from Ilopango dome. b) Separation of crystals with Sodium Polytungstate. c) Olivine crystals 0.5 mm.

2.3.2 **Major and trace elements**

Major and trace elements in whole rocks for Pacaya volcano were measured at the Activation Laboratories (Canada) using inductively coupled plasma–mass spectrometry (ICP-MS), in which rock samples digested under acidic attack were analyzed by a Perkin Elmer Sciex ELAN 6000, 6100, or 9000 ICP-MS device. Duplicate measurements indicate reproducibility was generally better than 3% for major-element analyses, 5% for highly incompatible elements (i.e., Rb, Ba, U, and Th), and 7% for rare-earth elements. Accuracy was quantified by comparing measured and certified values for standard references.

Chapter 3

3 Overview of the presented resulted and structure of the dissertation

In the following chapters, I report on the results of three years of research in which I conducted several measurement campaigns in Central America. The chapters constitute the main body of papers already published (chapter 4 and 5) or submitted (chapter 6). The last chapter, concerning the analisys of fluid inclusions hosted in olivine crystals (chapter 7), is currently being prepared for submission to a journal.

Chapter 4 "*The magmatic gas signature of Pacaya volcano, with implications for the volcanic CO_2 flux from Guatemala"* corresponds to content of a paper published on Geochemistry, Geophysics, Geosystems by A. Battaglia, M. Bitetto, A. Aiuppa, A.L. Rizzo, G. Chigna, I.M. Watson, R. D'Aleo, F.J. Juárez Cacao, and M.J. de Moor. In this chapter, I show the results of my first year of PhD during which I investigated Pacaya volcano using a multi-disciplinary approach. Results include Multi-gas plume measurements (8 days), direct gas sampling of fumaroles, UV dual camera measurements (for SO_2 Flux). Sampling of rocks erupted during some of the volcano's most recent eruptions was conducted, in order to explore the helium content and isotopes in fluid inclusions hosted in olivine crystals. Combining different information, our results contribute to understanding the magmatic gas signature of Pacaya volcano, to quantifying its gas output (CO_2, SO_2, H_2S, H_2), and to characterizing his helium isotopic signature with implication for regional geodynamics. Part of these rock results are also discussed, in a wider regional context, in chapter 7 "*Along arc variation".*

Chapter 5 *"Tracking Formation of a Lava Lake From Ground and Space: Masaya Volcano (Nicaragua), 2014–2017"* reports on the results contained in a paper published in Geochemistry, Geophysics, Geosystems by *Alessandro Aiuppa, J. Maarten de Moor, Santiago Arellano, Diego Coppola, Vincenzo Francofonte, Bo Galle, Gaetano Giudice, Marco Liuzzo, Elvis Mendoza, Armando Saballos, Giancarlo Tamburello, Angelo Battaglia, Marcello Bitetto, Sergio Gurrieri, Marco Laiolo, Andrea Mastrolia, and Roberto Moretti*. My main contribution in these scientific papers consisted in the installation of a permanent Multi-GAS instrument at Masaya volcano in Nicaragua, and in data processing/interpretation. In this work, we present a 3 years long and continuous volcanic gas record that illustrates the volcano's

degassing behaviour before and during the Masaya's lava lake formation event in 2015.

Chapter 6 *"Insights into the mechanisms of phreatic eruptions from high-rate instrumental observations of gas composition: Rincón de la Vieja volcano, Costa Rica"* makes the core of an article in revision (pending moderate revision) on Frontiers in Earth Science, authors *A. Battaglia, J.M. de Moor, A. Aiuppa, G. Avard, H. Bakkar, M. Bitetto, M. M. Mora Fernández, P. Kelly, G. Giudice, D. Delle Donne, H. Villalobos.* In this work, we present a ~3 month-long compositional record for the plume released by active crater lake of Rincón de la Vieja. During this interval, we detected and recorded several phreatic eruptions. Installation of a full-automated Multi-GAS at Rincón the la Vieja allowed characterizing, for the first time, the gas emitted during phreatic - phreatomagmatic events, to investigate the chemical proprieties and redox conditions of the sublimnic hydrothermal system, and to evaluate the possible explosion mechanisms and triggers.

Chapter 7 "*Along arc variation"* summarises work done on fluid inclusions in selected rocks samples collected in Central America during my PhD. In particular, the chapter reports results on helium isotopes in fluid inclusions from rocks of different volcanic systems in Central America: Pacaya (Guatemala), Santa Ana, San Miguel and Ilopango (El Salvador). Our aim is to refine our current understanding of the volcanic He signature along the Guatemala - El Salvador arc segment. In view of the lack of helium isotopes FI data for the northern part of CAVA, these new results add novel piece of knowledge in order to understand geodynamic and volcanic processes along the CAVA arc.

Chapter 4

4 The magmatic gas signature of Pacaya volcano[1]

4.1 Abstract

Pacaya volcano in Guatemala is one of the most active volcanoes of the Central American Volcanic Arc (CAVA). However, its magmatic gas signature and volatile output have received little attention to date. Here, we present novel volcanic gas information from in-situ (Multi-GAS) and remote (UV camera) plume observations in January 2016. We find in-plume H_2O/SO_2 and CO_2/SO_2 ratios of 2-20 and 0.6-10.5, and an end-member magmatic gas signature of 80.5 mol. % H_2O, 10.4 mol. % CO_2, and 9.0 mol. % SO_2. The SO_2 flux is evaluated at 885 ± 550 tons/d. This, combined with co-acquired volcanic plume composition, leads to H_2O and CO_2 fluxes of 2230±1390 and 700±440, and a total volatile flux of ~3800 tons/day. We use these results in tandem with previous SO_2 flux budgets for Fuego and Santiaguito to estimate the total volcanic CO_2 flux from Guatemala at ~1160±600 tons/day. This calculation is based upon CO_2/total S (S_t) ratios for Fuego (1.5±0.75) and Santiaguito (1.4±0.75) inferred from a gas (CO_2/S_t ratio) vs. trace-element (Ba/La ratio) CAVA relationship. The H_2O-poor and low CO_2/S_t ratio (~1.0-1.5) signature of Pacaya gas suggests dominant mantle-wedge derivation of the emitted volatiles. This is consistent with $^3He/^4He$ ratios in olivine hosted fluid inclusions (FIs), which range between 8.4 and 9.0 Ra (being Ra the atmospheric $^3He/^4He$ ratio) at the upper limit of MORB range (8±1 Ra). These values are the highest ever measured in CAVA and among the highest ever recorded in arc volcanoes worldwide, indicating negligible ^4He contributions from the crust/slab.

[1] Battaglia A., M. Bitetto, A. Aiuppa, A. L. Rizzo, G. Chigna, I. M. Watson, R. D'Aleo, F. J. Juárez Cacao, and M. J. de Moor, (2018). The Magmatic Gas Signature of Pacaya Volcano, With Implications for the Volcanic CO_2 Flux From Guatemala, *Geochemistry, Geophys. Geosystems*, vol. 19, no. 3, pp. 667–692.

4.2 Introduction

After nearly 200 years of dormancy, Pacaya volcano in southern Guatemala (Figs. 4.1and 4.2) entered a phase of renewed volcanic activity in 1961 (*Rose et al.,* 2013). Since then, open-vent volcanic activity has persisted at Pacaya, oscillating through periods of mild intra-crateric activity at the Mackenney cone and phases of more intense explosive (strombolian to lava fountaining) and effusive activity (*Matías Gomez et al., 2012; Rose et al.,* 2013). This nearly continuous activity has led to eruption of ≈0.2 km^3 of basaltic magma *(Rose et al.,* 2013), thought to have originated from de-compressional melting of a slightly metasomatized (by slab fluids/melts) mantle wedge (*Cameron et al.,* 2003*; Walker et al.,* 2003). Open-vent degassing activity at Pacaya during 1961-present has also produced sustained emission of magmatic volatiles into the atmosphere (*Rodriguez et al.,* 2004).

When considered against emissions from nearby Fuego and Santiaguito volcanoes (Fig. 4.1), Pacaya dominates the present-day Guatemalan contribution to the Central American Volcanic Arc (CAVA) gas budget (*Hilton et al.,* 2002*; Rodriguez et al.,* 2004*; Mather et al.,* 2006). Pacaya gas emissions are also likely to have been significant over the past several millennia, during which similar eruptive episodes, each lasting centuries, have occurred (*Eggers,* 1971*; Bardinzteff and Daniel,* 1992*; Conway et al.,* 1992).

In spite of the above, relatively little attention has been paid in characterizing magmatic degassing and gas signature at Pacaya. While magmatic gas compositions and fluxes are relatively well studied for other top gas CAVA emitters, such as Turrialba in Costa Rica (*Aiuppa et al.* 2014*; Conde et al.,* 2014*; Moussallam et al.,* 2014*; Di Piazza et al.,* 2015*; de Moor et al.,* 2016, 2017) and Masaya in Nicaragua (*Burton et al.,* 2000*; Martin et al.,* 2010*; de Moor et al.,* 2017), volcanic gas data are available for only two Pacaya fumaroles sampled in the early 1990s (*Goff and McMurtry,* 2000). The fumaroles sampled by *Goff and McMurtry,* (2000), however, were relatively low in temperature (84.5 and 342 °C), implying a non-negligible role of secondary processes (e.g., scrubbing of magmatic volatiles by hydrothermal reactions; (*Aiuppa et al.,* 2014, 2017)). According to the authors, the $\delta^{13}C$ values of these fumaroles were -2.8‰ and -3.1‰. On the other hand, *Sano and Williams* (1996) reported a very low $\delta^{13}C$ (-6.94‰) for a high-temperature volcanic gas sample (965°C) from Pacaya, although limited additional information is associated with this value for evaluating the extent of air contamination and magmatic degassing. In terms of $^3He/^4He$ ratio, only five data points (1 fluid inclusion and 4 fumaroles) are available from previous studies and yielded values between 2.9 and 7.9 Ra (*Poreda and Craig,* 1989*; Sano and Williams,* 1996*; Goff and McMurtry,* 2000), indicating

the influence of crustal contamination by radiogenic ^4He modifying the pristine signature. The volcano's SO_2 flux emissions have been repeatedly quantified in the past (*Andres et al.,* 1993*; Andres and Kasgnoc,* 1998*; GVN Bullettin,* 2002*; Rodriguez et al.,* 2004*; Bluth et al.,* 2007*; Dalton et al.,* 2010), but the fluxes of the two major magmatic gas components, H_2O and CO_2, have not yet been characterised.

Here, we report on the first magmatic gas (H_2O, CO_2, SO_2, H_2S, H_2) compositional data for Pacaya volcano. These results were obtained during a field campaign in January 2016, when a fully autonomous Multi-component Gas Analyser System (Multi-GAS) was deployed for 8 consecutive days on the rim of the Mackenney cone to measure the composition of the bulk plume released during continuous open-vent intra-crateric Strombolian activity. We combine these compositional data with simultaneous measurement of the volcanic SO_2 flux, obtained by a dual-UV Camera system (*Tamburello et al.*, 2012), to assess the Total (H_2O+CO_2+SO_2) Volatile Flux (TVF) from Pacaya. The source (mantle vs. slab) origin of the emitted magmatic volatiles is also explored by putting the inferred CO_2/SO_2 signature of Pacaya gas in the context of regional (CAVA) gas vs. trace element (in source magmas) relationships (*Aiuppa et al.,* 2014, 2017), and by reporting on the first $^3He/^4He$ results for olivine-hosted fluid inclusions from a set of recent Pacaya lavas.

Figure 4.1 Morphotectonic sketch of Central America, showing location of the active volcanic systems discussed in the text. Red, purple and yellow circles indicate Santiaguito, Fuego and Pacaya volcanoes, respectively. Grey symbols indicate position of other key CAVA volcanoes. Circles: Guatemalan volcanoes; triangles:

El Salvador volcanoes; squares: Nicaraguan volcanoes; rhombus: Costa Rica volcanoes. Symbols I, II, III, IV identify the morphotectonic zones described in Burkart et al., (1985). P= Ipala graben; G= Guatemala graben; JFZ= Jalpatagua fault zone.

4.3 Geological, volcanological and geochemical background

4.3.1 CAVA and Guatemala

The Central American Volcanic arc is a 1100 km-long volcanic front stretching along the continental margin associated with subduction of the Cocos plate beneath the Caribbean plate (Fig. 4.1). The convergence rate between the Cocos and Caribbean plates gradually increases toward the southeast, from about 7 to 9 cm/yr (*DeMets,* 2001) (Fig. 4.1). The age of the subducting Cocos lithosphere is approximately constant (about 26 Ma) along most part of the subduction zone, except along its south easternmost segment in central Costa Rica (17 to 25 Ma). The subducting lithosphere is divided into two segments by the Cocos Ridge, offshore of southern Costa Rica. The north-western segment is made of older and colder Cocos materials subducting at a relatively steep angle (65°) below El Salvador and Nicaragua, and at 55° beneath Guatemala (*Syracuse and Abers 2006*). The Cocos Ridge is generated by separation of the Cocos and Nazca Plates and is consequently younger and warmer (*Chan et al.,* 2002). According to *Carr* (1984) and *Case et al.* (1990), crustal thickness decreases from Guatemala (50-40 km) to Nicaragua (30 km), increases across Costa Rica and western Panama and then again thins in central Panama.

Variations in subduction parameters, including dip-angle, crustal thickness, extent of sediment under-plating, faulting style and subduction erosion (*Carr* 1984*; Carr* 1990*; Patino et al.*, 2000, *Walker et al.*, 2001), control the degree of source melting and determine a variable sedimentary fluid influx from the subducting Cocos plate. These in turn determine large along-arc geochemical variations in Central American lavas (*Carr et al.,* 1990*; Morris et al.,* 1990*; Leeman et al.,* 1994), with trace element proxies for slab fluids (such as Ba/La, U/Th, and Sr/Ce ratios) being highest in Nicaragua, and lowest in Costa Rica (*Sadofsky et al.,* 2008). The same geochemical tracers indicate that melts beneath Guatemala are generated by mixing of a Costa Rica MORB-like melt component with Nicaragua-like slab fluid-rich melts (*Sadofsky et al.,* 2008).

Volcanic gases do also exhibit significant along-arc variations. *Fischer et al.,* (2002) showed that N isotopes and N_2/He ratios in geothermal fluids vary along the volcanic arc, and indicate lower slab fluid contributions in Costa Rica than Guatemala and Nicaragua. Similar variations have also been observed for He and C isotopes (*Shaw et al.,* 2003*; Leeuw et al.,* 2007*; Di*

Piazza et al., 2015*; Robidoux et al.,* 2017), pointing to higher influx and recycling of C-rich sediments beneath Nicaragua, and a minimal slab contribution in the volcanic output in Costa Rica, in spite of similar sedimentary inputs at the trench (*Freundt et al.,* 2014). *Barnes et al.,* (2009), studying chlorine isotope variations along the Central American volcanic front, similarly demonstrated mantle-like Cl signatures in the northernmost (Guatemala and El Salvador) and southernmost (Costa Rica) ends of the front, and sediment- and/or serpentinite-derived signature in Nicaragua. Consistent results were obtained by (*Aiuppa et al.,* 2014) who explored the along-arc variations in volcanic gas CO_2/S ratios in the Costa Rica-Nicaragua segment of the arc.

Four different morphotectonic segments exist in Guatemala that result from the rotation of upper crustal blocks in northern Central America (Fig. 4.1). Zone I is un-affected by Neogene extensional tectonics, while extensional regime in Zone II resulted in large volcanic rock productivity. Zones I and II are separated by the Atitlan caldera complex. The structural line between zone II and zone III is the Misto fault, which also corresponds to the western margin of the Guatemala graben (Fig. 4.1), where the Amatitlan caldera complex is located. Zone III is a basin-and-range style structure and the principal movement is eastward, while Zone IV is characterized by arc-parallel pull apart-basins (*Burkart et al.,* 1985). In southern Guatemala, both E-W crustal extension (as evidenced by the existence of a series of N-S trending grabens; (*Burkart et al.,* 1985); Fig. 4.1) and right-lateral strike-slip movements (in the Jalpatagua Fault Zone, JFZ) are observed. Pacaya volcano lies at the intersection between the Guatemala graben and the JFZ (*Cameron et al.,* 2003).

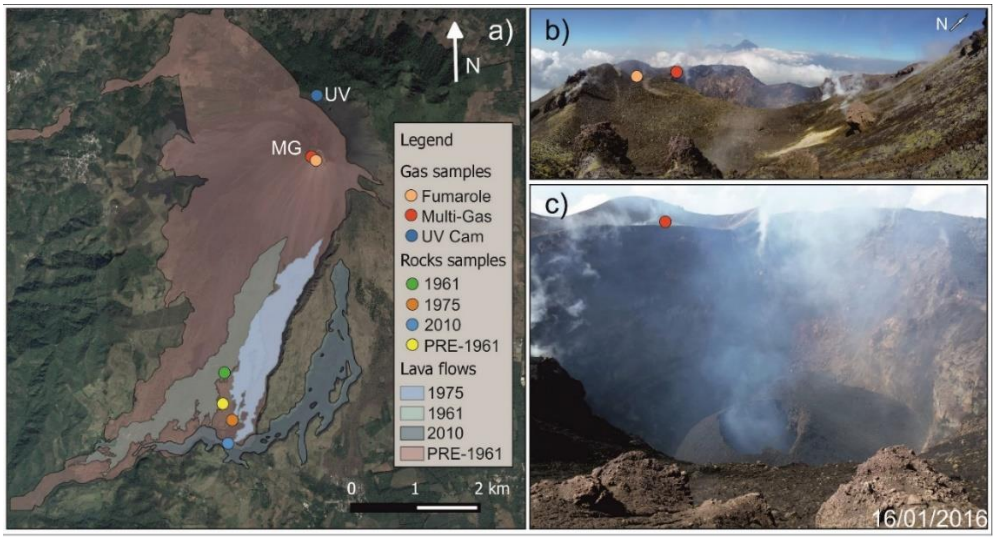

Figure 4.2 a) Simplified geological map of Pacaya volcano, modified from Matías Gomez et al., (2012). The figures shows fumarole and rock sampling sites, the UV camera measurement site (UV Cam), and the Multi-GAS installation site (MG); b)

view of Pacaya crater taken from the south-eastern crater rim. Fuego volcano is visible in the background. Symbols are as in a); c) View of Mackenney crater, taken from south-eastern portion of the crater rim. The Multi-GAS installation site is shown by red circle.

4.3.2 **Pacaya volcano**

Pacaya volcano, one the most active volcanoes in Central America, is a large volcanic complex on the southern fault zone of the Amatitlan Caldera (*Wunderman and Rose* 1984), only 20 km south of the centre of Guatemala City, the Guatemala capital. The Pacaya volcanic complex comprises an ancestral andesitic strato-volcano, a series of rhyodacitic to andesitic lava domes, and the modern Pacaya basaltic composite volcano (2552 m high) (*Conway et al.* 1992). *Eggers* (1971) subdivided the activity of Pacaya into three stages. Phase I was characterized by growth of a large, ancestral andesitic cone; this old volcano was largely eroded. The onset of phase II (about 0.16 Ma) was marked by an increase in the volcano's explosivity, with the eruption of voluminous pumice-bearing deposits, and the formation of andesitic-dacitic lava domes such Cerro Grande and Cerro Chiquito (these events are identified as phase III in (*Bardinzteff and Deniel,* 1992)). Phase III started ~400 B.P. (divided in initial, historical, and modern sub-phases) and produced primarily basaltic lava flows through to the present day. These lavas are mostly porphyritic olivine-bearing basalts exhibiting no significant temporal chemical or petrographic variation (*Egger* 1971; *Bardinzteff and Deniel,* 1992). A series of collapse events affected ancestral Pacaya between 400 and 2000 years B.P., forming a large collapse amphitheatre and a debris avalanche that travelled 25 km S-SW. Historical Pacaya encompasses the mid sixteenth century to 1861. Before this, Pacaya was possibly active in 1585, from ca. 1651 to 1678, and again in 1775 (*Rose et al.,* 2013). After a repose period between 1860 and 1960, volcanic activity resumed in 1961 with modern Pacaya, which has since then shown nearly continuous strombolian activity and extrusion of lava from the Mackenney cone (*Matías Gomez et al.,* 2012*; Schaefer,* 2012). The Mackenney cone, initially asymmetrical, began to grow in 1965 with the collapse of an amphitheatre that developed in 1961. There are not significant petrographic differences between initial, historic, and modern lavas, all showing olivine and plagioclase phenocrysts (up 45 wt. %) and microphenocrysts, and minor clino-pyroxene and magnetite microphenocrysts. Modern Pacaya lavas have progressively become slightly more mafic in composition (*Bardinzteff and Deniel,* 1992*; Matías Gomez et al.,* 2012).

4.4 Materials and Methods

4.4.1 Multi-GAS

The composition of the Pacaya volcanic gas plume was investigated using a custom-made Multi-component gas analyser system (Multi-GAS) (*Aiuppa et al.,* 2005*; Shinohara,* 2005). Gas measurements were carried out during January 14-22, 2016, when a fully autonomous Multi-GAS was temporarily installed on Pacaya summit to measure the in-plume concentrations of CO_2, SO_2, H_2S, H_2 and H_2O. The Multi-GAS was installed on the northwest rim of Mackenney cone (Lat, -14°22'55.48"N; Long 90°36'8.87"O), downwind the main direction of plume transport (Fig. 4.2). The Multi-GAS was powered by an external (12 V, 40 Ah) battery, and acquired data at 0.1 Hz rate during 4 measurement cycles per day, each 30 minutes long (start time of the cycles, 00:00, 06:00 and 12:00, 18:00 GMT-time). SO_2, H_2S and H_2 concentrations were measured with specific electrochemical sensors (models TD2G-1A, TC4E-1A, TE1G-1A, respectively; all from City Technology). CO_2 concentrations were measured using an on-board spectrometer (Gascard EDI030102NG), while H_2O concentrations were derived from co-acquired temperature, pressure and humidity readings, as in previous work (*Aiuppa et al.,* 2014, 2015). All data were acquired and stored in a Campbell scientific data logger (model CR6), and post-processed with the Ratiocalc software (*Tamburello,* 2015) to obtain ratios between volatile couples (Tab. 4.1). Ratiocalc automates the standard procedure (*Aiuppa et al.,* 2005*; Shinohara,* 2005) of inferring volcanic gas ratios by taking the gradient of the best-fit regression lines in scatter plots of co-measured gas species concentrations. The error associated with each Multi-GAS derived ratio is $\leq \pm 20\%$ for CO_2/SO_2 and $\leq \pm 30\%$ for H_2O/SO_2.

4.4.2 UV camera

On January 16, we used a dual-UV camera (same as in *Tamburello et al*.,(2012)) to acquire time-series of the volcanic SO_2 flux. Observations were carried out from an observational point situated on the northern volcano's flank (14°23'26.91"N, 90°36'5.91"O) at a distance of 940 m from the crater and 2273 m elevation a.s.l. (see Fig. 4.2) for 4 consecutive hours. The dual UV camera system used two co-aligned cameras (JAI CM 140 GR cameras, with 10 bit digitization and 1392 × 1040 pixels), with optical filters centred at either 310 nm (camera 1; affected by SO_2 absorption) or 330 nm (camera 2; not affected by SO_2 absorption). Absorbance *A* for each camera pixel was calculated as (*Kantzas et al.,* 2010*; Tamburello et al.,* 2012):

$$A = -log_{10}((IP_{310}/IB_{310})/(IP_{330}/IB_{330})) \qquad (1)$$

where IP and IB are, respectively, dark image-subtracted plume and background sky images taken with the two co-exposed cameras. Image sequences were post-processed using the Vulcamera software (*Tamburello et al.,* 2011) to derive time-series of integrated SO_2 column amounts (ICAs) along a cross-section of the plume. These were converted into SO_2 fluxes multiplying by a time series of plume transport speed, with the average of 8.2 ± 4 m/s, derived by an optical flow algorithm integrated in Vulcamera (see *D'Aleo et al.,* (2016) for details).

4.4.3 Direct sampling

During the field campaign, we collected gas samples from two low-temperature fumaroles (80°C), located on the northwest rim of the Mackenney cone. These fumaroles were aligned along a 15-20 m radial fracture trending away from the crater. For each of the two fumaroles, we sampled two glass flasks. Due to the ongoing Strombolian activity, access to the eastern part of the inner crater, where higher temperature fumaroles are possibly present, was not possible due to safety reasons. During sampling, a stainless steel tube was inserted into the fumarolic vent until thermal equilibration with the fumarole gases. Then, a 3-way valve was connected to the tube, a 100 ml syringe and a glass flask in order to collect the gases. The collected gas samples were analyzed for their chemical composition and $\delta^{13}C$ of CO_2 at INGV (Table 4.2). The concentrations of He, H_2, O_2, N_2, CO, CH_4, and CO_2 were determined using a Perkin Elmer Clarus 500 gas chromatograph equipped with a 3.5-m Carboxen 1000 column and 2 detectors (a thermal conductivity and a flame ionization detector, respectively), with analytical errors of < 3%. The C isotope composition of CO_2 (expressed as $\delta^{13}C$ ‰ vs. V-PDB) was determined using a Thermo (Finnigan) Delta Plus XP CF-IRMS, connected to a Trace GC gas chromatograph and a Thermo (Finnigan) GC/C III interface. The gas chromatograph, equipped with a Poraplot-Q column (length 30 m, i.d. 0.32 mm), kept at a constant temperature of 50 °C, uses He as the carrier gas. The analytical uncertainty was ±0.1‰. Due to the high extent of air contamination, samples were not analyzed for noble gases.

4.4.4 Chemistry of rocks and olivine crystals

In January 2016, fresh rock samples were collected on the southern flank of Pacaya volcano from outcrops of the following eruptions: Pre-1961 (Cerro Chino cinder cone and Pacaya composite cone with undivided lava flow, (*Egger*, 1971); hereafter referred as pre-1961), 1961, 1975, and 2010. All samples are basaltic lava flows, according to modern Pacaya behaviour. Outcrops were selected from volcanics of the recent eruptive activity that are

richest in olivines (based on previous results in *Bardinzteff and Deniel*, 1992*; Wardman et al.*, 2012*; Matias et al.*, 2012*; Rose et al.*, 2013). Olivine phenocrysts are the most suitable for studying He, Ne, and Ar in fluid inclusions (FI), because they effectively retain the small helium atoms within the crystal's structure, thus avoiding (or reducing) any diffusive effect. In addition, olivines are among the first mineral phases crystallizing from a basaltic melt. The collected rocks were initially characterised for their whole-rock chemistry and mineral chemistry of olivine host crystals. Major and trace elements in whole rocks (Suppl. Tab. 1 and 2) were measured at the Activation Laboratories (Canada) using inductively coupled plasma–mass spectrometry (ICP-MS), in which rock samples digested under acidic attack were analyzed by a Perkin Elmer Sciex ELAN 6000, 6100, or 9000 ICP-MS device. Duplicate measurements indicate reproducibility was generally better than 3% for major-element analyses, 5% for highly incompatible elements (i.e., Rb, Ba, U, and Th), and 7% for rare-earth elements. Accuracy was quantified by comparing measured and certified values for standard references (NIST694, DNC-1, GBW, W-2a, SY-4, and BIR-1a).

Olivine phenocrysts were then handpicked, prepared on Crystal-Bond™ resin, and polished on one side in order to have a flat surface. Major elements (Suppl. Tab. 3) were determined using a JXA-8200 combined WD/ED (energy-dispersive) electron microprobe (EMPA) at the High Pressure and High Temperature Laboratory of INGV, Sezione di Roma 1. The analytical conditions were a beam current of 7.5 nA, accelerating voltage of 15 kV, and beam size of 5 μm with counting times of 10 and 5 s for peaks and the background, respectively.

4.4.5 Noble gas isotopes in fluid inclusions

Olivine crystals were separated from the four rock samples previously fragmented and sieved in the fractions of 0.5 and 1 mm, with the aim of studying fluid inclusions trapped therein. Fluid inclusions are small (from tens to few microns in diameter) bubbles of fluid (generally gas) trapped within minerals during olivine growth at magmatic conditions. This means gases trapped in fluid inclusions represent an early stage of degassing, especially in olivine crystals that crystallize early from basaltic melts. The procedure of sample preparation and analysis is described in *Di Piazza et al.* (2015) and *Robidoux et al.* (2017). In samples from 1961, 1975, and 2010 eruptions, olivine crystals were separated in the two fractions (0.5 and 1 mm), while from pre-1961 only in the 0.5 mm fraction. Aliquots of 0.2 to 0.7 g were analysed by single-step crushing in replicate measurements for elemental and isotope composition of helium, neon, and argon in fluid inclusions hosted in olivine crystals (Tab. 4.3). These analyses were performed at the noble gas isotope laboratory of INGV, Sezione di Palermo, following internal protocol

(e.g., *Di Piazza et al.*, (2015); *Rizzo et al.*, (2015); *Robidoux et al.*, (2017)). Helium isotopes (^{3}He and ^{4}He) and ^{20}Ne were measured separately by two different split-flight-tube mass spectrometers (Helix SFT-Thermo). The ^{3}He/^{4}He ratio is expressed normalized to Ra (where Ra is the ^{3}He/^{4}He of air; i.e., 1.39×10^{-6}). The analytical uncertainty of He isotope ratio measurements was ≤2.5%. The ^{3}He/^{4}He ratios were corrected for atmospheric contamination based on the measured ^{4}He/^{20}Ne ratio (e.g., *Sano and Wakita*, (1985)) and are expressed as Rc/Ra values. Argon isotopes (^{36}Ar, ^{38}Ar, and ^{40}Ar) were analysed by a multicollector mass spectrometer (GVI Argus) at an analytical uncertainty of ≤0.9% (Tab. 4.3). The uncertainty in the measured amounts of He, Ne, and Ar elements was <5%. Typical blanks for He, Ne, and Ar were $<10^{-14}$, $<10^{-16}$ and $<10^{-14}$ mol, respectively, and were at least 1-2 orders of magnitude lower than values measured in the samples.

4.5 Results

4.5.1 Plume composition and SO_2 fluxes

During our observations on January 14-22, 2016, mild Strombolian activity persisted at a small pyroclastic cone inside the MacKenney crater (Fig. 4.2). Larger explosions, interspersed within continuous degassing and spattering activity, produced <100m high columns that deposited scoriae and bombs, mostly inside the inner crater. No major change in activity was observed during our reporting period, except for a small collapse event of the north-western sector of the crater on January 20 that produced a gray ash-rich column (*INSIVUMEH, 2016*). Direct observations indicated that intra-crateric Strombolian activity was somewhat more intense on 20-21 January, when some bombs reached the outer crater rim and damaged the outer case of the Multi-GAS.

The volcanic plume was dispersed toward north/north-west (e.g., toward the Multi-GAS measurement site) throughout most part of the Multi-GAS measurement interval, allowing regular plume detection (Fig. 4.2). The maximum gas concentrations we measured in the Pacaya plume were 120 ppm (SO_2), 550 ppm (CO_2), 1.5 ppm (H_2), and 3000 ppm (H_2O) (this latter is the excess H_2O content above an atmospheric background of 15,000-19,000 ppm). H_2S concentrations were typically below the sensor's 13% cross sensitivity to SO_2, and we therefore infer the Pacaya plume was typically H_2S-poor (at <1 ppm level). Occasionally, due to unfavourable plume transport directions, the Multi-GAS sensed a very dilute plume and/or the gas emitted from low temperature fumaroles in the inner crater's wall, close to the measurement site.

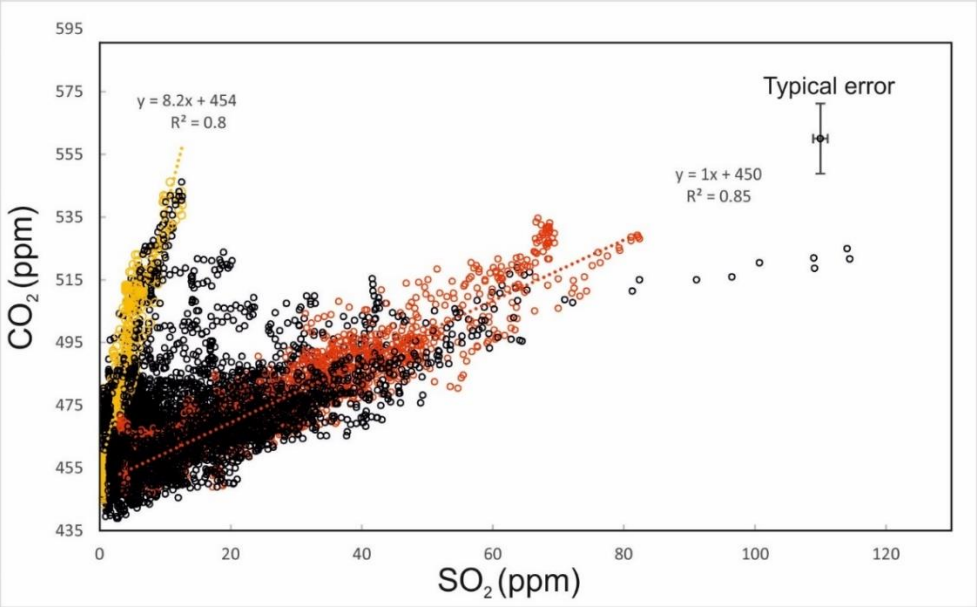

*Figure 4.3 Scatter plot of pairs of co-acquired CO_2 and SO_2 concentrations in the Pacaya plume. Open black circles identify all couples of co-acquired CO_2 and SO_2 obtained during January 14-22. We show results for all temporal windows in which CO_2 and SO_2 were correlated at significant levels (R^2 > 0.8) (implying plume fumigation at the Multi-GAS measurement site), and that concurred to calculation of the CO_2/SO_2 ratios listed in Table 4.1. The spread of compositions imply a large variability of CO_2/SO_2 ratios during January 14-22 (see Tab. 4.1). CO_2/SO_2 ratios were more constant on shorter timescales, e.g., over temporal timescales of minutes. We thus selected using the software Ratiocalc (*Tamburello*, 2015) a sequence of short (a few minutes long) temporal windows, in each of which the mean CO_2/SO_2 ratio was calculated from the slope of the best-fit regression line in CO_2 vs. SO_2 concentration plots. Results for two representative measurement intervals are shown in the Figure. Yellow circles: CO_2 vs. SO_2 sub-population for the 6:22-6:26 pm (GMT time) acquisition on January 18. The best-fit regression line has a slope of 8.2 (R^2 = 0.8). Red circles: CO_2 vs. SO_2 sub-population for the 12:00-12:28 (GMT time) acquisition on January 22. The best-fit regression line has a slope of 1 (R^2 = 0.85). Note the intercepts of both regression lines (CO_2 ~ 450 ppm) are well-above CO_2 levels in background air (~ 400 ppm), suggesting diffuse CO_2 loss from soils and warm grounds in the crater area. The typical errors in CO_2 and SO_2 concentrations are shown by the error bar.*

Figure 4.3 is a scatter plot of pairs of co-acquired CO_2 and SO_2 concentration data. The plot demonstrates that plume CO_2/SO_2 (molar) ratios fluctuated from <1 to >10 during the study period. This spread of CO_2/SO_2 ratios is evident from comparison of CO_2 vs. SO_2 sub-populations taken in two distinct measurement intervals (red: 22 January; yellow; 18 January), in which the slopes of the best-fit regression lines are 1 and 8.2, respectively. In view of this temporal variability, we calculated (using Ratiocalc) the "mean" CO_2/SO_2 ratio in individual, few minutes-long, temporal intervals, during which the plume was compositionally more constant (e.g. the obtained correlation coefficients between CO_2 and SO_2 concentrations were high: R^2 from 0.60 to 0.91). The obtained CO_2/SO_2 ratios ranged from 0.6 to 10.5 (Tab.

4.1), and their average (arithmetic mean) was 3.0±2.7 (1 standard deviation, SD). In figure 4.4a, the obtained CO_2/SO_2 ratios are plotted against the peak SO_2 concentration measured in the corresponding temporal window (see Tab. 4.1). This peak SO_2 concentration is here taken as a "plume marker", e.g. as a proxy for the density of the plume at the measurement site. We find that CO_2/SO_2 ratios are widely scattered and typically higher (mostly between 2 and 10.5) at low SO_2 (< 20 ppm) concentrations (dilute plume conditions), while they converge to low values (between 0.5 and 1.5) at higher peak SO_2 concentrations (dense plume conditions). A similar behaviour is also observed for H_2O/SO_2 (fig. 4.4b), in which stable and low ratios (range 2-20; average ~ 11) are obtained in dense plume conditions (peak SO_2 concentrations > 20 ppm). We also derived plume H_2/SO_2 ratios of 0.01 to 0.3, with a cluster at 0.04±0.01 in the subset of high SO_2 concentration data. Although H_2S/SO_2 ratios were not detected, we inferred a maximum ratio of 0.05 based on H_2S being below detection in all acquisitions. SO_2 was therefore the only substantial S component in the plume (i.e. $SO_2 \approx$ Total Sulfur, S_t).

Figure 4.5a is a pseudo-colour image of SO_2 column densities (in ppm·m) in the Pacaya plume, obtained from processing of couples of co-acquired images taken by our UV camera system in the morning of January 16, 2016. During the measurements, the plume was nearly transparent and vertically lofting above the crater (Fig. 4.5b). Sequences of images such as that shown in Figure 4.5a were obtained every 3 seconds. These were processed to obtain time-series of SO_2 ICA, using a cross-section orthogonal to the plume transport direction (see figure 4.5a). From these, and by using a plume transport speed of 8.2 ± 4 m/s, the SO_2 flux time-series of Figure 4.5c was obtained. The derived SO_2 fluxes varied largely, from ~100 to 4210 tons/d, consistent with visual observations (from the crater rim) of fluctuations in explosive and degassing activity at the pyroclastic cone inside the MacKenney crater. We caution that part of the large SO_2 flux temporal variability was caused by passage of clouds between ~16:50 and ~17:20 GMT, which partially obscured view of the crater area and resulted into reduced SO_2 fluxes (Fig. 4.5c). Excluding this subset of values, we obtain an averaged SO_2 flux of 885 ± 550 tons/d.

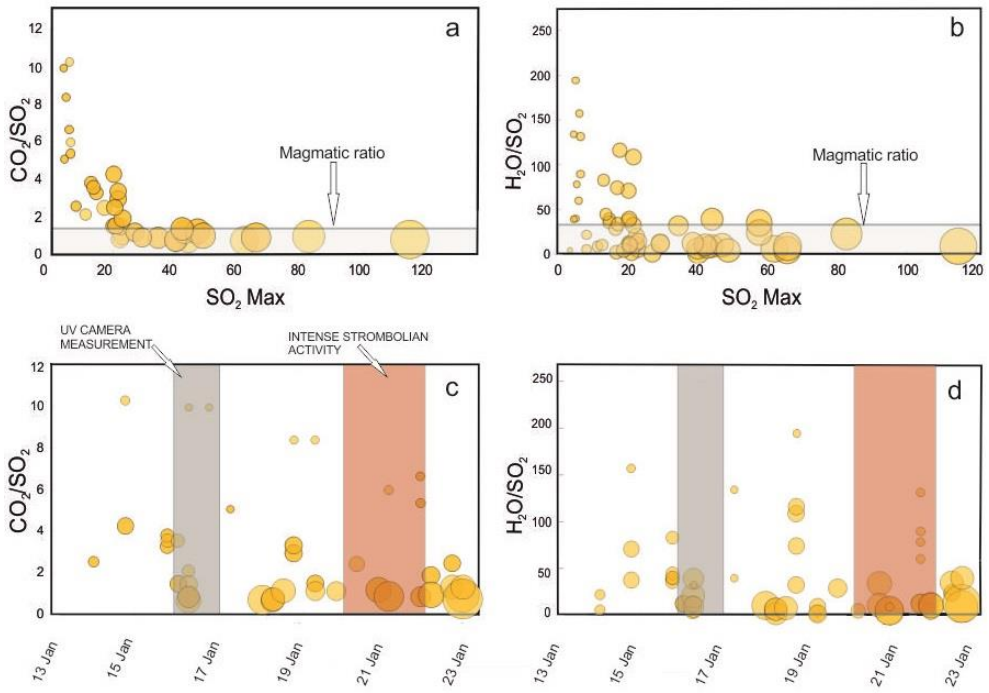

Figure 4.4 The CO_2/SO_2 and H_2O/SO_2 ratios obtained in individual acquisition windows (see Table 4.1). In each panel, size of bubbles is proportional to the peak (maximum) SO_2 concentration detected during each temporal window (listed in Tab. 4.1). In panels a) and b), ratios are plotted as a function of peak SO_2 concentrations. In both plots, CO_2/SO_2 and H_2O/SO_2 ratios are scattered at low SO_2 concentrations and converge to a narrow "magmatic" range (of 0.5-1.5 and 2-20, respectively) at high (> 20 ppm) SO_2 concentrations. c) and d) are temporal plots of CO_2/SO_2 and H_2O/SO_2 ratios, respectively. Grey and red shaded areas mark the UV camera measurement interval and a phase of especially intense strombolian activity, respectively.

4.5.2 **Chemical and carbon isotope composition of fumarole gases**

The chemistry of gases collected from the two low-temperature fumaroles displayed a strong air contamination, as demonstrated by the dominant O_2 and N_2 composition (19.3 %, 76. 8% respectively; Tab. 4.2). CO_2 concentrations were between 0.9 and 2.8%. The $\delta^{13}C$ of CO_2 varied in a narrow range, from -3.7‰ to -4.0‰. Based on theoretical values in air of CO_2 and $\delta^{13}C$ ($CO_2 \approx 400$ ppm and $\delta^{13}C$=-8‰), we calculated a fraction of contamination in our samples. Then, we used an isotope balance to quantify the effect of air mixing and recalculate the air-corrected magmatic gases $\delta^{13}C$. This procedure yields $\delta^{13}C$ of CO_2 between -3.5 and -3.9‰ (Tab.4. 2).

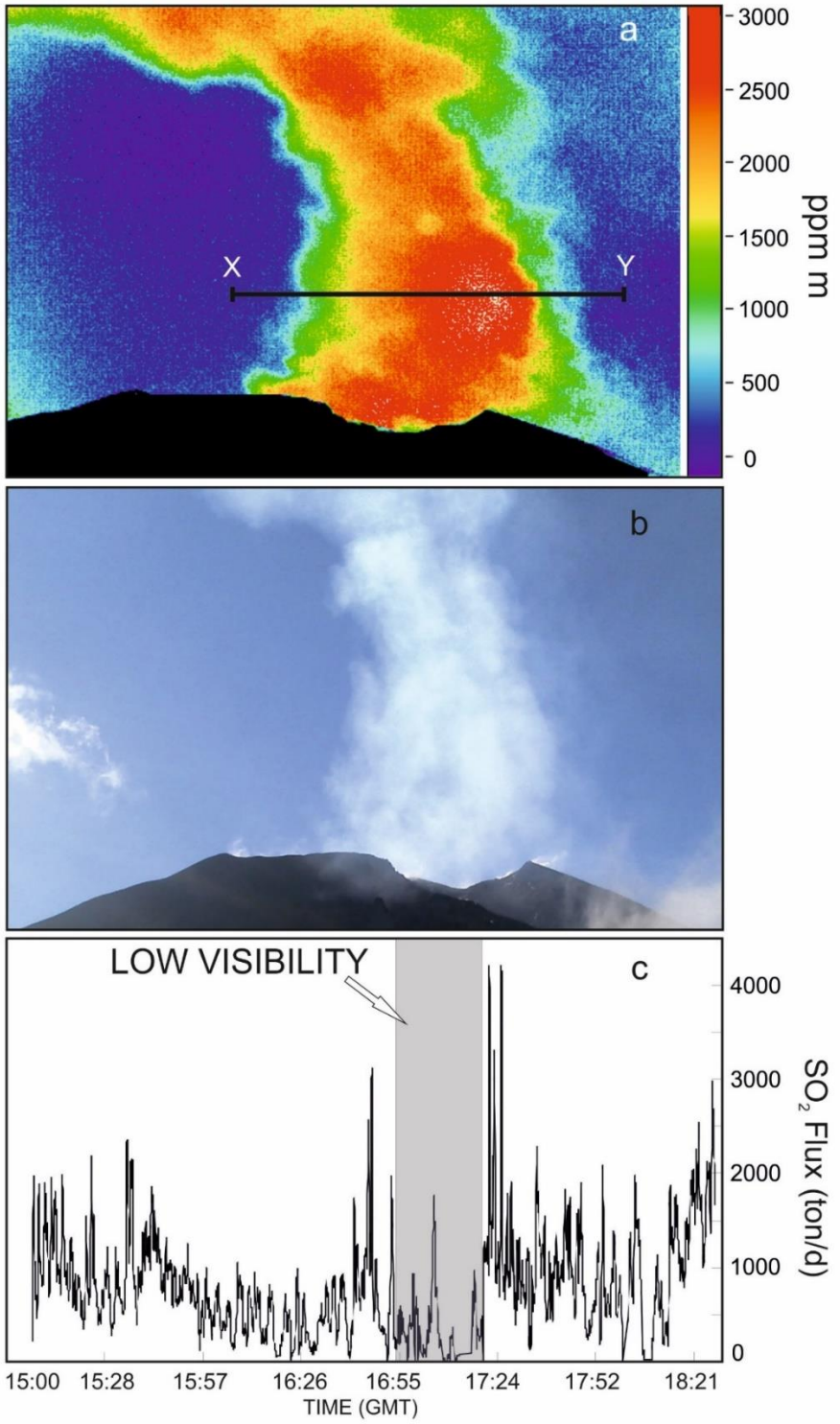

Figure 4.5 a) Pseudo-color image showing SO_2 slant column amounts (expressed in ppm·m) in the Pacaya plume, as derived from UV camera measurements. The horizontal X-Y section indentifies location of the orthogonal cross-section used to derive SO_2 ICAs (Integrated Column Amounts). b) Visible image of the Pacaya plume, taken from the same UV Camera measurement site (see Figure 1a). c) SO_2 flux time-series obtained for the 4-hours long UV Camera acquisition period on

January 16th, 2016. The grey shaded area identifies a period of reduced visibility due to cloud passage.

4.5.3 Chemistry of whole rocks and olivine crystals

The whole-rock composition of the studied samples is basaltic, with SiO_2 contents between 50.2 and 50.7 wt. % and total alkalis ($Na_2O + K_2O$) between 3.8 and 4.1 wt%. The MgO content is generally comprised between 2.9 and 4.0 wt. %, while total Fe varies between 7.9 and 9.5 wt%. These results agree well with published data on the same eruptions (*Bardinzteff and Deniel*, 1992; *Wardman et al*., 2012; *Matias et al*., 2012; *Rose et al.*, 2013), and confirm the basaltic composition of most of the products erupted from the volcano since historic time. In the K_2O vs. SiO_2 classification diagram (Fig. 4.6; after *Peccerillo and Taylor*, (1976)), Pacaya volcanics spread over the typical compositional field of the calc-alkaline magmatic series. Rock samples investigated in this work are among the most mafic ever erupted at Pacaya and in Guatemala (Fig. 4.6). Pacaya lavas also have relatively low fluid–mobile to less-fluid–mobile trace element ratios (Ba/La = 46.23 ± 2.2; U/Th = 0.42 ± 0.04; Ba/Th = 350 ± 18) (see also *Heydolph et al.*, (2012)), and plot therefore at the lower limit of the CAVA compositional range (*Sadowsky et al., 2008*). These low ratios suggest limited contribution from sediments in the subducted slab (*Sadowsky et al., 2008*).

Olivine phenocrysts (~10 vol.%), separated for the noble gases investigation in fluid inclusions, have euhedral to sub-hedral habitus and display a broad range of compositions at cores (Fo_{65}–Fo_{90}), with an unimodal distribution (mode at Fo_{65}–Fo_{73}) that suggests the lack of clear mixing processes.

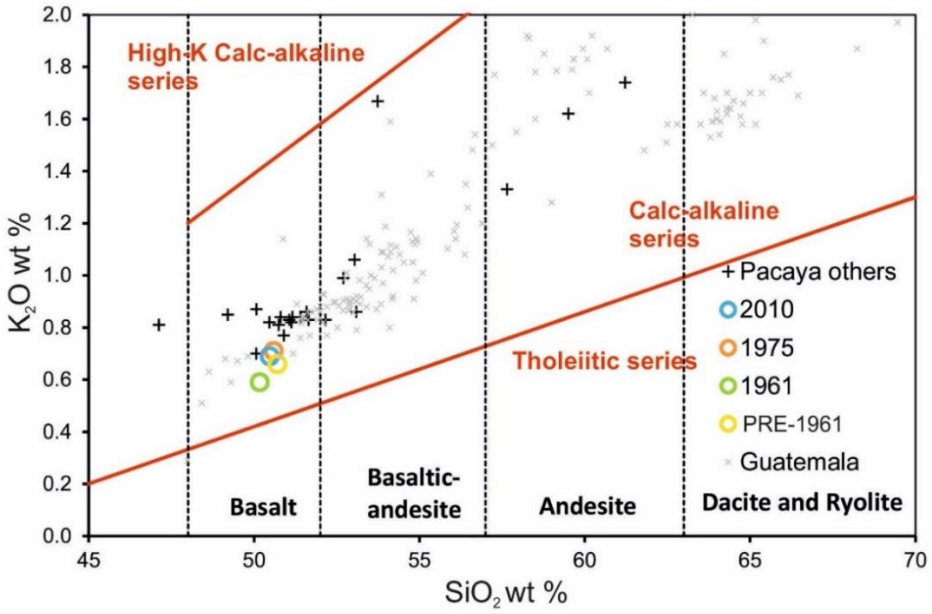

Figure 4.6 K_2O vs. SiO_2 plot for whole-rock Pacaya samples, modified from Peccerillo and Taylor (1976). Our samples (see legend) are compared with literature information on rocks from Pacaya and Guatemala. Black crosses referred as "Pacaya others" in the legend correspond to published results (data from Carr et al., (1984); Feigenson and Carr, (1986); Carr et al., (1990); Morris et al., (1990); Bardintzeff and Daniel, (1992); Leeman et al., (1994); Noll et al., (1996); Patino et al., (2000); Chan et al., (2002); Cameron et al., (2003); Walker et al., (2007); Walker et al., (2009)). The grey crosses referred as "Guatemala" in the legend correspond to published whole-rock information on Guatemalan volcanoes (data extracted from the earthchem portal; http://www.earthchem.org/portal).

4.5.4 Noble gases in fluid inclusions

The ^4He content in olivine crystals ranges between 7.8×10^{-14} and 2.7×10^{-13} mol/g (Fig. 4.7), ^{20}Ne varies from 1.2×10^{-15} to 8.2×10^{-15} mol/g, while ^{40}Ar between 2.2×10^{-13} and 2.7×10^{-12} mol/g. No systematic difference in concentrations is observed among the samples. All the data fall in the concentration range of the 1975 samples (Fig. 4.7). Assuming no differences in terms of fluid inclusions frequency within olivine crystals of different samples, this range of concentration could indicate that our samples crystallized at a small range of pressures. The $^4He/^{20}Ne$ ratio is an indicator of atmospheric contamination and ranges between 21 and 113, which is at least 66 times higher than the typical atmospheric ratio ($^4He/^{20}Ne = 0.318$). In Figure 4.8, we plot our data in order to evaluate the extent of air contamination. To do this we assume a binary mixing between an atmospheric end-member, having $^4He/^{20}Ne=0.318$ and R/Ra=1, and two magmatic end-members, having $^4He/^{20}Ne=1000$ and Rc/Ra of either 8.3 or 9.0. These two mixing curves practically cover the entire dataset of fluid inclusions,

indicating that the magmatic end-member varies in this range of $^{3}He/^{4}He$ ratio (8.3-9.0 Ra, Fig. 4.8). The $^{40}Ar/^{36}Ar$ varies from 298 to 328, which is slightly higher than atmospheric ($^{40}Ar/^{36}Ar$ = 295.5). Both $^{4}He/^{20}Ne$ and $^{40}Ar/^{36}Ar$ ratios are lower than those typical of fluids from the upper mantle ($^{4}He/^{20}Ne$>1000 and $^{40}Ar/^{36}Ar$>40000; *Ozima and Podosek,* (1983)), but fall within the range of subduction-related volcanism worldwide and in CAVA (*Hilton et al.,* 2002*; Fischer et al.,* 2005*; Di Piazza et al.,* 2015, *Rizzo et al.,* 2015*; Robidoux et al.,* 2017). This indicates that gases released from FIs contain an atmospheric-derived component, perhaps related to the recycling of noble gases in the subducting slab.

We selected the subset of samples having $^{40}Ar/^{36}Ar$ >300 and calculated the air-corrected ^{40}Ar content assuming that all the measured ^{36}Ar is atmospheric in origin:

$$^{40}Ar^{*}=^{40}Ar_{m}-((^{40}Ar/^{36}Ar)_{air}\times{}^{36}Ar_{m}) \qquad (2)$$

In relation (2), $^{40}Ar^{*}$ is the air-corrected ^{40}Ar, and the "m" subscript indicates "measured". The $^{40}Ar^{*}$ was not calculated for the 2010 eruption samples ($^{40}Ar/^{36}Ar$ < 300) and for one 1975 sample (for which the $^{40}Ar/^{36}Ar$ was not determined). The recalculated $^{4}He/^{40}Ar^{*}$ varies between 2.3 and 5.5, which is within the typical production ratio of the mantle ($^{4}He/^{40}Ar^{*}$=1–5; (*Ozima and Podosek,* 1983*; Marty,* 2012)). Considering that He is around 10 times more soluble than Ar in silicate melts, magmatic degassing would lead to an increase of $^{4}He/^{40}Ar^{*}$ especially in the late stages of degassing (e.g., *Iacono-Marziano et al*., (2010)). Thus, the small variability of this ratio in our fluid inclusions suggests that olivine crystals were entrapped in a small pressure range.

The $^{3}He/^{4}He$ ratios corrected for atmospheric contamination vary from 8.4 to 9.0 Ra (Fig. 4.7). These ratios are within the MORB-like range (R/Ra = 8.0 ± 1; *Graham,* (2002)), and are sensibly higher than the four data previously available results for Pacaya (Fig. 4.7). The reported $^{3}He/^{4}He$ ratios in the three volcanic gases collected in the 1990s (*Sano and Williams,* 1996*; Goff and McMurtry,* 2000) vary between 2.9 and 7.9 Ra, and a single R/Ra of 6.8±1.5 Ra was obtained for the only available olivine phenocrysts measurement (*Poreda and Craig,* 1989). Excluding the highest value measured by *Goff and McMurtry* (*2000*) (having a $^{3}He/^{4}He$ ratio of 7.9 Ra), the low ratios previously measured at Pacaya reasonably reflect the role of secondary processes, including air contamination or addition of radiogenic ^{4}He in the hydrothermal system.

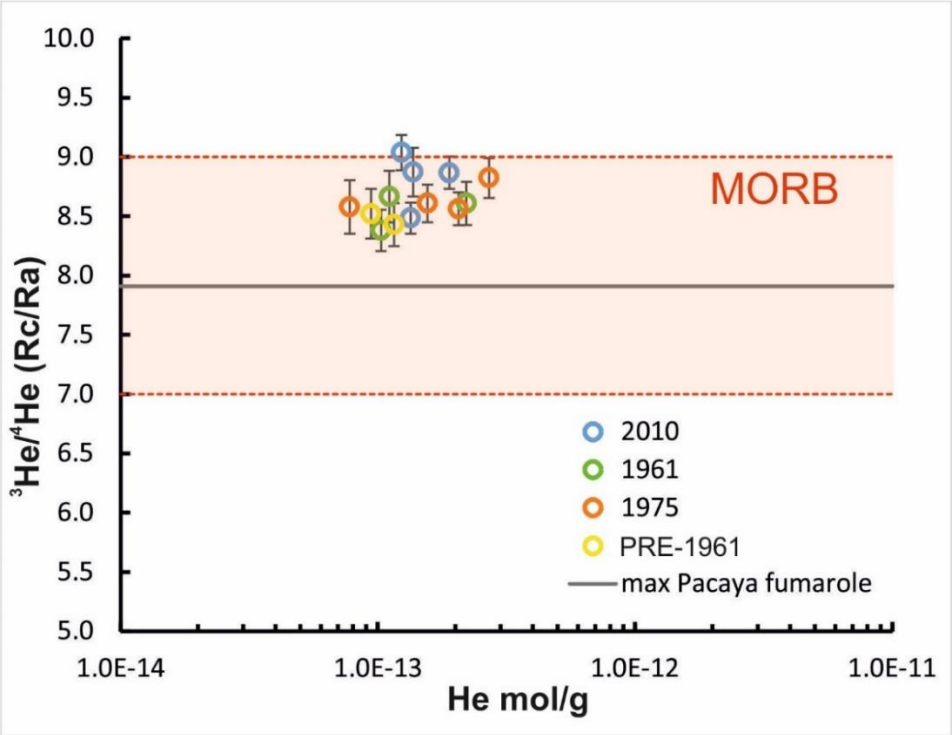

Figure 4.7 Air-corrected $^3He/^4He$ ratios (expressed as Rc/Ra) vs. He content (mol/g) in FIs hosted in olivine minerals. Our data are compared with the MORB range (7–9 Ra), taken from Graham (2002), see light orange area. The highest $^3He/^4He$ ratio measured in the Pacaya summit fumaroles in the 1990s (Goff and McMurtry, 2000) is shown by the dashed grey line.

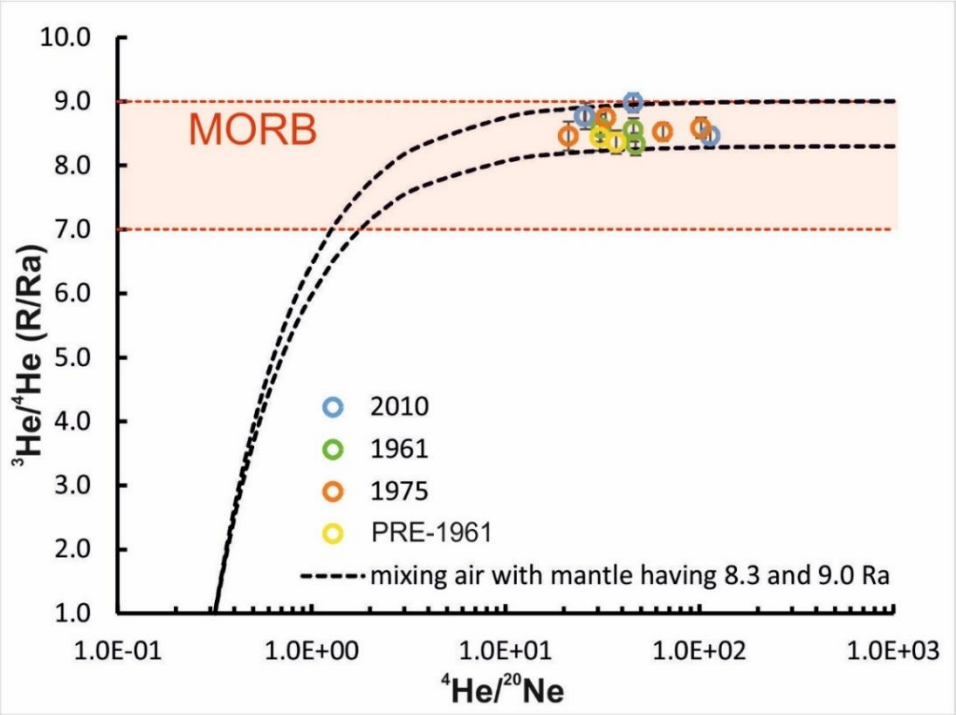

Figure 4.8 $^3He/^4He$ (expressed as R/Ra) vs. $^4He/^{20}Ne$ for Pacaya olivine-hosted FIs (this work). The black lines reproduce the mixing curves between air and mantle with respectively 8.3 and 9.0 Ra. The MORB range is also indicated as in Figure 4.7.

4.6 Discussion

4.6.1 The chemical signature of magmatic gases at Pacaya

To the best of our knowledge, the only available volcanic gas composition for Pacaya was reported in (*Goff and McMurtry* 2000) for 2 directly sampled fumaroles in 1992. *Sano and Williams* (1996) reported on $\delta^{13}C$, R/Ra, $CO_2/^3He$ information for one high-temperature Pacaya gas, but did not quote a complete gas analysis. The results of *Goff and McMurtry* (2000) indicated a volcanic gas dominated by H_2O (~ 90 mol. %), CO_2 (~ 4-7 mol. %), and minor sulphur species. Unfortunately however, the low temperatures (84.5 and 342 °C) and the high N_2 content (of the hottest sample) implied a non-trivial role of secondary processes, such as scrubbing of reactive volatiles by wall-rocks or hydrothermal fluids upon cooling, and mixing with atmospheric fluids (*Symonds et al.,* 2001*; Fischer and Chiodini,* 2015). Our 2016 Multi-GAS results therefore, that were obtained on the summit crater plume directly released by a hot, erupting open-vent (Fig. 4.2), provide the first assessment of the "magmatic" gas signature for Pacaya.

Our results (Tab. 4.1) suggest a variable gas composition during January 14-22, 2016 (Fig. 4.4 c, d). We find that the CO_2/SO_2 and H_2O/SO_2 ratios both varied widely, and that the two ratios were linearly correlated (Fig. 4.9a). Using each couple of co-acquired ratios, we recalculate the molar proportions (in mol. %) of the three major volatiles in the magmatic gas phase. Validity of this procedure is based on the assumption that the above three species make together the totality of the source magmatic gas (a condition commonly encountered in volcanic gases; *Symonds et al.,* (1994), *Fischer and Chiodini,* (2015)). The derived compositions, shown in the triangular plot of Figure 4.9b, again show large variability, ranges being 38.4-96.8 mol. % (H_2O), 1.7-36.9 mol. % (CO_2) and 0.3-29.4 mol. % (SO_2).

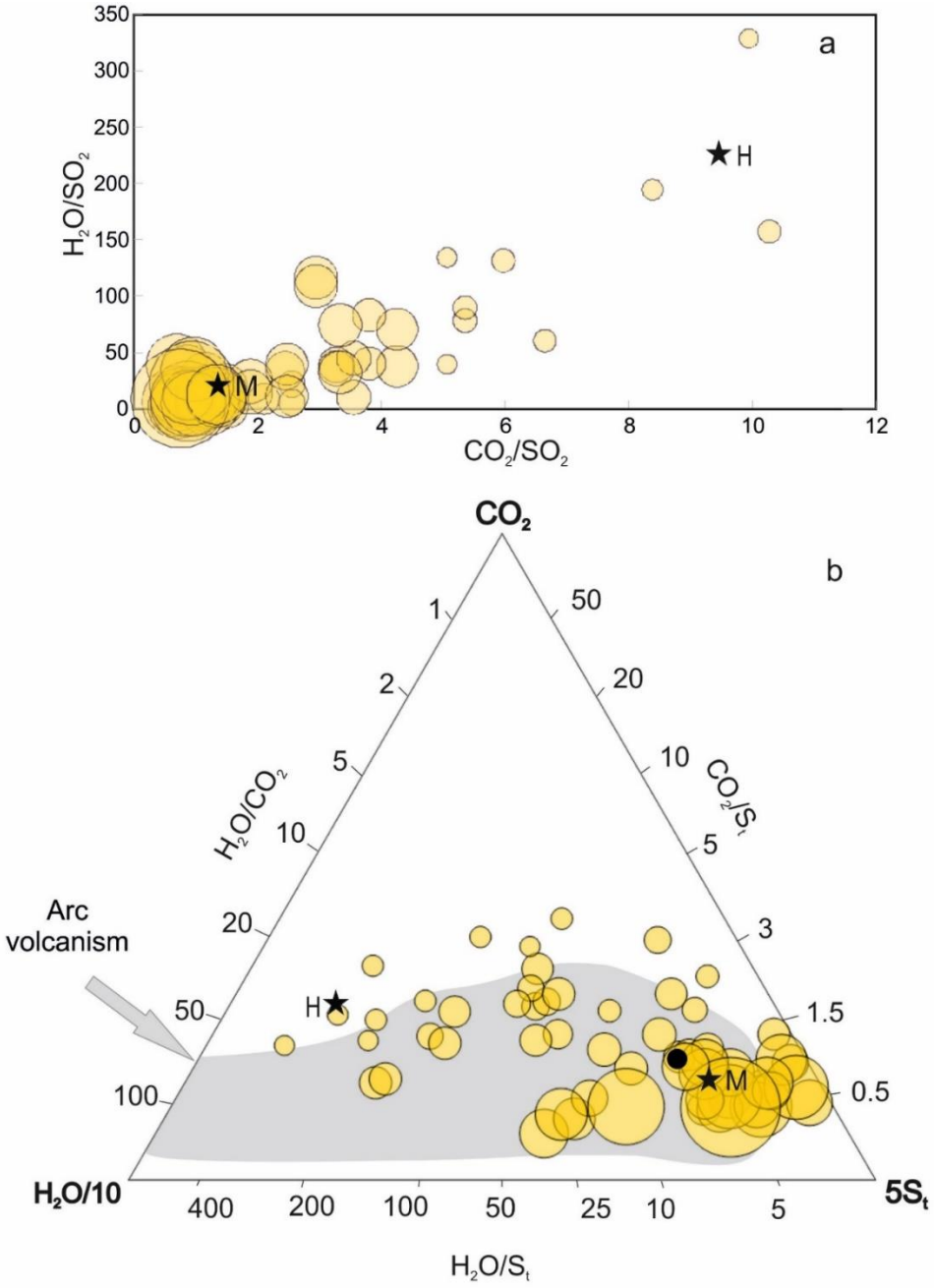

Figure 4.9 a) H2O/SO2 vs. CO2/SO2 scatter plot (data from Table 4.1); b) H2O/10-CO2-5St triangular plot, obtained from plume compositional data (of Table 4.1) recalculated to 100%. The grey background identifies the compositional range of volcanic arc gases globally (from Aiuppa, (2015)). Data are interpreted as reflecting mixing of hydrothermal (H) and magmatic (M) end-member components. The composition of end-member H is fixed as the arithmetic mean of the three Multi-GAS data with highest CO2/SO2 (>8) and H2O/SO2 (> 150) ratios (see panel a)). The composition of the magmatic end-member M is the arithmetic mean of all Multi-GAS data with peak SO2 concentrations > 20 ppm. The black circle in b) corresponds to composition of the Pacaya fumarole of Goff and Mc Murtry (2000).

Several processes may have concurred to determine the observed compositional variability. One possibility is that the observed gas changes

responded to variations in the volcano's degassing/activity state. However, strombolian intra-crateric activity and degassing both persisted at rather steady levels in the MacKenney crater during our study period. Except for a brief period in January 20-21, when strombolian activity was somewhat more vigorous, no major change was observed that could have explained the large diversity in gas composition. We instead propose that the observed gas variations reflected time-changing gas contributions from two distinct gas components, which we refer to as *H* and *M* (see Fig. 4.9). Two-component mixing is fully supported by the linear compositional array in the ratio/ratio scatter plot of Figure 4.9a. We find that all gas compositions taken in high-SO_2 "dense plume conditions" were systematically characterized by low CO_2/SO_2 and H_2O/SO_2 ratios (Figs. 4.4, 4.9). Since SO_2 is commonly recognized as a tracer of high-temperature magmatic degassing (see reviews by *Oppenheimer et al.,* (2014)*; Fischer and Chiodini,* (2015)), we conclude that the SO_2-rich, H_2O-CO_2-poor end-member composition *M* is likely to most closely approximate the Pacaya magmatic gas component. High CO_2/SO_2 and H_2O/SO_2 compositions were instead systematically observed when the plume sensed by the Multi-GAS was more dilute (<20 ppm SO_2; Fig. 4.4). In analogy with observations made at other open-vent volcanoes (e.g., Etna; *Shinohara et al*., (2008)), we propose that this low-SO_2 component (*H*) likely reflected gas contribution from lower temperature, hydrothermal fumaroles that were widespread on the crater rim/inner crater wall around the Multi-GAS site. Hydrothermal fumaroles are typically H_2O-rich (*Chiodini and Marini, 1998; Fischer and Chiodini,* 2015) and exhibit high CO_2/S_t ratios due to scrubbing of reactive sulfur during reactions with hydrothermal rocks/fluids (*Aiuppa et al.,* 2014, 2017). The Pacaya fumaroles reported in *Goff and McMurtry* (2000) may well be representative of this hydrothermal component.

Based on the above, we calculate our best-guess for the Pacaya magmatic gas composition by averaging all results taken in "dense plume" conditions (peak SO_2 concentration > 20 ppm). We obtain a magmatic gas with 80.5 mol. % H_2O, 10.4 mol. % CO_2, and 9.0 mol. % SO_2, thus sitting at the H_2O-poor range of the population of volcanic arc gases worldwide (*Aiuppa,* 2015) (Fig. 4.9b).

This unusual H_2O-poor gas composition could partially reflect our Multi-GAS measurements actually under-estimating the real magmatic gas H_2O abundances, due to in-plume H_2O condensation during transport and dispersion, from the active degassing vent to the measurement site. Although we have no arguments to rule out this possibility completely, the Multi-GAS site was only 80 m distant from the vent, implying that a short-lived plume was actually measured (e.g. the transport time, from vent to the Multi-GAS, is inferred at < 10 s, assuming a typical transport speed of 8.2 m/s).

Alternatively, our results could imply a H_2O-poor magma source at Pacaya. *Walker et al.,* (2003) analyzed a set of glass inclusions from the 1996-1999 activity of Pacaya, and found H_2O contents of ≈ 2 wt. % (range, 1.7-2.4). This is still within the normal range of H_2O abundances in arc magmas (*Wallace,* 2005*; Wallace et al.,* 2015), but below (or, at least, at the lower range of) the observed glass inclusion H_2O contents in other Guatemalan volcanoes such as Agua (2.65-3.4), Atitlan (2.34-3.3), Fuego (up to 6 wt. %), and Santa Maria (1.5-3.5) (*Roggensack,* 2001*; Sadofsky et al.,* 2008*; Wehrmann et al.,* 2011). Based on these results, *Walker et al.,* (2003) argued that the contribution of H_2O-rich slab fluids is likely more limited (0.1-0.3 wt. %) in the Pacaya mantle source region than underneath other Guatemalan volcanoes (0.5-0.7 wt. %). Clearly, additional near-vent gas observations, and possibly new glass inclusion data, are required to better confine the magmatic H_2O abundance at Pacaya.

4.6.2 Constraints on the magmatic source

Our inferred magmatic gas composition above implies a magmatic CO_2/S_t ratio for Pacaya of ~1.1 (± 1). This relatively low ratio, falling at the lower range of high-temperature arc volcanic gases worldwide (0.2-9.2; *Aiuppa,* 2015*; Aiuppa et al.,* 2017), deserves some discussion. Recently, *Aiuppa et al.,* (2014) analyzed the CO_2/S_t ratio signature of magmatic gases from the Costa Rica – Nicaragua segment (SNVS) of CAVA, and found distinct along-arc variations between its southern (Costa Rica, CO_2/S ratios: ~0.5-1) and northern (Nicaragua; CO_2/S_t ratios: ~3) branches. Based on positive correlations between magmatic gas CO_2/S_t ratios and trace-element tracers (e.g., Ba/La and U/Th) in the source magmas, *Aiuppa et al.,* (2014, 2017) ascribed the increasing carbon-rich compositions in Nicaragua to the involvement of increasing proportions of recycled C-Ba-U-rich slab sediment fluids in magma genesis, compared to more mantle-like gas signature in Costa Rica.

Our novel results from Pacaya, with recent magmatic gas data from El Salvador (*Granieri et al.,* 2015*; Aiuppa et al.,* 2017), allow extending scrutiny of the gas vs. trace element relation further to the north (Fig. 4.10). Overall, these novel results corroborate the hypothesis of *Aiuppa et al.,* (2014), indicating that, at the scale of the entire arc (CAVA), the linear correlation between gas CO_2/S_t ratios and Ba/La ratios (Fig. 4.10a) is statistically significant (R^2=0.86), and follows the best-fit regression line:

$$CO_2/S_{t(m,\ gas)} = 0.007 \cdot (Ba/La_{\ m,rock}) + 0.0959 \qquad (4.3)$$

where $CO_2/S_{t(m,\ gas)}$ is the mean CO_2/S_t ratio in magmatic gases for each volcano (data from *Aiuppa et al.,* (2014, 2017); *Granieri et al.,* (2015));

($Ba/La_{m,rock}$) is the corresponding mean Ba/La ratio derived from published whole-rock analyses (extracted from the earthchem portal; http://www.earthchem.org/portal) and 0.007 and 0.0959 are best-fit regression coefficients.

We find that the new Pacaya (and El Salvador) gas data allow filling the compositional gap between Central Costa Rica (e.g., Poás and Turrialba) and Nicaragua (Fig. 4.10a). As such, these results are suggestive for the Pacaya magmatic gas having intermediate origin between mantle-like and slab-like end-member compositions in Costa Rica and Nicaragua, respectively. A higher mantle affinity of Pacaya magmas, relative to more sedimentary-derived signature of Nicaraguan magmas, is well consistent with available trace element and isotopic signatures of CAVA volcanites (Fig. 4.10b; (*Carr et al.,* 1990*; Morris et al.,* 1990*; Leeman et al.,* 1994*; Patino et al.,* 2000*; Sadofsky et al.,* 2008)), based on evidence from Cl isotopes, low U/Th ratios and $^{10}Be/^{9}Be$ in volcanic rocks, similarly suggested a slightly contaminated mantle source for Guatemala.

4.6.3 C and He isotopes

Further and even clearer evidence on the mantle affinity of Pacaya magmas come from the $^{3}He/^{4}He$ ratios measured in fluid inclusions hosted in olivine crystals separated from the studied rocks. In fact, ^{3}He is typically mantle-sourced while ^{4}He is crustal and comes from the radiogenic decay of U and Th. This implies that strong contribution of mantle-derived gases can be detected in terms of strong increase of $^{3}He/^{4}He$ up to values higher than MORB range (i.e., >9 Ra), in case of lower mantle (i.e., plume) contribution (e.g., hot spot geodynamic setting). Our measured Rc/Ra vary between 8.3 and 9.0 Ra (Fig. 4.7), which fall at the upper limit of MORB-like range (R/Ra = 8±1; *Graham,* 2002). More importantly, our $^{3}He/^{4}He$ ratios are the highest ever measured in CAVA and are among the highest ever recorded in arc volcanoes worldwide (*Hilton et al.,* 2002*; Oppenheimer et al.,* 2014 and references therein). Pacaya magmas thus point to a non-contaminated (by slab fluids) mantle wedge source beneath this segment of the volcanic arc, with no evidence of crustal contamination. According to *Cameron et al.,* (2003), the southern portion of Guatemala undergoes E-W crustal extension, as evidenced by a series of N-S trending grabens (*Burkart et al.,* 1985). At Pacaya in particular, extensional regime is determined by the volcano laying at the intersection between the JFS and the Guatemala graben (Fig. 4.1). Extensional forces are thought to control the degree of melting, and to facilitate rapid magma ascent, causing limited magma differentiation (*Cameron et al.,* 2003). Modern Pacaya has erupted lavas of progressively more mafic composition, and uniquely basaltic rocks since historic time (*Bardintzeff and Deniel, 1992*). Another important aspect to consider is the

role of decompression melting in south-eastern Guatemala. *Cameron et al.*, (2003), based on major, trace elements and Sr isotopes in volcanic rocks, identified systematic differences between Pacaya and Agua (where decompression melting may play an important role) and other volcanoes in south-eastern Guatemala (i.e., Tecuamburro and Moyuta). They argued that Pacaya volcanics have compositions similar to back-arc cinder cones in southeastern Guatemala. These observations support the idea that the exceptionally high $^{3}He/^{4}He$ measured at Pacaya may reflect fast magma ascent from the mantle, limiting crustal contamination by radiogenic ^{4}He. Accordingly, the $^{3}He/^{4}He$ signature of the mantle wedge below this segment of Guatemala is not modified by subduction-related fluids.

The corrected $\delta^{13}C$ (CO_2) values of fumaroles sampled in this work are -3.5 and -3.9‰, respectively (cfr. 4.2). Considering the natural variability of the magmatic system, these values are comparable to the $\delta^{13}C$ values reported by *Goff and McMurtry* (2000) (-2.8‰ and -3.1‰) for two fumaroles (at 84.5 and 342 °C) sampled in the early 1990s. On the contrary, *Sano and Williams* (1996) reported a very low $\delta^{13}C$ (-6.9‰) for a high-temperature volcanic gas sample (965°C) from Pacaya. Because *Sano and Williams* (1996) did not report on the extent of air contamination of this sample, we cannot evaluate if the low $\delta^{13}C$ was the effect of a strong air dilution. In fact, a high extent of air contamination on a magmatic $\delta^{13}C$ of -3‰ would lead to more negative ratios (air $\delta^{13}C$=-8‰). Alternatively, their low $\delta^{13}C$ (CO_2) could reflect a residual (degassed) magmatic source (see below). As detailed below, $\delta^{13}C$ of CO_2 may suffer an isotope fractionation during magmatic degassing that leads to more negative ratios. For the above reasons, we discarded this low ratio, and we hereafter assume an average $\delta^{13}C$ = -3.5±0.4‰ as representative of the magmatic signature of carbon at Pacaya. We caution that, in contrast to $^{3}He/^{4}He$ ratios that can be directly used to constrain the origin of fluids, $^{13}C/^{12}C$ ratios are more problematic to interpret, owing to the existence of isotopic fractionations during magmatic degassing and gas-water interactions. Experiments demonstrate that, in basaltic melts, C isotopes have vapour-melt enrichment factors ($\varepsilon_{CO2\text{-}melt}$) of 2 to 4‰, e.g., ^{13}C is preferentially extracted from melt. Because of this, the $\delta^{13}C$ signature of magmatic CO_2 decreases along both open- and closed-system magma degassing paths (*Javoy et al.*, 1978*; Mattey*, 1991*; Trull et al.*, 1993). Unfortunately, no independent constraint is available at Pacaya to quantify the degassing extent of the magma source feeding our Pacaya fumaroles. In addition, a possible gas-water-rock interaction control on $\delta^{13}C$ (and $CO_2/^{3}He$) cannot be ruled out in our Pacaya example, in view of the low fumarole temperatures (at which scrubbing is important; *Symonds et al.*, (2001)). It follows from the above that caution is needed when interpreting $\delta^{13}C$ and $CO_2/^{3}He$ variations at any single volcano or along an arc segment. These

tracers may not necessarily provide direct access to the relative slab vs. mantle contributions to magmatism (*Sano and Marty*, 1998). In the limit-case assumption that secondary processes are negligible, the magmatic signature in the gaseous phase of Pacaya melts would have $\delta^{13}C$ of -3.5±0.4‰. This is in the range of MORB-like mantle, whose inferred $\delta^{13}C$ range is between -8‰ and -4‰ (*Marty and Jambon*, 1987*; Javoy and Pineau*, 1991*; Macpherson and Mattey*, 1994*; Sano and Marty*, 1995*; Deines*, 2002).

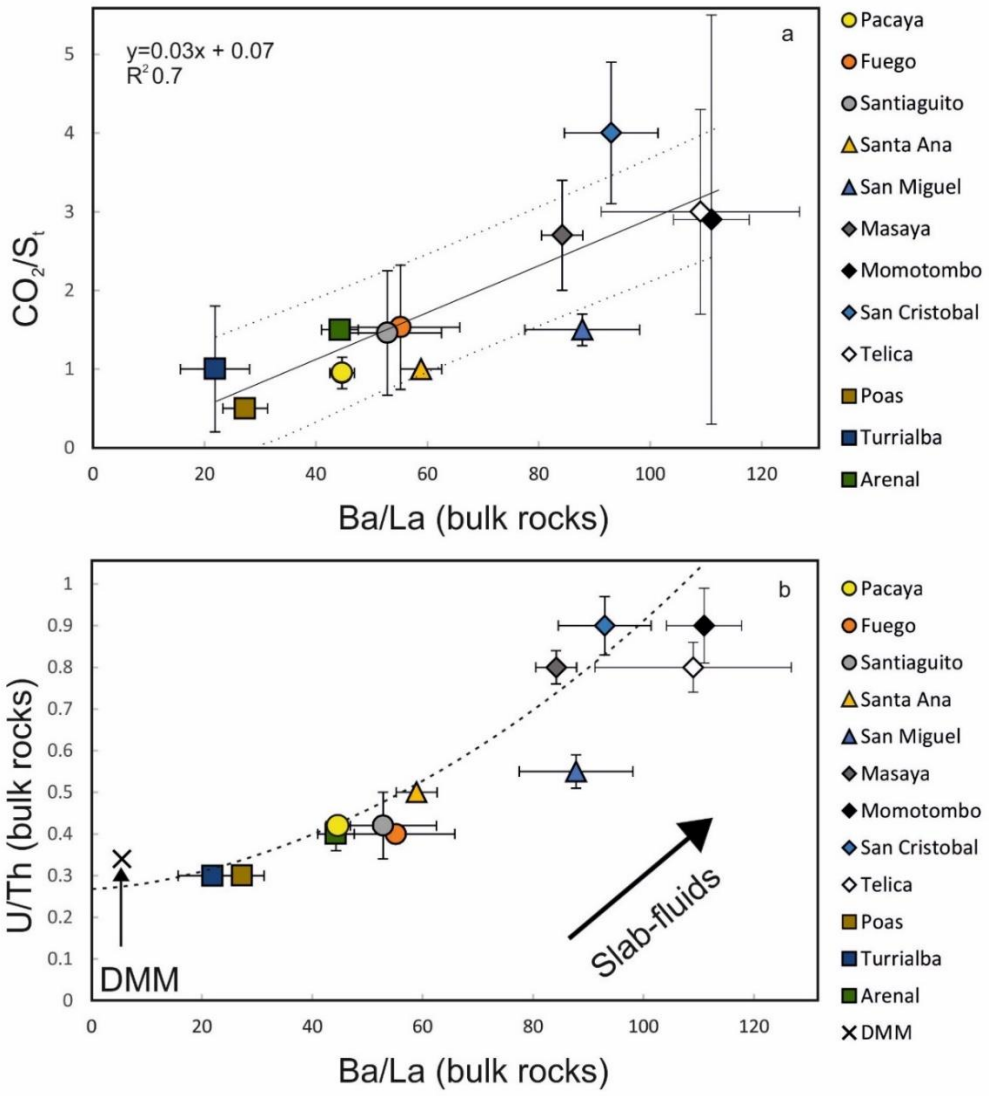

Figure 4.10 a) Scatter plot of mean CO_2/S_t vs. mean Ba/La and b) mean U/Th vs. mean Ba/La for CAVA volcanoes. For each volcano, the mean gas CO_2/S_t ratio is plotted, taken from this study (Pacaya) or from Aiuppa et al., (2014, 2017). The mean Ba/La and U/Th ratios were calculated averaging published whole-rock analyses (extracted from the earthchem portal; http://www.earthchem.org/portal). The error bars show one standard deviation. CO_2/S_t ratios for Fuego and Santiaguito are derived from equation (3) using available Ba/La information (from earthchem portal). The dashed lines in (a) represent the confidence intervals (± 0.75 at 1 σ) on

the estimated CO_2/S_t ratios. DMM is the composition of Depleted MORB Mantle source (Salters and Stracke, 2004).

In order to put our novel $^3He/^4He$-$\delta^{13}C$ results in the context of CAVA (Fig. 4.11), we need to make some general considerations on data selection. Detailed $^3He/^4He$-$\delta^{13}C$ datasets are available for CAVA in comparison to other arc segments (e.g., *Hilton et al.,* (2002)*; Fischer et al.,* (2007)*; Oppenheimer et al.,* (2014) and references therein). However, the measured range is large for both $^3He/^4He$ (0.7-8.1 Ra) and $\delta^{13}C$ (from -14‰ to 0‰). Large He and C variations are observed not only among different CAVA volcanoes, but also within the same volcanic system (*Fischer et al.,* 2007). This variability is largely an effect of the disparate use of different gas (high- and low-temperature crater fumaroles, flank gases, geothermal springs, and distal gas emissions) and sample (FIs in olivine phenocrysts vs. gas emissions) types. In the majority of CAVA volcanoes analyzed so far (*Fischer et al.,* 2005*; Shaw et al.,* 2006*; Di Piazza et al.,* 2015*; Robidoux et al.,* 2017), the $^3He/^4He$ ratios in olivine-hosted fluid inclusions are typically higher than in (or at the upper range of) volcanic gases from the same volcanic system. FIs should thus be prioritized as more reliable indicators of the magmatic/mantle signature, where available. $^{13}C/^{12}C$ ratios are currently difficult to measure in olivine-hosted fluid inclusions, except in mantle xenoliths or in phenocrysts crystallized at high depth (*Deines,* 2002*; Correale et al.,* 2015*; Gennaro et al.,* 2017). Thus, volcanic gases remain in most cases the only source of information, but should be limited to sample types showing greater magmatic affinity (e.g., high-temperature crater fumaroles should be preferred to hydrothermal or distal gas emissions).

In view of the above, our selected CAVA $^3He/^4He$-$\delta^{13}C$ population includes, for each volcano, the maximum Rc/Ra values measured (in FIs where available), and the mean $\delta^{13}C$ of crater fumaroles only (Fig. 4.11). This selected CAVA subset (Tab. 4.4) gives the opportunity to make some considerations on along-arc variations of these tracers. Before our study, the highest $^3He/^4He$ values along CAVA had been measured at Turrialba (Costa Rica), with values up to 8.1 Ra in fumarole gases (*Shaw et al.,* 2003*; Tassi et al.,* 2004*; Hilton et al.,* 2010*; Vaselli et al.,* 2010*; Di Piazza et al.,* 2015) and up to 8.3 Ra in fluid inclusions in olivines (*Fischer et al.,* 2005*; Shaw et al.,* 2006*; Di Piazza et al.,* 2015). Slightly lower ratios (up to 7.6 Ra; *Poreda and Craig,* (1989)*; Shaw et al.,* (2003)*; Hilton et al.,* (2010)*; Fischer et al.,* (2015)), but still within the MORB range, have also been measured in crater fumaroles from the nearby Póas volcano (*Sano and Williams,* 1996*; Shaw et*

al., 2003*; Hilton et al.,* 2010*; Fischer et al.,* 2015) (Fig. 4.11). These high ratios have widely been interpreted as representative of the signature of the mantle wedge beneath this segment of CAVA, with no (or very limited) contribution from the subducting Cocos plate lithosphere. This MORB affinity of Costa Rican volcanism is supported by several independent geochemical indicators such as the low Ba/La, Ba/Th, and U/Th ratios in the erupted rocks (*Patino et al.,* 2000*; Sadofsky et al.,* 2008). The few measurements carried out in El Salvador at Santa Ana volcano gave a $^{3}He/^{4}He$ up to 7.6 Ra (*de Leeuw et al.,* 2007), while in Nicaragua the $^{3}He/^{4}He$ ration ranged from 7.2 Ra at San Cristobal (*Robidoux et al.,* 2017) to 7.6 at Mombacho (*Shaw et al.,*2003) (Fig. 4.11). In consideration of the high $^{3}He/^{4}He$ we measured at Pacaya, Figure 4.11 strongly reinforces the hypothesis of a mantle signature with no appreciable addition of radiogenic ^{4}He from the slab or the crust in SE-Guatemala, similar to Southern Costa Rica. The increased sediment input from the subducting slab beneath Nicaraguan segment of CAVA, highlighted by high Ba/La and U/Th ratios (*Sadofsky et al.,* 2008), only leads to a minor decline of the $^{3}He/^{4}He$ ratio.

As for $\delta^{13}C$ (Tab. 4.4; Fig. 4.11), the Pacaya $\delta^{13}C$ signature (-3.5±0.4‰) approaches the average isotope compositions of Costa Rican ($\delta^{13}C$ -3.1±1.3; *Sano and Williams,* (1996)*; Shaw et al.,* (2003)*; Tassi et al.,* (2004)*; Hilton et al.,* (2010)*; Vaselli et al.,* (2010)*; Fischer et al.,* (2015)*)* and Guatemalan *($\delta^{13}C$ = -3.3±0.4‰; Janik et al.,* (1992)*; Sano and Williams,* (1996)*; Goff and McMutry,* (2000)*; this work*) volcanoes, and reflect high mantle contributions. Slightly more positive signatures are observed in El Salvador and Nicaragua ($\delta^{13}C$ = -2.9±0.6‰ and -2.7±0.6‰, respectively; *Allard,* (1983)*; Sano and Williams,* (1996)*; Snyder et al.,* (2001)*; Shaw et al.,* (2003)) that could be compatible with an enhanced limestone contribution ($\delta^{13}C$ = 0‰; *Sano and Marty,* (1995)) with possible addition of organic carbon up to 10% in the central CAVA segment. This is shown in figure 4.11 by the dashed mixing curve, which supports the hypothesis that this is a mantle feature of the subducting slab common to most of the volcanoes of CAVA.

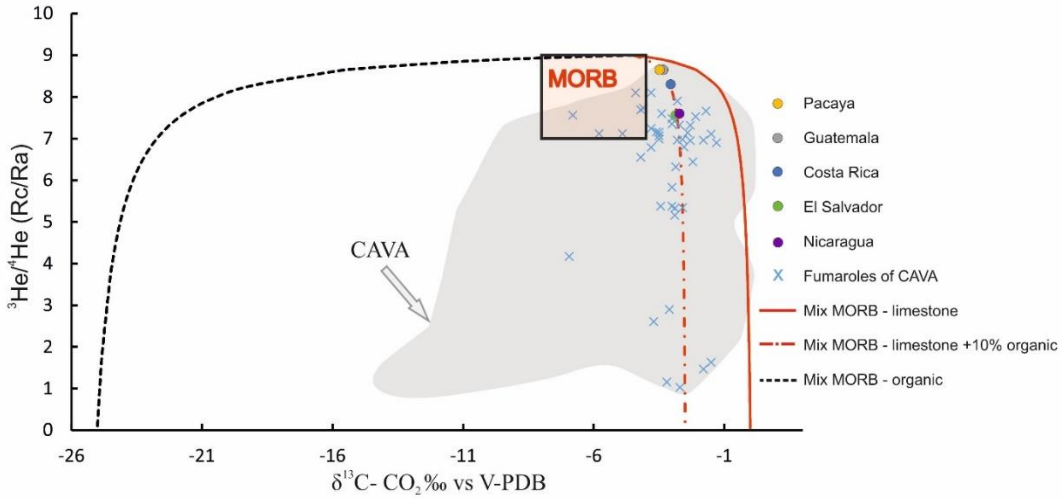

Figure 4.11 Scatter plot of $\delta^{13}C$ of CO_2 vs. $^3He/^4He$ ratio in CAVA volcanic gas samples. Colored circles represent average compositions for Pacaya and for the different CAVA volcanic arc segments. For each CAVA volcano that contributed to calculation of the averaged CAVA segment values, we considered the maximum Rc/Ra values measured in fumarole gases and FIs (where available), and the mean $\delta^{13}C$ of crater fumaroles only (see text for further details). See Table 4.4 for data sources. The blue crosses are compositions of individual fumarolic gas samples from CAVA (including low- and high-temperature fumaroles). The grey shaded area identifies the whole CAVA gas compositional field (including data from springs, flank fumaroles, peripheral gases; modified from Oppenheimer et al., (2014), see the original work for data sources). The $\delta^{13}C$ of CO_2 for Pacaya is an average on data from this work and those reported by Goff and McMurtry (2000) (-2.8‰ and -3.1‰) for two fumaroles (at 84.5 and 342 °C) sampled in the early 1990s. Details are reported in the Table 4.4. The red solid line represents mixing between MORB ($\delta^{13}C$= -4.5‰, Rc/Ra=9, $CO_2/^3He$=2E+9) and limestones ($\delta^{13}C$=0‰, Rc/Ra =0.05, $CO_2/^3He$ =E+13) (end-members taken from Sano and Marty, (1995), and Graham, (2002)). The black dashed line depicts mixing between MORB and organic carbon having $\delta^{13}C$=-25‰ (Sano and Marty, 1995). The red dashed line corresponds to mixing between MORB and limestones plus addition of 10% organic carbon.

4.6.4 **Volatile fluxes**

Our results also set the basis for a first assessment of the total volatile flux from Pacaya. Our measured SO_2 flux on January 16, 2016 was 885 ± 550 tons/d (Fig. 4.5c), thus falling in the middle of previously reported SO_2 fluxes for the volcano. These have fluctuated substantially since onset of the ongoing eruptive period in 1965. Published SO_2 fluxes have remained at low levels in

the 1970s-1990s, from 260 tons/day (1973-1993 mean; *Andres et al., 1993*) to 510 tons/day (1972-1997 mean; *Andres and Kasgnoc,* 1998). They then apparently peaked at 1350-1540 in the 1999-2002 period (*GVN,* 2002*; Rodriguez et al.,* 2004*; Mather et al.,* 2006), to decrease again in the mid- to late-2000s, from 270-400 tons/day (in 2004-2005; *Bluth et al.,* 2007) to <120 tons/day (in 2008; *Dalton et al.,* 2010). Our 2016 data therefore suggest intensification of degassing activity relative to the low fluxes seen in the most recent (2004-2008) published reports.

We combine our SO_2 flux results with the above best-guess for the Pacaya magmatic gas composition (80.5 mol. % H_2O, 10.4 mol. % CO_2, and 9.0 mol. % SO_2) to infer the H_2O and CO_2 fluxes for Pacaya for the first time. So doing, our SO_2 fluxes and compositions convert into H_2O and CO_2 fluxes of 2230±1390 and 700±440 tons/day for January 16, 2016. The large associated uncertainties reflect the huge temporal variability of SO_2 fluxes (62% variation at 1 SD) during our measurement interval, and underscore for the need of longer, more systematic observations to better constrain the volcano's degassing strength. We also infer a H_2 flux of ~1.1±0.7 tons/day based on a H_2/SO_2 of 0.04±0.01. Based on our results, the Total Volatile Flux in January 2016 was ~3800±2375 tons/day (Tab. 4.5), ranking Pacaya as a medium volcanic arc emitter. For example, our measured CO_2 flux ranks Pacaya at #18 in the list of the #44 volcanoes for which CO_2 information is available (*Burton et al.,* 2013*; Aiuppa,* 2015).

4.6.5 Implications for the volcanic CO_2 output in Guatemala

We use our novel results for Pacaya to attempt at a preliminary characterization of the CO_2 output from the Guatemalan segment of CAVA. Refining the arc CO_2 output, both globally and at the scale of individual arc segments, is mandatory for better constraining the CO_2 arc budget, e.g. to infer the fraction of subducted carbon (with slab sediments and altered oceanic crust) that is recycled via volcanic arc magmatism and, by difference, the fraction transported back into the deep mantle (*Dasgupta,* 2013*; Kelemen and Manning,* 2015). Owing to the lack of magmatic gas data, the Guatemalan contribution to the CAVA CO_2 output has only been indirectly established in past studies, by using either gas information from other, better studied segments of the arc (e.g. *Hilton et al.,* (2002)), or a "mean arc gas CO_2/SO_2 ratio" proxy (*Mather et al.,* 2006).

In addition to Pacaya, Fuego and Santiaguito (Fig. 4.1) are the two other Guatemalan volcanoes showing sustained, persistent degassing activity (*Rodriguez et al.,* 2004). In the classic SO_2 flux compilation study of *Andres*

and Kasgnoc, (1998), the two volcanoes had reported time-averaged (1972-1997 period) SO_2 emissions of 640 and 230 tons/day, respectively. For comparison, *Rodriguez et al.,* (2004) reported SO_2 flux data for the 1999-2002 period being twice as low (337±145 and 127±58 tons/day, respectively). These data confirm Pacaya as the strongest degassing source in Guatemala, but also imply a not trivial CO_2 contribution from Fuego and Santiaguito.

The volcanic gas CO_2/SO_2 ratio signature and the CO_2 output are unfortunately undetermined for Fuego and Santiaguito. However, plenty of whole-rock information is available for magmas erupted at both volcanoes. Importantly, trace-element co-variation diagrams (e.g., Fig. 4.10b) suggest magmas erupted at Fuego and Santiaguito plot along the same compositional array of other CAVA magmas (*Sadowsky et al.,* 2008, and references cited therein). This opens the possibility to estimate the magmatic gas CO_2/SO_2 ratio signature of Fuego and Santiaguito based on the CAVA gas (CO_2/S_t ratio) vs. trace-element (Ba/La ratio) relationship of Figure 4.10a. Using equation (3), and with the specific $Ba/La_{m,rock}$ derived in earthchem for each volcano (Fuego: 55.1±10.6; Santiaguito: 52.8±9.7), we derive $CO_2/S_{t(m,\ gas)}$ ratios of respectively 1.5±0.75 and 1.4±0.75. Here, the confidence interval or delta (± 0.75), calculated from the regression line and one standard deviation (Fig. 4.10a), is taken as a proxy for the uncertainty in predicted $CO_2/S_{t(m,\ gas)}$ ratios.

We caution the above procedure is likely to provide only a rough approximation of the real magmatic gas CO_2/S_t ratio for each volcano, and that direct volcanic gas observations remain needed here. Yet, we can use our predicted CO_2/S_t ratios above (1.5±0.75 and 1.4±0.75) in tandem with time-averaged SO_2 fluxes (337±145 and 127±58 tons/day, respectively), to preliminary evaluate the CO_2 flux at respectively 347±375 (Fuego) and 122±121 (Santiaguito). With these numbers, and considering the Pacaya CO_2 flux determined above, the total volcanic CO_2 flux from Guatemala would be ~1160±600 tons/day. This would respond to ~30% of the CO_2 flux from the Costa Rica – Nicaragua Volcanic Segment (CNSV: 2835-3184 tons/day, (*Aiuppa et al.,* 2014)), and ~16% of the total CAVA output (~6932 tons/day; *Hilton et al.,* 2002).

4.7 **Conclusions**

We have here investigated (i) the composition of the volcanic gas plume released by Pacaya volcano in Guatemala, and (ii) the noble gas composition of FIs trapped in olivines separated from rocks of some of the volcano's most recent eruptions. This novel dataset is used to characterise the magmatic gas

signature and the Total Volatile Flux budget for one of the most active CAVA volcanoes for the first time.

Our plume compositional data suggest Pacaya exhibits a H_2O-poor (for an arc volcano) composition (80.5 mol. %), with a characteristic magmatic CO_2/S_t ratio of ~1.0 to 1.5. Both the H_2O-poor and low CO_2/S_t ratio composition concur to suggest a limited slab-fluid contribution (at least compared to other volcanoes/arc segments; *Aiuppa et al.*, 2017), and a dominant mantle-wedge derivation of the emitted volatiles. The $^3He/^4He$ ratios measured in fluid inclusions hosted in olivines (Ra) are within the MORB range (8±1Ra) and among the highest values in CAVA volcanism. This strongly supports that the mantle source beneath Pacaya lacks of any contamination of radiogenic ^4He from the slab or the crust, as observed in Costa Rica segment of CAVA. This mantle affinity for He (and C) is consistent with independent petrological/geochemical evidence for magmas underneath Pacaya forming by decompressional melting rather than by slab-fluid addition, and also points to rapid magma transit in the crust, favoured by local extensional regime.

We have also estimated the Pacaya Total Volatile Flux at ~3800 tons/day in January 2016, a period of relatively mild intra-crateric strombolian activity. The Pacaya CO_2 flux accounts at 700±440 tons/day (January 16, 2016), implying the volcano is a moderate volcanic arc CO_2 emitter. By combining this measured Pacaya CO_2 flux with inferred CO_2 fluxes from Fuego and Santiaguito (using the CAVA CO_2/S_t ratio vs. Ba/La ratio association), we tentatively assess the total volcanic CO_2 flux from Guatemalan segment of CAVA at ~1160 tons/day.

4.7.1 **Acknowledgements**

This research received funding from the Deep Carbon Observatory Deep Earth Carbon Degassing program and from the European Research Council (FP7/ERC grant agreement n. 305377). We wish to thank Dulce María Esther González Domínguez for help during rocks sampling, Philippe Robidoux and Andrea Di Piazza for mineral preparation as well as Manuela Nazzari for EMPA measurements at INGV, Sezione di Roma 1. We are also grateful to Mariano Tantillo and Mariagrazia Misseri for their support in sample preparation and noble gases analysis of fluid inclusions. We finally thank Mauro Martelli and Francesco Salerno for chemical composition of fumaroles as well as Fausto Grassa, Ygor Oliveri and Aldo Sollami for the following carbon isotopes measures. Comments by the Associate Editor (T. Fischer) and two anonymous Reviewers improved the manuscript. All the data used for this paper are available in the Tables reported in the text (Tables 4.1-4.5)

and in Supplementary information (S1–S4) and by contacting the corresponding author.

4.8 Tables

Table 4.1 CO_2/SO_2 and H_2O/SO_2 ratios in the Pacaya plume derived from Multi-GAS measurements. Each value corresponds to the average ratio obtained within a short (a few minutes long) temporal window, calculated from the slope of the best-fit regression line between co-acquired CO_2 and SO_2 and H_2O and SO_2 concentrations, respectively (see examples of two temporal intervals in Figure 4.3). Duration (start and end time) of each of these temporal windows is indicated in the Table. For each ratio, the quoted error represents the confidence radius of the slope calculated with a level of certainty of 99.99 %, and corresponds to the probability that the best fit falls between lower and upper bounds. This depends on the number of samples and the quality of the best-fit, and therefore changes from ratio to ratio. SO_2 max is the peak SO_2 concentration (in ppm) in the plume measured within each considered temporal window.

Date	Start	End	SO_2 max	CO_2/SO_2	Error on CO_2/SO_2	H_2O/SO_2	Error on H_2O/SO_2
14/01/2016	00:13	00:15	8.2	2.6	0.5	22.0	6.6
14/01/2016	00:15	00:18	8.2	2.5	0.5	5.5	1.6
14/01/2016	18:12	18:21	6.1	10.3	0.8	157	47
14/01/2016	18:21	18:24	20	4.2	0.4	37.7	11.3
14/01/2016	18:25	18:29	20	4.3	0.4	70.8	21.2
15/01/2016	18:05	18:07	15	3.3	0.3	39.1	11.7
15/01/2016	18:08	18:10	15	3.3	0.3	35.9	10.8
15/01/2016	18:10	18:12	13	3.9	0.4	40.2	12.0
15/01/2016	18:12	18:16	13	3.8	0.4	83.0	24.9
15/01/2016	18:16	18:19	14	3.6	0.3	10.2	3.1
15/01/2016	18:20	18:23	14	3.5	0.3	44.8	13.4
16/01/2016	00:24	00:27	20	1.6	0.2	13.1	3.9
16/01/2016	00:27	00:29	20	1.5	0.2	11.7	3.5
16/01/2016	06:02	06:12	23	0.9	0.1	5.2	1.6
16/01/2016	06:06	06:08	11	2.1	0.2	8.8	2.7
16/01/2016	06:09	06:11	22	0.8	0.1	12.3	3.7
16/01/2016	06:14	06:18	22	1.5	0.2	20.6	6.2
16/01/2016	06:20	06:23	44	0.7	0.1	39.2	11.8
16/01/2016	06:24	06:26	34	0.9	0.1	8.9	2.7
16/01/2016	06:27	06:30	34	0.9	0.1	32.4	9.7
16/01/2016	18:00	18:05	4.3	9.8	1.0	329	98
17/01/2016	06:02	06:04	4.5	5.1	0.9	134	40
17/01/2016	06:05	06:08	4.5	5.0	0.9	39.6	11.9
18/01/2016	06:09	06:13	62	0.7	0.1	6.1	1.8
18/01/2016	06:14	06:20	40	0.7	0.1	1.7	0.5
18/01/2016	06:21	06:23	40	0.8	0.1	10.5	3.1
18/01/2016	06:24	06:27	40	0.7	0.1	6.5	1.9
18/01/2016	12:12	12:16	43	1.2	0.1	7.7	2.3
18/01/2016	18:00	18:04	22	2.9	0.2	116	34.9
18/01/2016	18:05	18:10	22	3.3	0.1	74.2	22.3
18/01/2016	18:11	18:14	22	2.9	0.2	109	32.7
18/01/2016	18:15	18:17	22	3.3	0.1	32.5	9.7
18/01/2016	18:18	18:20	5.1	8.5	1.0		
18/01/2016	18:22	18:26	5.1	8.2	1.0	194	58.3
19/01/2016	06:07	06:09	21	1.6	0.2	9.2	2.8
19/01/2016	06:09	06:12	21	1.5	0.2	1.6	0.5
19/01/2016	06:24	06:26	27	1.0	0.1	28.9	8.7
19/01/2016	06:27	06:30	27	1.1	0.1	1.5	0.4
20/01/2016	18:16	18:22	17	2.4	0.7	33.8	10.2
20/01/2016	18:22	18:24	47	1.3	0.4	4.5	1.3
20/01/2016	18:25	18:28	47	1.2	0.4	10.7	3.2

21/01/2016	00:01	00:20	66	0.9	0.3	4.2	1.3
21/01/2016	00:22	00:29	66	0.9	0.3	8.9	2.7
21/01/2016	18:08	18:12	6.4	6.0	1.8	131	39.4
21/01/2016	18:12	18:14	6.0	6.6	2.0	-	-
21/01/2016	18:16	18:19	6.0	6.7	2.0	60.3	18.1
21/01/2016	18:20	18:23	6.5	5.4	1.6	78.2	23.5
21/01/2016	18:24	18:26	6.5	5.4	1.6	89.8	26.9
21/01/2016	18:27	18:28	29	0.9	0.3	12.7	3.8
21/01/2016	18:28	18:29	29	0.9	0.3	11.8	3.5
22/01/2016	00:03	00:05	23	2.0	0.6	24.5	7.4
22/01/2016	00:06	00:10	23	1.9	0.6	14.8	4.4
22/01/2016	00:11	00:14	49	1.0	0.3	35.0	10.5
22/01/2016	00:15	00:17	49	1.0	0.3	4.5	1.4
22/01/2016	00:17	00:20	21	2.4	0.7	39.7	11.9
22/01/2016	00:21	00:24	21	2.5	0.7	11.1	3.3
22/01/2016	00:28	00:29	42	1.3	0.4	10.1	3.0
22/01/2016	12:00	12:28	82	1	0.3	22.8	6.8
22/01/2016	18:00	18:25	114	0.8	0.2	9.2	2.8
22/01/2016	00:27	00:30	42	1.3	0.4	12.7	3.8

Table 4.2 Chemistry (in ppm and % vol.) and carbon isotope composition (V-PDB) of gases collected from the two fumaroles at Pacaya volcano. Analytical uncertainty is < 3 % for chemical composition and ±0.1‰ for $\delta^{13}C$.

Sample	**Date**	**T (°C)**	**He (ppm)**	**H_2 (ppm)**	**O_2 (%)**	**N2 (%)**	**CH_4 (ppm)**	**CO (ppm)**	**CO_2 (%)**	**$\delta^{13}C$ CO_2 (‰)**
PA-1	22/01/2016	80	6	64	19.33	76.78	1.3	58	2.34	-3.9
PA-1 bis	22/01/2016	80	-	90	19.19	76.78	0.5	83	2.83	-4
PA-2	22/01/2016	80	-	71	20.05	77.83	0.8	1.5	0.93	-3.7
PA-2 bis	22/01/2016	80	-	629	20.11	77.57	0.7	167	0.96	-3.8

Table 4.3 Noble gas concentration and isotope composition in olivine-hosted fluid inclusions.

Sample	Mineral	Weight of loaded minerals (g)	Crystal size fraction (mm)	(^{4}He) (mol/g)	(^{20}Ne) (mol/g)	(^{40}Ar) (mol/g)	(^{36}Ar) (mol/g)	^{40}Ar/^{36}Ar	Error on (^{40}Ar/^{36}Ar) (%)	^{38}Ar/^{36}Ar	Error on (^{38}Ar/^{36}Ar) (%)	R/Ra	^{4}He/^{20}Ne	Rc/Ra Total	Error +/-
2010	Ol	0.23130	1	1.4E-13	5.3E-15	2.2E-13	7.3E-16	298.4	0.9	0.218	0.2	8.77	25.8	8.87	0.2
1961	Ol	0.19088	1	2.2E-13	4.8E-15	2.7E-12	9.0E-15	302.5	0.1	0.188	0.2	8.55	45.7	8.61	0.2
2010	Ol	0.48897	1	1.9E-13	7.4E-15	6.7E-13	2.0E-15	328.5	0.3	0.191	0.2	876	25.5	8.87	0.1
2010	Ol	0.74272	0.5	1.37E-13	1.2E-15	6.9E-13	2.2E-15	313.6	0.1	0.189	0.2	8.46	113.5	8.48	0.1
1975	Ol	0.41451	0.5	2.0E-13	3.2E-15	1.5E-12	5.00E-15	313.4	0.2	0.187	0.2	8.52	64.8	8.56	0.1
1961	Ol	0.45078	0.5	1.0E-13	2.2E-15	1.1E-12	3.6E-15	303.9	0.1	0.187	0.2	8.33	46.8	8.38	0.2
1961	Ol	0.47792	0.5	1.1E-13	3.6E-15	1.6E-12	5.4E-15	300.1	0.1	0.186	0.2	8.58	31.0	8.67	0.2
PRE-1961	Ol	0.45588	0.5	1.1E-13	3.1E-15	5.2E-13	1.7E-15	309.3	0.2	0.193	0.2	8.36	37.2	8.43	0.2
2010	Ol	0.67055	0.5	1.2E-13	2.7E-15	1.2E-12	3.9E-15	303.3	0.1	0.187	0.2	8.98	45.5	9.04	0.1
1975	Ol	0.41887	0.5	7.8E-14	3.7E-15	7.0E-13	2.3E-15	301.9	0.2	0.187	0.2	8.46	21.1	8.58	0.2
1975	Ol	0.41702	1	2.7E-13	8.2E-15	1.5E-12	3.2E-15			0.187	0.2	8.774	32.9	8.82	0.2
1975	Ol	0.53080	1	1.5E-13	1.5E-15	9.8E-13	3.2E-15	308.7	0.1	0.189	0.2	8.58	102.0	8.61	0.2
PRE-1961	Ol	0.50041	0.5	9.4E-14	3.1E-15	5.3E-13	1.7E-15	305.3	0.2	0.191	0.2	8.44	30.7	8.52	0.2

Table 4.4 Geochemical tracers, isotopic carbon composition and Rc/Ra for selected sub-dataset of CAVA segment. U/Th and Ba/La ratios are average whole-rock values calculated from rock compositions extracted from the earthchem portal (http://www.earthchem.org/portal). See also Aiuppa et al., (2014) for reference (Uncertainties in the mean values are given as error bars in Figure 4.10). $CO_2/^3He$ and $\delta^{13}C$ are mean of fumaroles reported in Fig. 4.11 as blue x symbol. Rc/Ra are air-corrected $^3He/^4He$ ratios normalized to the atmospheric $^3He/^4He$ ratio (Ra). The maximum value measured in each volcanic system is reported (except for end-members). [a] = Goff and McMutry, 2000; [b] = Sano and Williams 1996; [c] = Leeuw et al., 2007; [d] = Shaw et al., 2003; [e] = Fisher et al., 2015; [f] = Hilton et al., 2010; [g] = Tassi et al., 2004; [h] = Vaselli et al., 2010; [i] = Lucic et al., 2014; [l] = Allard 1983; [m] = this work; [n] = Robidoux et al., 2017;. [o] = Graham, 2002, [p] = Sano and Marty 1995, [q] = Fluid inclusion; [r] = Janik et al., 1992, [t] = Fumaroles. Average values for nations are the same reported in Fig. 4.11.

Volcano	U/Th	Ba/La	$CO_2/^3He$		$\delta^{13}C$		Rc/Ra	
Pacaya	0.45	44	1.89E+10	a, b	-3.46	a , m	8.65	m, q
Tecuamburro					-3.0	r	5.96	r
Zunil			1.14e+10	b	-2.86	b	6.32	b
Guatemala	**0.45**	**44**	**1.89E+10**	a, b	**-3.33**	b	**8.65**	m
Santa Ana	0.50	60	2.07E+10	c	-2.55	c	7.56	c, t
El Salvador	**0.50**	**60**	**2 .07E+10**		**-2.55**	c	**7.56**	c
Masaya	0.80	85	2.30E+10	d	-1.50	d	7.23	d, t
Cerro Negro	0.84	118.71	2.01E+10		-2.72	b, d, i	7.38	i, t
Momotombo	0.90	110	2.70E+10	d	-2.60	d, l	7.40	d, q
Mombacho	0.67	59.19	1.78E+10	d	-3.25	d	7.60	d, t
San Cristobal	0.90	90	3.20E+10	d	-2.95	d	7.20	n, q
Nicaragua	**0.82**	**92.58**	**2.40E+10**	d	**-2.60**	b, d, i	**7.60**	d
Poás	0.30	26	2.02E+10	e, f	-3.54	b, e, f	7.60	e, f
Turrialba	0.30	20	1.41E+10	d, g, h	-3.01	d, g, h	8.30	g, q
Costa Rica	**0.30**	**23.00**	**1.72E+10**	d, g, h	**-3.27**	d, g, h	**8.30**	g, t
DMM	0.35	7	2.00E+09	p	-4.50	p	8±1 Ra	o
Organic carbon			1.00E+13		-25		0.05	
Carbonate sediments	1.63	244.36	1.00E+13		0		0.05	

Table 4.5 Volatile fluxes on January 16, 2016

Gas	mol %	Flux (tons/day)
H_2O	80.5	2230±1390[£]
CO_2	10.4	700±440[£]
SO_2	9.0	885±550[&]
H_2	0.1	1.1±0.7[£]
Total Volatile flux[$]	100	3800±2375

[&]From UV camera, data from Figure 4.5
[£]Calculated scaling the each X/SO_2 ratio by the mean SO_2 flux
[$]Sum of H_2O, CO_2, SO_2 and H_2 fluxes

4.9 Supplementary Tables

Supplementary Table 4.1

Analysis Method	Unit Symbol	Analyte Symbol	P2010	P1975	P1961	Ppre1961
FUS-ICP	%	SiO2	50.47	50.59	50.17	50.70
FUS-ICP	%	Al2O3	20.30	21.89	23.56	21.35
FUS-ICP	%	Fe2O3(T)	9.54	8.30	7.95	8.89
		FeO	8.58	7.47	7.15	8.00
FUS-ICP	%	MnO	0.16	0.14	0.13	0.15
FUS-ICP	%	MgO	3.97	3.32	2.94	3.62
FUS-ICP	%	CaO	10.63	10.97	11.58	10.82
FUS-ICP	%	Na2O	3.39	3.38	3.20	3.24
FUS-ICP	%	K2O	0.69	0.71	0.59	0.66
FUS-ICP	%	TiO2	0.99	0.93	0.82	0.94
FUS-ICP	%	P2O5	0.22	0.20	0.17	0.20
FUS-ICP	%	LOI	-0.51	-0.44	-0.38	-0.18
FUS-ICP	%	Total	99.84	99.99	100.70	100.40

Supplementary Table 4.2

Analysis Method	Unit Symbol	Analyte Symbol	P2010	P1975	P1961	Ppre1961
FUS-ICP	ppm	Sc	25	23	18	23
FUS-ICP	ppm	Be	< 1	< 1	< 1	< 1
FUS-ICP	ppm	V	246	213	192	227
FUS-MS	ppm	Cr	30	50	30	70
FUS-MS	ppm	Co	26	21	19	22
FUS-MS	ppm	Ni	30	30	< 20	30
FUS-MS	ppm	Cu	90	80	50	60
FUS-MS	ppm	Zn	60	50	50	50
FUS-MS	ppm	Ga	22	21	21	21
FUS-MS	ppm	Ge	2	2	1	2
FUS-MS	ppm	As	< 5	< 5	< 5	< 5
FUS-MS	ppm	Rb	11	11	10	10
FUS-ICP	ppm	Sr	635	678	736	639
FUS-ICP	ppm	Y	16	14	12	15
FUS-ICP	ppm	Zr	75	74	61	70
FUS-MS	ppm	Nb	2	2	2	2
FUS-MS	ppm	Mo	< 2	< 2	< 2	3
FUS-MS	ppm	Ag	< 0.5	< 0.5	< 0.5	< 0.5
FUS-MS	ppm	In	< 0.2	< 0.2	< 0.2	< 0.2
FUS-MS	ppm	Sn	2	1	1	1
FUS-MS	ppm	Sb	0.9	0.9	0.9	1
FUS-MS	ppm	Cs	0.5	0.5	< 0.5	0.5
FUS-ICP	ppm	Ba	370	369	323	373
FUS-MS	ppm	La	8.4	8.2	6.9	7.6
FUS-MS	ppm	Ce	18.8	18.2	15.1	16.6
FUS-MS	ppm	Pr	2.79	2.68	2.2	2.43
FUS-MS	ppm	Nd	13.2	12.4	10.4	11.4
FUS-MS	ppm	Sm	3.1	3.1	2.5	3
FUS-MS	ppm	Eu	1.07	1.05	0.88	1.01
FUS-MS	ppm	Gd	3.5	3.4	2.6	3.1
FUS-MS	ppm	Tb	0.5	0.5	0.4	0.5
FUS-MS	ppm	Dy	3.2	3	2.5	2.9
FUS-MS	ppm	Ho	0.7	0.6	0.5	0.6
FUS-MS	ppm	Er	1.9	1.8	1.5	1.7
FUS-MS	ppm	Tm	0.27	0.25	0.2	0.24
FUS-MS	ppm	Yb	1.8	1.6	1.3	1.5
FUS-MS	ppm	Lu	0.28	0.25	0.19	0.25
FUS-MS	ppm	Hf	2	2	1.6	1.9
FUS-MS	ppm	Ta	0.3	0.3	0.2	0.2
FUS-MS	ppm	W	3	2	2	2

FUS-MS	ppm	Tl	< 0.1	< 0.1	< 0.1	0.1
FUS-MS	ppm	Pb	6	6	5	6
FUS-MS	ppm	Bi	< 0.4	< 0.4	< 0.4	< 0.4
FUS-MS	ppm	Th	1.1	1.1	0.9	1
FUS-MS	ppm	U	0.5	0.4	0.4	0.4

Supplementary Table 4.3

SiO_2	FeO	MnO	MgO	CaO	Sample number	Mineral/Phase
37.71	25.34	0.61	37.39	0.20	P1961b4r	olivine
38.27	24.90	0.46	37.47	0.18	P1961b4c	olivine
38.74	25.49	0.50	38.69	0.19	P1961b2r	olivine
38.90	24.85	0.50	37.85	0.19	P1961b1c	olivine
38.69	24.82	0.46	38.30	0.18	P1961b1r	olivine
39.24	24.72	0.50	38.57	0.20	P1961b5r	olivine
37.61	23.34	0.40	36.37	0.17	P1961a8c	olivine
38.14	24.83	0.42	38.97	0.23	P1961b2c	olivine
39.25	24.42	0.53	38.57	0.19	P1961b6r	olivine
38.24	24.82	0.56	39.62	0.26	P1961b3r	olivine
38.01	20.52	0.36	39.06	0.18	P1961a7c	olivine
37.51	21.89	0.38	42.26	0.24	P1961b6c	olivine
39.78	21.37	0.30	41.97	0.15	P1961b5c	olivine
39.29	26.93	0.52	34.77	0.21	P1975a7r	olivine
38.34	26.96	0.54	35.06	0.24	P1975a1c	olivine
38.61	26.92	0.60	35.52	0.31	P1975a8r	olivine
37.95	27.03	0.42	35.44	0.27	P1975a4c	olivine
38.15	26.52	0.55	35.04	0.29	P1975a1r	olivine
38.43	27.06	0.55	35.84	0.30	P1975a6r	olivine
37.99	28.20	0.57	37.47	0.27	P1975b4c	olivine
37.98	27.38	0.56	36.94	0.24	P1975a8c	olivine
38.05	25.96	0.53	35.09	0.24	P1975a5r	olivine
38.34	26.58	0.54	36.20	0.24	P1975a4r	olivine
37.89	26.68	0.52	36.40	0.22	P1975a3r	olivine
38.38	26.85	0.57	36.78	0.24	P1975b4r	olivine
37.31	26.82	0.43	36.95	0.31	P1975a7c	olivine
38.63	25.25	0.48	35.41	0.21	P1975a5c	olivine
36.51	27.38	0.51	38.90	0.29	P1975a6c	olivine
38.81	25.91	0.54	37.08	0.21	P1975b5r	olivine
38.58	25.73	0.50	36.99	0.25	P1975b3r	olivine
36.06	26.26	0.48	38.70	0.24	P1975a3c	olivine
38.59	24.10	0.43	36.65	0.18	P1975b2c	olivine
38.08	25.32	0.44	39.24	0.18	P1975b6r	olivine

39.27	22.34	0.33	40.80	0.19	P1975b5c	olivine
41.65	20.50	0.30	37.92	0.20	P1975b1c	olivine
39.19	20.95	0.36	41.73	0.18	P1975b3c	olivine
38.62	20.87	0.27	43.31	0.19	P1975b6c	olivine
39.00	15.17	0.20	43.90	0.13	P1975a2c	olivine
40.24	14.27	0.23	45.80	0.13	P1975a2r	olivine
36.70	29.20	0.65	31.06	0.24	P2010a1c	olivine
36.70	29.39	0.48	31.30	0.23	P2010a4c	olivine
37.90	30.25	0.59	32.67	0.27	P2010b3c	olivine
37.50	29.77	0.65	32.93	0.27	P2010b3r	olivine
38.21	28.47	0.70	34.65	0.24	P2010b4c	olivine
37.71	26.27	0.52	35.61	0.18	P2010b4r	olivine
37.60	26.14	0.46	35.96	0.18	P2010b2r	olivine
39.26	25.70	0.58	37.04	0.24	P2010b7c	olivine
39.08	24.26	0.50	37.40	0.16	P2010b1r	olivine
39.79	24.03	0.42	38.00	0.16	P2010b1c	olivine
38.18	24.41	0.37	39.51	0.21	P2010b7r	olivine
38.75	22.98	0.40	39.46	0.18	P2010b5r	olivine
39.54	20.45	0.21	41.98	0.20	P2010b5c	olivine
38.14	30.37	0.65	33.33	0.25	PP1961b3r	olivine
37.80	30.05	0.61	35.01	0.22	PP1961b4c	olivine
37.96	29.44	0.61	34.92	0.20	PP1961b3c	olivine
37.70	28.18	0.63	33.79	0.23	PP1961a4c	olivine
37.80	28.78	0.52	36.09	0.26	PP1961b4r	olivine
38.99	28.22	0.61	35.63	0.26	PP1961a4r	olivine
38.19	28.28	0.57	36.12	0.23	PP1961b2c	olivine
38.00	28.14	0.47	36.24	0.17	PP1961b2r	olivine
37.86	27.01	0.53	36.53	0.36	PP1961a6c	olivine
38.72	25.77	0.39	38.48	0.18	PP1961a2c	olivine
38.08	23.98	0.28	39.29	0.15	PP1961a7r	olivine
38.35	24.09	0.38	40.94	0.09	PP1961b5r	olivine
39.49	23.00	0.33	39.48	0.17	PP1961a2r	olivine
39.31	23.50	0.50	40.81	0.22	PP1961b5c	olivine
38.89	21.00	0.34	42.76	0.17	PP1961a5c	olivine
39.29	20.54	0.30	42.44	0.16	PP1961a5r	olivine
39.65	12.86	0.10	46.57	0.13	PP1961a1r	olivine
40.13	11.16	0.21	48.15	0.07	PP1961a3r	olivine
40.57	10.81	0.19	48.39	0.11	PP1961a1c	olivine
40.66	9.70	0.10	48.31	0.10	PP1961a3c	olivine

Ref.	Volcano	Location	Sample	4He/20Ne	R/Ra	$^3He/^4He$ (Ra)	err.
Elkins et al., 2006	Mombacho	V. Mombacho	Nic-15/1			7.59	0.10
Elkins et al., 2006	Mombacho	V. Mombacho	Nic-15/2			6.86	0.05
Elkins et al., 2006	Masaya	V. Masaya	Nic-7			1.98	0.02
Elkins et al., 2006	Masaya	Tipitapa	Nic-8			2.99	0.06
Elkins et al., 2006	Masaya	Xiloa	Nic-1			7.14	0.11
Elkins et al., 2006	Momotombo	Ormat power plant	Nic-14			6.86	0.10
Elkins et al., 2006	Momotombo	Ormat power plant	Nic-13			6.35	0.10
Elkins et al., 2006	Momotombo	V. Momotombo	Nic-2			6.99	0.07
Elkins et al., 2006	Momotombo	V. Momotombo	Nic-3			6.99	0.07
Elkins et al., 2006	Momotombo	San Francisco Libre	Nic-12			1.83	0.03
Elkins et al., 2006	Cerro Negro	V. Cerro Negro	Nic-22			1.26	0.02
Elkins et al., 2006	Cerro Negro	V. Cerro Negro	Nic-23			1.72	0.03
Elkins et al., 2006	Cerro Negro	V. Cerro Negro	Nic-24			6.99	0.07
Elkins et al., 2006	Telica	San Jacinto	Nic-17			5.68	0.07
Elkins et al., 2006	Telica	V. Telica	Nic-27			7.41	1.90
Elkins et al., 2006	San Cristobal	V. San Cristobal	Nic-20			5.74	0.09
Elkins et al., 2006	San Cristobal	V. San Cristobal	Nic-21			5.74	0.09
Elkins et al., 2006	Conseguina	V. Conseguina	Nic-29			2.96	0.06
Ref.	**Volcano**	**Location**	**Sample**	**4He/20Ne**	**R/Ra**	**Rc/Ra**	**err.**
Shaw et al., 2003	Mombacho	V. Mombacho	N-35 dup			7.60	0.10
Shaw et al., 2003	Mombacho	V. Mombacho	N-20			6.86	0.05
Shaw et al., 2003	Masaya	Cerro el Comolito	N-14			1.98	0.02
Shaw et al., 2003	Masaya	Tipitapa	N-32			3.03	0.04
Shaw et al., 2003	Masaya	Tipitapa	N-33 dup			2.94	0.08
Shaw et al., 2003	Masaya	Xiloa	N12			7.23	0.20
Shaw et al., 2003	Masaya	Xiloa	N-13 dup			7.04	0.06
Shaw et al., 2003	Momotombo	V. Momotombo	N-11			6.99	0.07
Shaw et al., 2003	Momotombo	V. Momotombo	N-31 dup				
Shaw et al., 2003	Momotombo	Ormat power plant	N-16			6.86	0.09
Shaw et al., 2003	Momotombo	Ormat power plant	N-34			6.40	0.10
Shaw et al., 2003	Momotombo	Ormat power plant	N-17 dup			6.40	0.10
Shaw et al., 2003	Momotombo	La Chistata	I-149			3.39	0.08
Shaw et al., 2003	Momotombo	La Chistata	I-189 dup			3.40	0.09
Shaw et al., 2003	Momotombo	San Francisco Libre	N-15			1.79	0.02
Shaw et al., 2003	Momotombo	San Francisco Libre	I-118			1.88	0.03
Shaw et al., 2003	Cerro Negro	V. Cerro Negro	N-7			1.26	0.02
Shaw et al., 2003	Cerro Negro	V. Cerro Negro	N-6			1.72	0.03
Shaw et al., 2003	Cerro Negro	V. Cerro Negro	N-4	14.1		6.99	0.07
Shaw et al., 2003	Telica	V. Telica	I-084			2.90	0.20
Shaw et al., 2003	Telica	V. Telica	N-8			7.50	0.07

Shaw et al., 2003	Telica	V. Telica	N-9 dup			7.33	4.00
Shaw et al., 2003	Telica	San Jacinto	N-21			5.50	0.08
Shaw et al., 2003	Telica	San Jacinto	N-23 dup			5.86	0.05
Shaw et al., 2003	San Cristóbal	V. San Cristobal	N-2			5.65	0.09
Shaw et al., 2003	San Cristóbal	V. San Cristobal	N-5 dup			5.74	0.08
Shaw et al., 2003	Conseguina	La Validora	N-38			3.37	0.06
Shaw et al., 2003	Conseguina	La Validora	I-087 dup			3.22	0.08
Shaw et al., 2003	Conseguina	La Validora	I-110			2.31	0.07
Shaw et al., 2003	Cerro Negro	Fumarole A1	CN-7	11.6		6.77	0.22
Shaw et al., 2003	Cerro Negro	Fumarole A2	CN-7	12.9		6.37	0.21
Shaw et al., 2003	Cerro Negro	Fumarole B	CN-8	38.3		7.38	0.17
Ref.	**Volcano**	**Location**	**Sample**	**4He/20Ne**	**R/Ra**	**Rc/Ra**	**err.**
Di Piazza et al., 2015	Turrialba	SW Crater	SW1	44.8		7.93	0.08
Di Piazza et al., 2015	Turrialba	SW Crater	F1	60.6		7.96	0.08
Di Piazza et al., 2015	Turrialba	Central Crater	FC4	30.8		7.88	0.08
Di Piazza et al., 2015	Turrialba	Central Crater	FC2	7.4		7.82	0.09
Di Piazza et al., 2015	Turrialba	Central Crater	FC3	170.7		7.78	0.10
Di Piazza et al., 2015	Turrialba	NE to CCr	108	6.0		7.08	0.10
Ref.	**Volcano**	**Location**	**Sample**	**4He/20Ne**	**R/Ra**	**3He/4He (Rc/Ra)**	**err.**
Snyder et al., 2003	Miravalles	Miravalles	PGM05			6.23	
Snyder et al., 2003	Miravalles	Miravalles	PGM10			6.64	
Snyder et al., 2003	Miravalles	Miravalles	PGM11			6.86	
Snyder et al., 2003	Miravalles	Miravalles	PGM12			6.49	
Snyder et al., 2003	Miravalles	Miravalles	PGM20			6.67	
Snyder et al., 2003	Miravalles	Miravalles	PGM21			6.81	
Snyder et al., 2003	Miravalles	Miravalles	PGM29			6.68	
Snyder et al., 2003	Miravalles	Miravalles	PGM31			6.24	
Snyder et al., 2003	Miravalles	Miravalles	PGM45			6.66	
Snyder et al., 2003	Miravalles	Miravalles	PGM46			6.55	
Snyder et al., 2003	Poa´s	Poa´s	CL,FC			7.08	
Snyder et al., 2003	Ahuachapa´n	Ahuachapa´n	AH06			7.01	
Snyder et al., 2003	Ahuachapa´n	Ahuachapa´n	AH16A			6.77	
Snyder et al., 2003	Ahuachapa´n	Ahuachapa´n	AH17			7.00	
Snyder et al., 2003	Ahuachapa´n	Ahuachapa´n	AH20			6.93	
Snyder et al., 2003	Ahuachapa´n	Ahuachapa´n	AH21			7.08	
Snyder et al., 2003	Ahuachapa´n	Ahuachapa´n	AH22			6.86	
Snyder et al., 2003	Ahuachapa´n	Ahuachapa´n	AH23			7.07	
Snyder et al., 2003	Ahuachapa´n	Ahuachapa´n	AH4B			6.90	
Snyder et al., 2003	Berlı´n	Berlı´n	TR02			5.59	
Snyder et al., 2003	Berlı´n	Berlı´n	TR4B			5.80	
Snyder et al., 2003	Berlı´n	Berlı´n	TR4C			5.54	

Snyder et al., 2003	Berlı´n	Berlı´n	TR09			5.71	
Snyder et al., 2003	San Vicente	San Vicente	HS			6.27	
Snyder et al., 2003	San Vicente	San Vicente	FC			6.41	
Snyder et al., 2003	Chinameca	Chinameca	FCLV01			3.47	
Snyder et al., 2003	Chinameca	Chinameca	FCIF01			5.95	
Snyder et al., 2003	Momotombo	Momotombo	MT20			6.71	
Snyder et al., 2003	Momotombo	Momotombo	MT27			6.75	
Snyder et al., 2003	Momotombo	Momotombo	MT27			6.80	
Snyder et al., 2003	Momotombo	Momotombo	MT35			6.75	
Snyder et al., 2003	Momotombo	Momotombo	MT35			6.76	
Snyder et al., 2003	Momotombo	Momotombo	MT36			n.d.	
Snyder et al., 2003	Momotombo	Momotombo	MT36-43			6.96	
Snyder et al., 2003	Momotombo	Momotombo	MT38			6.74	
Snyder et al., 2003	Momotombo	Momotombo	MT38A			7.05	
Snyder et al., 2003	Momotombo	Momotombo	MT40			6.99	
Snyder et al., 2003	Momotombo	Momotombo	MT40B			7.04	
Snyder et al., 2003	Momotombo	Momotombo	MT42			6.79	
Snyder et al., 2003	Momotombo	Momotombo	MT42			6.78	
Snyder et al., 2003	Momotombo	Momotombo	MT43			6.72	
Snyder et al., 2003	El Carol	El Carol	HSc			7.40	
Snyder et al., 2003	Najo	Najo	FCc			6.86	
Snyder et al., 2003	Najo	Najo	FCc			6.55	
Snyder et al., 2003	Najo	Najo	HSc			6.49	
Snyder et al., 2003	Mecatepe	Mecatepe	HSc2			7.50	
Snyder et al., 2003	Casita	Casita	FCc4			7.37	
Snyder et al., 2003	Mombacho	Mombacho	FCc3			7.72	
Snyder et al., 2003	Canas	Canas	CAS02			4.34	
Snyder et al., 2003	Miravalles	Miravalles	PGM01			6.52	
Snyder et al., 2003	Miravalles	Miravalles	PGM02			7.15	
Ref.	**Volcano**	**Location**	**Sample**	**4He/20Ne**	**R/Ra**	**RC/RA**	**err.**
Leeuw et al., 2007	Agua Shuca	Flank location 1	ES02-5a			6.67	0.10
Leeuw et al., 2007	Agua Shuca	Flank location 1	ES02-5b			6.72	0.09
Leeuw et al., 2007	Agua Shuca	Flank location 2	ES02-4			6.13	0.09
Leeuw et al., 2007	Ahuachapan La Labor	Flank location 1	ES02-3			7.24	0.20
Leeuw et al., 2007	Cuyanaul volcano	Flank location 1	ES02-6			6.37	0.09
Leeuw et al., 2007	Cuyanaul volcano	Flank location 2	ES02-7			6.38	0.09
Leeuw et al., 2007	El Tortuguero	Flank location 1	ES02-8			3.99	0.38
Leeuw et al., 2007	El Tortuguero	Flank location 2	ES02-9			6.69	0.11
Leeuw et al., 2007	V. Izalco	Crater location 1	ES02-12			1.06	0.02
Leeuw et al., 2007	V. Santa Ana	Crater location 1	ES02-10			7.56	0.11
Leeuw et al., 2007	V. Santa Ana	Crater location 2	ES02-11			7.37	0.10

Leeuw et al., 2007	San Vincente geothermal area	La Carbonera, Location 1	ES02-1			6.03	0.15
Leeuw et al., 2007	San Vincente geothermal area	La Carbonera, Location 2	ES02-2			6.24	0.12
Leeuw et al., 2007	Berlin geothermal area	TR2	ES02-17a			1.71	0.03
Leeuw et al., 2007	Berlin geothermal area	TR2	ES02-17b			3.65	0.05
Leeuw et al., 2007	Berlin geothermal area	TR7	ES02-18a			5.97	0.08
Leeuw et al., 2007	Berlin geothermal area	TR7	ES02-18b			6.16	0.09
Leeuw et al., 2007	Chinameca	La Viejona	ES02-13			3.39	0.13
Leeuw et al., 2007	Chinameca	Los Hervidos	ES02-14			6.47	0.09
Leeuw et al., 2007	Meanguera	Infiernillos, location 1	ES02-15			5.11	0.08
Leeuw et al., 2007	Meanguera	Infiernillos, location 1	ES02-16			5.19	0.08

Ref.	**Volcano**	**Location**	**Sample**	**4He/20Ne**	**R/Ra**	**RC/RA**	**err.**
Poreda and Craig, 1989	Zunil field	GM-1-80	AS			7.20	21.10
Poreda and Craig, 1989	Zunil field	GM-3-80	AS			7.38	
Poreda and Craig, 1989	Zunil field	GM-8-80	W			6.49	
Poreda and Craig, 1989	Poás	SF	SF			7.20	14.40
Poreda and Craig, 1989	Marivalles	85-3130	W			7.38	36.00
Poreda and Craig, 1989	Marivalles	85-3131	W			6.49	90.00
Poreda and Craig, 1989	Marivalles	85-3132	W			7.37	160.00
Poreda and Craig, 1989	Marivalles	85-136	W			7.05	72.00

Ref.	**Volcano**	**Location**	**Sample**	**4He/20Ne**	**R/Ra**	**RC/RA**	**err.**
Shaw et al., 2003	Turrialba		CR-2				
Shaw et al., 2003	Turrialba		CR-3 dup			7.74	0.07
Shaw et al., 2003	Turrialba		CR2-1 (Mar)			8.10	0.10
Shaw et al., 2003	Turrialba		CR2-2 (Mar)			8.10	0.10
Shaw et al., 2003	Turrialba		CR3-2 (Jul)			7.70	0.07
Shaw et al., 2003	Irazu		CR-4				
Shaw et al., 2003	Irazu		CR-5 dup			7.24	0.06
Shaw et al., 2003	Poás		CR-6				
Shaw et al., 2003	Poás		CR-8			7.10	0.10
Shaw et al., 2003	Poás		CR-9 dup			6.90	0.10
Shaw et al., 2003	Poás		CR2-6 (Mar)			7.22	0.07
Shaw et al., 2003	Poás		CR2-14 (Mar)			7.60	0.10
Shaw et al., 2003	Poás		CR3-17 (Jul)			7.14	0.07
Shaw et al., 2003	Chocosuela-Platanar	Recreo Verde	CR-11	14.2		1.04	0.05
Shaw et al., 2003	Chocosuela-Platanar	Recreo Verde	CR-13			1.98	0.05
Shaw et al., 2003	Chocosuela-Platanar	La Marina	CR-14			2.53	0.02
Shaw et al., 2003	Chocosuela-Platanar	Poco Sol	CR-15				
Shaw et al., 2003	Chocosuela-Platanar	Poco Sol	CRT-1			6.19	0.05

Shaw et al., 2003	Chocosuela-Platanar	Poco Sol	CRT-2 dup			6.27	0.07
Shaw et al., 2003	Arenal	Quebrada Lava	CR-16	46.5		1.02	0.02
Shaw et al., 2003	Arenal	Quebrada Lava	CRT-3	88.0		0.74	0.04
Shaw et al., 2003	Arenal	Quebrada Lava	CRT-4 dup	67.0		0.77	0.03
Shaw et al., 2003	Arenal	Quebrada Naranja	CR-17				
Shaw et al., 2003	Arenal	Quebrada Naranja	CRT-5			7.00	0.10
Shaw et al., 2003	Arenal	Quebrada Naranja	CRT-6 dup			7.04	0.07
Shaw et al., 2003	Arenal	Baldi Thermal Resort	CRT-7	61.0		1.60	0.04
Shaw et al., 2003	Arenal	Baldi Thermal Resort	CRT-8 dup	121.0		1.51	0.05
Shaw et al., 2003	Miravalles	Hornillas	CRT-9			6.77	0.06
Shaw et al., 2003	Miravalles	Miravalles power plant	CR-10			5.20	0.07
Shaw et al., 2003	Miravalles	Miravalles power plant	CR-20 sup			5.29	0.05
Shaw et al., 2003	Miravalles	Miravalles power plant	CR-21			3.61	0.07
Shaw et al., 2003	R. de la Vieja	Las Paillas	CR-22				
Shaw et al., 2003	R. de la Vieja	Las Paillas	CRT-10			6.51	0.07
Shaw et al., 2003	Rincón de la Vieja	Las Paillas	CR-23			6.50	0.10
Shaw et al., 2003	R. de la Vieja	Las Paillas	CR2-9 (Mar)			6.34	0.07
Shaw et al., 2003	R. de la Vieja	Borinquen	CR-24			5.10	0.10
Shaw et al., 2003	R. de la Vieja	Borinquen	CR-25 dup			5.10	0.10

Ref.	**Volcano**	**Location**	**Sample**	**4He/20Ne**	**R/Ra**	**RC/RA**	**err.**
Goff and McMutry, 2000	Pacaya		PV92-22		7.9	7.91	
Goff and McMutry, 2000	Pacaya		PV92-29		2.9		
Sano and Williams, 1996	Pacaya				4.17		
Janik et al., 1992	Tecuamburro		#80		5.83	5.96	
Sano and Williams, 1996	Zunil				6.32		
Lucic et al., 2014	Cerro Negro		CN-7 A1	11.6		6.77	0.22
Lucic et al., 2014	Cerro Negro		CN-7 A2	12.9		6.37	0.21
Lucic et al., 2014	Cerro Negro		CN-8 B	38.3		7.38	0.17
Sano and Williams, 1996	Cerro Negro				6.8		
Allard, 1983	Momotombo				5.34		
Fischer et al., 2015; Hilton et al., 2010	Poàs		P1			7.1	0.1
Fischer et al., 2015; Hilton et al., 2010	Poàs		P5		7.56	7.6	0.1
Fischer et al., 2015; Hilton et al., 2010	Poàs		P7		7.12	7.14	0.1
Fischer et al., 2015; Hilton et al., 2010	Poàs		PO-03-1		7.07	7.14	0.1
Fischer et al., 2015; Hilton et al., 2010	Poàs		PO-03-2		7.15	7.16	0.1
Fischer et al., 2015; Hilton et al., 2010	Poàs		PO-05-1		6.9	6.92	0.1
Fischer et al., 2015; Hilton et al., 2010	Poàs		Pt 06-1-1		7.14	7.15	0.1
Fischer et al., 2015; Hilton et al., 2010	Poàs		Pt 06-1-3		6.44	6.64	0.1

Fischer et al., 2015; Hilton et al., 2010	Poàs	P007-1a	7.12	7.13	0.2
Fischer et al., 2015; Hilton et al., 2010	Poàs	CR07-05	6.99	7.01	0.3
Fischer et al., 2015; Hilton et al., 2010	Poàs	Pnar-06a	6.96	6.96	0.1
Hilton et al., 2010	Poàs	Costa 7-dup	7.11	7.14	0.1
Fischer et al., 2015; Hilton et al., 2010	Poàs	P007-3a	6.55	6.66	0.2
Hilton et al., 2010	Poàs	CR-3 dup	6.96	7	0.2
Hilton et al., 2010	Poàs	CR07-02	7.24	7.29	0.3
Hilton et al., 2010	Poàs	CR07-03 dup	7.16	7.18	0.3
Fischer et al., 2015; Hilton et al., 2010	Poàs	ICE-2	6.79	7.01	0.1
Fischer et al., 2015; Hilton et al., 2010	Poàs	TF10		7.06	0.1
Sano and Williams, 1996	Poàs		5.38		
Tassi et al., 2004; Vaselli et al., 2010	Turrialba	west 02-1999	7.33		
Vaselli et al., 2010	Turrialba	west	7.32	7.32	
Vaselli et al., 2010	Turrialba	west	7.66	7.66	
Vaselli et al., 2010	Turrialba	Central	7.48	7.48	

Supplementary table 4: Fluid inclusions

Ref.	Lat	Long	D. Along Arc km	Volcano	Sample	Material	Phase	4He mol/g	Rc/Ra (corrected for air)	Err.
Poreda and Craig, 1989	14.383	-90.6	201.6	Pacaya	Pacaya		Ol		6.8	1.5
Di Piazza et al. 2015	10.025	-83.767	1067.6	Turrialba	TU5	ash	Ol	2.97E-13	7.86	0.086
Di Piazza et al. 2015	10.025	-83.767	1067.6	Turrialba	TU6	ash	Ol	3.25E-13	7.91	0.084
Di Piazza et al. 2015	10.025	-83.767	1067.6	Turrialba	TU6	ash	Ol	4.76E-13	7.96	0.097
Di Piazza et al. 2015	10.025	-83.767	1067.6	Turrialba	TU6	ash	Ol	4.04E-13	8.02	0.107
Di Piazza et al. 2015	10.025	-83.767	1067.6	Turrialba	TU16	ash	Ol	4.88E-13	8.02	0.078
Di Piazza et al. 2015	10.025	-83.767	1067.6	Turrialba	TU16	ash	Ol	4.78E-13	8.04	0.073
Di Piazza et al. 2015	10.025	-83.767	1067.6	Turrialba	TU16	ash	Ol	7.35E-13	8.07	0.082
Di Piazza et al. 2015	10.025	-83.767	1067.6	Turrialba	TU37/1	ash	Ol	1.35E-13	7.9	0.233
Di Piazza et al. 2015	10.025	-83.767	1067.6	Turrialba	TU7	ash	Ol	8.4E-14	7.13	0.107
Di Piazza et al. 2015	10.025	-83.767	1067.6	Turrialba	TU7	ash	Ol	1.62E-13	7.06	0.093
Di Piazza et al. 2015	10.025	-83.767	1067.6	Turrialba	TU8	ash	Ol	1.23E-13	7.2	0.104
Di Piazza et al. 2015	10.025	-83.767	1067.6	Turrialba	TU4	ash	Ol	2.31E-13	7.95	0.132
Di Piazza et al. 2015	10.025	-83.767	1067.6	Turrialba	TU6	ash	Px	3.1E-14	6.11	0.278
Di Piazza et al. 2015	10.025	-83.767	1067.6	Turrialba	TU37/1	ash	Px	1.05E-13	7.87	0.217
Di Piazza et al. 2015	10.025	-83.767	1067.6	Turrialba	TU7	ash	Px	1.6E-14	6.34	0.157
Ref.	**Lat**	**Long**	**D. Along Arc km**	**Volcano**	**Sample**	**Material**	**Phase**	**4He mol/g**	**Rc/Ra (corrected for air)**	**Err.**
Fisher et al., 2005	12.507	-86.701	662.9	Cerro Negro	CN92	ash	Ol	4.46429E-14	6.10	

Fisher et al., 2005	9.9843	-83.845	1067.6	Irazu	IR	Lava	Px	7.32143E-14	4.10	
Fisher et al., 2005	13.817	-89.633	321.2	Izalco	IZ	Lava	Ol	7.41071E-14	8.50	0.42
Fisher et al., 2005	10.025	-83.767	1067.6	Turrialba	TU	Lava	Ol	1.56696E-13	8.30	0.3

Ref.	Lat	Long	D. Along Arc km	Volcano	Sample	Material	Phase	4He mol/g	Rc/Ra (corrected for air)	Err.
Fisher et al., 2010	12.507	-86.701	662.9	Cerro Negro	CN-01	1992 ash	Ol	1.26E-14	3.43	1.577
Fisher et al., 2010	12.507	-86.701	662.9	Cerro Negro	CN-02	1995 ash	Ol	1.28E-14	3.47	0.479
Fisher et al., 2010	12.477	-86.605	673.3	Momotombo	MO-02	Mix of 0.1 - 1 Kyrs	Ol	3.20E-15	5.08	2.691
Fisher et al., 2010	12.477	-86.605	673.3	Momotombo			Ol		7.4	4.45
Fisher et al., 2010	12.188	-86.333	714.5	Nejapa	NE-01	<Kyrs	Ol	1.36E-14	3.34	0.778

Ref.	Lat	Long	D. Along Arc km	Volcano	Sample	Material	Phase	4He mol/g	Rc/Ra (corrected for air)	Err.
Shaw et al., 2006	12.507	-86.701	662.9	Cerro Negro	CN-92-1	ash	Ol	4.73214E-14	6.1	0.46
Shaw et al., 2006	12.507	-86.701	662.9	Cerro Negro	CN-95-1	ash	Ol	8.66071E-14	6.97	0.28
Shaw et al., 2006	12.507	-86.701	662.9	Cerro Negro	CN-95-2	lava	Ol	3.03571E-14	7.11	0.47
Shaw et al., 2006	12.507	-86.701	662.9	Cerro Negro	CN-99-2	ash	Ol	1.32589E-13	6.67	0.34
Shaw et al., 2006	12.507	-86.701	662.9	Cerro Negro	CN-99-1	lava	Ol	2.5E-14	6.95	0.41
Shaw et al., 2006	12.507	-86.701	662.9	Cerro Negro	CN-95-2	lava	Ol	5.58036E-14	6.69	0.37
Shaw et al., 2006	12.507	-86.701	662.9	Cerro Negro	CN-92-1	ash	Px	1E-13	5.62	0.24
Shaw et al., 2006	12.507	-86.701	662.9	Cerro Negro	CN-95-1	ash	Px	1.21429E-13	5.82	0.21
Shaw et al., 2006	12.507	-86.701	662.9	Cerro Negro	CN-95-2	lava	Px	1.89286E-13	6.79	0.18
Shaw et al., 2006	12.507	-86.701	662.9	Cerro Negro	CN-99-2	ash	Px	3.20536E-13	4.73	0.13
Shaw et al., 2006	12.507	-86.701	662.9	Cerro Negro	CN-99-1	lava	Px	1.24554E-13	7	0.18
Shaw et al., 2006	12.507	-86.701	662.9	Cerro Negro	CN-95-2	lava	Px	2.15625E-13	6.41	0.15
Shaw et al., 2006	9.9843	-83.845	1067.6	Irazu	IZ-63F*	lava	Px	6.69643E-14	4.58	0.2
Shaw et al., 2006	12.188	-86.333	714.5	Nejapa	Nejapa-2	wall lava	Ol	3.92857E-14	7.14	0.39
Shaw et al., 2006	12.188	-86.333	714.5	Nejapa	Nejapa-1	pit lava	Ol	8.66071E-14	7.22	0.19
Shaw et al., 2006	12.188	-86.333	714.5	Nejapa	NE201	lava	Ol	5.9375E-14	6.89	0.57
Shaw et al., 2006	12.188	-86.333	714.5	Nejapa Asuseca	Asuseca	lava	Ol	3.79911E-13	7.49	0.21
Shaw et al., 2006	12.188	-86.333	714.5	Nejapa-C.L. Martinez	C.L. Martinez	lava	Ol	5.53571E-14	7.1	0.28
Shaw et al., 2006	12.188	-86.333	714.5	Nejapa-Motastepe	Motastepe	lava	Ol	1.91518E-13	7.1	0.14
Shaw et al., 2006	12.188	-86.333	714.5	Nejapa	Nejapa-2	wall lava	Px	3.52679E-14	5.32	0.38
Shaw et al., 2006	12.188	-86.333	714.5	Nejapa	Nejapa-1	pit lava	Px	3.75E-14	6.76	0.4
Shaw et al., 2006	12.188	-86.333	714.5	Nejapa-Motastepe	Motastepe	lava	Px	2.90179E-14	5.95	0.44

Shaw et al., 2006	10.025	-83.767	1067.6	Turrialba	4.1.01-1	lava	Ol	1.19196E-13	7.53	0.16
Ref.	**Lat**	**Long**	**D. Along Arc km**	**Volcano**	**Sample**	**Material**	**Phase**	**4He mol/g**	**Rc/Ra (corrected for air)**	**Err.**
Robidoux et al., 2017	12.700	-87.000	620	San Cristobal	SC5K		Ol	7.01871E-14	6.44	0.39
Robidoux et al., 2017	12.700	-87.000	620	San Cristobal	SC11D		Ol	4.59999E-14	7.01	0.40
Robidoux et al., 2017	12.700	-87.000	620	San Cristobal	SC11D (1)		Ol *	6.30187E-14	7.07	0.23
Robidoux et al., 2017	12.700	-87.000	620	San Cristobal	SC11D (2)		Ol *	3.48985E-14	7.02	0.58
Robidoux et al., 2017	12.700	-87.000	620	San Cristobal	SC02B		Ol	1.4233E-14	7.20	0.41
Robidoux et al., 2017	12.700	-87.000	620	San Cristobal	SC02B		Cpx	1.59134E-14	6.45	0.75

Chapter 5

5 Tracking Formation of a Lava Lake From Ground and Space: Masaya Volcano (Nicaragua), 2014–2017[2]

5.1 Abstract

A vigorously degassing lava lake appeared inside the Santiago pit crater of Masaya volcano (Nicaragua) in December 2015, after years of degassing with no (or minor) incandescence. Here we present an unprecedented-long (3 years) and continuous volcanic gas record that instrumentally characterizes the (re)activation of the lava lake. Our results show that, before appearance of the lake, the volcanic gas plume composition became unusually CO_2 rich, as testified by high CO_2/SO_2 ratios (mean: 12.2 ± 6.3) and low H_2O/CO_2 ratios (mean: 2.3 ± 1.3). The volcanic CO_2 flux also peaked in November 2015 (mean: 81.3 ± 40.6 kg/s; maximum: 247 kg/s). Using results of magma degassing models and budgets, we interpret this elevated CO_2 degassing as sourced by degassing of a volatile-rich fast-overturning (3.6–5.2 m^3 s^{-1}) magma, supplying CO_2 -rich gas bubbles from minimum equivalent depths of 0.36–1.4 km. We propose this elevated gas bubble supply destabilized the shallow (<1 km) Masaya magma reservoir, leading to upward migration of vesicular (buoyant) resident magma, and ultimately to (re)formation of the lava lake. At onset of lava lake activity on 11 December 2015 (constrained by satellite-based MODIS thermal observations), the gas emissions transitioned to more SO2-rich composition, and the SO2 flux increased by a factor ~ 40% (11.4 ± 5.2 kg/s) relative to background degassing (8.0 kg/s), confirming faster than normal (4.4 versus ~ 3 m^3 s^{-1}) shallow magma convection. Based on thermal energy records, we estimate that only ~0.8 of the 4.4 m^3 s^{-1} of magma actually reached the surface to manifest into a convecting lava lake, suggesting inefficient transport of magma in the near-surface plumbing system.

[2] Aiuppa, A., de Moor, J. M., Arellano, S., Coppola, D., Francofonte, V., Galle, B., Battaglia. A., ……A Moretti, R. (2018). Tracking formation of a lava lake from ground and space: Masaya volcano (Nicaragua), 2014‐2017. Geochemistry, Geophysics, Geosystems, 19. https://doi. org/10.1002/2017GC007227

5.2 Introduction

Emergence of a new lava lake is a relatively rare and exceptional event in Nature. Stable, nearly-persistent lava lakes are scarce volcanic features on Earth, existing at Ambrym volcano in Vanuatu (*Allard et al., 2015*), Erebus in Antarctica (*Oppenheimer et al., 2009*), Erta Ale in Ethiopia (*Vergnoille and Bouche, 2016*), Nyiragongo in Congo (*Burgi et al., 2014*) and Villarrica in Chile (Palma et al., 2008). Formation or re-birth of lava lakes is even less frequently observed. Recent examples of lava lake emergence include Halemaʻumaʻu Crater on Kilauea in 2008-present (*Patrick et al., 2013, 2016*) and Nyamuragira in 2012-2014 (*Coppola et al., 2016a*). The processes leading to (re)formation of a lava lake are not well understood due to the limited observations available.

Masaya volcano (Fig. 5.1) in Nicaragua has nearly continuous historical record of magma appearing and disappearing in the crater floor since the time of the first sightings by the Spanish conquistadors in 1524-1529 (*Rymer et al., 1998; GVP, 2013*). Since its formation in 1858-59 (*McBirney, 1956*), Masaya's Santiago pit crater (Fig. 5.1) has intermittently hosted one or more incandescence vents of variable size and degassing activity (*Rymer et al., 1998*). Occasionally, these vents have enlarged in dimension, most likely due to magma level increase in the conduit and crater floor collapse, ultimately leading to formation of an "active lava lake". Such a lava lake formation events in the Santiago crater floor have typically been associated with strong degassing episodes, each lasting years to decades (*Stoiber et al., 1986; Delmelle et al., 1999*), making Masaya one of the strongest degassing sources in the Central America Volcanic Arc (*Aiuppa et al., 2014; Martin et al., 2010; Mather et al., 2006*).

The latest Santiago degassing crisis started in 1993 and has persisted with fluctuating vigor until present (*Delmelle et al., 1999; Stix, 2007; Williams-Jones et al., 2003*). Although little or no magma has been erupted out of the crater, voluminous amounts of magmatic gas have been vented into the atmosphere (*Stoiber et al., 1986; Burton et al., 2000; Horrocks, 2001; Nadeau and Williams-Jones, 2009; Martin et al., 2010; Moune et al., 2010; de Moor et al., 2013*), resulting in substantial environmental impact on the surroundings and local communities (*Delmelle et al., 1999, 2002*). This unusually persistent degassing activity has also motivated extensive geophysical work in the attempt to resolve the structure of the shallow plumbing system (*Rymer et al., 1998; Delmelle et al., 1999; Williams-Jones et al., 2003*), and the magma circulation pathways/rates therein (*Stix, 2007*). Based on results of periodic gravity surveys, *Rymer et al.* (1998) and *Williams-Jones et al.* (2003) proposed that the Masaya cyclic degassing crises are caused by convective replacement of dense, degassed magma by gas-rich

vesicular magma in the shallow (<1 km depth) plumbing system. These authors also argued such convective overturning is not necessarily triggered by intrusion of fresh (gas-rich) magma, but may simply be initiated by degassing/crystallization (and consequent sinking) of shallow resident magma. However, volcanic gas information has never been available for the onset of a degassing crisis to test the likelihood of the two possible scenarios, i.e. intrusion of fresh magma versus convention of resident magma.

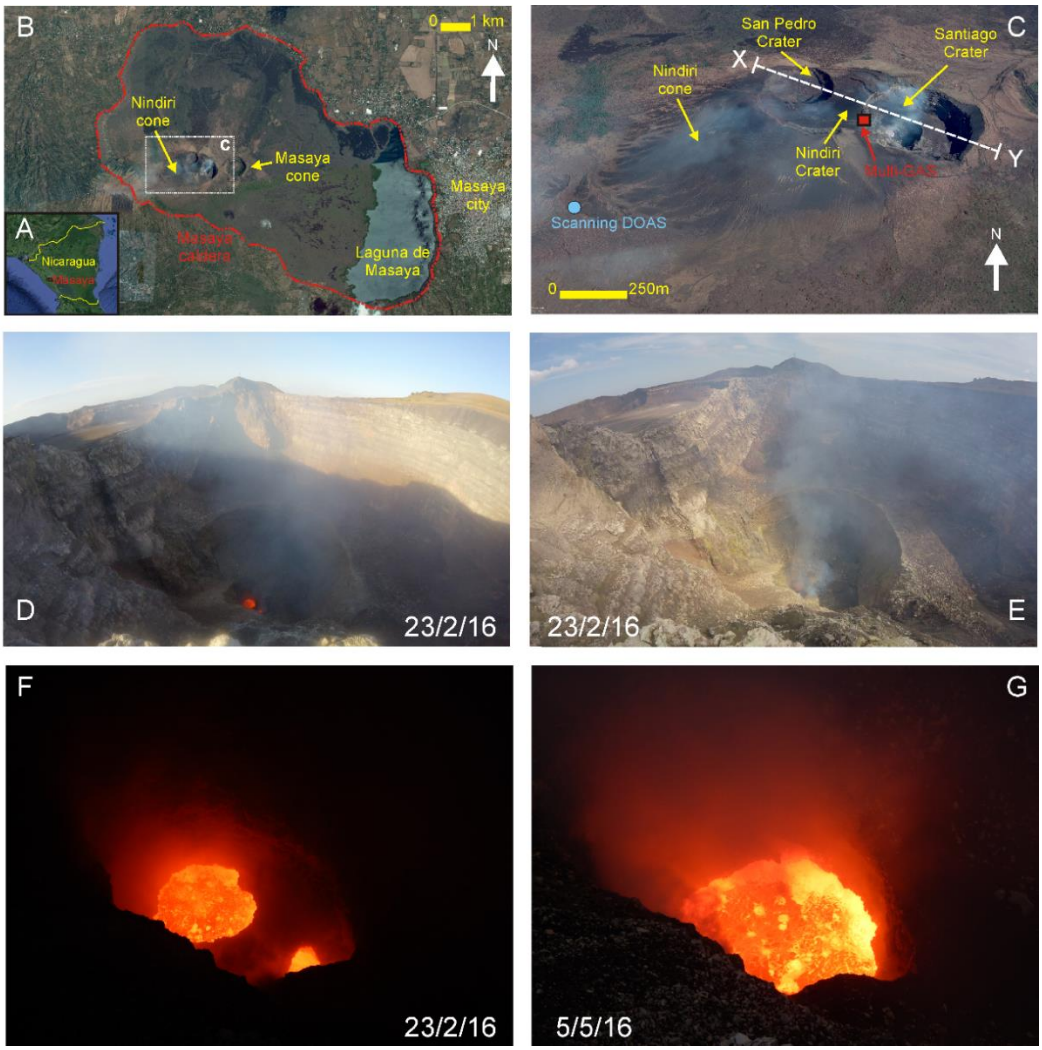

Figure 5.1 A) Google Earth map showing location of Masaya volcano in Nicaragua; B) the Masaya caldera (red dotted line), with the Masaya and Nindiri cones in its centre; C) A zoom of the Nindiri cone (see white box in B for location), showing the active Santiago pit crater along with the currently quiescent Nindiri and San Pedro craters. Locations of the DECADE Multi-GAS and the scanning NOVAC spectrometer are also shown; D-E) panoramic views of the inner Santiago crater, taken on 23 February 2016, with the active lava lake visible on the crater bottom; F) night view of the Santiago crater floor on 23 February 2016, showing two distinct lakes; G) night view of the Santiago crater floor on 5 May 2016. The 2-3 lava lakes formed during December 2015 to February 2016 had merged into a single, vigorously active lake.

A vigorously degassing, actively convecting lava lake formed in the Santiago crater between December 2015 and March 2016, marking the end of a 3 year-long period of reduced activity and the onset of a new period of elevated degassing. Before, during, and after formation of the lava lake, the composition and flux of volcanic gases were systematically measured using a permanent gas network that includes a Multi-Component Gas Analyzer System (Multi-GAS, (*Aiuppa et al., 2005*)) of the DECADE network and a scanning Differential Optical Absorption Spectrometer (DOAS) of the NOVAC (Network for Observation of Volcanic and Atmospheric Change) network (*Galle et al., 2010*). At the same time, infrared images acquired by the Moderate Resolution Imaging Spectroradiometer (MODIS), elaborated by the Middle Infrared Observation of Volcanic activity (MIROVA) system (*Coppola et al., 2016b*), were used to detect and quantify thermal anomalies related to the lava lake activity inside Santiago crater. Thanks to integration of these ground- and satellite-based data, transition to a lava lake phase was observed for the first time, yielding novel information on the underlying driving processes. Summarizing the key observations obtained, and their implications for our knowledge of the volcano's degassing mechanisms and behavior, are the objectives of the present study.

5.3 Materials and methods

5.3.1 Masaya Volcano

Masaya is a tholeiitic basaltic shield volcanic complex (*Walker et al*., 1993) in Central Nicaragua (Fig. 5.1a), world-renown for its nearly persistent open-vent degassing activity (*Stix, 2007*) and for having produced some of the few examples of basaltic plinian eruptions (*Williams*, 1983; *van Wyk de Vries*, 1993; *Kutterolf et al*., 2007; *Pérez et al*., 2009). The Masaya volcano *sensu strictu* is the youngest shield edifice of the complex, and sits on an older sequence of nested calderas and craters. Masaya is cut on its summit by a NW-SE elongated caldera that is 11 km long by 6 km wide (Fig. 5.1b) and was formed by at least 3 major (plinian) basaltic eruptions between ~6 and 1.8 ka ago (*Williams*, 1983; *Bice*, 1985; *van Wyk de Vries*, 1993; *Pérez and Freundt*, 2006; *Kutterolf et al.*, 2007, 2008; *Pérez et al*., 2009). The post 1.8 ka activity has been concentrated in the caldera center along a semicircular set of vents/cones, today topped by four pit craters, among which is the currently active Santiago crater (*Rymer et al.*, 1998) (Fig. 5.1c).

The Santiago pit crater (Fig. 5.1d, e) formed in a sequence of collapse/explosion events in 1858-59 (*McBirney*, 1956; *Rymer et al*., 1998),

and has since remained the main site of activity at Masaya. During its short-lived history, Santiago has alternated between (i) periods of intense degassing associated with opening of active vents on the crater floor eventually culminating with lava lake formation (such as in 1965-69, 1972-79, 1989, and 1993-94), and (ii) phases of reduced activity. Each "degassing crisis" has typically lasted years to decades (the most recent started in 1993), and has typically fluctuated between vent-opening phases (mostly due to unroofing of small chambers beneath the crater floor) and vent-closing phases (due to rockfalls inside the crater; *Rymer et al.*, (1998)). Occasionally, the latter crater wall collapse events have been followed by vent-clearing ash explosions, such as in 2001 (*Duffel et al*., 2003) and in April-May 2012 (*Pearson et al*., 2012; *GVP*, 2016). After a period of reduced volcanic activity between late 2012 and late 2015, incandescence was again reported on the crater floor by INETER on 11 December 2015 (*GVP*, 2016). Between mid-December 2015 and March 2016, 2-3 incandescent vents (Fig. 5.2f) became visible, which progressively widened to merge into a single, vigorously active lava lake (Fig. 5.2g), perhaps due to collapsing of the crater floor. Intense seismicity and SO_2 degassing have been associated with formation of the lava lake (*GVP*, 2016). The lava lake is still active at the time of writing.

5.3.2 **Gas measurements**

We field deployed a Multi-GAS on Masaya in March 2014, as part of the global network of the Deep Earth CArbon DEgassing (DECADE; https://deepcarboncycle.org/home-decade/) project funded by the Deep Carbon Observatory (DCO; https://deepcarbon.net/).

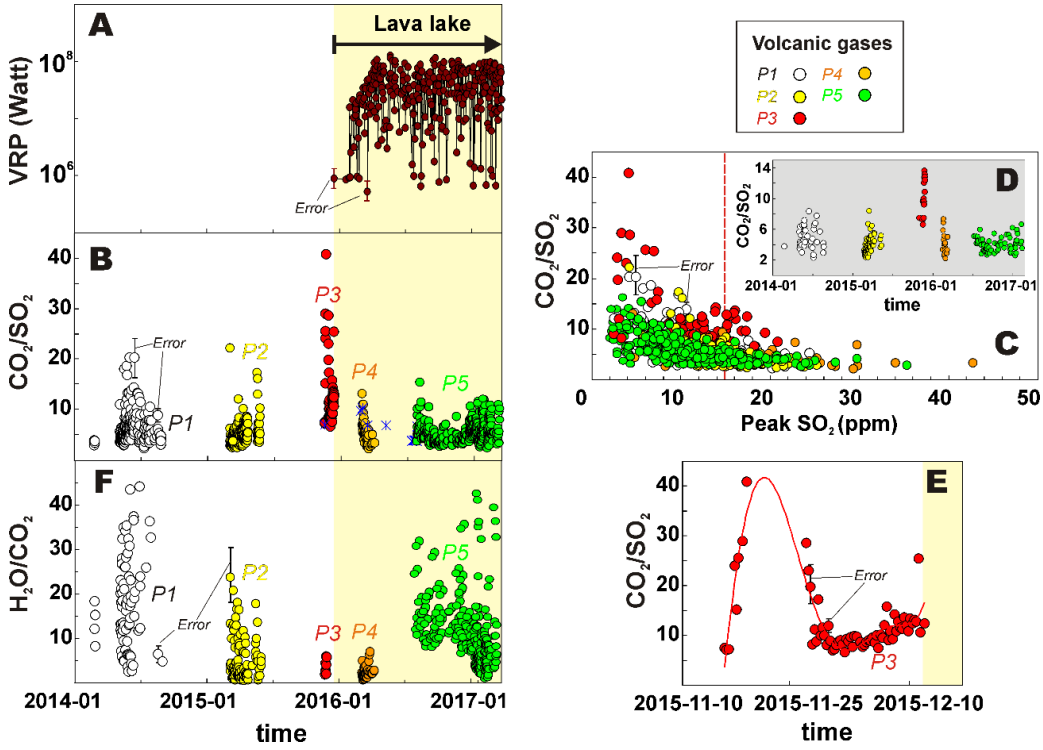

Figure 5.2 A) Time-series of the Volcanic Radiant Power (VRP, in W), January 2014-March 2017. The lake is first detected on December 11, 2015. Thermal radiance then grows from December to mid February 2016, when a plateau is reached. B) Time-series of molar CO_2/SO_2 ratios. Each point corresponds to the time-averaged CO_2/SO_2 ratio calculated in a 30 minute-long Multi-GAS acquisition window (raw data and CO_2/SO_2 ratios are accessible at http://dx.doi.org/10.1594/IEDA/100651). Data are divided into 5 sub-intervals (which we refer to as sub-intervals P1 to P5), during which data acquisition was continuous. The five cycles are shown in different colors: P1, white; P2, yellow; P3, red; P4, orange; P5, green. CO_2/SO_2 ratios are anomalously high in sub-interval P3, prior to lake formation. The blue stars identify the periodic survey results reported in de Moor et al., (2017); C) Plot of molar CO_2/SO_2 ratios vs. peak SO_2 concentration (the maximum SO2 value recorded in the corresponding 30 minute-long Multi-GAS acquisition window). The 5 Masaya gas populations converge to relatively constant (and SO2-independent) CO2/SO2 ratios in dense plume conditions (>10 ppm peak SO2 concentrations). D) The CO_2/SO_2 ratio gas population (of Fig. 5.2B) filtered using a 15 ppm SO2 threshold. E) Time-series of the CO_2/SO_2 ratio for period P3, from October 11 to December 10, 2015. F) Time-series of molar H_2O/CO_2 ratios. Each point corresponds to the time-averaged H_2O/CO_2 ratio calculated in a 30 minute-long Multi-GAS acquisition window (raw data and H_2O/CO_2 ratios are accessible at http://dx.doi.org/10.1594/IEDA/100651). Error bars for some representative measurement points are shown.

This fully autonomous gas sensing unit was installed on the outer rim of the Santiago pit crater (coordinates: 11° 59' 14.410" N, - 86° 10' 3.734" W, see Fig. 5.1c). The Multi-GAS is still operating by November 2017, but 3 years

of results (March 2014-March 2017) are discussed here. The instrument measured in-situ the mixing ratio of CO_2, SO_2, and H_2S in the volcanic gas plume, using the established combination of Near Dispersive Infra Red spectrometers (NDIR) and electrochemical sensors described in previous work (*Aiuppa et al*., 2014, 2017). Ambient pressure, temperature and relative humidity were also co-measured, from which the in-plume H_2O mixing ratio were obtained using the Arden Buck equation (*Buck*, 1981). Data acquisition was controlled by a Moxa embedded computer (model 7112plus), and the whole system was powered by 2 batteries and a 120 W solar panel. The Multi-GAS unit was programmed to acquire data (at 0.1 Hz) during 4 daily measurement cycles, each 30 minute-long. The acquired data were stored in an onboard data logger, and telemetered to the INETER base station in Managua using a radio link. Concentration data were then post-processed using the Ratiocalc software (*Tamburello*, 2015) to obtain time-series of the volcanic gas CO_2/SO_2 and H_2O/CO_2 molar ratios. The dataset is accessible at (http://dx.doi.org/10.1594/IEDA/100651), which lists (i) raw (mixing ratio) data and (ii) time-averaged CO_2/SO_2 and H_2O/CO_2 ratios for 30 minute-long Multi-GAS acquisition windows. No ratio was derived for acquisition windows in which the maximum SO_2 concentration was <3 ppmv threshold and/or low correlation coefficients ($R^2 \leq 0.6$) between gas species were observed. Based on laboratory tests with standard gases, errors in derived ratios are typically ≤15% and ≤30% for CO_2/SO_2 and H_2O/CO_2 ratios, respectively. The sensors' calibration was also regularly checked in the laboratory using calibration gases at the beginning and end of each measurement sub-interval *P1* to *P5* (see below), and no substantial drift or change was observed.

The volcanic CO_2 flux is calculated from combination of co-acquired CO_2/SO_2 ratios and SO_2 fluxes. SO_2 flux is obtained for the period March 2014 to February 2017, from evaluation of data of one scanning-DOAS station from the NOVAC network, located ~1.5 km WSW of Santiago crater at an altitude of 387 m a.s.l. (see Fig. 5.1C). The instrument points to the Santiago crater and scans the plume over a flat surface from horizon to horizon, at steps of 3.6 deg, recording at each step spectra of solar scattered radiation in the 280-450 nm wavelength range (effective range between 300-360 nm due to atmospheric and optical filters). The system is a standard NOVAC-Mark I instrument, which specifications are described by *Galle et al.* (2010). Each scan is completed in about 5 min during daylight. By integrating the column densities of SO_2, derived by the DOAS method (*Platt and Stutz*, 2008), over a cross-section of the plume, and multiplying by the transport speed, the flux of SO_2 is derived. For this evaluation, we used wind speed from the ECMWF ERA-interim database (*Dee et al.*, 2011) with a spatial resolution of 0.125×0.125 deg and a temporal resolution of 6 h, which

was then interpolated to the coordinates of the crater and time of each measurement. Plume direction was obtained by observing the distribution of column densities on each scan, and assuming that the plume centre of mass was drifted at the summit level. Only measurements that were elevated (to ensure complete plume coverage and availability of a background spectrum for cancellation of instrumental and atmospheric effects) were used for further analysis. A total of 28754 flux measurements were obtained (for details see http://dx.doi.org/10.1594/IEDA/100672), each with an estimated uncertainty of <26% (after *Galle et al.* (2010)). This uncertainty mostly comes from uncertainty in wind speed data, since radiative transfer effects are likely less important due to close proximity to an ash-free plume. Available SO_2 flux data were averaged to obtain mean values for each valid Multi-GAS temporal window. The cumulative error in derived CO_2 fluxes is estimated at 40% from propagation of Multi-GAS and NOVAC uncertainties.

5.3.3 Space-based thermal data

Thermal data acquired by MODIS sensors were analyzed using MIROVA, an automated, near real time volcanic hot-spot detection system, developed at the University of Turin (*Coppola et al*., 2016b; www.mirovaweb.it). The MIROVA system uses the MIR radiance measured by the two MODIS sensors (carried on Terra and Aqua NASA's satellites, respectively) that scan the entire earth surface approximately four times per day (2 nighttime and 2 daytime) with a nominal ground resolution of 1 km. These features, together with the presence of a low-gain middle infrared (MIR) channel (MODIS band 21), make MODIS particularly suitable for near-real time monitoring of worldwide volcanic activity (*Wright et al*., 2002, 2004, 2008; *Rothery et al*., 2005; *Coppola et al*., 2013, 2016b).

The hot-spot detection algorithm consists of contextual spectral and spatial principles specifically designed to efficiently detect small to large-scale thermal anomalies (from < 1 MW to >40 GW) while maintaining false detections low (<1 % according to *Coppola et al*. (2016b)). This procedure allows to track a large variety of volcanic activity, including lava flows (*Coppola et al*., 2017a,b) and domes (*Coppola et al*., 2015; *Werner et al*., 2017), as well as strombolian activity (*Coppola et al.*, 2014). Nonetheless, MIROVA has shown its efficiency in detecting previously unknown effusive activity at remote volcanoes (i.e. Nevados del Chillan; *Coppola et al*., 2016c), in tracking the development of intense fumarolic activity at Santa Ana volcano (*Laiolo et al*., 2017) and in detecting the recent re-birth of Nyamulagira lava lake (*Coppola et al*., 2016a).

The *Wooster* et al. (2003) formulation is used to retrieve the volcanic radiant power (VRP; W) from MODIS data, starting from hot spot pixels detected by MIROVA:

$VRP = 1.89 \times 10^7 \times (L_{MIR} - L_{MIRbk})$ (eq. 5.1)

where L_{MIR} and L_{MIRbk} are the MIR radiances ($W \cdot m^{-2} \cdot sr^{-1} \cdot \mu m^{-1}$) characterizing the single hot spot pixel and the background. The coefficient 1.89×10^7 ($m^2 \cdot sr \cdot \mu m$) results from best-fit regression analysis between above background MIR radiance and radiant power (*Wooster et al*., 2003), and allows estimations of VRP (±30%) of hot surfaces having temperatures ranging from 600-1500 K.

Visual inspection of acquired images is used to discard false alerts, isolated fires, thermal data contaminated by clouds, or images affected by poor viewing geometry conditions. Between 2015 and 2017, MIROVA identified 282 hotspots over Masaya volcano. Of these, 8 hotspots were due to false detections, and 31 were associated with wild fires. All of these non-volcanic sources were easily identified because they occurred at more than 5 km from the volcano summit. Of the remaining 243 thermal anomalies associated with volcanic activity, 88 images were discarded because of the presence of clouds and/or because the high satellite zenith angle (i.e. > 45°) impeded a clear view of the Masaya summit craters. The supervised VRP measurements collected during the analyzed period are listed in the Supplementary Material (Tab. S1).

5.4 Results

The MIROVA thermal record (March 2014-March 2017; see Table S1), illustrated in Figure 5.2a, confirms the Masaya lava lake formation time as established by visual observations. No thermal anomaly is detected above the Masaya summit between January 2014 and December 2015 (Fig. 5.2a). This suggests that no magma is ponding in the Santiago crater in this temporal interval, and that the thermal anomalies associated to the degassing vent(s) are below the MIROVA detection limit. The first hot-spot (~0.9 MW) is detected on 11 December 2015, the same day of the first direct lava lake observations in the field (*GVP*, 2016). Since then, the thermal anomalies become increasingly frequent, from 1 alert per week in December 2015 up to ~2 alerts per day in late March 2016. At the same time, the Volcanic Radiant Power (VRP) increases regularly, reaching >10 MW on 21 January 2016 and >100 MW on 03 April 2016. After peaking at 126 MW on 9 May, 2016, the VRP fluctuates around a mean value of 60.8 MW (1σ = 25.5 MW) until March 2017 (the end of our observation interval; see Tab. S1).

The temporal record of CO_2/SO_2 ratios in the Masaya volcanic plume, March 2014 to March 2017, is illustrated in Figure 5.2b. The several data-gaps are due to recurrent damage to electronics/mechanical parts of the Multi-GAS, caused by the corrosive action of the acidic volcanic plume. Our time-series is therefore divided into 5 sub-intervals (which we refer to as phases *P1* to *P5*), during which the Multi-GAS was continually operating (Tab. 5.1).

The mean CO_2/SO_2 ratio is similar for phases *P1* (6.3±3.1), *P2* (4.9±2.0), *P4* (5.4±2.1) and *P5* (5.5±1.9) (Fig. 5.2b). In contrast, interval *P3*, which encompasses formation of the lava lake in early December 2015, is characterised by higher mean CO_2/SO_2 ratio (12.2±6.3), and peak values >20 (and up to 41) (Fig. 5.2b and Tab. 5.1). To test if this factor >2 difference in the CO_2/SO_2 ratio between phases *P3* and *P1-P2-P4-P5* is real, and not simply due to different total volcanic gas concentration in the plumes being measured, we investigate the relationship between CO_2/SO_2 ratios and peak SO_2 concentrations in Figure 5.2c. The peak SO_2 concentration is the maximum SO_2 value recorded within each 30 minute-long Multi-GAS acquisition window, and is commonly used (e.g. *Shinohara et al*., (2008)) as a proxy for the measured plume being rich in volcanic gases, and less air-diluted. As first noted at Etna by *Shinohara et al*. (2008), a Multi-GAS based CO_2/SO_2 ratio population is often inversely correlated to peak SO_2 concentrations in diluted-plume conditions (low peak SO_2). In our Masaya case, the gas population shows more dispersed CO_2/SO_2 ratios at low (<15 ppm) peak SO_2 concentrations (Fig. 5.2c), but the *P3* gases still stand out for their unusually C-rich compositions (relative to *P1-P2-P4-P5*). In each of the five sub-intervals above, the CO_2/SO_2 ratio then levels out at relatively constant (and SO_2-independent) values in dense plume conditions (>15 ppm peak SO_2 concentrations). Filtering our dataset using a SO_2 threshold of 15 ppm, the filtered time-series of Figure 5.2d is obtained. The figure confirms the CO_2/SO_2 ratio difference between phases *P3* (10.3±2.3), and *P1-P2-P4-P5* (means from 3.9±1.1 to 5.0±1.5) at statistically significant level (e.g., well above 1 standard deviation, and beyond analytical uncertainty in individual CO_2/SO_2 ratios, ± 15%). In summary, we conclude that the compositional contrast between *P3* and *P1-P2-P4-P5* gas is significant at any gas concentration level reported here (both at < and > 15 ppm SO_2).

The anomalous CO_2/SO_2 ratio variations during period *P3* are detailed in Figure 5.2e. The figure highlights a phase of anomalous CO_2/SO_2 ratio increase in mid-November 2015, followed by a drop on 26-27 November 2015, preceding the first reports of incandescence inside the Santiago crater on December 11.

The volcanic gas plume H_2O/CO_2 ratio also varies markedly (Fig. 5.2f). The ratio progressively decreases in time, from *P1* (17.3±10.3), *P2* (5.7±5.1), *P3* (3.7±1.6) and *P4* (2.3±1.3), and then increased again in sub-interval *P5* (12.8±10.1) (Fig. 5.2f). In phases *P3* and *P4*, thus, the plume exhibits more uniform, H_2O-poorer composition, relative to other temporal intervals.

Table 5.1 Gas composition and fluxes at Masaya volcano, 2014-2017. Results are presented for six distinct sub-intervals (P1-P5 and LFP, see text). Multi-GAS derived (molar) gas ratios (CO_2/SO_2 and H_2O/CO_2) are only available for sub-intervals P1 to P5. They are expressed as mean values (±1 standard deviation, σ) calculated by averaging all results obtained in each of the 5 distinct temporal windows (raw Multi-GAS data used to calculated the means are available in the EarthChem Library at http://dx.doi.org/10.1594/IEDA/100651). The $_{SO2}$ flux (in kg·s-1) is the mean± standard deviation obtained by averaging all valid DOAS scans of the plume in the same temporal sub-intervals (available at http://dx.doi.org/10.1594/IEDA/100672). CO_2 and H_2O fluxes are obtained from combination of gas compositional and SO_2 flux. The total volatile flux is the sum of the 3 fluxes. The magma degassing rates and volume are calculated from either SO_2 or CO_2 fluxes, using a magma density of 2600 kg·m-3 and total (pre-degassing) S and CO_2 contents in magma of respectively 500 and 6000 mg·kg-1. Total degassing is assumed (e.g., S and CO_2 contents in matrix glasses from erupted volcanics are neglected).

Sub-interval name	Sub-interval duration	Mean CO_2/SO_2 (molar)	1σ	Mean H_2O/CO_2 (molar)	1σ	Mean SO_2 flux ($kg{\cdot}s^{-1}$)	1σ	Mean CO_2 flux ($kg{\cdot}s^{-1}$)	1σ	Mean H_2O flux (kg/s)	Total volatile flux ($kg{\cdot}s^{-1}$)	Magma degassing rate (from SO_2) ($m^3{\cdot}s^{-1}$)	Magma degassing volume (from SO_2) (M m^3)	Excess[§] magma degassing volume (M m^3)	Magma degassing rate (from CO_2) ($m^3{\cdot}s^{-1}$)	Magma degassing volume (from CO_2) (M m^3)	Excess[£] Magma degassing volume (M m^3)
P1	5/3/14-1/9/14	6.3	3.1	17.3	10.3	8.6	2.4	37.3	21.1	-	-	3.3±0.9	-	-	2.4±1.3	-	-
P2	4/3/15-28/5/15	4.9	2.0	5.7	5.1	7.8	1.6	26.2	11.8	61	95	3.0±0.6	-	-	1.7±0.8	-	-
P3	15/11/15-10/12/15	12.2	6.3	3.7	1.6	9.5	3.2	81.3	40.6	123	214	3.6±1.2	8.2*	1.2	5.2±2.6	11.7*	7.2
LFP	11/12/15-15/2/16	n.d.	n.d.	n.d.	n.d.	11.4	5.2	-	-	-	-	4.4±2.0	24.2**	7.0	-	-	-
P4	22/2/16-28/3/16	5.4	2.1	2.3	1.3	8.0	2.6	32.3	18.2	30	71	3.1±1.0	-	-	2.1±1.1	-	-
P5	19/7/16-1/3/17	5.5	1.9	12.8	10.1	7.9	3.5	34.1	22.4	-	-	3.0±1.3	-	-	2.2±1.4	-	-

*Calculated from extrapolation of the magma degassing rate over the entire duration of sub-interval *P3* (26 days); **Calculated from extrapolation of the magma degassing rate over the entire duration of sub-interval *PLF* (64 days); §The excess magma degassing volume is calculated from the magma degassing rate difference between P3 (3.6 $m^3{\cdot}s^{-1}$**)** and P1-P2-P4-P5 average (3.1 $m^3{\cdot}s^{-1}$). £The excess magma degassing volume is calculated from the magma degassing rate difference between P3 (5.2 $m^3{\cdot}s^{-1}$) and *P1-P2-P4-P5* average (2.1 $m^3{\cdot}s^{-1}$).

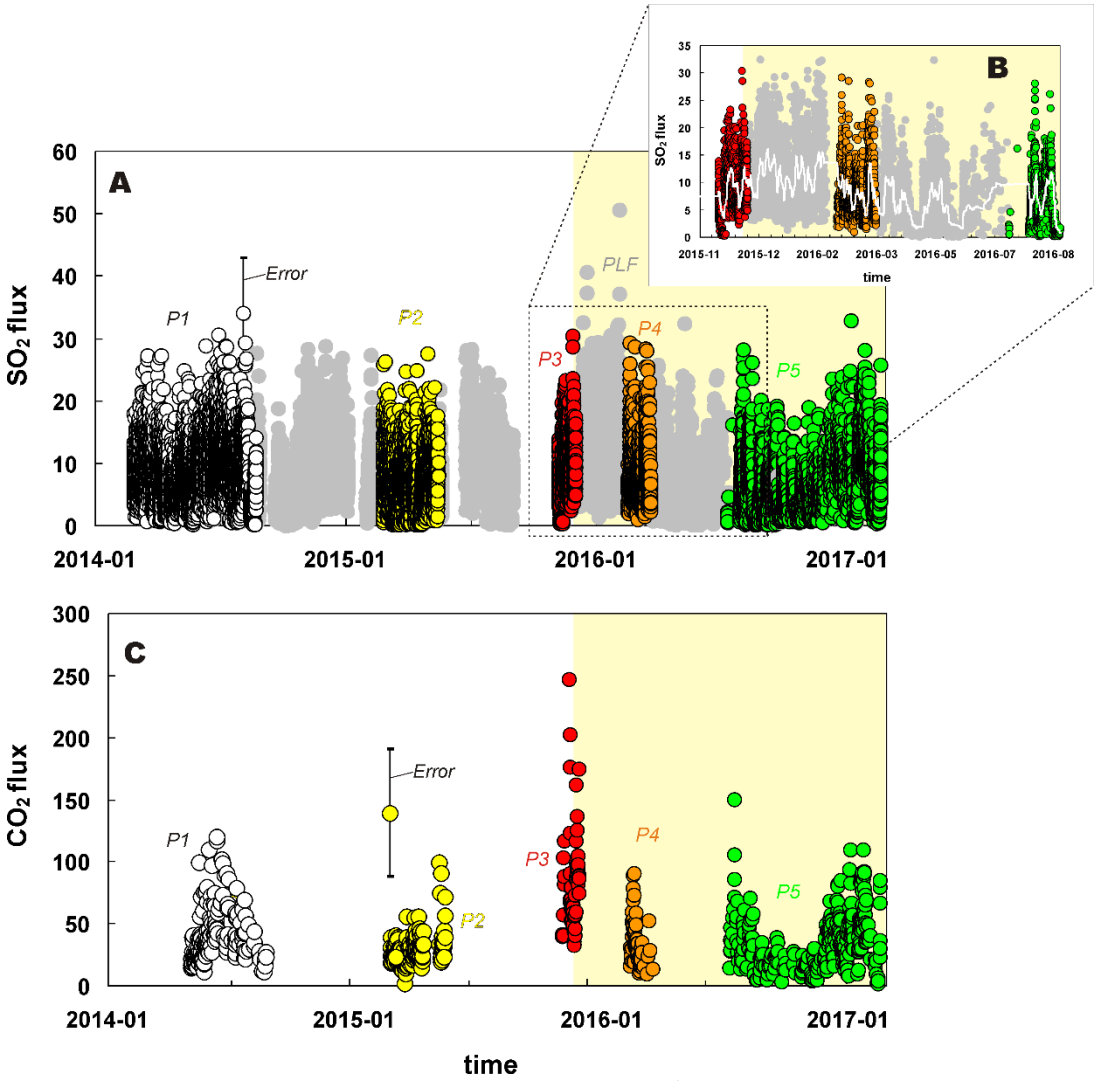

Figure 5.3 A) Time-series of the volcanic SO_2 flux ($kg \cdot s^{-1}$), January 2014-February 2015, based on measurements with a permanent scanning DOAS of the NOVAC network. Data obtained during the five Multi-GAS acquisition sub-intervals are coloured as in Figure 5.2, grey symbols identify DOAS data with no contemporaneous compositional (Multi-GAS) record, including the phase of lake formation (PLF). B) Zoom of A) for the period before and during lava lake formation. The white line is a 3-month moving average. The SO_2 flux peaks in the PLF phase. C) Time-series of the volcanic CO_2 flux ($kg \cdot s^{-1}$), calculated combining sets of co-acquired CO_2/SO_2 ratio values (of Fig. 5.2b) and SO_2 fluxes (the DOAS records closest in time to each 30-minute Multi-GAS temporal interval are averaged and used for scaling). The CO_2 flux peaks in the P3 sub-interval, right before appearance of the lava lake. Error bars for some representative measurement points are shown.

The NOVAC-based SO_2 flux time-series (Fig. 5.3a) is more continuous than the Multi-GAS time-series. Each of the 5 phases above exhibits a wide SO_2 flux range, with no obvious temporal trend, the mean SO_2 fluxes (±1 standard deviation) being: *P1* (8.6±2.4 kg/s), *P2* (7.8±1.6 kg/s), *P3* (9.5±3.2 kg/s) *P4* (8.0±2.6 kg/s), *P5* (7.9±3.5 kg/s). The mean SO_2 flux in interval *P3* is thus

close, or only slightly (17 %) higher than, the 8.0 kg/s average for *P1-P2-P4-P5*. The highest peak SO_2 fluxes (up to 50.7 kg/s) are recorded in the temporal interval between *P3* and *P4*, e.g. between December 11 2015 and February 15, 2016 (Fig. 5.3b), when the lava lake was first visually observed and was reported to be more vigorously degassing (*GVP*, 2016). The mean SO_2 flux in this *Phase of Lake Formation* (*PLF)* is 11.4±5.2 kg/s, or 40 % higher than the *P1-P2-P4-P5* average (8.0 kg/s). We yet caution that this SO_2 flux increase, while significant (Fig. 5.3b), is still within uncertainty (45%). Our SO_2 flux results (Fig. 5.3a), including those in the *PLF*, are within the range of those obtained by *de Moor et al.,* (2017). These authors conducted periodic surveys at a number of Central American volcanoes including Masaya (12 measurements between November 2015 and July 2016), where SO_2 fluxes of 10.1 to 58.1 kg/s were obtained using the traverse technique (e.g., traversing underneath the plume with a vertically pointed DOAS).

The volcanic CO_2 flux time-series (Fig. 5.3c) is calculated by multiplying each CO_2/SO_2 ratio value (of Fig. 5.2b) by the time-averaged SO_2 flux during the same temporal interval. The CO_2 flux peaks during sub-interval *P3* (mean, 81.3±40.6 kg/s; maximum, 247 kg/s on November 25, 2015). Both the mean (26.2-37.3 kg/s, Tab. 5.1) and maximum (149 kg/s) CO_2 flux are systematically lower during sub-intervals *P1-P2-P4-P5.* For comparison, the CO_2 flux results reported in *de Moor et al* (2017) range from 50 to 161 kg/s (10 measurements between November 2015 and July 2016).

5.5 Discussion

Visual observations and satellite data concur to indicate that a stable, vigorously degassing lava lake resumed at Masaya on December 11, 2015 (Fig. 5.1, 5.2a), after ~3 years of passive degassing but no visible incandescence (*GVP*, 2016). The lava lake has been, since its formation, a sizeable heat source. By using the volcanic radiant power (VRP) results illustrated in Figure 5.2a, we estimate a cumulative thermal radiance from the Masaya lava lake, between 11 December 2015 and 31 December 2016, of ~$1.53\pm0.46\cdot10^{15}$ J, and a mean radiant flux of 46.5± 3.9 MW. This radiant power is similar to the long-term thermal output produced by the Erta Ale lava lake (20-100 MW; *Barnie et al*., (2016) and references therein), which yet contributes an order of magnitude less SO_2 (~1.3 kg/s; *Oppenheimer et al.,* (2004)). The Masaya radiant flux is only ~5-10 % the radiant power recently recorded above the Nyiragongo lava lake (~1000 MW; *Spampinato et al*., (2013); *Coppola et al*., (2016a)).

The presence of an operating ground-based gas observational network, combined with satellite thermal sensing, allows us to track resumption of lava lake activity with relatively high temporal resolution, and to derive novel information on the driving magmatic processes.

5.5.1 **A CO_2-rich gas**

Since onset of the 1993-present degassing unrest, and prior to our study, the H_2O-CO_2-SO_2 signature of the Masaya volcanic gas plume has been determined in six occasions during field surveys in 1998, 1999, 2000, 2001, 2006 and 2009 (see *Martin et al.* (2010) for a review). These previous studies indicated plume CO_2/SO_2 ratios of 1.5-3.5 (mean: 2.5±0.7) and a hydrous gas signature (H_2O/CO_2 ratios of 27.9±11.2) (Fig. 5.4a).

Our systematic gas observations demonstrate a systematically more CO_2-rich gas vented by Masaya in 2014-2017 (Fig. 5.4a). The time-averaged (all data, 2014-2017 period) CO_2/SO_2 ratio is 6.2±3.5 (range 2.2-41), well beyond the 1998-2009 range. Our derived H_2O/CO_2 ratios are also lower (2014-2017 average: 10.3±8.8). An especially CO_2-rich composition (Figs. 5.2, 5.4a) is observed in mid- to late-November 2015 (our sub-interval *P3*), a few weeks prior to "re-birth" of the Masaya lava lake in December 2015. In the same sub-interval *P3*, the CO_2 flux (Fig. 5.3c) is 2-3 times the average 2014-2017 levels (26.2 to 37.3 kg/s), and 7.5 times the *Martin et al*. (2010) estimate of ~10.7 kg/s (in March 2009). After P3, gas parameters (composition and fluxes) are back to P1-P2 levels. In summary, our results point to a perturbed degassing regime at Masaya in 2014-2017, and suggest unusually elevated CO_2 release prior to appearance of the lava lake in late 2015.

5.5.2 **Measured vs. modeled gas compositions**

The time-evolving volcanic gas composition in 2014-2017, and especially the elevated CO_2 degassing phase *P3*, are quantitatively interpreted from results of model runs performed with a volatile saturation code (Fig. 5.4). As in previous work (*Aiuppa et al.*, 2007, 2010, 2016; *de Moor et al.*, 2016), the model of *Moretti et al*. (2003) and *Moretti and Papale* (2004) is used to simulate the pressure-dependent compositional evolution (in the C-O-H-S system) of the Masaya magmatic gas phase formed upon magma decompression in the 400-0.1 MPa interval (Fig. 5.4b).

The model runs are initialized at conditions representative of the Masaya magmatic system (Tab. 5.2). Temperature is set constant throughout the runs at 1116 °C (from *de Moor et al*. (2013), calculated from the olivine-liquid geothermometer of *Putirka* (2008)). Oxygen fugacity of Masaya melt is fixed at 1.7 Log units above the QFM (ΔQFM = +1.7, whereby QFM is the quartz-fayalite-magnetite buffer of *Frost* (1991)), based on measured iron speciation (*de Moor et al.*, 2013). Melt composition and total volatile contents (Tab. 5.2) are inferred from compositions of Masaya melt inclusions (MIs) (*Atlas and Dixon*, 2006; *Sadofski et al.*, 2008; *Wehrmann et al*., 2011; *de Moor et al.*, 2013; *Zurek*, 2016) and glasses from laboratory degassing experiments performed at Masaya-like conditions (*Lesne et al., 2011*).

Melt-inclusion results suggest that Masaya volcano is fed by relatively water-poor (1.5-1.6 wt.%) magma, similar to other primitive magmas in Central Nicaragua (e.g., Granada and Nejapa volcanoes; *Wehrmann et al.*, 2011). Available melt inclusion data for Masaya show therefore no evidence of the water-rich (H_2O = 3.0-6.1 wt.%) magma component seen at other Nicaraguan volcanoes, including Cerro Negro, Telica, San Cristóbal and Cosigüina (*Roggensack et al.*, 1997; *Portnyagin et al.*, 2014; *Longpré et al.*, 2014; *Robidoux et al.*, 2017a, b). Note that although the degassing experiments of *Lesne et al.*, (2011) were initially prepared and run at 1.5-1.7 wt.% H_2O, final total H_2O contents in experimental charges (fluid+glass) were > 2.6 wt. % because of water production due to hydrogen exchange and reduction of ferric iron (*Lesne et al.*, 2011) (Tab. 5.2). The experimental results of *Lesne et al.*, (2011) are unique for Masaya, but their higher (than MIs) H_2O contents are likely to have determined vapor-melt partitioning unrepresentative of natural conditions (see below).

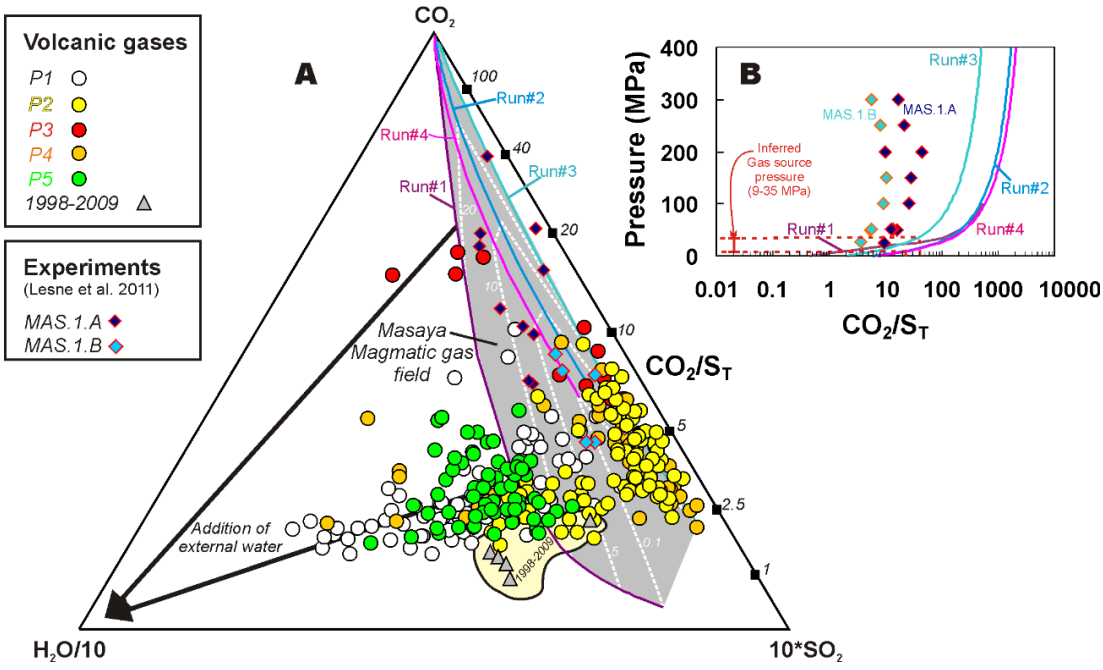

Figure 5.4 A) Triangular plot comparing the measured compositions of Masaya volcanic gases (circles; symbols as in Figure 5.2) with model gas compositions calculated in the four model runs with the saturation model of Moretti et al. (2003). Runs #1 to #4 differ in the model initialization parameters used (see Table 5.2 for details) but all describe a pressure-dependent magmatic gas evolution, from CO_2-rich (high pressure) to SO_2-rich (low pressure). Isobars are indicated by the white dashed lines (numbers stand for pressure, in MPa). The model lines confine the Masaya Magmatic gas field (grey filled area). The calculated experimental fluid compositions (MAS.1.A and MAS.1.B) of Lesne et al. (2011) consistently fall within this magmatic field. However, different initial conditions prevent a quantitative comparison between model results and experimental runs (see text for details). Volcanic gas samples obtained in 2014-2017 (this study) are systematically richer

in CO_2 relative to 1998-2009 gas data (triangles, see Martin et al. (2010) for data source). P1 and P5 gases mostly fall out of the Masaya Magmatic gas field, suggesting addition of non-magmatic (meteoric or atmospheric) H_2O. P3 gases are the richest in CO_2, implying separation pressures of >10 MPa. B) Pressure dependence of the (molar) CO_2/S_T ratio in the four model runs (S_T stands for total S, and corresponds to SO_2+H_2S at the conditions explored here). Runs#1, #2 and #4 output overall consistent trends, while the S-rich run#3 yields systematically lower CO_2/S_T ratio compositions. A gas source pressure of 9-35 MPa is inferred by combing the measured P3 gas compositions with the model trends. The experimental fluids of Lesne et al. (2011) diverge from the model trends at high pressure, and are shifted to lower CO_2/S_T ratios. We ascribe this to higher H_2O contents and formation of solid/liquid sulphides in the experiments of Lesne et al., (2011).

The *Lesne's et al.*, (2011) experiments will be thus considered in the following for comparative purposes only, but not as stringent constraints for our interpretation.

Melt inclusion information also converges to indicate a pre-eruptive S content of ~500 mg·kg^{-1} (Tab. 5.2). This implies that the MAS.1.A experiment of *Lesne et al*. (2011) (our *run#2*) is likely the closest to natural conditions (apart from the aforesaid issues on the total water content), while the MAS.1.B experiment of *Lesne et al*. (2011) (our *run#3*) should only be viewed as a hypothetic S-rich example. As commonly observed at arc volcanoes (*Wallace*, 2005; *Wallace et al*., 2015), the pre-eruptive melt CO_2 content is the least well constrained. *Wehrmann et al*., (2011) reported one single inclusion with a measured CO_2 content of 369 mg·kg^{-1}, and this is used as the basis for our *run#1* simulation. In *run#4*, we consider a CO_2-richer magmatic content, based on the maximum melt inclusion CO_2 content (~6000 mg·kg^{-1}) of *Atlas and Dixon* (2006). *Lesne et al*. (2011) assumed a similarly high CO_2 content (~7000 mg·kg^{-1}; adopted in our *run#2 and run#3*).

Model results (Fig. 5.4) show that, at any explored condition, the magmatic gas in equilibrium with the Masaya melt is rich in CO_2 at high pressure. As pressure decreases, the gas composition becomes H_2O-dominated and richer in S in all model runs (Fig. 5.4). The different model trends obtained in the 4 runs reflect the distinct initial volatile contents used, with the most hydrous gas compositions obtained in the CO_2-poor *run#1* and the least hydrous in the S-rich *run#3*. The four model lines together identify the compositional field of *Masaya magmatic gases* (Fig. 5.4a), which also encompass the inferred compositional range of fluids formed in the experiments of *Lesne et al*. (2011).

The model runs also confirm the strong pressure-dependence of the CO_2/S ratio (Fig. 5.4b), as seen in other mafic systems (*Aiuppa et al*., 2007, 2010, 2017; *de Moor et al*., 2016). The model-derived CO_2/S vs. pressure trends are less steep, and shifted toward CO_2-enriched compositions, relative to the experimental trends obtained by *Lesne et al*. (2011). This discrepancy,

particularly evident at high pressure, reflects the 80% higher total water contents in the experiments of *Lesne et al*., (2011) (see above), which may have acted to determine a gas phase enriched in H_2O and S (at the expense of CO_2). We additionally argue that the CO_2/S ratios in the experiments of *Lesne et al*., (2011), being relatively constant over a wide P-range (Fig. 5.4b), are inconsistent with a sulfur dissolution behavior simply determined by gas-melt partitioning. Rather, they suggest that the sulfur saturation content at sulfide saturation (SCSS) was likely reached during the experiments, leading to formation of solid/liquid iron sulfides (*Mavrogenes and O'Neill*, 1999; *Moretti and Baker*, 2008). Sulfide saturation, while not reported by *Lesne et al*. (2011), is well consistent with the hydrous nature of their experimental melts (*Moune et al*., 2009; *Fortin et al*., 2015). H_2O-rich conditions determine a high Fe^{2+}/Fe_{tot} ratio (> 0.7; *Lesne et al*., (2011) and our modeling) even at oxidation states of NNO+1 or more (*Moretti and Baker*, 2008). In contrast, no sulfide separation is predicted by our model runs (conducted at the less hydrous conditions of Masaya natural melts), justifying the disagreement between model (this study) and experimental (*Lesne et al.*, 2011) results at high pressures (Fig. 5.4b). Model and experimental trends converge at low pressure (Fig. 5.4b).

Comparison between models and observations (Fig. 5.4a) suggests that the CO_2-rich gas detected in sub-interval *P3*, prior to emergence of the lava lake (Fig. 5.2e), cannot originate from a shallow source, e.g. from near-surface (0.1 MPa pressure) gas-melt separation. The four most CO_2-enriched *P3* gases in Figure 5.4a, in particular, have CO_2/SO_2 ratios of 24.1 to 40.8. Depending on the model run used, these correspond to model magmatic gas compositions at respectively ~9-25 and ~15-35 MPa pressure (Fig. 5.4b). Note that even higher equilibrium pressures (~100-200 MPa; Fig. 5.4b) would be obtained using the MAS.1.A experimental fluid line of *Lesne et al*. (2011). In contrast, the CO_2-poorer gases observed in sub-intervals *P1-P2-P4-P5* mostly fall within the low-pressure (0.1-10 MPa; Fig. 5.4a) domain of the *Masaya magmatic gas* compositional field, indicating more shallow origin. A cluster of *P1-P2-P4-P5* gases, finally, plots outside the *Masaya magmatic gas* field, and is displaced toward the H_2O corner. Most of the 1998-2009 Masaya gas data are similarly more H_2O-rich than the predicted (model) magmatic gas compositions. We ascribe these hydrous gas compositions to entrainment of non-magmatic H_2O in the plume. Interestingly, these H_2O-rich compositions dominate in sub-intervals *P1*, *P2* and *P5* (mostly referring to the Masaya wet season), while they are typically missing during sub-intervals *P3* and *P4* (Fig. 5.2f) (encompassing a typical Masaya dry season). We argue that sampling of recirculated meteoric water, perhaps emitted by low-temperature meteoric-H_2O dominated hydrothermal

fumaroles along the inner crater's walls, may justify the non-magmatic H_2O-rich gas compositions in sub-intervals *P1*, *P2* and *P5*.

Table 5.2 Initialization parameters of model runs. Runs are isothermal at 1116 °C (from the de Moor et al. (2013), calculated from the olivine-liquid geothermometer of Putirka (2008)) and at oxygen fugacity of 1.7 Log units above the QFM (□QFM = +1.7, whereby QFM is the quartz-fayalite-magnetite buffer of Frost, (1991)). Volatile contents and major elements are from melt inclusion studies on Masaya volcanics (§Atlas and Dixon (2006); Sadofski et al. (2008); Wehrmann et al. (2011)) or results of degassing experiments on Masaya-like melts (Lesne et al., 2011).

Run ID	**Run conditions**	**T** (°C)	**fO_2** (ΔQFM)	**logfO_2**	**H_2O** (wt. %)	**CO_2** (mg·kg^{-1})	**S** (mg·kg^{-1})	**SiO_2** (wt. %)	**TiO_2** (wt. %)	**Al_2O_3** (wt. %)	**FeO*** (wt. %)	**MnO** (wt. %)	**MgO** (wt. %)	**CaO** (wt. %)	**Na_2O** (wt. %)	**K_2O** (wt. %)	**P_2O_5** (wt. %)	**Source** (major and volatile element composition)
Run#1	Closed-system from saturation to 0.1 Mpa	1116	1.7	-7.63	1.59	369	411	53.23	1.22	15.80	11.97	0.25	3.95	8.78	3.02	1.48	0.31	*Wehrmann et al*. (2011)
Run#2	" " " " "	1150°C	" "	" "	1.54 (2.74)*	7000	595	49.39	1.24	19.16	13.26	0.25	3.58	8.53	3.31	1.51	0.31	MAS.1.A; *Lesne et al.* (2011)
Run#3	" " " " "	1150°C	" "	" "	1.66 (2.86)*	7000	1700	49.42	1.18	18.76	12.44	0.25	3.17	8.7	3.3	1.29	0.31	MAS.1.B; *Lesne et al.* (2011)
Run#4	" " " " "	" "	" "	" "	1.56	6000§	400	52.4	1.2	15.5	11.7	0.2	3.9	8.7	3.0	1.5	0.31	*Sadofski et al*. (2008) Except §, from *Atlas and Dixon* (2006)

*The Masaya experiments in *Lesne et al*., (2011) were actually carried out at a total water content increased by 1.2 wt.% relative to initial run charges (1.54 wt.% and 1.66 , respectively), due to water production via reaction $Fe_2O_{3(melt)} + H_{2(vap)} \Leftrightarrow 2FeO_{(melt)} + H_2O_{(vap)}$.

5.5.3 **A deep trigger?**

The above model results imply that the CO_2-rich signature of *P3* gas is inconsistent with a shallow magma source. To preserve equilibrium compositions corresponding to ~9-35 MPa pressure, the source magmatic gas phase must have last equilibrated with (and separated from) the melt at equivalent depths of 0.36-1.4 km (calculated using a magma density of 2600 $kg \cdot m^{-3}$ for Masaya; *Stix* (2007)). This depth interval corresponds to the roots of the shallow magma reservoir identified by *Rymer et al*. (1998) and *Williams-Jones et al*. (2003), based on modeling of gravity data. According to these authors, a shallow magmatic body (<~1 km) is located directly beneath the currently active Nindiri cone (Fig. 5.5), and the temporal changes in its degree of vesiculation (and thus density) govern the observed gravity variations at Masaya. Vesicularity of the shallow resident magma would, in turn, be modulated by temporal variations in gas bubble supply from deeper convecting magma (*Stix*, 2007), with a larger bubble influx resulting in periods of decreased gravity and elevated degassing at the surface (e.g., a degassing crisis; *Delmelle et al*., (1999); *Williams-Jones et al*., (2003)).

Our observations here suggest an increasing supply of CO_2-rich gas bubbles to the shallow magmatic body (*Rymer et al*., 1998) in November 2015 (Figs. 5.3c, 5.5b). We propose this (factor ~3) higher than usual gas bubble supply is sourced by degassing of faster convecting magma, at minimum equivalent depths of 0.36-1.4 km (Fig. 5.5b). We infer below the increase in magma convection rate that is required to justify elevated degassing during *P3*.

The rate at which magma is convectively rising and degassing (*magma degassing rate*; Tab. 5.1) is initially calculated from the measured SO_2 flux, as in *William-Jones et al*., (2003) and *Stix*, (2007). In these calculations, we use a 2600 $kg \cdot m^{-3}$ magma density (*Stix*, 2007), and assume complete degassing of a magma with 500 $mg \cdot kg^{-1}$ initial S content (Tab. 5.2). We neglect crystal content owing to the poorly porphyric (<<10%) nature of Masaya magmas (*Zurek*, 2016). Using these numbers, the mean SO_2 flux of 9.5±3.2 $kg \cdot s^{-1}$ converts into a magma degassing rate for sub-interval *P3* of 3.6±1.2 $m^3 \cdot s^{-1}$ (Tab. 5.1). This calculation implies a ~20% increase in magma transport rate, relative to *P1-P2-P4-P5* (mean 3.1 $m^3 \cdot s^{-1}$; range 3.0-3.3, Tab. 5.1) is required to account for the elevated SO_2 degassing in *P3*. Integrated over the 26 days of duration, we infer that ~8 Mm^3 must have completely degassed during *P3* to account for surface SO_2 emissions, or ~1.2 Mm^3 in excess to what would have degassed in the same time interval at the background rate of 3.1 $m^3 \cdot s^{-1}$ (Tab. 5.1)

We also argue that, during *P3*, the SO_2 flux increases by only ~17% (relative to *P1-P2-P4-P5*), while the CO_2 flux increases by a factor 157% (Tab. 5.1). As such, the CO_2 flux would in principle be more appropriate to confine the magma degassing rate increase. However, this operation is complicated by

the total CO_2 content in Masaya magmas being poorly constrained (Tab. 5.2). Assuming a total (parental melt) CO_2 content of 6000 mg·kg^{-1}, the *P3* CO_2 flux would imply magma degassing rate of 5.2±2.6 m^3·s^{-1}, higher than the 3.6±1.2 m^3·s^{-1} obtained above from SO_2. This mismatch is reconciled by assuming (i) a higher parental melt CO_2 content (8600 mg·kg^{-1} of CO_2 are required to obtain a 3.6 m^3·s^{-1} magma degassing rate), or (ii) that there is deeply degassing magma that contributes lots of CO_2 but little SO_2 to the shallow convecting part of the plumbing system, or (iii) by considering that only a fraction (~70%) of total S (500 mg·kg^{-1}) is actually degassed, the remaining fraction remaining dissolved in the melt. The latter is well consistent with the relatively deep (~9-35 MPa pressure) gas source in sub-interval *P3*, and considering that the model melts still contain 295 to 462 mg·kg^{-1} S in dissolved form at 10 MPa (model runs#1, 2, 4). Although we cannot entire resolve between the three hypotheses above, owing to the lack of more precise knowledge on parental melt CO_2 content, we still consider our "deep degassing" hypothesis (a combination of (ii) and (iii) above) well motivated. The CO_2 flux-based magma degassing rate of 5.2 m^3·s^{-1} would imply a degassing magma volume (in 26 days) of 11.7 Mm^3, and an excess magma degassing magma volume of ~7.2 M m^3 (Tab. 5.1)

In view of the above calculations, we consider likely that degassing of an unusually high (8.2-11.7 Mm^3) magma volume, circulating at >~9-35 MPa pressure (0.36-1.4 km depth) at an average rate of 3.6-5.2 m^3·s^{-1}, sustained elevated CO_2-rich gas supply during the 26 days of sub-interval *P3*. Interestingly, our results are consistent with a general inflation of the Masaya edifice since late 2015, interpreted as due to volume change/pressure increase at ~2.3-3.8 km beneath the surface (*Stephens et al.*, 2017; *Wauthier*, 2017, pers. comm).

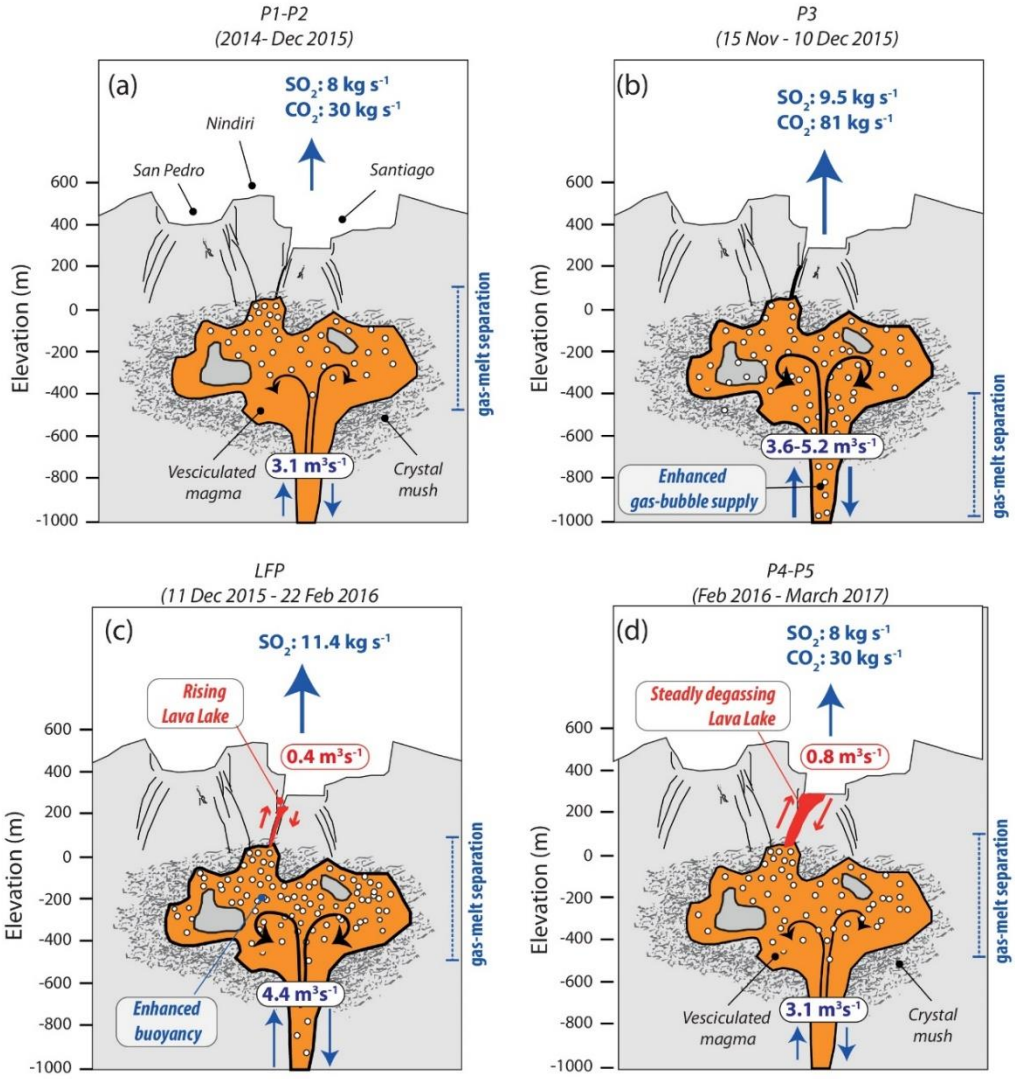

Figure 5.5 Cartoons showing a schematic cross-section of the shallow Masaya plumbing system (modified from Rymer et al. (1998) and Williams-Jones et al. (2003)). During sub-intervals P1-P2 (A), SO_2 and CO_2 emissions are stable, implying magma circulation and degassing at ~3.1 $m^3 \cdot s^{-1}$. The CO_2 flux peaks in phase P3 (panel B), suggesting enhanced gas bubble supply from deep volatile-rich magma. The magma degassing rate increases (3.6-5.2 $m^3 \cdot s^{-1}$) and gas-melt separation level is deeper in the pluming system (0.36-1.4 km depth). C) Enhanced vesicularity (and thus buoyancy) of shallow resident magma, plus further magma ascent of deep-rising magma, lead to magma level rise and formation of the lake on December 11, 2015 (sub-interval LFP); The SO_2 flux peaks at 11.4 $kg \cdot s^{-1}$ and the lake irradiates thermal energy consisted with surface overturning of ~0.4 $m^3 \cdot s^{-1}$ of magma. D) During sub-intervals P4-P5, the lake is now formed and steadily degassing. The surface magma circulation (~0.8 $m^3 \cdot s^{-1}$) represents 20-30% of the magma degassing rate (returning to the pre-eruptive level of ~3.1 $m^3 \cdot s^{-1}$). The lake will likely persists until the magma supply (degassing) rate will not drop down to <<3.1 $m^3 \cdot s^{-1}$.

5.5.4 Formation of the lava lake

An elevated gas bubble supply from depth may impact stability of the shallow magma reservoir that feeds the lava lake in many different ways. According to *Stix* (2007), the long-lived (1993-present) degassing unrest at Masaya, occurring with essentially no eruption of magma, can be explained by either one of the two models below (or from a combination of the two). In the *conduit convection model* (*Kazahaya et al.*, 1994; *Stevenson and Blake*, 1998), persistent open-vent activity is thought to be driven by density contrast between continuously ascending (and degassing) buoyant gas-rich magma, and degassed (denser) resident magma, being recycled back in the conduit. In the *foam accumulation model* (*Jaupart and Vergniolle*, 1989), instead, open-vent activity is controlled by development of a foam layer at the reservoir-conduit discontinuity, in which quiescent leakage from the foam feeds continuous passive gas emissions, while catastrophic collapse of the foam (by reaching a critical thickness) generates explosive magmatic eruptions (not recently recorded at Masaya). In both models, the gas bubble supply is a critical factor. In the *conduit convection model*, gas bubbles control density of the ascending magma, with an increase in bubble supply leading to greater buoyancy and faster convection. In the *foam accumulation model*, a larger influx of gas bubbles leads to thickening of the foam layer, increased gas transport from the foam to the conduit (and, hence, enhanced surface degassing), and to increasing magma level in the conduit. A variable gas bubble supply from depth has, for instance, been evoked as the mechanism driving lava lake level fluctuations at Erta Ale volcano in Ethiopia (*Vergniolle and Bouche*, 2016).

In view of these considerations, it is reasonable to establish a cause-effect relationship between the elevated gas bubble supply (and surface discharge) in sub-interval *P3*, and the ensuing formation of the Masaya lava lake. Although we cannot exclude the concomitant action of additional factors, including gravitational collapse of the unstable crater floor (*Rymer et al*., 1998; *Harris*, 2009), we find it unlikely that the elevated degassing pulse in mid- to late- November 2015, and the appearance of the lava lake on December 11, 2015, is a mere temporal coincidence. We propose, instead, that a combination of (i) further upward migration of the bubble-rich magma, and (ii) rejuvenation of shallow resident magma by deeply sourced gas bubbles, caused the more buoyant column to migrate upward, driving collapse of the crater floor and ultimately manifesting in a vigorous lava lake (Fig. 5.5c). No gas composition information is available for the most vigorous lava lake activity period (*PLF;* Fig. 5.3a). However, a decreasing CO_2/SO_2 ratio is observed in the last 12 days of sub-interval *P3* (Fig. 5.2e), and a carbon-poor composition (relative to *P3*) is observed in sub-interval *P4* (22 February to 28 March, 2016), with the lake still being present and active (Fig.

5.1). Our gas compositional data are therefore consistent with shallowing of the magmatic source (Fig. 5.4).

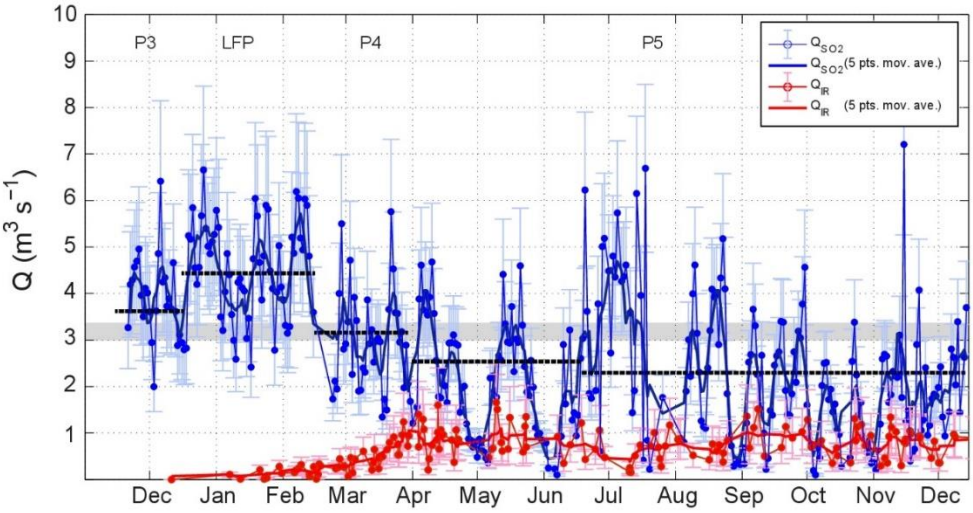

Figure 5.6 Time-series of magma degassing rate (QSO2 in blue) and "surficial" magma flux retrieved using thermal data (QIR in red). The two magma fluxes describe the rate of convective magma transport inside two distinct portions of the plumbing system: (i) the degassing cell located above the exsolution level of SO2 (QSO2) and (ii) the lava lake system at the surface. Only 1 to 10% of the degassing magma reaches the free surface of the lake during phases LFP and P4. The efficiency of magma transport increases up to 20-30% during P5, characterized by a stable magma level. The long-term mean magma degassing rate typical of Masaya is represented by the grey horizontal bar.

Enhanced shallow magma convection in late 2015 to early 2016 is clearly supported by the elevated SO_2 fluxes in sub-interval *PLF* (Fig. 5.3a, b). The SO_2 flux during *PLF* averages at 11.4±5.2 kg/s (versus the 8.1 kg/s mean for sub-intervals *P1-P2-P4-P5*), and implies degassing of 4.4±2.0 m^3 of magma per second (Tab. 5.1; Figs. 5.5, 5.6). For the *PLF* duration of 64 days, this corresponds to convective ascent, complete degassing, and recycling of ~24 Mm^3 of magma. The excess magma volume, e.g. the mass of magma exceeding what would have degassed in 64 days at the background rate of 3.1 $m^3 \cdot s^{-1}$, is thus ~7 M m^3.

In total, we thus infer that ~7.2 to ~8.2 M m^3 more magma than during background intervals (*P1-P2-P4-P5)* circulated (and degassed) underneath Masaya between November 2015 and February 2016 (Tab. 5.1). This elevated shallow magma circulation ultimately culminated in formation and growth of the lava lake (Fig. 5.5c).

Further clues on the processes leading to formation of the lake can be obtained by comparing the above SO_2-derived magma degassing rate (Tab. 5.1) with the volumetric magma flux inferred from MIROVA-derived thermal data (Fig. 5.6). In fact, while the SO_2 data allows constraint on the rate at which

the magma is convectively rising and degassing within the shallow plumbing system (Q_{SO2}), the thermal data can be used to infer the rate at which the magma reaches the uppermost levels of the magma column (i.e. the lava lake), where it radiates and cools before being cycled back (Q_{IR}).

Following *Coppola et al*. (2013) this magma flux can be calculated from:

$$Q_{IR} = \frac{VRP}{6.45 \times 10^{25} \times \left(X_{SiO_2}\right)^{-10.4}} \qquad \text{(eq. 5.2)}$$

where X_{SiO2} is the silica content of the erupted lavas (51.5 wt% for Masaya; *Walker et al*., 1993). This approach and other similar thermal proxies (see *Harris and Baloga* (2009)) are commonly applied during effusive eruptions in order to estimate the "TimeAveraged Lava Discharge Rate" (*TADR*) feeding an active lava flow. The typical error associated to satellite-based estimates of magma flux is ± 50%, a value comparable with field-based estimates (*Harris et al., 2007, Coppola et al., 2013*). This uncertainty mostly comes from the implicit assumption of two end-member thermo-rheological models (defined as hot and cold models by *Harris*, (2007)) that may characterize the spreading and cooling processes of active lava flows. The two models thus provide an upper and lower value of magma flux for any VRP measurement, being representative of large areas/poorly-insulated conditions (the hot model – higher radiant density) and small areas/highly-insulated conditions (the cold model – lower radiant density). The real volumetric flux may thus vary within these two boundary estimates depending on the local conditions of area and temperature.

In the case of a convecting lava lake, where no magma is discharged from the magmatic system, the thermal proxy (eq. 5.2) can be used to evaluate what would be the equivalent magma discharge rate in the absence of magma recycling (*Coppola et al., 2012, 2013*). This corresponds to the volumetric magma flux that would need to be supplied to a lava flow in order to radiate an equivalent amount of thermal energy into the atmosphere. In other words, Q_{IR} provides the rate at which magma is supplied to the surface before being "discharged" (effusive eruptions) or cycled back into the feeding system (lava lakes/open vent volcanoes).

In this view, we interpret the two magma fluxes (Q_{SO2} and Q_{IR}) as sampling the rate of magma transport at different depths, being the SO_2-derived flux relative to the magma circulation above the exsolution level of SO_2, and the IR-derived flux relative to surficial magma circulation (i.e. few tens of meters at most) (Fig. 5.6). The two magma fluxes may be non-synchronous due, for example, to the different ascent rate of gas and magma within the shallow plumbing system, or due to the delay it takes a degassing-induced collapses

in the crater to reveal the magma. However, on a reasonable timescale of few days, the two fluxes can only be equivalent in the limit condition that all magma entering and degassing within the shallow plumbing system ultimately reaches the free air-magma interface.

During sub-interval *P3*, Q_{IR} is equal to zero (Fig. 5.5b, 5.6), since no lava lake is exposed at the bottom of the Santiago crater. However, the higher than normal magma degassing rate (see 4.3) suggests ascent (and degassing) of a new batch of gas-rich magma in the magmatic system (see above, Fig. 5.5b). We propose that such increased gas supply, and the added magma volume, lead to over-pressurization of the shallow magmatic system, causing a gradual rise of the magma column and the subsequence appearance of the lava lake during sub-interval *PLF* (Fig. 5.5c). During this period, the magma degassing rate (Q_{SO2}) is enhanced by ~0.8 $m^3 \cdot s^{-1}$, thus reaching ~4.4 $m^3 \cdot s^{-1}$ (Fig. 5.6). At the same time, Q_{IR} gradually increases from 0 to ~0.4 $m^3 \cdot s^{-1}$ (about one tenth of the total SO_2-derived flux), suggesting that ≤10% of the degassing magma can finally make its way to the surface in a lava lake (Fig. 5.6). The progressive increase in the magma level continues until March 2016, when Q_{IR} stabilizes at ~0.8 $m^3 \cdot s^{-1}$ and the *magma degassing rate* returns back to normal values (i.e. ~3 $m^3 \cdot s^{-1}$) (Fig. 5.6). In these periods (*P4* and *P5;* Fig. 5.5d), the proportion of degassing magma reaching the free surface of the lake increases to ~20-30%, thus suggesting an improved, but still incomplete efficiency of the plumbing system in transporting the ascending magma up to the free surface. This condition persists to the time of writing, and will likely continue until a further decrease of the magma degassing rate (e.g., in magma feeding into the shallow plumbing system) may cause the lava lake to disappear (as previously seen at Masaya in historical time). On the contrary, the upper limit condition of magma transport efficiency (~100%, i.e. with all the degassing magma reaching the lava lake) would be hypothetically reached for $Q_{IR}=Q_{SO2} \cong 3.1$ $m^3 \cdot s^{-1}$, at which the lava lake would be radiating ~400 MW (eq. 5.2). In view of the rarity of historical eruptions at Masaya, this condition is reached very infrequently. However, a maximum efficiency of transport to the surface could result in further rise of the lava lake level or even eventual production of a lava flow.

5.5.5 Comparison with other lava lakes

The calculations above suggest an evident unbalance between magma input (Q_{SO2}) and output (Q_{IR}) at Masaya. We speculate this unbalance may be causing the rarity of overflow or lateral eruptions at this volcano, and perhaps at other systems (e.g., Villarrica, Erebus) that exhibit similarly stable lava lakes. We anticipate that a systematic analysis of Q_{SO2} vs. Q_{IR} relationships is required to test, and eventually corroborate, our hypothesis, including observations and modelling at those lava lakes characterized by more

dynamic eruptive behavior (such as Nyiragongo (*Burgi et al.,* 2015) and Erta Ale (*Vergnoille and Bouche*, 2016)).

The Q_{SO2} vs. Q_{IR} unbalance at Masaya requires a very efficient extraction of gas bubbles from the melt, perhaps due to reduced melt viscosity (in the ~10^2 Pa·s order; *Stix* (2007)). Gas separation from melt during open-system degassing drives sinking of degassed magma back into the conduit (*Shinohara*, 2008), thus posing a limit to the surface emplaced magma volume (Q_{IR}).

The contrasting magma rheologies can also justify the distinct 2015 behaviours of Masaya and Villarrica lava lakes (degassed, crystal-rich basaltic andesites feeding the Villarrica lava lake have inferred viscosity in the ~10^3 Pa·s range (*Witter et al*., 2004), or a factor 10 higher than Masaya). As reported by *Aiuppa et al*. (2017), a period of elevated supply of deeply-sourced CO_2-rich gas bubbles, similar in duration and magnitude to that seen at Masaya (this study), was observed in early 2015 at Villarica. However, the elevated CO_2 degassing phase at Villarrica culminated into a violent (VEI, Volcanic Explosivity Index = 2) paroxysmal explosion, while no eruption was observed at Masaya, only the emergence of a vigorously degassing lava lake. A combination of different initial volatile contents, magma overpressures and decompression rates, in addition to distinct magma rheologies, may have concurred to explain the contrasting volcanic behaviours. In any case, the "quiet" lava lake emergence at Masaya is clearly indicative of efficient magma degassing.

5.6 Conclusions

We have presented novel ground-based (volcanic gas) and space-based (thermal) observations to systemically characterise a (re)formation event of the Masaya lava lake for the first time. Our results show that appearance of the lava lake in December 2015 was anticipated in mid- to late-November by a noticeable volcanic gas plume compositional change toward more CO_2-rich compositions, and by a sizeable CO_2 flux increase. We interpret these observations as evidence for usual supply of CO_2-rich gas bubbles, sourced by enhanced (3.6-5.2 $m^3 \cdot s^{-1}$) magma transport and degassing at >~9-35 MPa pressure (0.36-1.4 km depth). This interpretation is consistent with a measured (late 2015-early 2016) inflation, having an inferred deformation source at ~ 2.3-3.8 km depth km beneath the surface (*Stephens et al.*, 2017; *Wauthier*, 2017, pers. comm). Further upward magma migration, and/or rejuvenation of shallow resident magma by deep-rising gas bubbles, ultimately caused the lava lake to appear on 11 December 2015. Shallow-level, faster than normal (4.4 vs. ~3 $m^3 \cdot s^{-1}$) magma circulation since mid-December 2015 is proved by a return to more SO_2-rich composition, by a ~40% SO_2 flux increase, and by a progressive volcanic radiant power

increase, peaking at 126 MW in May 2016. Modeling of the thermal anomaly irradiated by the lava lake is consistent with a lava lake supplied at ~0.4-0.8 $m^3 \cdot s^{-1}$ rate, implying that only ~10-30% of shallow circulating (and degassing) magma (4.4 to 3.1 $m^3 \cdot s^{-1}$) ultimately reached the surface. We anticipate the lava lake will likely persist until magma feeding in the shallow plumbing system declines to <<3 $m^3 \cdot s^{-1}$.

5.7 Acknowledgements

This research received funding from the Deep Earth CArbon DEgassing (DECADE) program of the Deep Carbon Observatory (DCO), and by the European Research Council (FP7/ERC grant agreement n 305377) (Pi, Aiuppa). Field support in terms of vehicles and equipment was provided by OVSICORI-UNA and INETER. Raw (mixing ratio) and processed (molar ratio) Multi-GAS data and processed NOVAC data are downloadable from the EarthChem Library at http://dx.doi.org/10.1594/IEDA/100651 and http://dx.doi.org/10.1594/IEDA/100672, respectively. Insightful comments by Tamsin Mather and an anonymous reviewer contributed to improving the quality of the manuscript.

5.8 Supplementary Table

Supplementary Table 5.1 Supervised dataset of MIROVA alerts detected at Masaya volcano between 1 January 2014 and 30 March 2017

Date	VRP (Watt)
06/12/2015 04:20	884676.9307
02/01/2016 04:00	8066945.808
07/01/2016 04:20	851139.2637
16/01/2016 04:15	15598944.95
18/01/2016 04:00	924711.3851
19/01/2016 07:35	2507983.663
25/01/2016 04:05	20943213.67
26/01/2016 07:40	10454812.28
01/02/2016 04:15	11429354.01
01/02/2016 16:30	14653099.09
03/02/2016 04:00	18579024.54
04/02/2016 07:35	24245364.31
08/02/2016 04:20	8735223.067
08/02/2016 07:10	4543249.586
10/02/2016 04:05	20891840.91
11/02/2016 07:40	899689.4465
12/02/2016 03:55	8351857.117
12/02/2016 16:10	25270175.15
13/02/2016 07:25	22057473.76
20/02/2016 07:35	17663275.76
21/02/2016 19:05	20374537.41
22/02/2016 07:20	33747744.49
24/02/2016 04:20	20216234.46
24/02/2016 07:10	22408703.28
26/02/2016 04:05	5458495.567
27/02/2016 07:40	35479793.19
28/02/2016 03:55	11016347.88
29/02/2016 07:25	33259835.7
04/03/2016 04:10	46332838.42
08/03/2016 03:50	15879582.14
08/03/2016 19:05	27319952.97
09/03/2016 07:20	49071845.44
11/03/2016 04:20	34486938.6
11/03/2016 07:10	17847157.4
13/03/2016 04:05	37465156.75
15/03/2016 03:55	49058754.42
16/03/2016 07:25	60479237.22
18/03/2016 07:15	69504728.67
20/03/2016 04:10	57054627.46
20/03/2016 16:25	40514674.3
22/03/2016 04:00	72951699.5
22/03/2016 19:20	94236471.75
24/03/2016 19:05	54643039.15
25/03/2016 07:20	71755602.31
29/03/2016 16:20	106977540
29/03/2016 19:25	53568645.58
31/03/2016 19:15	98354933.63
01/04/2016 07:30	81968989.36
03/04/2016 07:15	15911320.08
03/04/2016 16:40	33810222.2
05/04/2016 04:10	56313697.82
07/04/2016 04:00	65285522.05
07/04/2016 16:15	77314922.8
07/04/2016 19:20	121799288
08/04/2016 07:35	49858921.56
09/04/2016 03:50	80857632.65
10/04/2016 07:20	73284509.83
14/04/2016 04:05	64738249.14
15/04/2016 07:40	28233778.41
16/04/2016 03:55	81303914
16/04/2016 19:15	60626554.38
17/04/2016 07:30	65391254.37
01/05/2016 07:40	35822651.67
02/05/2016 19:15	49877610.9
03/05/2016 07:25	50996393.18
04/05/2016 19:00	126415063
05/05/2016 07:15	115016224.1
07/05/2016 04:15	60613193.73
07/05/2016 16:30	46473694.06
10/05/2016 07:35	49957715.91
11/05/2016 03:50	101390743.5
17/05/2016 07:40	45165486.83
18/05/2016 03:55	87113155.14
18/05/2016 16:10	102736396.1
18/05/2016 19:10	53205622.7
02/06/2016 07:40	70406620.7
05/06/2016 03:45	26657556.88
08/06/2016 04:15	56764452.96

13/06/2016 07:20	92527395.86	21/10/2016 07:10	89667045.03
15/06/2016 04:20	33032916.79	23/10/2016 04:05	55679275.57
19/06/2016 19:10	49765327.13	25/10/2016 16:10	72004048.01
21/06/2016 19:00	80716280.02	30/10/2016 04:15	22427057.44
24/06/2016 04:15	36030936.6	01/11/2016 04:00	35400071.22
05/07/2016 16:10	12618140.92	02/11/2016 07:30	27023058.76
05/07/2016 19:10	19363688.45	03/11/2016 03:50	70438529.51
06/07/2016 07:25	11788090.73	03/11/2016 19:05	101952038.5
08/07/2016 07:15	38806545.36	04/11/2016 07:20	85542719.72
10/07/2016 16:30	56294884.43	06/11/2016 07:10	77882454.01
15/07/2016 07:20	54883820.44	08/11/2016 16:20	22788937.38
17/07/2016 07:10	76417729.89	10/11/2016 03:55	61017773.49
19/07/2016 04:05	52894427.06	10/11/2016 16:10	65903904.66
19/07/2016 19:25	34334138	10/11/2016 19:10	59558060.17
20/07/2016 07:40	21426564.02	12/11/2016 19:00	79582715.15
22/07/2016 07:25	54625502.41	13/11/2016 07:15	75022062.16
24/07/2016 07:15	88787152.01	17/11/2016 04:00	71600537.58
28/07/2016 04:00	65594949.34	17/11/2016 16:15	69268239.22
29/07/2016 07:35	66993311.88	22/11/2016 16:35	35086480.48
04/08/2016 04:05	39480108.52	24/11/2016 04:05	62777775.81
11/08/2016 16:30	32076528.37	26/11/2016 03:55	27366912.61
13/08/2016 04:00	58279134.18	26/11/2016 16:10	27183116.15
15/08/2016 03:50	46569219.95	03/12/2016 04:00	73915873.73
16/08/2016 07:20	56580427.55	03/12/2016 16:15	69906502.46
18/08/2016 04:20	28869082.55	12/12/2016 03:55	68792893.52
18/08/2016 07:10	42948291.14	13/12/2016 07:25	66070122.36
20/08/2016 04:05	64018910.55	15/12/2016 07:15	80083592.58
29/08/2016 04:00	103444050.9	19/12/2016 04:00	37368738.33
30/08/2016 07:30	51804744.93	20/12/2016 07:35	46585624.97
01/09/2016 07:20	85241992.19	27/12/2016 07:40	10020362.25
03/09/2016 07:10	115380618.9	28/12/2016 03:55	54963315.76
06/09/2016 07:40	38109096.43	28/12/2016 19:10	52265349.08
14/09/2016 04:00	52326448.19	29/12/2016 07:25	61723907.24
16/09/2016 03:50	86670042.02	31/12/2016 07:15	90525367.7
19/09/2016 07:10	68001045.49	02/01/2017 07:00	20099502.48
23/09/2016 19:10	77923127.05	02/01/2017 16:25	49791464.26
26/09/2016 07:15	98077288.4	04/01/2017 16:15	14741770.09
28/09/2016 04:15	52873626.2	05/01/2017 07:35	44574781.76
02/10/2016 16:05	63372585.25	09/01/2017 04:20	51604960.61
07/10/2016 19:25	26691052.59	09/01/2017 07:10	70290394.42
09/10/2016 19:10	51555862.13	09/01/2017 16:35	28104704.74
10/10/2016 07:25	39042896.74	11/01/2017 04:05	28833989.43
16/10/2016 04:00	27398803.62	11/01/2017 16:20	35315959.31
18/10/2016 03:50	99695362.48	13/01/2017 03:55	94516766.97
18/10/2016 19:05	63799258.13	16/01/2017 07:15	70845584.98
19/10/2016 07:20	85911862.15	18/01/2017 04:10	66872144.48

20/01/2017 04:00	72880276.65	03/03/2017 07:25	63797567.03
20/01/2017 16:15	93775745.19	05/03/2017 07:15	85604139.97
21/01/2017 07:35	79263337.29	07/03/2017 04:10	70599989.24
25/01/2017 07:10	57366075.56	09/03/2017 04:00	71135037.73
27/01/2017 04:05	78547135.49	14/03/2017 07:10	51850232.34
28/01/2017 07:40	57714059.13	16/03/2017 04:05	58363014.16
29/01/2017 03:55	66213868.13	17/03/2017 07:40	37837108.07
29/01/2017 19:10	96592054.25	18/03/2017 03:55	52132786.31
30/01/2017 07:25	54121046.57	18/03/2017 16:10	58073165.23
03/02/2017 04:10	61542312.43	21/03/2017 07:15	56946047.41
05/02/2017 04:00	54680537.52	25/03/2017 04:00	61501314.26
06/02/2017 07:35	73509414.11	27/03/2017 03:50	49771233.64
07/02/2017 03:50	58302510.45	28/03/2017 07:20	56450091.5
07/02/2017 19:05	50920586.31	01/04/2017 04:05	45445274.69
08/02/2017 07:20	90963517.71	02/04/2017 07:40	25572869.88
12/02/2017 04:05	88958245.48	03/04/2017 03:55	49291271.04
14/02/2017 03:55	50573286.72	04/04/2017 07:25	46720544.14
14/02/2017 16:10	56229417.93	06/04/2017 07:15	65375673.52
15/02/2017 07:25	12523273.66	08/04/2017 04:10	69405992.97
17/02/2017 07:15	13175314.48	10/04/2017 04:00	73735764.51
19/02/2017 04:10	63427110	12/04/2017 03:50	54104740.19
21/02/2017 04:00	101952965.1	13/04/2017 07:20	73370823.2
23/02/2017 03:50	76123542.23	15/04/2017 04:20	43077890.83
24/02/2017 07:20	67392040.69	17/04/2017 04:05	64801194.35
26/02/2017 04:20	42869992.91	18/04/2017 07:40	31796091.6
26/02/2017 07:10	77368339.97	20/04/2017 07:25	22742013.2
28/02/2017 04:05	63527651.35	22/04/2017 07:15	57429448.36
02/03/2017 03:55	76153847.48		

Chapter 6

6 Insights into the mechanisms of phreatic eruptions from continuous high frequency volcanic gas monitoring: Rincón de la Vieja volcano, Costa Rica[3]

6.1 Abstract

Understanding the trigger mechanisms of phreatic eruptions is key to mitigating the effects of these hazardous but poorly forecastable volcanic events. It has recently been established that high-rate volcanic gas observations are potentially very suitable to identifying the source processes driving phreatic eruptions, and to eventually detecting precursory changes prior to individual phreatic blasts. In February-May 2017, we deployed a Multi-GAS instrument to continuously monitor gas concentrations in the crater lake plume of Rincón de la Vieja, a remote and poorly monitored active volcano in Costa Rica, site of frequent phreatic/phreatomagmatic eruptions. Forty-two phreatic/phreatomagmatic eruptions were seismically recorded during our investigated period, 9 of which were also recorded for gas by the Multi-GAS. To the best of our knowledge, these represent the first instrumentally measured gas compositions during individual phreatic/phreatomagmatic explosions at an active volcano. Our results show that during background quiescent degassing the Rincón de la Vieja crater lake plume was characterized by high CO_2/SO_2 ratios of 64±59 and H_2S/SO_2 ratios of 0.57±0.20. This composition is interpreted as reflecting hydrothermal (re)processing of magma-sourced gas in the sub-limnic environment. Phreatic blasts were recorded by the Multi-GAS as brief (1-2 minutes long) pulses of elevated gas mixing ratios (up to ~ 52 ppmv SO_2 and > 3000 ppmv CO_2), or more than an order of magnitude higher than during background degassing (~ 1 ppmv SO_2 and ~ 450 ppmv CO_2). During the phreatic eruption(s), the H_2S/SO_2 ratio was systematically lower (<0.18) than during background degassing, but the CO_2/SO_2 ratio remained high (and variable), ranging from 37 to 390. These S-poor compositions for the eruptive gas imply extensive processing of the source magmatic gas during pre-eruptive hydrothermal storage, likely by deposition of native S and/or sulfate. Our gas results are thus overall consistent with a mechanism of phreatic eruptions triggered by

[3] Battaglia A., J.M. de Moor, A. Aiuppa, G. Avard, H. Bakkar, M. Bitetto, M. M. Mora Fernández, P. Kelly, G. Giudice, D. Delle Donne, H. Villalobos (2018). Insights into the mechanisms of phreatic eruptions from continuous high frequency volcanic gas monitoring: Rincón de la Vieja volcano, Costa Rica. Submitted to Frontiers.

accumulation of magmatic-hydrothermal gases beneath a hydrothermal seal. We claim that real-time Multi-GAS monitoring is urgently needed at other crater lake-hosting volcanoes (e.g., Ruapehu, Aso), where phreatic eruptions may similarly be preceded by phases of reduced S degassing at the surface.

6.2 Introduction

Phreatic eruptions are among the most unpredictable and hazardous volcanic phenomena (*Mastin and Witter, 2000; Browne and Lawless, 2001*). These blasts involve the violent, explosive discharge of pressurised pockets of external (non-volcanic, mostly meteoric) water, and are therefore particularly common at "wet" volcanoes whose summits are topped by crater lakes (*Rouwet and Morrisey, 2015; Stix and de Moor, 2018*). In addition to the large availability of exogenous water, active crater lakes are especially prone to developing phreatic eruptions owing to the presence of a persistent heat source (conductive/convective heating from shallow magma, and/or rising magmatic volatiles), and the frequent formation of permeability barriers at the lake bottom (e.g., impermeable layers of precipitated native sulfur or alteration minerals) that favour gas accumulation (*Christenson et al., 2010; Delmelle and Bernard, 2015; Christenson and Tassi, 2015, and references cited therein*). The exact mechanisms driving crater lake breaching eruptions are still not entirely understood, and the respective roles of the magmatic and sublimnic hydrothermal systems in triggering the eruptions are still a matter of debate (*Takano et al., 1994; Christenson and Tassi, 2015; Rouwet and Morrisey, 2015*).

Phreatic eruptions have typically occurred in the past without being preceded by any obvious precursor, as recently dramatically demonstrated by the deadly Ontake (*in 2014, Oikawa et al. 2016*) and Kusatsu-Shirane (in 2018) eruptions in Japan. The recent technical advances in real-time observation of lake plume gas compositions (*Di Napoli et al., 2013; Shinohara et al. 2015; Tamburello et al., 2015; de Moor et al., 2016; Gunawan et al., 2016*) bring a new perspective on eruption forecasting. Using measurements from a permanently installed "lake" Multi-GAS (Multi-component Gas Analyser System; *Aiuppa, 2015*), *de Moor et al.,* (2016a) identified for the first time systematic short-term (days to weeks) variations in plume gas compositions prior to individual phreatic explosions at Laguna Caliente crater lake, Poás volcano (Costa Rica). These observations indicated an increase of magmatic volatiles input prior to individual phreatic blasts, which demonstrates the potential of high-frequency real-time gas monitoring.

Here, we report on the results of three months of instrumental monitoring of volcanic gas composition at Rincón de la Vieja volcano (10.49 N, 85.19 W), in the Costa Rican segment of the Central American volcanic arc (CAVA). Rincón de la Vieja is one of the most active and remote volcanoes in Costa

Rica (*Barquero and Segura, 1983; Alvarado et al. 1992*), and hosts a highly acidic crater lake (*Tassi et al., 2005, 2009*), the source of recurrent phreatomagmatic to phreatic eruptions (*Boudon et al., 1996*). The intense (SO_2> 60 tons/day; *de Moor et al., 2017*) gas emissions have only occasionally been studied in the past (*Tassi et al., 2005, 2009; Aiuppa et al., 2014; de Moor et al., 2017*), due to the limited accessibility of the volcano summit. Our study here provides the first near-continuous gas dataset taken during a period of recurrent phreatic activity at Rincón de la Vieja, including the first measurement of the syn-explosive gas phase. The aim is to use our novel gas observations to derive new insights into the mechanisms driving crater lake phreatic explosions and assess the potential for forecasting eruptions at Rincón de la Vieja.

Figure 6.1 Structural and volcanological setting of the Costa Rica segment of the Central American Volcanic Arc. Modified from Brandes et al., 2007. Map data: Google, Landsat/Copernicus image, SIO, NOAA, U.S. Navy, NGA, GEBCO.

6.3 Rincón de la Vieja volcano

Rincón de la Vieja volcano is part of the Guanacaste volcanic range (Fig. 6.1), a Quaternary magmatic range related to subduction of the Cocos plate underneath the Caribbean plate (*Carr 1984, 1990; DeMets, 2010; DeMets et al., 2001*). The Guanacaste volcanic range consists of four andesitic central edifices (Orosí-Cacao, Rincón de la Vieja-Santa María, Miravalles, and

Tenorio-Montezuma). Before construction of the Quaternary andesitic chain, intense explosive silicic volcanism generated a series of collapse events and associated calderas (*Molina et al., 2014*). The Rincón de la Vieja-Santa María volcanic complex (maximum elevation 1916 m) was constructed within one of these calderas, the 120 km^2 Cañas Dulces Caldera (*Molina and Marti, 2016*). The Cañas Dulce caldera hosts several hydrothermal fields (*Giggenbach and Corrales, 1992*), including several thermal manifestations on the Rincón de la Vieja massif itself (*Tassi et al., 2005*), aligned along a NW-SE trend running roughly parallel to the volcano's axis.

Rincón de la Vieja (10.49 N, 85.19 W) is the only currently active andesitic stratovolcano in the Guanacaste Cordillera. The volume of the massif is estimated at 130 km3 (*Carr, 1984*). The most recent magmatic eruption (with significant juvenile component) took place ~3500 years B.P. (*Alvarado et al., 1992*). This eruption left the dacitic Rio Blanco tephra deposit (volume, 0.25 km^3), which also includes a small fraction (<3 %) of andesitic scoria and pumice indicating a mixed magma reservoir (*Kempter, 1997*). The historically active crater has produced frequent phreatic to phreatomagmatic eruptions since 1851 (*Boudon et al., 1996*). Major eruptions in the mid-1990s caused large lahars and significant damage to local communities. The 1995, 1991, 1983, 1967, 1966, and 1922 eruptions expelled part of the crater lake, producing acidic lahars (*Kempter, 1997; OVSICORI, 1995; Barquero and Segura, 1983*), mostly breaching through the topographically lower northern crater rim.

Rincón de la Vieja is monitored by Observatorio Vulcanológico y Sismológico de Costa Rica-Universidad Nacional (OVSICORI-UNA) and the Instituto Costaricense de Electricidad (ICE). Volcano monitoring is complicated by remote location and extreme field conditions (high rainfall, frequent fog and extremely windy). The active crater today hosts a large hyper-acidic lake (pH = 0.7-1 and T = 26-30 °C in February-March 2017) (Fig. 6.2), characterized by vigorous degassing and continuous overturning (*Tassi et al., 2005, 2009; de Moor et al., 2017*). Dark-grey spherules of colloidal sulfur are widespread on the lake's surface (Fig. 6.2), while fumarolic emissions up to 130 °C are observed on the inner crater walls (*Tassi et al., 2005; Aiuppa et al., 2014*).

Phreatic/phreatomagmatic activity resumed in September 2011, after 13 years of quiescence. During 2012-2013, Rincón de la Vieja exhibited low seismicity and very infrequent eruptions. From September 2014, eruptive activity escalated to an average of 25 phreatic-phreatomagmatic events per month, peaking in October 2015 and March 2016 when 43 and 220 eruptions were recorded, respectively. Visual binocular microscope observations (made by G. Avard at OVSICORI-UNA, following the procedure described in *Alvarado et al., 2016*) revealed that erupted ash fragments (250-500 µm

portion) contain well-preserved greenish minerals and a small portion (~5%) of fresh-looking glassy and vesicular shards. These observations were interpreted as indicative of the involvement of shallow magma in 2015-2016, as is the case at many volcanoes with phreatic eruptions (e.g. *Stix and de Moor, 2018*). Native sulphur fragments were also systematically observed in the erupted products of 2015 to 2017, especially in the 1-2 mm ash grain-size fraction (G. Avard, pers. comm.). Sulphur-rich minerals were also repeatedly observed as veins and fillings in fractures of large ejecta and blocks dispersed throughout the crater. The frequency and seismic energy of eruptions increased in early 2017. During our gas monitoring interval (February 3 – May 9, 2017) 42 seismic signals associated to phreatic/phreatomagmatic eruptions were recognized, and 9 of these eruptions were also identified geochemically (see below). Some of these 9 eruptions (eruptions 1-3 and 9; Fig. 6.3) were preceded by a long period (LP) seismic signal several seconds before the explosion. In almost all cases (eruptions 1, 3, 4-7), pulses of spasmodic tremor occurred a few hours before the eruption. Two major phreatic/phreatomagmatic eruptions (generating hot lahars that traveled outside the crater to the north) took place on May 23 and on June 11 (*Global Volcanism Program, 2017*), just a few weeks after our Multi-GAS stopped acquiring. The explosion on June 11 generated a 1-2 km high plume, and ejected coarse materials to the W and NW onto the upper N flank. This event, the largest (based on seismic energy) registered during 2011 to 2018, was preceded by a LP swarm two hours before the explosion. Material collected from the May 23 lahar down the river contained only ~1% juvenile component, but fragments erupted from the June 11 eruption (also collected

from a lahar) contained ~44% juvenile material (OVSICORI-UNA). Phreatic activity has intermittently continued until the time of writing (late 2018).

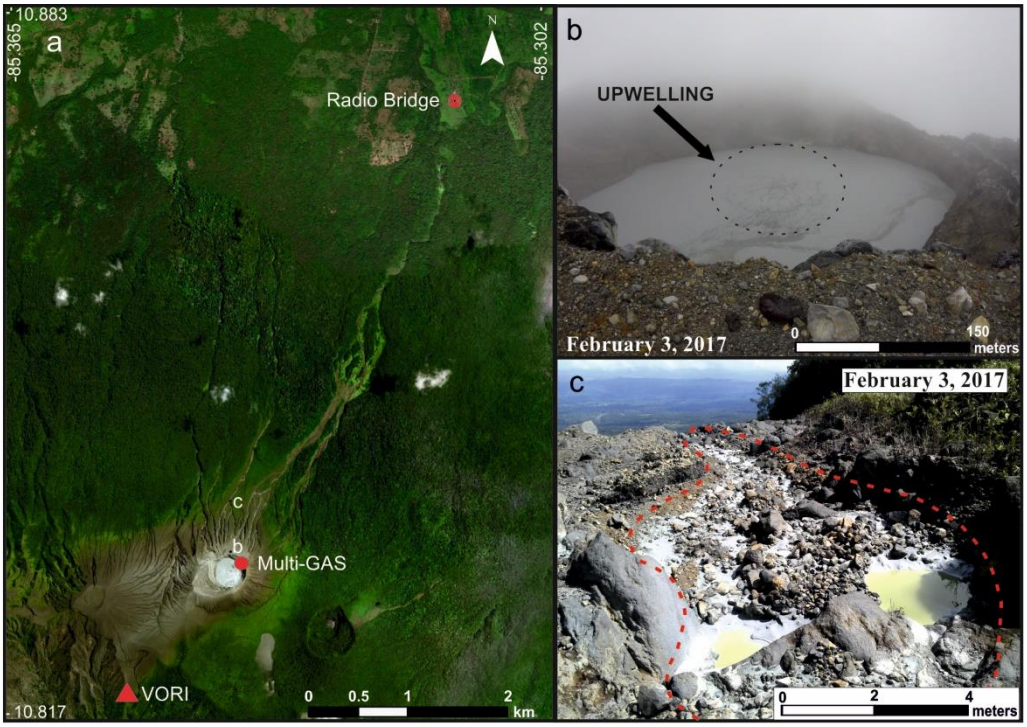

Figure 6.2: (a) Satellite image of Rincón de la Vieja volcano showing location of the Multi-GAS measurement site, the VORI seismic station, and the Radio Bridge, map data: Google, Landsat/Copernicus image, SIO, NOAA, U.S. Navy, NGA, GEBCO; (b) The Rincón de la Vieja active crater, with convection cells and abundant gray sulfur spherules floating on the lake surface; (c) Water and sulfur deposits in a canyon on the Northern slope of Rincón de la Vieja.

6.4 Materials and methods

The gas dataset we report on in this study was recorded using two distinct fully autonomous Multi-GAS instruments, one designed by the Instituto Nazionale di Geofisica e Vulcanologia (INGV) and one designed by the U.S. Geological Survey (USGS). The two instruments (INGV and USGS-campaign) operated sequentially at the same site, located on the northern inner wall of the active crater ~1 m downwind the lake shore (Lat. 10.8327 Long. -85.3355; see Fig. 6.2). This site was selected because its position ensured regular fumigation by the lake gas plume, while minimizing any potential gas contribution from low-temperature crater fumaroles (not observed at the measurement site during our study). The Multi-GAS instruments were powered by an external (12 V, 40 Ah) battery and 3 solar panels in order to ensure proper operation in all climatic conditions. A PVC tube with two filters served as gas inlet, and allowed gas to be pumped (at 1.2

L/m) inside the Multi-GAS instruments. The first (INGV-type) Multi-GAS was installed on February 3, 2017 and operated until March 17, 2017, when it was dismantled (for use at a different volcano) and replaced by a second (USGS-campaign type; *Gunawan et al., 2016*) Multi-GAS. This latter operated until May 09, 2017, when it stopped transmitting data before being finally destroyed during the May 23 lahar-producing phreatic blast (*Global Volcanism Program, 2017*).

The two Multi-GAS instruments used very similar sensor kits (see below) and were re-calibrated at OVSICORI with the same standard gases before the installation, showing very similar response. The INGV-type Multi-GAS was recalibrated after returning from the field (in late March 2017), and the original calibration was reproduced within sensor precision. Both Multi-GAS instruments measured SO_2 and H_2S mixing ratios (precision within ± 15% at 2σ; *Lewicki et al., 2017*) with the same specific electrochemical sensors (models TD2G-1A and TC4E-1A, respectively; all from City Technology and with ± 5% repeatability). Interference of SO_2 gas on the H_2S sensor (15%) was determined during calibration procedure and corrected with the Ratiocalc software. CO_2 mixing ratios were measured using an on-board spectrometer (INGV-type: Gascard EDI030102NG, measurement range = 0–3000 ppmv, precision, ± 3% at 2σ; USGS-type LI-COR LI-840A, measurement range = 0–5000 ppmv, precision, ± 1.5% at 2σ). The INGV-type Multi-GAS instrument, controlled by an arduino2 datalogger, acquired data at 0.1 Hz rate during 4 sampling periods per day, of 30 minutes duration each. In the USGS-type Multi-GAS, all data acquisition and scheduling was controlled by a Campbell Scientific data logger (CR1000 with NL115 module) outfitted with 2 GB of onboard memory. The station completed four data acquisition cycles per day, in which data were acquired for 1 hour at a 1 Hz rate. Before and after each measurement cycle, the station performed sensor baseline checks by activating two miniature 3-way teflon solenoid valves (Cole-Parmer WU-01540-11) that formed a closed-loop and recirculated trapped sample gases through soda lime and desiccant for 3 min to remove acid gases and water vapor in order to provide a measure of within-run baseline drift and to clean and dry the instrument prior to shutting down. For both Multi-GAS instruments, data were telemetered (at the end of each acquisition cycle) via radio modem (Xetawave) to OVSICORI using a radio bridge installed on the northern base of the volcano (Fig. 6.2). The acquired gas mixing ratios data were post-processed using the Ratiocalc software (*Tamburello, 2015*) to derive gas ratios between volatile couples (CO_2/SO_2 and H_2S/SO_2) using linear regression. In order to derive accurate gas ratios, the different response time (~2-4 s) between the spectroscopic sensor and the electrochemical sensors was corrected for during data processing with the Ratiocalc software. No pressure correction was applied to the electrochemical sensors owing to

very similar altitude between calibration site (Heredia, ~1200 m) and Rincón 's summit (~1500 m). Based on laboratory tests with standard gases, errors in the derived ratios are typically ≤15%. Unfortunately, the plume was condensing at all conditions encountered during observations, so it was not possible to determine a robust volcanic H_2O signal.

Seismic activity was characterized using the reference station VORI, operated by the Observatorio Sismológico y Vulcanológico de Arenal y Miravalles (OSIVAM) of the Instituto Costarricense de Electricidad (ICE). This station is located 1.8 km SW of the active crater, and is equipped with a digital 3-component broadband TRIMBLE REFTEK 151B sensor with flat response from 0.016 (60 s) to 50 Hz. Signals were sampled at 100 Hz. Close inspection of seismic records was carried out to extract discrete events and, in the particular case of eruptive signals, to estimate the associated seismic energy (Eseismic). Seismic energy was calculated using the relation for bodywaves generated by an isotropic source at the top of a homogeneous half space (*Boatwright, 1980; Arámbula-Mendoza et al., 2011*):

$$E_{seismic} = 2\pi r^2 \rho_{earth} c_{earth} \frac{1}{A} \int S^2 U(t)^2 dt \quad \text{(Eq. 6.1)}$$

where r is the distance from the source to the seismic station, ρ is rock density, c is the P wave velocity, S is the site effect, U is seismic amplitude and A is attenuation. We used r = 1800 m, c = 1500 m/s, ρ = 2600 kg/m3. The site and attenuation effects were neglected for simplicity.

The temporal evolution of seismic activity was explored using Real-time Seismic Energy Measurement, or RSEM (*De la Cruz-Reyna and Reyes-Dávila, 2001*), which considers the square of the amplitude (directly related to seismic energy). The seismic signal was filtered in the band of 1 - 10 Hz in order to avoid strong ambient noise present in the records.

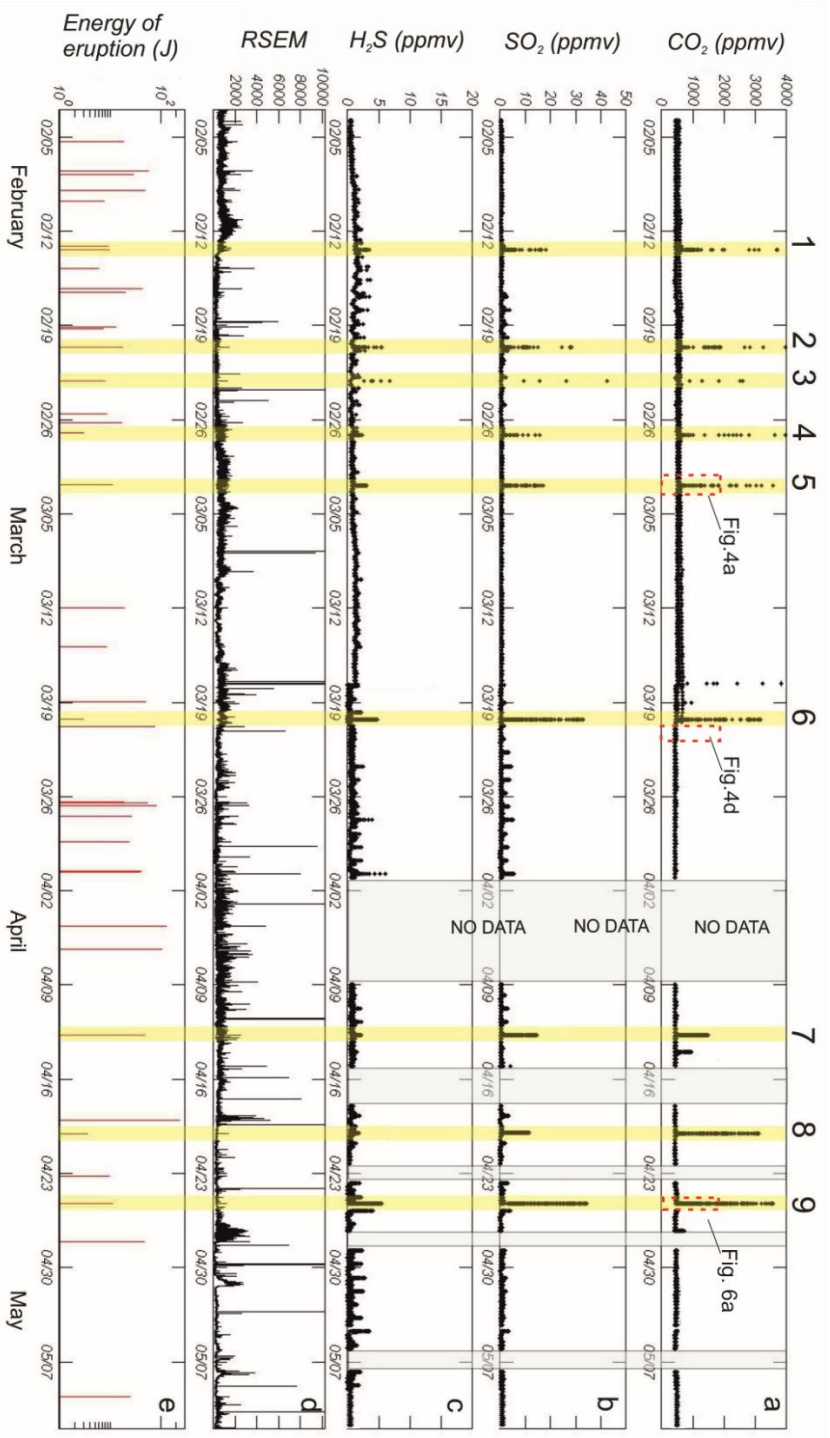

Figura 6.3 Time-series of (a, b, c) gas mixing ratios (in ppmv); (d) RSEM, (e) eruptive energy. Note that Multi-GAS data (CO_2, SO_2 and H_2S mixing ratios) are not continuous but obtained during 4 daily cycles, each 30-60 minutes long. The shaded yellow bands identify the 9 explosions (numbered #1 to #9) during which the Multi-GAS was operating, allowing the syn-explosive gas composition to be determined. The five light grey areas identify all periods with no MultiGAS data. The small red insets in the CO_2 plot identify the expanded portions shown in figure 6.4 and figure 6.6.

6.5 Results

Figure 6.3 is a temporal record of CO_2, SO_2 and H_2S concentrations measured by the two Multi-GAS instruments. The RSEM time-series is shown in panel (d) for comparison, along with (e) the timing of each of the seismically-identified phreatic explosions.

The temporal plots exhibit a sequence of gas peaks (numbered #1 to #9 in Fig. 3) that clearly emerge above a persistent background (characterized by low concentration of all gases). By comparison with seismic data (Fig. 6.3d, e; 6.4a), we find that each of the gas peaks corresponds to a Multi-GAS recording of a phreatic explosion, i.e. the peaks are records of the composition of the gas released during a phreatic blast (referred as syn-explosive gas). CO_2 and SO_2 (Fig. 6.3a, 6.3b, 6.4a) exhibit the most pronounced peaks in the syn-explosive gas, with peak concentrations of >3000 ppmv and ~52 ppmv, respectively. H_2S peaks are more moderate (typically < 5 ppmv).

Nine (Fig. 6.3) of the 42 phreatic events that occurred during February 3 - May 9, 2017 are captured by our Multi-GAS record (the remaining explosions took place outside the four daily Multi-GAS acquisition cycles). The background gas mixing ratios thus correspond to continuous passive degassing between the explosions, in what we refer to as the quiescent gas. The quiescent gas is typically characterized by low SO_2 and H_2S mixing ratios (< 2 ppmv), and CO_2 (<500 ppmv) slightly above atmospheric background values.

As in other recent work (*Aiuppa et al., 2017, 2018; de Moor et al., 2017*), the Multi-GAS-derived gas mixing ratios data are post-processed to calculate the ratios between the various volatiles using the procedure of *Tamburello* (2015). To this aim, the gas mixing ratios time-series are sequentially examined with Ratiocalc to identify individual temporal windows (of ≥ 250 s, corresponding to subsets of ≥ 30 data points) with high correlation coefficients (R2> 0.6) between gas couples.

The procedure is illustrated in Figure 6.4: panels (a) and (d) are temporal plots of mixing ratios recorded during a single explosion (a-c), and during a typical quiescent degassing phase (d-f) (see insets in Fig. 6.4). By sequentially scanning the two sub-datasets, we identify the temporal intervals where the best correlations (R2> 0.6) between gas mixing ratio pairs are observed (yellow bands in Figs. 6.4a and 6.4d). These subsets of CO_2, SO_2 and H_2S mixing ratios are then used to build CO_2 vs. SO_2 (Figs. 6.4b and 6.4e) and H_2S vs. SO_2 (Figs. 6.4c and 6.4f) correlation plots, and to calculate the time-averaged CO_2/SO_2 and H_2S/SO_2 ratios (within the yellow-colored temporal windows) from the slopes of the best-fit regression lines. The procedure is repeated for the entire dataset, and all the obtained gas ratio pairs are listed in Table 6.2.

Our gas ratios, listed in Table 6.2 and illustrated in Figure 6.5, show contrasting H_2S/SO_2 ratios composition for the quiescent gas and the syn-explosive gas. The quiescent gas composition is characterized by H_2S/SO_2 ratios of 0.57±0.2 (1 σ) (range, 0.01-1.5), or well above the H_2S/SO_2 of the gas released during the phreatic eruptions. This syn-explosive gas exhibits H_2S/SO_2 ratios of 0.04±0.06 (range, 0.0003 to 0.18) (Fig. 6.5). The quiescent gas H_2S/SO_2 ratio exhibits a weak but appreciable declining trend, from February (~1) to early May (~0.5) (Fig. 6.5b), but remains systematically above the syn-explosive gas range (which shows no systematic trend).

Table 6.2 shows that quiescent gas and syn-explosive gas released by the lake have overlapping CO_2/SO_2 ratio compositions (64±59 and 136±110 at 1σ; Fig. 6.5a). Both show a tendency of decreasing CO_2/SO_2 ratios from February (~120±51) to early May (~70±20).

Prior to each individual explosion, the CO_2, SO_2 and H_2S mixing ratios are typically very low (see Figs. 6.4a and 6.6a). Thus, the composition of the quiescent gas released in the minutes/seconds before an explosion, here refereed as pre-explosive gas, is not well constrained. One important aspect is, however, that the compositional change from pre-explosive gas to syn-explosive gas is large and abrupt at the onset of eruption (Fig. 6.4a and 6.6a). To highlight this observation, we show in Figure 6.4a the CO_2/SO_2 and H_2S/SO_2 ratios calculated by simply taking the ratio of individual couples of co-acquired mixing ratios. This point-to-point ratio approach (e.g., Pering et al., 2014) provides high-resolution (1 Hz) records of CO_2/SO_2 and H_2S/SO_2 ratios, see Figures 6.4a and 6.6a. The errors associated with this methodology are potentially very large (~ 50 %, as based on laboratory tests) at the few ppm level (e.g., before the explosions), so the ratios displayed in Figures 6.4a and 6a should only be viewed as semi-quantitative estimates. However, for the specific example shown in Figure 6.4a, the ratios calculated with the point-to-point ratio technique (respectively of 640 and 1.1 for CO_2/SO_2 and H_2S/SO_2) are reasonably close to those obtained with the scatter plot methodology described above (respectively of 628 and 0.9 for CO_2/SO_2 and H_2S/SO_2). A comparable similarity of point-to-point-derived and scatter plot-derived ratios is obtained for the explosion detailed in Figure 6.6a (see Tab. 6.2). We thus argue that the abrupt changes in CO_2/SO_2 and H_2S/SO_2 ratios at eruption onsets (Figs. 6.4a e 6.6a) are real, and point to very distinct gas signatures for pre-explosive gas and syn-explosive gas, with the former being typically more SO_2-poor. Very similar abrupt variations in gas ratios are observed for all 9 recorded explosions, followed by a gradual return to quiescent gas compositions over timescales of minutes (Figs. 6.4a and 6.6a). The point-to-point-derived compositions of the pre-explosive gas are listed in Table 6.2.

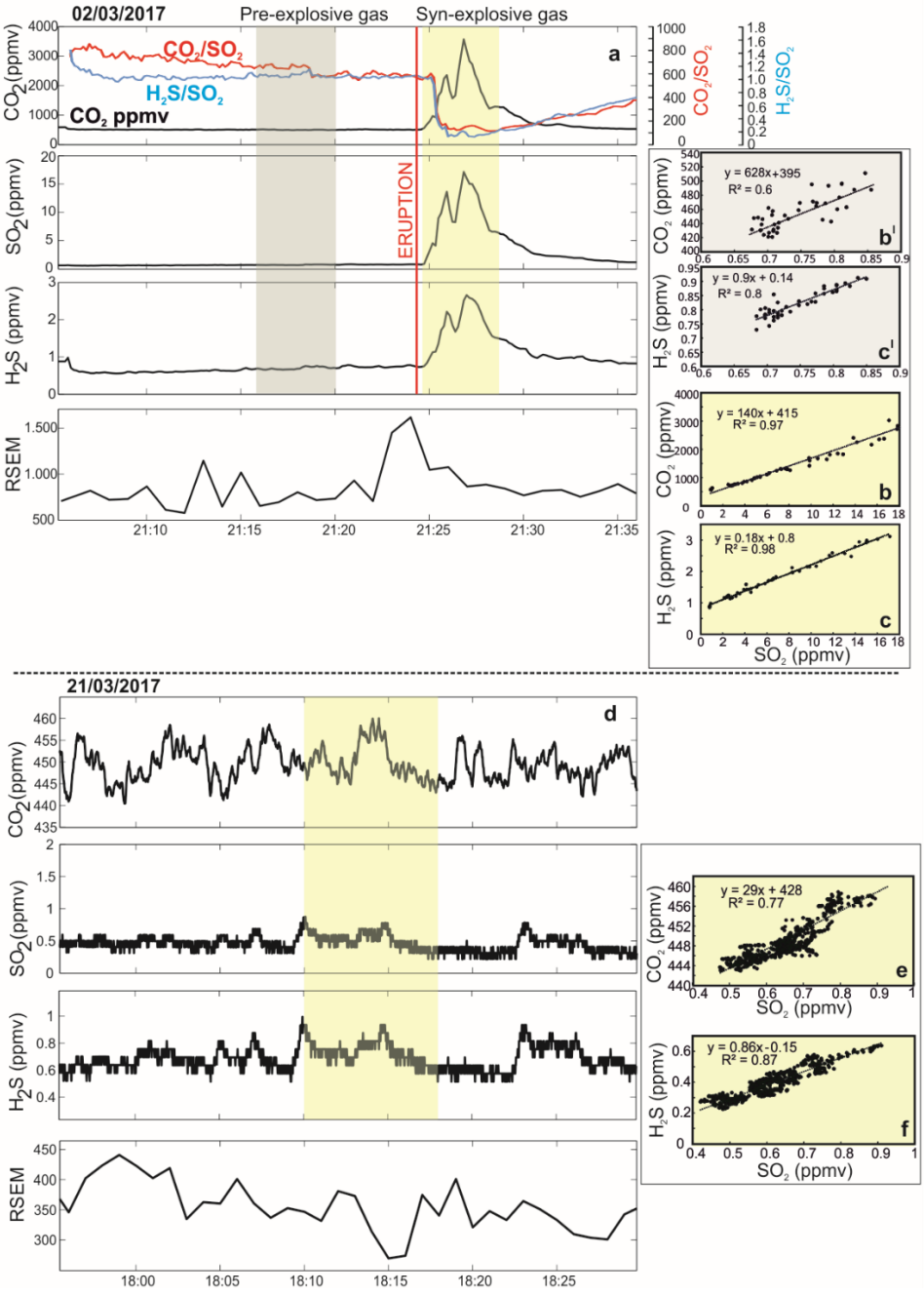

Figure 6.4 (a) Detail of gas and seismic records taken on March 02, 2017 between ~21:05 to ~21:35 GMT. The eruption (event #5 in Figure 3, see inset) occurred at ~21:24 GMT. Mixing ratios increase after the blast, starting at ~21:24 GMT. The yellow-colored area corresponds to the sub-interval (identified with Ratiocalc) where CO_2, SO_2 and H_2S are positively correlated at statistically significant level (R2> 0.6). These subsets of CO_2, SO_2 and H_2S mixing ratios are used to draw (b) CO2 vs. SO_2 and (c) H_2S vs. SO_2 correlation plots, and to calculate the time-averaged CO_2/SO_2 and H_2S/SO_2 ratios (within the yellow-colored temporal windows) from the slopes of the best-fit regression lines (listed in Table 6.2). In (a) the red and blue lines are high-resolution (1 Hz) records of CO_2/SO_2 and H_2S/SO_2 ratios, respectively, calculated by taking the ratio of individual couples of co-acquired mixing ratios. This point-to-point ratios (e.g., Pering et al., 2014) have large (~ 50 %) associated errors at the ppm level (e.g., before the explosion, Fig.

4a), so they should only be viewed as semi-quantitative estimates. Nevertheless, the contrasting gas signatures for pre-explosive and syn-explosive gas are clearly observed. Example of CO_2 vs. SO_2 and H2S vs. SO_2 correlation plots for the pre-explosive gas (built from data within the grey-colored temporal windows in (a)), shown in (b') and (c'), confirm a very CO_2-rich (or SO_2-poor) gas composition prior to the blast. Gas ratios progressively return to the pre-eruptive levels towards the end of the Multi-GAS acquisition. (d) Example of gas and seismic records taken during a quiescent phase (March 21, 2017 between ~17:55 and ~18:30 GMT). Very low gas mixing ratios are observed throughout, as characteristic of the quiescent gas. The yellow-colored area corresponds to the only sub-interval (identified with Ratiocalc) where CO_2, SO_2 and H_2S are positively correlated at statistically significant level (R2> 0.6). These subsets of CO_2, SO_2 and H_2S mixing ratios are used to construct (e) CO_2 vs. SO_2 and (f) H_2S vs. SO_2 correlation plots, from which the time-averaged CO_2/SO_2 and H_2S/SO_2 ratios (within the yellow-colored temporal windows) are calculated (listed in Table 6.2).

6.6 Discussion

Our Multi-GAS results, in tandem with previous results (*Aiuppa et al., 2014; de Moor et al., 2017*), constrain the composition of the gas plume released by the Rincón de la Vieja crater lake (Fig. 6.7). Our 2017 results confirm that SO_2 is the prevalent S gas species in the Rincón de la Vieja crater lake plume during both quiescent and explosive degassing, with H_2S/SO_2 <1 in all except six cases (Tab. 6.2). This is in line with previous reports (all Multi-Gas measurements) of *Aiuppa et al*., (2014) (1 survey in April 2013; H_2S/SO_2 = 0.9±0.15) and *de Moor et al., 2017* (3 surveys between April 2014 and March 2016; H_2S/SO_2 of 0.05-0.3) (Fig. 6.7). In contrast, low-temperature (<80 °C) fumaroles, scattered on the inner crater walls, and around the lake shore, typically exhibit high H_2S/SO_2 ratios of ~4 (*Tassi et al., 2005*). In these weaker hydrothermal manifestations, S re-equilibration (e.g., SO_2 conversion to H2S) during cooling and reaction with wall-rocks in the fumarole's feeding conduits is very likely. Similarly, de Moor et al. (2016b) showed that Poás fumaroles have higher H_2S/SO_2 than the plume from the acid crater lake.

The 2017 crater lake plume is richer in CO_2 (CO_2/SO_2 ratios of 64±59 to 136±110 for quiescent gas and syn-explosive gas, respectively) than in 2013 (CO_2/SO_2 = 27±15; *Aiuppa et al., 2014*) and 2014-2016 (CO_2/SO_2 of 4.3 to 9.5; *de Moor et al., 2017*) (a period over which Rincón's activity was progressively intensifying) (Fig. 6.7). Thus, degassing at Rincón de la Vieja appears to be highly dynamic on yearly time scales in terms of gas compositions. Our continuous record from 2017 has much improved temporal resolution than past (campaign) surveys, and thus allows evaluation of the extent to which gas composition responds to high-frequency changes in volcanic activity. Three key observations emerge:

i) the plume H_2S/SO_2 ratio varied little during quiescent lake degassing in 2017: 0.57±0.20 (Figs. 6.5b and 6.7); this limited variability is suggestive of S speciation buffering by fluid + solid phase reaction(s) (at least partially) (Giggenbach, 1987, 1996);

ii) during phreatic blasts, the gas emissions shift to more oxidized conditions (H_2S/SO_2 <0.18) than during quiescent degassing (Figs. 6.5b and 6.6); the compositional change at the eruption onset is rapid and abrupt, as indicated by the gas ratio contrast between the *pre-explosive gas* and *explosive gas* (Figs. 6.4a and 6.6a);

iii) both the quiescent gas and syn-explosive gas are similarly CO_2-rich (relative to S;) compared to magmatic gases in Costa Rica and Nicaragua (see Fig. 6.7 and reference therein).

iv) The quiescent gas vented prior to an explosion (the pre-explosive gas) has systematically higher CO_2/SO_2 ratios than the corresponding explosive gas (Figs. 6.4 and 6.6). This difference can only partially reflect the different data processing technique (point-to-point vs. scatter plot, see Figs. 6.4 and 6.6). Thus, also in view of the H_2S/SO_2 records discussed above (see point ii), we conclude that the explosive gas is especially SO_2-rich.

These peculiar features of the Rincón de la Vieja crater lake plume have implications for the nature of the magmatic-hydrothermal system producing the emissions, and for the trigger mechanisms of the recurrent explosions, as detailed below.

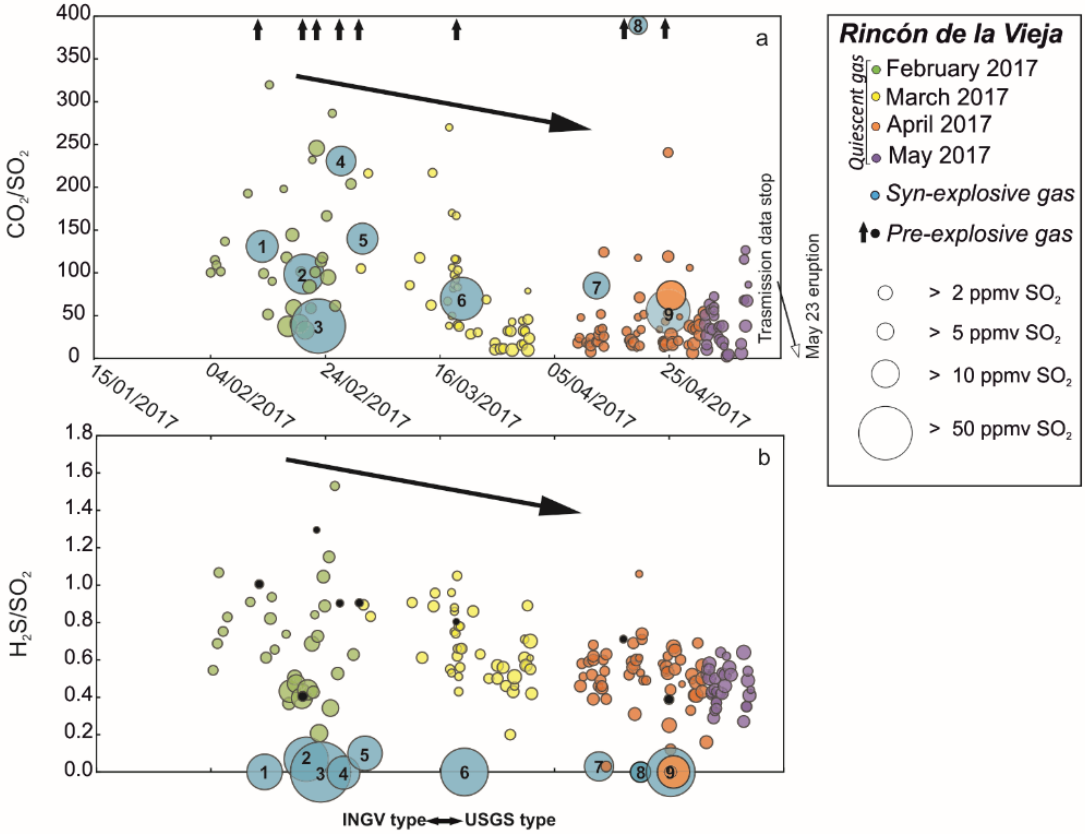

Figure 6.5 Time-series of gas (a) CO_2/SO_2 and (b) H_2S/SO_2 (molar) ratios. Quiescent gases, pre-explosive gases and syn-explosive gases are plotted with different colors. Symbol size is proportional to SO_2 mixing ratios. In (a), all pre-explosive gases plot at higher CO_2/SO_2 ratios (as shown by the arrows).

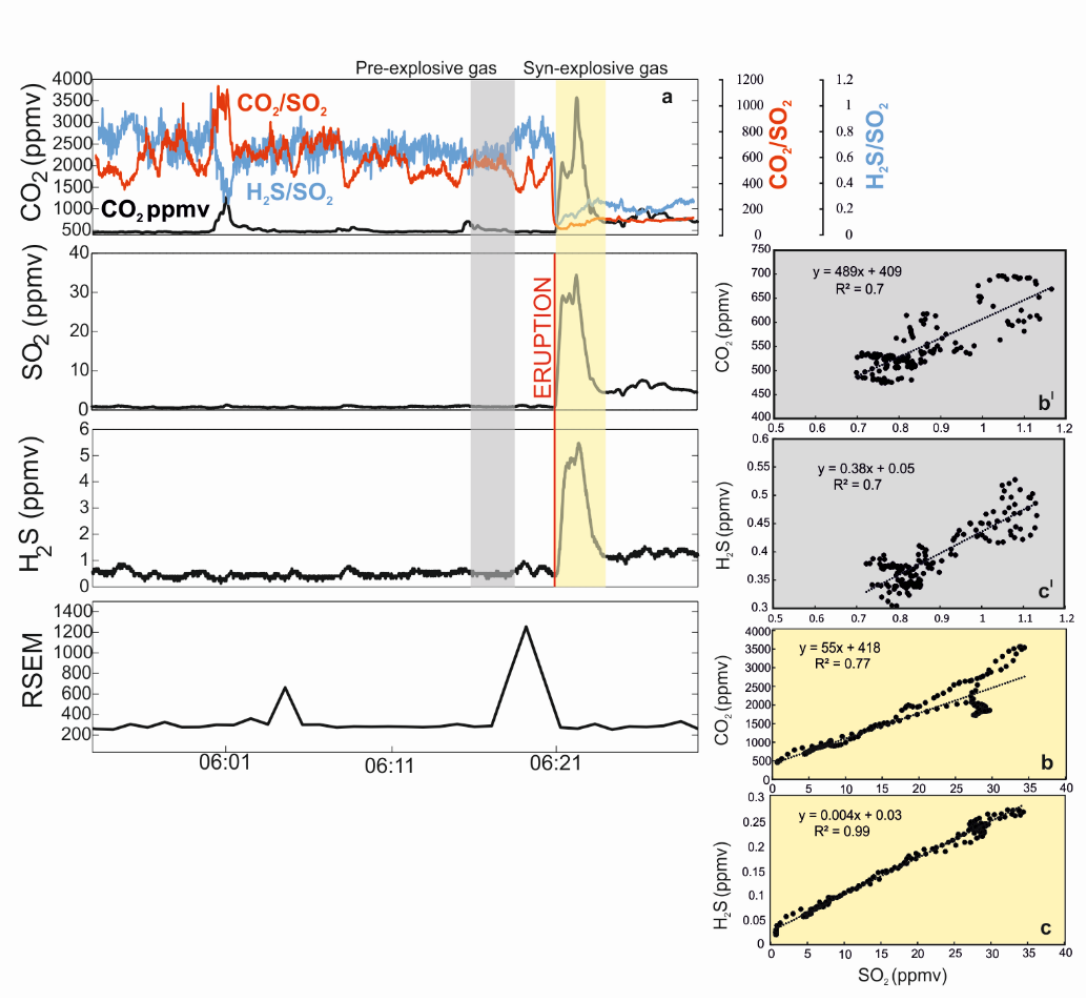

Figure 6.6 (a) Detail of gas and seismic records taken on April 25, 2017 between ~5:51 to ~6:31 GMT. The eruption (event #9 in Figure 3, see inset) occurred at ~6.21 GMT. Mixing ratios increase after the blast. The yellow-colored area corresponds to the sub-interval (identified with Ratiocalc) where CO_2, SO_2 and H_2S are positively correlated at statistically significant level (R2> 0.6). These subsets of CO_2, SO_2 and H_2S mixing ratios are used to draw (b) CO_2 vs. SO_2 and (c) H_2S vs. SO_2 correlation plots, and to calculate the time-averaged CO_2/SO_2 and H_2S/SO_2 ratios (within the yellow-colored temporal windows) from the slopes of the best-fit regression lines (listed in Table 2). In (a) the red and blue lines are high-resolution (1 Hz) records of CO_2/SO_2 and H_2S/SO_2 ratios, respectively, calculated by taking the ratio of individual couples of co-acquired mixing ratios. This point-to-point ratios suggest contrasting gas signatures for pre-explosive and syn-explosive gas. Example of CO_2 vs. SO_2 and H_2S vs. SO_2 correlation plots for the pre-explosive gas (built from data within the grey-colored temporal windows in (a)), shown in (b') and (c').

6.6.1 **Rincón de la Vieja gas signature: magmatic or hydrothermal?**

In contrast to the less active (e.g., less acidic) volcanic lakes fed by hydrothermal H_2S only (e.g., *Hasselle et al., 2018*), the low (typically <1) H_2S/SO_2 ratios in the Rincón de la Vieja crater lake gas suggest supply of oxidized (SO_2-dominated) magmatic fluids into the lake system (*Christenson et al., 2010; Christenson and Tassi, 2015*). Magmatic gases typically display equilibrium H_2S/SO_2 ratios buffered by redox conditions in the coexisting silicate melt, according to (*Giggenbach, 1987*):

$$SO_2 + 3H_2 = H_2S + 2H_2O \qquad \text{(Eq. 6.2)}$$

This magma-inherited H_2S/SO_2 ratio is then generally preserved during rapid ascent and cooling of magmatic gases, unless hydrothermal storage and re-equilibration occurs (Giggenbach, 1987). Resolving equation (2) over a range of magmatic temperatures, and at redox conditions (e.g., H_2/H_2O ratios) buffered by the silicate melt at QFM (quartz-fayalite-magnetite) and NNO (Nickel-Nickel oxide) buffers (Carmichael and Ghiorso, 1986), a range of equilibrium H_2S/SO_2 ratios can be obtained (as illustrated in Fig. 6.8), well encompassing the Rincón de la Vieja crater lake gas range. For example, gases separating from magma at ~900 °C and QFM will have equilibrium H_2S/SO_2 of ~1 (constituting the so-called magmatic gas H_2S/SO_2 buffer of Giggenbach, 1987), similar to gases from the Rincón de la Vieja crater lake (Figs. 6.7, 6.8).

A continuous supply of SO_2-rich magmatic gases to the lake is also consistent with the dissolved ion composition of the crater lake water, placing Rincón de la Vieja in the field of high-activity volcanic lakes according to the classification of *Varekamp* (1997) and *Varekamp and Rowe* (2000). *Tassi et al.*, (2005, 2009) argue that the high Cl^-/Na^+ ratio in the Rincón de la Vieja crater lake requires supply of magmatic HCl into the lake, a process also responsible for the high SO_4^{2-} and F^- concentrations (from the dissolution of magmatic SO_2, H_2S, and HF). The hyper-acidic chloride–sulfate brine filling the crater lake is also rich in aluminum, iron, zinc, copper, and boron (because of elemental input via both magmatic gases and enhanced rock dissolution), and is thus compositionally similar to the magmatic gas-fed Laguna Caliente Crater Lake, Poás volcano (*Tassi et al., 2009*).

Whereas S speciation and lake chemistry clearly support magmatic gas feeding the lake, the high CO_2/SO_2 signature of the Rincón de la Vieja crater lake gas is inconsistent with a "pure magmatic" hypothesis. Figure 6.7 compares the Rincón de la Vieja gas compositions (this work and previous studies) with gases emitted by other recently active Costa Rican volcanoes (Poás and Turrialba; *de Moor et al., 2016a, b, 2017*). Both Poás and Turrialba

datasets show a spread of volcanic gas compositions, which have been interpreted as reflecting variable extents of mixing between magmatic and hydrothermal end-members (*Fischer et al., 2015; de Moor et al., 2016a, b*). The magmatic CO_2/SO_2 end-members (see stars in Fig. 6.7) have been estimated at ~0.3-0.5 (Poás) and ~1-2 (Turrialba), well below the Rincón de la Vieja crater lake gas range for both quiescent and syn-explosive gas types. Similarly, gas observations at nearby Nicaraguan volcanoes Masaya and Momotombo imply a magmatic gas CO_2/SO_2 ratio of ~3-6 (*Aiuppa et al., 2014, 2017, de Moor et al., 2017*), again implying that the Rincón de la Vieja crater lake gas in 2017 has too high CO_2/SO_2 to be interpreted as pure magmatic (see Fig. 6.7).

The CO_2-rich composition of Rincón de la Vieja crater lake gases also does not agree with magmatic degassing models (*Moretti et al., 2003*) using input conditions relevant to Costa Rica-like magma (see *de Moor et al., 2016b* for details). These numerical simulations (see Fig. 6.7) predict equilibrium CO_2/SO_2 ratios of 20 to 0.07 for gases exsolved from a Turrialba-like andesitic magma (at redox condition of QFM +1 to +3 and temperatures of 900-1100°C) decompressed from 250 MPa to 0.1 MPa pressure. The measured CO_2/SO_2 ratios in Rincón de la Vieja crater lake gas (64±59 and 136±110 for the *quiescent* and *syn-explosive gas*, respectively) are clearly higher than the typical magmatic range, unless very high gas-melt separation pressures (>> 250 MPa, equivalent to > 9 km depth) are assumed. Such a deep magma source is unlikely, however, because heat pipes typically sustaining intense degassing and convective overturning at crater lakes require shallow magma (Fig. 6.9; *Christenson and Tassi, 2015*). Also, magma involvement in the recent Rincón de la Vieja eruptions (implicated by the small but ubiquitous juvenile fragments in the eruption deposits) is indicative of shallow storage (Fig. 6.9).

To summarize, the CO_2-rich gas compositions with low H_2S/SO_2 ratios (Fig. 6.7) are incompatible with a direct shallow magmatic source for the gas vented by the Rincón de la Vieja crater lake. We propose that the pristine chemical composition of deep magmatic gases is altered during upward migration by gas-water-rock reactions within the (sub)limnic hydrothermal

system.

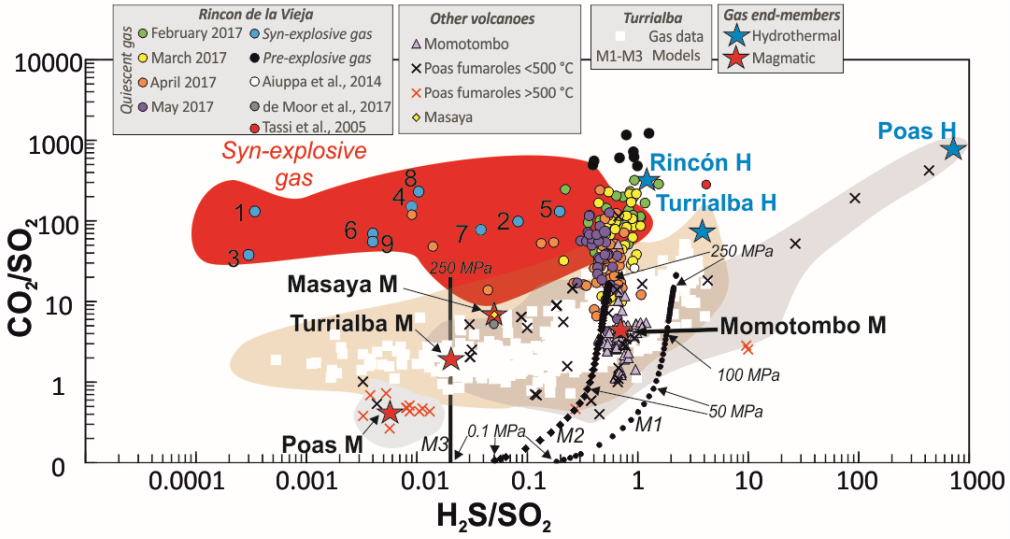

Figure 6.7 H_2S/SO_2 vs.CO_2/SO_2 scatter plot of Costa Rica and Nicaraguan volcanic gases. The Rincón de la Vieja gas (both quiescent gas and syn-explosive gas; same symbols as in Figure 6.5) is contrasted with the composition of volcanic gases from other volcanoes of the Costa Rica-Nicaragua arc segment. Momotombo and Masaya: Aiuppa et al., 2014, 2017; de Moor et al., 2017; Poás: de Moor et al., 2017; Aiuppa et al., 2017. Estimated compositional fields for hydrothermal (H) and magmatic (M) end-members are indicated (this study; based on averaging of magmatic and hydrothermal compositions quoted in the previous studies). The hypothetical composition of the Rincón hydrothermal pole (H) was estimated by averaging composition of the two measurements of quiescent gases with the lowest SO_2 concentrations (e.g., the most hydrothermal endmember). Numbers alongside the syn-explosive gas data-points identify the explosions (see Figure 6.3). The curves labeled M1 to M3 indicate the model-derived H_2S/SO_2 vs.CO_2/SO_2 compositions obtained by model simulations of degassing upon decompression (from 250-0.1 MPa) for a Turrialba-like magma (taken from de Moor et al., 2016b). M1 and M2 models have been initialized at slightly different H_2O contents (3 and 2 wt. %, respectively). In model M3, gas compositions obtained in runs M1-M2 are re-calculated at surface discharge conditions (QFM+3, 0.1 MPa, 650°C), yielding H_2S/SO_2 ratio of ~0.02 (see the original work of de Moor et al., 2016b for further details).

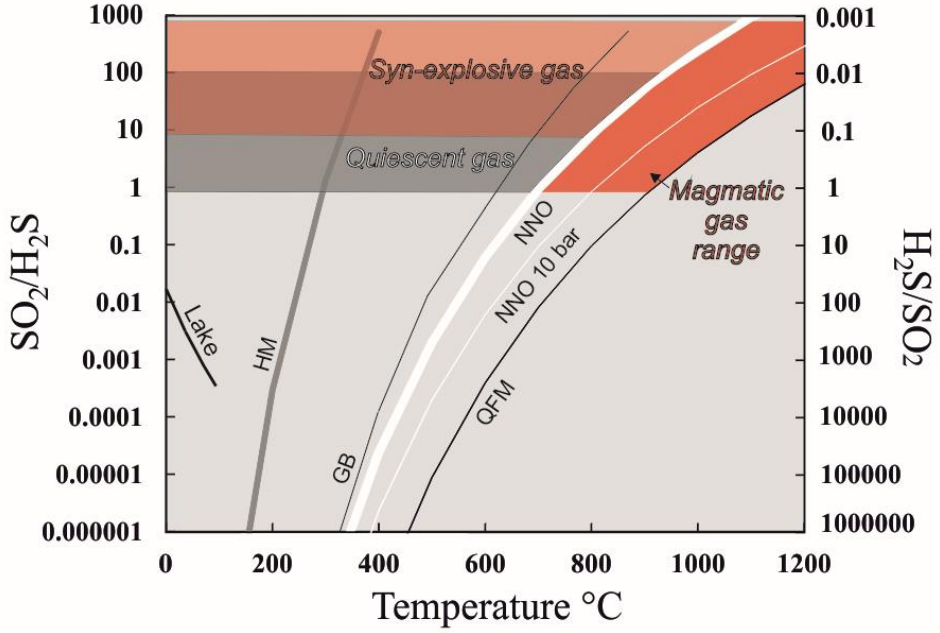

Figura 6.8 Temperature dependence of the SO_2/H_2S ratio, as predicted by the common magmatic and hydrothermal redox buffers (modified from Aiuppa et al., 2005). The solid lines represent the H2S/SO2 ratios at equilibrium with redox conditions (oxygen fugacity, fO2) fixed by QFM (Quartz-Fayalite-Magnetite), NNO (Nickel-Nickel oxide), and HM (Hematite-magnetite) redox buffers (Giggenbach, 1987, 1996). The magmatic gas range is from Aiuppa et al., (2005). The curve labelled GB and Lake illustrate the equilibrium H_2S/SO_2 ratios at redox conditions fixed by the Giggenbach (1987) FeO-FeO1.5 hydrothermal buffer (Eq. 6.6) and dissolved S species in the lake buffer water (Eq. 6.2), respectively. Pressure is 1 bar except where specified. The measured H_2S/SO_2 ranges for both the quiescent and syn-explosive gas are indicated by grey and red bands, respectively.

6.6.2 **The role of the sublimnic hydrothermal system**

The interactions of magmatic gases with either the crater lake or the subjacent hydrothermal system are the most obvious candidates for generating the observed CO_2-rich (S-depleted) Rincón de la Vieja gas. Magmatic gas-lake and/or magmatic-hydrothermal reactions, if occurring, could also effectively control S partitioning between reduced and oxidised forms, thus modifying the original magmatic H_2S/SO_2 ratio (*Christenson et al., 2010; Christenson and Tassi, 2015*).

One often-invoked mechanism of magmatic SO_2 dissolution into active volcanic lakes is via disproportionation reactions such as (Kusakabe et al., 2000):

$$3\ SO_2 + 2H_2O \rightarrow 2HSO_4^- + S_{(e)} + 2H^+ \qquad \text{(Eq. 6.3a)}$$

$$4\ SO_2 + 4H_2O \rightarrow 3HSO_4^- + H_2S + 3H^+ \qquad \text{(Eq. 6.3b)}$$

The two relationships can be combined into the following equilibrium:

$$SO_2 + S_{(e)} + 2H_2O = H_2S + H^+ + HSO_4^- \qquad \text{(Eq. 6.4)}$$

To assess the role played by magmatic gas-lake water reactions, we test if the measured H_2S/SO_2 ratios in the Rincón de la Vieja gas (Figs. 6.4-6.8) are consistent with the equilibrium ratio predicted by eq. 6.4 at lake water conditions, i.e. if the measured gas S speciation is controlled/buffered by dissolved S species in the crater lake water. In the Rincón de la Vieja crater lake, oxidized (exavalent) dissolved S species prevail (*Tassi et al., 2005*), and sulfur spherules are always observed on the lake surface (Fig. 6.2), implying that all of the ingredients for reaction 4 are available in abundance. Solving eq. 6.4 for the H_2S/SO_2 gas ratio, at crater lake water conditions (T = 30-50°C; $H_2SO_4 = 8.16 \times 10^{-12}$ M at pH= 0.77 and SO_4^{2-}=0.146 M), and using the thermodynamic data from HSC thermochemical software (http://www.hsc-chemistry.com/), we obtain the curve labeled "*Lake*" in Figure 6.8. The H_2S/SO_2 gas ratios predicted by reaction (4) are, however, H_2S-dominated, pointing against a lake-buffered H_2S/SO_2 ratio hypothesis (Fig. 6.8). Our calculations thus suggest that either a kinetic process prevails (e.g., that eq. 6.4 does not go to completion in the lake, leading to only partial conversion of magmatic SO_2 into H_2S) (*Rye 2005; Ohmoto and Lasaga, 1982*), or that magmatic gas-water interactions occur deeper in the system, such as in the hotter sublimnic hydrothermal system (Fig. 6.9).

A variety of magmatic gas-water-rock reactions have been proposed to occur in sublimnic hydrothermal systems (*Christenson and Tassi, 2015; Shinohara et al. 2015*). These hydrothermal reactions, typically occurring in the upper portion of a heat pipe (Fig. 6.9), invariably enrich the gas phase in CO_2 relative to more reactive SO_2 and H_2S (*Symonds et al., 2001, 2003*), and may thus generate the high CO_2/SO_2 ratios in Rincón de la Vieja crater lake gas. In addition to leading to S depletion, these reactions can also act as controls on the H_2S/SO_2 ratio (see below).

In addition to the reaction described by Eq. 6.4, S scrubbing can occur via (*Giggenbach, 1987; Christenson and Tassi, 2015*):

$$2\,H_2S_{(g)} + SO_{2(g)} = 3S_{(e)} + 2H_2O \qquad \text{(Eq. 6.5)}$$

This reaction scavenges H_2S and SO_2 in 2:1 proportions, and can thus (at least partially) justify the oxidised nature ($SO_2 > H_2S$) of the Rincón de la Vieja gas. In fact, the situation is more complicated, because as pointed out by *Shinohara et al. (2011)*, S deposition via Eq. 6.5 can either increase or decrease the gas H_2S/SO_2 ratio, depending on the original S speciation (SO_2-dominated or H_2S-dominated) in the feeding magmatic gas entering the hydrothermal system (unconstrained for Rincón). Also, concurrently with

hydrothermal S deposition, iron minerals in the hydrothermal rock matrix can contribute buffering redox conditions (e.g., the gas H_2/H_2O ratio), via (*Giggenbach, 1987*):

$$4FeO1.5 + 2H_2 = 4(FeO) + 2H_2O \quad \text{(Eq. 6.6)}$$

$$4Fe_3O_4 + 2H_2O = 6Fe_2O_3 + 2H_2 \quad \text{(Eq. 6.7)}$$

These reactions can then buffer, via Eq. 6.2, the residual (after S deposition) hydrothermal gas H_2S/SO_2 ratio. For example, the H_2S/SO_2 gas ratios predicted (as a function of temperature) from Eq. 6.2, and redox conditions buffered by either the Fe(II)-Fe(III) hydrothermal buffer (Eq. 6.6; *Giggenbach, 1987*) or the Hematite-Magnetite buffer (HM) hydrothermal (Eq. 6.7), are graphically illustrated in Figure 6.8. The figure shows that the measured H_2S/SO_2 ratios in the Rincón de la Vieja gas would be consistent with those imposed by hydrothermal buffering at HM redox conditions, 290-400 °C, and 1 bar (Fig. 6.8). Coexistence of oxidized (hematite) and reduced (magnetite, pyrite) iron forms is suggested at both Rincón de la Vieja (*Tassi et al., 2005*) and in the nearby Borinquen and Miravalles hydrothermal fields (*Gherardi et. al., 2002; Molina and Marti, 2016*). However, since a second independent redox couple (e.g., the H_2/H_2O ratio; *Aiuppa et al., 2011*) is not measured in the Rincón gas, evidence for hydrothermal (HM) buffering of S speciation remains speculative.

In summary, available gas information at Rincón de la Vieja is suggestive of extensive hydrothermal processing of magmatic gases within the sublimnic hydrothermal system. These hydrothermal reactions consume S (compared to relatively inert C, thus explaining the high observed CO_2/S ratio), but the exact S deposition mechanisms (Eq. 6.3 to 6.5), and perhaps the role of hydrothermal redox buffering (Eq. 6.7), cannot be quantitatively constrained with the present data. However the observed difference in H_2S/SO_2 between the *quiescent gas* (0.57±0.20) and the *syn-explosive gas* (0.04±0.06), and the abrupt gas ratio changes at eruption onsets (Figs 6.4a and 6.6a), clearly imply less hydrothermal interaction (e.g., less SO_2 deposition) during the phreatic blasts (Fig. 6.9). This can be explained by a combination of faster gas transit, transient disruption of the sublimnic hydrothermal envelop, and/or deeper (hotter) gas source during the explosions (Fig. 6.9)

6.6.3 The eruption trigger

Whatever the exact process (Eq. 6.3 to 6.6), S scrubbing reactions are likely to lead to rapid and effective formation of native S seals (*Christenson and Tassi, 2015*). The presence of S spherules in the Rincón de la Vieja crater lake points to the existence of a native sulfur layer at the lake bottom (*Hurst et al., 1991; Takano et al., 1994; Christenson et al., 2010*) (Fig. 6.9).

The physical state of this S pool is known to be dependent on temperature, with a ~2000-times viscosity increase upon heating in the 150-200 °C temperature range (*Hurst et al., 1991; Oppenheimer, 1992; Takano et al., 1994*). It is possible that magmatic-hydrothermal gases, while persistently fluxing through the Rincón de la Vieja sublimnic hydrothermal system, progressively heat the S pool, thus ultimately creating the conditions for the development of a viscous impermeable seal (Fig. 6.9a).

We envision a mechanism in which, during quiescence (Fig. 6.9a), the feeding magmatic gas interacts with the sublimnic hydrothermal system, undergoes S deposition (± buffering by hydrothermal minerals) and develops a CO_2-rich gas. A fraction of this gas, perhaps after further S deposition into the lake, is emitted to the surface as quiescent gas, but the remaining fraction is accumulated at depth as the impermeable S seal develops (Fig. 6.8a). The quiescent gas released shortly prior to explosions, e.g. the pre-explosive gas, is characterized by low gas mixing ratios and especially high CO_2/SO_2 ratios, consistent with a reduction of gas transfer from underneath the seal, and extensive S loss to hydrothermal minerals (Figs. 6.4a and 6.6a).

Ultimately, gas accumulation underneath the seal leads to pressure buildup and seal failure to trigger a phreatic explosion (Fig. 6.9b). This mechanism is also supported by the recurrent observation in the erupted products, especially in the 1-2 mm ash grain-size fraction, of native sulphur fragments. We argue that, during the phreatic blasts, rapid gas ascent reduces hydrothermal interactions as supported by the observed short-term variations in gas chemistry. In fact, our high-resolution (1 Hz) of CO_2/SO_2 and H_2S/SO_2 records (see Figs. 6.4a and 6.6a) show that both ratios suddenly decrease at the eruption onset, implying the each syn-eruptive gas is SO_2-richer than its corresponding pre-explosive gas. Rapid gas ascent, perhaps combined with gas ascent from deeper/hotter portions of the magmatic-hydrothermal vapor zone (Fig. 6.9b), are likely implicated in producing the relatively SO_2-richer syn-explosive gas.

We caution that our interpretation is based on only ~3 months of observations and the capturing of only 9 out of 42 explosions in that time interval. Thus, longer observations are required to draw more concrete conclusions. However, our results confirm that continuous instrumental geochemical monitoring, in tandem with seismic monitoring, can contribute to understanding the mechanisms that drive the Rincón de la Vieja magmatic system toward potentially hazardous critical states. It is interesting to note that both the H_2S/SO_2 and CO_2/SO_2 ratios in the Rincón de la Vieja quiescent gas decreased from February to early May (Figs. 6.5, 6.7), implying a decreasing extent of hydrothermal re-equilibration of the feeding magmatic gases. This trend toward more magmatic-like gas composition may tentatively be interpreted as reflecting an increase in the magmatic gas supply

to the lake conduit, and thus a more unstable magmatic system leading to the major lahar-generating phreatic eruption of May 23 (Global Volcanism Program, 2017), which occurred just a few weeks after our Multi-GAS dataset ended (and actually destroyed the instrument). As stated above, this event (and the following June 11 event) erupted a sizeable juvenile fragment component, claiming for escalating magmatic activity.

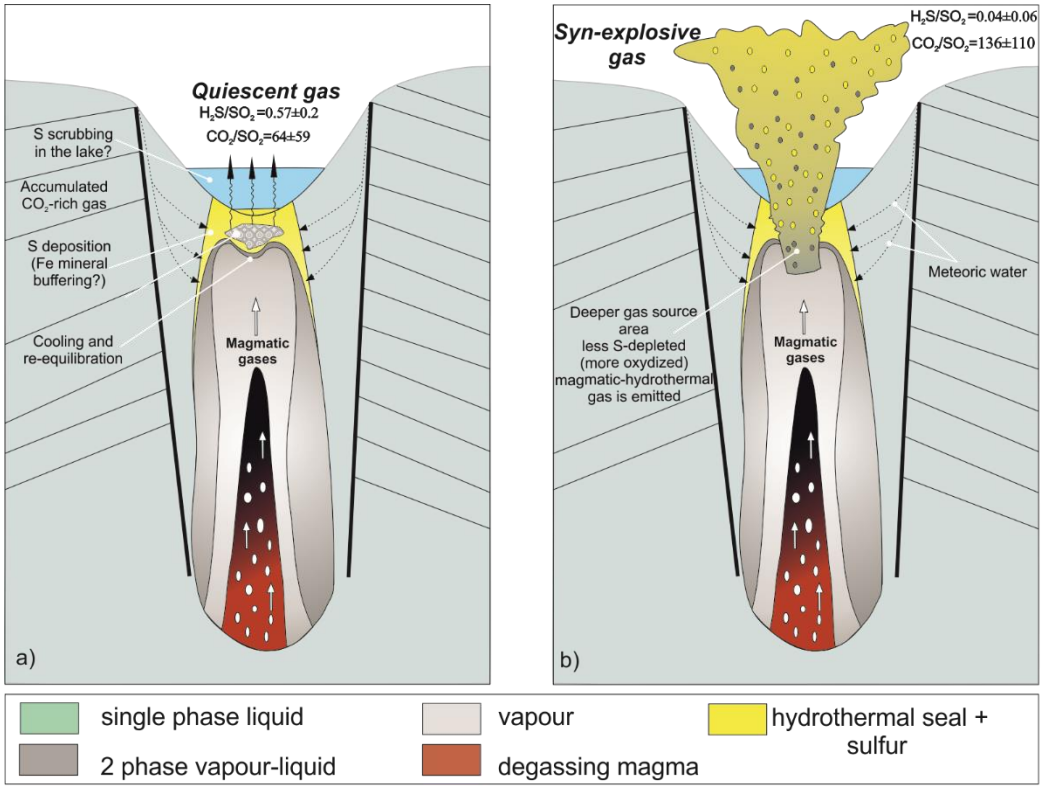

Figure 6.9 A schematic model for the Rincón de la Vieja volcano shallow feeding system, detailing the structure of the sublimnic hydrothermal/magmatic system (modified from Christenson et al., 2000). (a) During quiescence, the feeding magmatic gas undergoes S deposition (± buffering by hydrothermal minerals) within the sublimnic hydrothermal system. The resulting CO_2-rich gas is partially surface-vented as quiescent gas, and partially accumulated beneath an impermeable S seal; (b) pressure buildup below the S seal triggers a phreatic explosion, characterized by rapid gas ascent, limited hydrothermal interaction, and deeper gas source. This syn-explosive gas retains a C-rich signature, implying a magmatic-hydrothermal nature.

6.6.4 **Implications for monitoring of active crater lakes**

Our measurements of the syn-explosive gas, the first of their nature at an active volcano, provide observational evidence for that formation of hydrothermal S seals may strongly be implicated in the generation of phreatic eruptions, as originally proposed at Ruapehu volcano in New Zeeland (*Hurst et al., 1991; Takano et al., 1994; Christenson et al., 2010*). It is arguable that hydrothermal seal formation may fuel phreatic/phreatomagmatic activity at other recurrently erupting volcanic lakes worldwide (*Christenson and Tassi, 2015; Stix and de Moor, 2018*). As our Rincón de la Vieja dataset shows,

continuous gas records may help tracking such seal formation events, as marked by phases of reduced surface S degassing (see the low SO_2 and H_2S mixing ratios, and high CO_2/SO_2 ratios, in the pre-explosive gas; Figs. 6.4a, 6.6a and 6.7). To test this hypothesis further, our results thus claim for the need of augmenting the number of volcanic crater lakes that are monitored by permanent gas instrumentation.

It is also interesting to note that the rapid and abrupt transition between pre-explosive and explosive gas at Rincón de la Vieja (Fig. 6.4a and 6.6a), pointing to reduced surface S outgassing prior to each blast, is in stark contrast with what recurrently reported at Poás, where precursory trends toward more magmatic (more S-rich) gas composition are observed instead (*de Moor e al., 2016a*). We argue this difference may imply an overall lower magmatic gas input, or a more effective seal (or both), at Rincón de la Vieja, compared to the more active Poás volcano (where the magmatic system appears more implicated as eruption trigger). This comparison suggests that distinct trigger mechanisms, with different relative roles played by hydrothermal sealing vs. magmatic as influx, may in fact be operating at active crater lakes. This diversity in potential trigger mechanisms (*Stix and de Moor, 2018*) reinforces the need for more robust (and temporally continuous) gas records at volcanic crater lakes.

6.5.5 Conclusion

This study investigates degassing dynamics of Rincón de la Vieja during a period of intense phreatic activity. For the first time at any volcano, the composition of the gas released during discrete phreatic events (confirmed seismically) was resolved using Multi-GAS. Our results demonstrate chemically distinct gas compositions during quiescent degassing versus explosive eruptive degassing. The *quiescent* gas is characterized by very low concentrations of sulfur gas species (SO_2 and H_2S < 2 ppmv) and relatively high H_2S/SO_2 ratios (mean 0.57), whereas the *syn-explosive* gas shows much higher gas mixing ratios of SO_2 and CO_2 and a systematic decrease of H_2S/SO_2 ratio (mean, 0.04). Both the *quiescent* and *syn-explosive* gases exhibit high CO_2/S ratios relative to regional magmatic gases, but each *explosive gas* has lower CO_2/S ratio than its corresponding *pre-explosive gas*. These C-rich gases, if interpreted as magmatic, would require a very deep (P > 250 MPa) magmatic source, which is unlikely in view of the recent magma involvement in the 2017 Rincón phreatomagmatic eruptions. We thus favour a mechanism in which magmatic gas-water-rock reactions in the sublimnic hydrothermal system lead to deposition of native S and sulfate formation, and thus enrich the gas phase in C relative to SO_2 and H_2S. The presence of abundant native sulfur spherules in the lake is consistent with this scenario, as the presence of S spherules suggests a native sulfur layer at the lake bottom.

We propose that continuous gas fluxing may progressively lead to development of an impermeable seal near the lake/hydrothermal system interface. Gas accumulates underneath the seal, and ultimately ruptures this seal resulting in phreatic eruptions. The trend of decreasing *quiescent* CO_2/SO_2 and H_2S/SO_2 ratios from February to May 2017 can be interpreted as an increase in the magmatic gas supply, providing a precursor to the major eruption of 23 May.

These results, the first volcano reports for the gas phase released by discrete phreatic eruptions, confirm (Christenson and Tassi, 2015) that the complex interplay between rising magmatic gases and the sublimnic hydrothermal system likely plays a decisive role in triggering the explosions.

6.7 Acknowledgements

We wish to thank Franco Tassi, Orlando Vaselli, Giulio Bini and ICE staff for help during Multi-GAS installation. We gratefully acknowledge OVSICORI for logistical support. We also thank Bill Evans (USGS), Ryunosuke Kazahaya, the second anonymous reviewer and Jacob Lowenstern, whose thoughtful comments improved the quality of this work. MdM gratefully acknowledges support through the Deep Carbon Observatory's Biology Meets Subduction project. Any use of trade, firm, or product names is for descriptive purposes only and does not imply endorsement by the U.S. Government.

6.8 Tables

Table 6.1 Time (in GMT), duration (in seconds) and associated energy (in Joule) of the phreatic-phreatomagmatic eruptions occurring during February-May 2017. Nine of these eruptions were also recorded by the Multi-GAS (the "Multi-GAS peak Time" identifies the temporal window of Multi-GAS over which the syn-explosive gas was detected). The nine eruptions are numbered as in Figure 6.3.

Date	Time eruption (GMT)	Duration (s)	Seismic energy (J)	Multi-GAS peak Time (GMT)	##eruption number
05/02/2017	7:47:50	42	18.42		
07/02/2017	12:53:06	52	56.03		
07/02/2017	18:19:29	72	28.67		
08/02/2017	22:44:32	61	48.58		
09/02/2017	17:49:41	51	7.74		
13/02/2017	2:59:04	16	9.16		
13/02/2017	9:16:49	138	9.69	9:12:06 - 9:16:35	1
14/02/2017	17:47:42	62	5.96		
16/02/2017	7:12:50	112	42.73		
16/02/2017	13:27:24	173	20.07		
19/02/2017	1:56:00	88	12.86		

19/02/2017	5:49:24	198	7.38		
20/02/2017	15:22:06	106	17.43	15:23:04	2
23/02/2017	3:34:16	94	7.80	03:34:50	3
25/02/2017	12:56:36	106	8.42		
26/02/2017	5:30:48	175	16.94		
27/02/2017	n/a	n/a	n/a	03:16:20	4
02/03/2017	21:24:35	n/a	n/a	21:25:56 – 21:26:50	5
11/03/2017	22:49:17	342	18.88		
14/03/2017	20:53:19	155	8.69		
18/03/2017	23:34:14	272	50.12		
20/03/2017	n/a	n/a	n/a	06:16:00	6
20/03/2017	19:03:50	227	73.83		
26/03/2017	10:11:07	174	18.73		
26/03/2017	10:28:39	115	54.56		
26/03/2017	10:55:42	88	52.67		
26/03/2017	15:49:39	124	80.15		
27/03/2017	10:15:39	70	26.25		
29/03/2017	9:31:17	253	23.58		
31/03/2017	12:46:49	n/a	40.95		
31/03/2017	14:10:50	n/a	38.31		
04/04/2017	14:48:20	122	24.00		
04/04/2017	15:03:49	90	128.66		
06/04/2017	7:48:06	606	103.30		
12/04/2017	17:46:18	175	48.14	17:53:00	7
19/04/2017	0:38:16	200	234.62		
19/04/2017	1:49:19	195	89.22		
20/04/2017	00:02:00	n/a	n/a	00:05:00	8
23/04/2017	5:12:41	111	9.74		
25/04/2017	6:18:40	114	11.47	06:21:00	9
28/04/2017	1:26:16	381	46.28		
09/05/2017	14:59:47	312	24.02		

Table 2 - *Multi-GAS-derived (molar) CO_2/SO_2 and H_2S/SO_2 ratios in the Rincón de la Vieja crater lake plume. The R^2 values (≥0.6 in all cases) identify the regression coefficients in the CO_2 vs. SO_2 and H_2S vs. SO_2 scatter plots that concurred to determine each ratio. SO_2 max identifies the peak SO_2 concentration within each measurement interval. All data refer to quiescent gas except for those associated with an eruption number (which correspond to the syn-explosive gas). The quiescent gas measured prior to each explosion is referred as pre-explosive gas (PRE-EXPL in the table). The quoted compositions for the pre-explosive gas are 20-minute averages of point-to-point ratios, e.g. calculated by taking the ratios of individual co-acquired gas concentration couples. Based on laboratory tests, we estimate error in these point-to-point ratios at ~50%, so the quoted values should only be viewed as semi-quantitative estimates. Only in 2 cases (out of 9 explosions), gas mixing rates were correlated to significant levels (R^2 > 0.6) to allow ratios to be derived with the correlation plot methodology also (see Figs 4a and 6a). The scatter plot-derived gas ratios are listed in parenthesis for comparison in the table.*

Time	*Ratio*	*Ratio value*	*R^2*	*Ratio*	*Ratio value*	*R^2*	*SO_2max (ppmv)*	*##eruption numb*
04/02/2017 09:05	*CO_2/SO_2*	*100*	*0.65*	*H_2S/SO_2*	*0.54*	*0.62*	*0.68*	
05/02/2017 03:05	*CO_2/SO_2*	*115*	*0.68*	*H_2S/SO_2*	*0.69*	*0.65*	*0.70*	
05/02/2017 09:05	*CO_2/SO_2*	*109*	*0.67*	*H_2S/SO_2*	*1.07*	*0.60*	*0.69*	
06/02/2017 03:05	*CO_2/SO_2*	*102*	*0.65*	*H_2S/SO_2*	*0.75*	*0.70*	*0.67*	
06/02/2017 21:05	*CO_2/SO_2*	*137*	*0.70*	*H_2S/SO_2*	*0.83*	*0.68*	*0.67*	
10/02/2017 21:05	*CO_2/SO_2*	*193*	*0.64*	*H_2S/SO_2*	*0.91*	*0.63*	*0.63*	
13/02/2017 09:08	*CO_2/SO_2*	*502*		*H_2S/SO_2*	*1.03*	*0.94*	*0.66*	***PRE-EXPL***
13/02/2017 09:12	*CO_2/SO_2*	*131*	*0.78*	*H_2S/SO_2*	*0.0003*	*0.84*	*18.17*	***1***
13/02/2017 15:05	*CO_2/SO_2*	*99*	*0.70*	*H_2S/SO_2*	*0.61*	*0.75*	*0.86*	
14/02/2017 09:05	*CO_2/SO_2*	*51*	*0.70*	*H_2S/SO_2*	*0.82*	*0.70*	*0.97*	
14/02/2017 15:05	*CO_2/SO_2*	*320*	*0.65*	*H_2S/SO_2*	*0.94*	*0.68*	*0.59*	
15/02/2017 03:05	*CO_2/SO_2*	*90*	*0.64*	*H_2S/SO_2*	*0.65*	*0.60*	*0.58*	
17/02/2017 03:05	*CO_2/SO_2*	*198*	*0.60*	*H_2S/SO_2*	*0.74*	*0.64*	*0.47*	
17/02/2017 15:05	*CO_2/SO_2*	*118*	*0.62*	*H_2S/SO_2*	*0.37*	*0.70*	*1.08*	
17/02/2017 21:05	*CO_2/SO_2*	*38*	*0.65*	*H_2S/SO_2*	*0.43*	*0.65*	*3.71*	
18/02/2017 15:05	*CO_2/SO_2*	*144*	*0.60*	*H_2S/SO_2*	*0.52*	*0.60*	*1.52*	
18/02/2017 21:05	*CO_2/SO_2*	*59*	*0.65*	*H_2S/SO_2*	*0.49*	*0.62*	*2.34*	
19/02/2017 21:05	*CO_2/SO_2*	*41*	*0.65*	*H_2S/SO_2*	*0.41*	*0.67*	*3.16*	
20/02/2017 03:05	*CO_2/SO_2*	*101*	*0.68*	*H_2S/SO_2*	*0.46*	*0.63*	*0.87*	
20/02/2017 15:17	*CO_2/SO_2*	*567*		*H_2S/SO_2*	*0.40*	*0.79*	*1.08*	***PRE-EXPL***
20/02/2017 15:23	*CO_2/SO_2*	*99*	*0.82*	*H_2S/SO_2*	*0.08*	*0.93*	*28.38*	***2***
20/02/2017 21:05	*CO_2/SO_2*	*33*	*0.65*	*H_2S/SO_2*	*0.45*	*0.92*	*2.98*	
21/02/2017 15:05	*CO_2/SO_2*	*84*	*0.63*	*H_2S/SO_2*	*0.70*	*0.94*	*1.60*	
21/02/2017 21:05	*CO_2/SO_2*	*59*	*0.81*	*H_2S/SO_2*	*0.44*	*0.83*	*1.06*	
22/02/2017 03:05	*CO_2/SO_2*	*232*	*0.75*	*H_2S/SO_2*	*0.86*	*0.97*	*0.49*	
22/02/2017 15:05	*CO_2/SO_2*	*101*	*0.80*	*H_2S/SO_2*	*0.74*	*0.84*	*1.02*	
22/02/2017 21:05	*CO_2/SO_2*	*246*	*0.75*	*H_2S/SO_2*	*0.22*	*0.90*	*2.19*	
23/02/2017 03:12	*CO_2/SO_2*	*1296*		*H_2S/SO_2*	*1.30*	*0.60*	*0.40*	***PRE-EXPL***
23/02/2017 03:34	*CO_2/SO_2*	*38*	*0.68*	*H_2S/SO_2*	*0.0003*	*0.86*	*52.61*	***3***
23/02/2017 15:05	*CO_2/SO_2*	*113*	*0.62*	*H_2S/SO_2*	*1.06*	*0.75*	*1.14*	
23/02/2017 21:05	*CO_2/SO_2*	*118*	*0.65*	*H_2S/SO_2*	*0.90*	*0.86*	*1.00*	
24/02/2017 15:05	*CO_2/SO_2*	*167*	*0.74*	*H_2S/SO_2*	*1.17*	*0.84*	*0.96*	
24/02/2017 21:05	*CO_2/SO_2*	*95*	*0.69*	*H_2S/SO_2*	*0.36*	*0.90*	*1.99*	
25/02/2017 15:05	*CO_2/SO_2*	*286*	*0.65*	*H_2S/SO_2*	*1.54*	*0.80*	*0.59*	
26/02/2017 03:05	*CO_2/SO_2*	*62*	*0.70*	*H_2S/SO_2*	*0.54*	*0.83*	*1.08*	
27/02/2017 03:11	*CO_2/SO_2*	*730*		*H_2S/SO_2*	*0.90*	*0.89*	*0.75*	***PRE-EXPL***
27/02/2017 03:16	*CO_2/SO_2*	*231*	*0.97*	*H_2S/SO_2*	*0.010*	*0.89*	*15.70*	***4***
28/02/2017 21:05	*CO_2/SO_2*	*204*	*0.98*	*H_2S/SO_2*	*0.64*	*0.83*	*0.97*	
02/03/2017 15:05	*CO_2/SO_2*	*105*	*0.70*	*H_2S/SO_2*	*0.91*	*0.78*	*0.79*	
02/03/2017 21:16	*CO_2/SO_2*	*640 (628)*	*0.60*	*H_2S/SO_2*	*1.1 (0.9)*	*0.82*	*0.85*	***PRE-EXPL***
02/03/2017 21:25	*CO_2/SO_2*	*140*	*0.97*	*H_2S/SO_2*	*0.18*	*0.98*	*17.14*	***5***
03/03/2017 21:05	*CO_2/SO_2*	*216*	*0.68*	*H_2S/SO_2*	*0.85*	*0.80*	*0.70*	
11/03/2017 03:05	*CO_2/SO_2*	*86*	*0.85*	*H_2S/SO_2*	*0.92*	*0.89*	*0.74*	

12/03/2017 21:05	*CO_2/SO_2*	*118*	*0.82*	*H_2S/SO_2*	*0.63*	*0.85*	*0.95*	
14/03/2017 21:05	*CO_2/SO_2*	*62*	*0.70*	*H_2S/SO_2*	*0.90*	*0.84*	*0.91*	
15/03/2017 03:05	*CO_2/SO_2*	*217*	*0.75*	*H_2S/SO_2*	*0.97*	*0.86*	*0.70*	
17/03/2017 17:58	*CO_2/SO_2*	*67*	*0.66*	*H_2S/SO_2*	*0.56*	*0.66*	*0.60*	
17/03/2017 23:57	*CO_2/SO_2*	*38*	*0.63*	*H_2S/SO_2*	*0.97*	*0.74*	*0.44*	
18/03/2017 00:20	*CO_2/SO_2*	*270*	*0.70*	*H_2S/SO_2*	*0.53*	*0.60*	*0.45*	
18/03/2017 11:59	*CO_2/SO_2*	*170*	*0.65*	*H_2S/SO_2*	*0.86*	*0.63*	*0.45*	
18/03/2017 12:02	*CO_2/SO_2*	*106*	*0.62*	*H_2S/SO_2*	*0.88*	*0.75*	*0.45*	
18/03/2017 12:21	*CO_2/SO_2*	*50*	*0.62*	*H_2S/SO_2*	*0.75*	*0.63*	*0.53*	
18/03/2017 17:55	*CO_2/SO_2*	*82*	*0.61*	*H_2S/SO_2*	*0.74*	*0.61*	*0.54*	
18/03/2017 23:59	*CO_2/SO_2*	*98*	*0.64*	*H_2S/SO_2*	*0.62*	*0.62*	*0.73*	
19/03/2017 00:03	*CO_2/SO_2*	*86*	*0.52*	*H_2S/SO_2*	*1.05*	*0.77*	*0.63*	
19/03/2017 05:58	*CO_2/SO_2*	*93*	*0.69*	*H_2S/SO_2*	*0.51*	*0.76*	*0.45*	
19/03/2017 06:16	*CO_2/SO_2*	*167*	*0.62*	*H_2S/SO_2*	*0.43*	*0.62*	*0.53*	
19/03/2017 06:19	*CO_2/SO_2*	*115*	*0.61*	*H_2S/SO_2*	*0.78*	*0.73*	*0.64*	
19/03/2017 12:07	*CO_2/SO_2*	*103*	*0.67*	*H_2S/SO_2*	*0.56*	*0.63*	*0.64*	
19/03/2017 12:14	*CO_2/SO_2*	*39*	*0.61*	*H_2S/SO_2*	*0.66*	*0.89*	*0.73*	
19/03/2017 00:27	*CO_2/SO_2*	*116*	*0.68*	*H_2S/SO_2*	*0.66*	*0.60*	*0.50*	
19/03/2017 12:19	*CO_2/SO_2*	*83*	*0.60*	*H_2S/SO_2*	*0.78*	*0.72*	*0.50*	
19/03/2017 18:14	*CO_2/SO_2*	*37*	*0.63*	*H_2S/SO_2*	*0.66*	*0.94*	*0.80*	
20/03/2017 06:13	*CO_2/SO_2*	*1265*	*0.98*	*H_2S/SO_2*	*0.81*	*0.60*	*0.44*	***PRE-EXPL***
20/03/2017 06:16	*CO_2/SO_2*	*70*	*0.98*	*H_2S/SO_2*	*0.004*	*0.99*	*32.80*	***6***
21/03/2017 18:14	*CO_2/SO_2*	*29*	*0.77*	*H_2S/SO_2*	*0.86*	*0.90*	*0.90*	
23/03/2017 00:17	*CO_2/SO_2*	*30*	*0.68*	*H_2S/SO_2*	*0.63*	*0.70*	*0.70*	
24/03/2017 12:19	*CO_2/SO_2*	*69*	*0.61*	*H_2S/SO_2*	*0.50*	*0.75*	*0.70*	
26/03/2017 00:25	*CO_2/SO_2*	*18*	*0.74*	*H_2S/SO_2*	*0.50*	*0.69*	*0.90*	
26/03/2017 00:27	*CO_2/SO_2*	*10*	*0.68*	*H_2S/SO_2*	*0.57*	*0.94*	*1.00*	
27/03/2017 00:17	*CO_2/SO_2*	*11*	*0.64*	*H_2S/SO_2*	*0.56*	*0.93*	*1.01*	
27/03/2017 12:19	*CO_2/SO_2*	*12*	*0.61*	*H_2S/SO_2*	*0.46*	*0.83*	*0.85*	
28/03/2017 06:17	*CO_2/SO_2*	*32*	*0.79*	*H_2S/SO_2*	*0.20*	*0.74*	*0.80*	
28/03/2017 18:25	*CO_2/SO_2*	*32*	*0.61*	*H_2S/SO_2*	*0.43*	*0.79*	*1.00*	
29/03/2017 00:10	*CO_2/SO_2*	*43*	*0.61*	*H_2S/SO_2*	*0.46*	*0.97*	*0.50*	
29/03/2017 00:26	*CO_2/SO_2*	*10*	*0.69*	*H_2S/SO_2*	*0.51*	*0.96*	*1.40*	
30/03/2017 18:09	*CO_2/SO_2*	*15*	*0.62*	*H_2S/SO_2*	*0.61*	*0.76*	*1.02*	
30/03/2017 18:24	*CO_2/SO_2*	*44*	*0.65*	*H_2S/SO_2*	*0.71*	*0.79*	*0.50*	
31/03/2017 00:12	*CO_2/SO_2*	*17*	*0.64*	*H_2S/SO_2*	*0.57*	*0.85*	*0.61*	
31/03/2017 00:29	*CO_2/SO_2*	*32*	*0.71*	*H_2S/SO_2*	*0.57*	*0.92*	*1.10*	
31/03/2017 06:24	*CO_2/SO_2*	*32*	*0.75*	*H_2S/SO_2*	*0.89*	*0.74*	*0.77*	
31/03/2017 18:06	*CO_2/SO_2*	*79*	*0.68*	*H_2S/SO_2*	*0.61*	*0.96*	*0.30*	
31/03/2017 18:14	*CO_2/SO_2*	*10*	*0.71*	*H_2S/SO_2*	*0.70*	*0.92*	*1.40*	
31/03/2017 18:26	*CO_2/SO_2*	*46*	*0.75*	*H_2S/SO_2*	*0.55*	*0.67*	*0.85*	
31/03/2017 23:53	*CO_2/SO_2*	*24*	*0.62*	*H_2S/SO_2*	*0.42*	*0.79*	*1.02*	
09/04/2017 12:24	*CO_2/SO_2*	*18*	*0.77*	*H_2S/SO_2*	*0.46*	*0.77*	*1.00*	
09/04/2017 18:12	*CO_2/SO_2*	*24*	*0.62*	*H_2S/SO_2*	*0.58*	*0.92*	*0.70*	
10/04/2017 00:08	*CO_2/SO_2*	*48*	*0.82*	*H_2S/SO_2*	*0.51*	*0.75*	*0.50*	
11/04/2017 00:02	*CO_2/SO_2*	*19*	*0.62*	*H_2S/SO_2*	*0.59*	*0.92*	*0.80*	
11/04/2017 12:21	*CO_2/SO_2*	*16*	*0.75*	*H_2S/SO_2*	*0.52*	*0.86*	*0.90*	
11/04/2017 18:10	*CO_2/SO_2*	*16*	*0.69*	*H_2S/SO_2*	*0.68*	*0.99*	*0.70*	
11/04/2017 18:13	*CO_2/SO_2*	*8*	*0.64*	*H_2S/SO_2*	*0.39*	*0.75*	*1.00*	
11/04/2017 18:15	*CO_2/SO_2*	*23*	*0.80*	*H_2S/SO_2*	*0.60*	*0.92*	*0.92*	
11/04/2017 18:23	*CO_2/SO_2*	*15*	*0.89*	*H_2S/SO_2*	*0.62*	*0.83*	*0.93*	***PRE-EXPL***
12/04/2017 17:53	*CO_2/SO_2*	*85*	*0.91*	*H_2S/SO_2*	*0.03*	*0.92*	*12.34*	***7***
12/04/2017 18:15	*CO_2/SO_2*	*20*	*0.70*	*H_2S/SO_2*	*0.46*	*0.88*	*0.93*	
13/04/2017 00:20	*CO_2/SO_2*	*20*	*0.80*	*H_2S/SO_2*	*0.49*	*0.91*	*0.90*	
13/04/2017 06:18	*CO_2/SO_2*	*28*	*0.61*	*H_2S/SO_2*	*0.45*	*0.73*	*1.10*	
13/04/2017 06:25	*CO_2/SO_2*	*33*	*0.63*	*H_2S/SO_2*	*0.46*	*0.48*	*0.80*	
13/04/2017 12:16	*CO_2/SO_2*	*52*	*0.67*	*H_2S/SO_2*	*0.60*	*0.94*	*0.70*	
13/04/2017 18:01	*CO_2/SO_2*	*35*	*0.67*	*H_2S/SO_2*	*0.54*	*0.86*	*0.68*	
14/04/2017 00:09	*CO_2/SO_2*	*14*	*0.69*	*H_2S/SO_2*	*0.03*	*0.79*	*0.80*	
14/04/2017 00:11	*CO_2/SO_2*	*26*	*0.66*	*H_2S/SO_2*	*0.39*	*0.88*	*0.80*	
14/04/2017 00:19	*CO_2/SO_2*	*124*	*0.94*	*H_2S/SO_2*	*0.63*	*0.91*	*0.91*	
18/04/2017 00:19	*CO_2/SO_2*	*32*	*0.60*	*H_2S/SO_2*	*0.52*	*0.86*	*0.76*	
18/04/2017 12:27	*CO_2/SO_2*	*21*	*0.60*	*H_2S/SO_2*	*0.59*	*0.78*	*0.90*	
18/04/2017 18:06	*CO_2/SO_2*	*21*	*0.61*	*H_2S/SO_2*	*0.57*	*0.95*	*0.70*	
18/04/2017 18:11	*CO_2/SO_2*	*17*	*0.60*	*H_2S/SO_2*	*0.69*	*0.72*	*0.90*	
18/04/2017 18:20	*CO_2/SO_2*	*22*	*0.86*	*H_2S/SO_2*	*0.56*	*0.90*	*1.20*	
19/04/2017 00:15	*CO_2/SO_2*	*16*	*0.86*	*H_2S/SO_2*	*0.31*	*0.57*	*1.17*	
19/04/2017 05:58	*CO_2/SO_2*	*19*	*0.67*	*H_2S/SO_2*	*0.60*	*0.82*	*0.93*	
19/04/2017 18:09	*CO_2/SO_2*	*29*	*0.68*	*H_2S/SO_2*	*0.61*	*0.88*	*0.40*	
19/04/2017 18:24	*CO_2/SO_2*	*12*	*0.60*	*H_2S/SO_2*	*1.06*	*0.90*	*0.36*	
20/04/2017 00:01	*CO_2/SO_2*	*118*	*0.76*	*H_2S/SO_2*	*0.53*	*0.88*	*0.44*	
20/04/2017 00:01	*CO_2/SO_2*	*628*		*H_2S/SO_2*	*0.70*	*0.74*	*0.75*	***PRE-EXPL***
20/04/2017 00:05	*CO_2/SO_2*	*390*	*0.98*	*H_2S/SO_2*	*0.014*	*0.95*	*6.00*	***8***

20/04/2017 06:02	*CO_2/SO_2*	*15*	*0.71*	*H_2S/SO_2*	*0.71*	*0.90*	*0.76*	
20/04/2017 06:19	*CO_2/SO_2*	*71*	*0.71*	*H_2S/SO_2*	*0.74*	*0.87*	*1.00*	
20/04/2017 12:11	*CO_2/SO_2*	*34*	*0.71*	*H_2S/SO_2*	*0.49*	*0.74*	*0.60*	
20/04/2017 23:55	*CO_2/SO_2*	*51*	*0.76*	*H_2S/SO_2*	*0.49*	*0.95*	*0.60*	
23/04/2017 18:02	*CO_2/SO_2*	*34*	*0.75*	*H_2S/SO_2*	*0.58*	*0.98*	*0.40*	
24/04/2017 12:11	*CO_2/SO_2*	*13*	*0.68*	*H_2S/SO_2*	*0.54*	*0.98*	*0.80*	
24/04/2017 12:23	*CO_2/SO_2*	*19*	*0.72*	*H_2S/SO_2*	*0.56*	*0.89*	*1.20*	
24/04/2017 17:58	*CO_2/SO_2*	*19*	*0.81*	*H_2S/SO_2*	*0.53*	*0.89*	*1.20*	
24/04/2017 18:17	*CO_2/SO_2*	*43*	*0.69*	*H_2S/SO_2*	*0.62*	*0.91*	*0.61*	
25/04/2017 00:21	*CO_2/SO_2*	*17*	*0.89*	*H_2S/SO_2*	*0.25*	*0.60*	*1.50*	
25/04/2017 06:01	*CO_2/SO_2*	*53*	*0.65*	*H_2S/SO_2*	*0.12*	*0.74*	*0.85*	
25/04/2017 06:02	*CO_2/SO_2*	*241*	*0.81*	*H_2S/SO_2*	*0.44*	*0.90*	*0.84*	
25/04/2017 06:08	*CO_2/SO_2*	*119*	*0.64*	*H_2S/SO_2*	*0.01*	*0.99*	*1.15*	
25/04/2017 06:15	*CO_2/SO_2*	*638 (489)*	*0.71*	*H_2S/SO_2*	*0.54 (0.38)*	*0.99*	*1.13*	***PRE-EXPL***
25/04/2017 06:21	*CO_2/SO_2*	*55*	*0.77*	*H_2S/SO_2*	*0.004*	*0.99*	*34.42*	***9***
25/04/2017 18:11	*CO_2/SO_2*	*28*	*0.60*	*H_2S/SO_2*	*0.67*	*0.96*	*1.40*	
25/04/2017 18:19	*CO_2/SO_2*	*74*	*0.95*	*H_2S/SO_2*	*0.50*	*0.95*	*7.62*	
26/04/2017 00:10	*CO_2/SO_2*	*19*	*0.77*	*H_2S/SO_2*	*0.55*	*0.96*	*1.01*	
26/04/2017 00:27	*CO_2/SO_2*	*16*	*0.67*	*H_2S/SO_2*	*0.65*	*0.93*	*1.20*	
27/04/2017 00:01	*CO_2/SO_2*	*21*	*0.66*	*H_2S/SO_2*	*0.60*	*0.93*	*0.77*	
27/04/2017 06:07	*CO_2/SO_2*	*49*	*0.94*	*H_2S/SO_2*	*0.47*	*0.77*	*0.30*	
28/04/2017 18:13	*CO_2/SO_2*	*16*	*0.62*	*H_2S/SO_2*	*0.33*	*0.76*	*0.70*	
29/04/2017 00:21	*CO_2/SO_2*	*106*	*0.67*	*H_2S/SO_2*	*0.49*	*0.98*	*0.40*	
29/04/2017 00:08	*CO_2/SO_2*	*38*	*0.63*	*H_2S/SO_2*	*0.52*	*0.89*	*1.20*	
29/04/2017 12:25	*CO_2/SO_2*	*7*	*0.65*	*H_2S/SO_2*	*0.41*	*0.88*	*1.30*	
29/04/2017 18:00	*CO_2/SO_2*	*17*	*0.90*	*H_2S/SO_2*	*0.41*	*0.73*	*1.42*	
29/04/2017 18:20	*CO_2/SO_2*	*35*	*0.62*	*H_2S/SO_2*	*0.48*	*0.89*	*1.34*	
30/04/2017 00:10	*CO_2/SO_2*	*35*	*0.84*	*H_2S/SO_2*	*0.69*	*0.96*	*0.80*	
30/04/2017 18:14	*CO_2/SO_2*	*45*	*0.70*	*H_2S/SO_2*	*0.57*	*0.81*	*1.20*	
30/04/2017 18:00	*CO_2/SO_2*	*27*	*0.65*	*H_2S/SO_2*	*0.43*	*0.82*	*1.18*	
30/04/2017 18:19	*CO_2/SO_2*	*39*	*0.63*	*H_2S/SO_2*	*0.50*	*0.92*	*1.20*	
01/05/2017 12:06	*CO_2/SO_2*	*54*	*0.68*	*H_2S/SO_2*	*0.16*	*0.38*	*1.20*	
01/05/2017 17:55	*CO_2/SO_2*	*40*	*0.70*	*H_2S/SO_2*	*0.52*	*0.92*	*1.26*	
01/05/2017 18:10	*CO_2/SO_2*	*51*	*0.90*	*H_2S/SO_2*	*0.55*	*0.97*	*1.08*	
02/05/2017 00:04	*CO_2/SO_2*	*10*	*0.75*	*H_2S/SO_2*	*0.50*	*0.99*	*1.20*	
02/05/2017 00:09	*CO_2/SO_2*	*16*	*0.77*	*H_2S/SO_2*	*0.55*	*0.99*	*0.91*	
02/05/2017 00:21	*CO_2/SO_2*	*27*	*0.82*	*H_2S/SO_2*	*0.58*	*0.92*	*1.25*	
02/05/2017 12:10	*CO_2/SO_2*	*35*	*0.74*	*H_2S/SO_2*	*0.43*	*0.88*	*1.01*	
02/05/2017 12:25	*CO_2/SO_2*	*63*	*0.81*	*H_2S/SO_2*	*0.42*	*0.95*	*1.10*	
02/05/2017 18:14	*CO_2/SO_2*	*56*	*0.84*	*H_2S/SO_2*	*0.29*	*0.78*	*1.00*	
03/05/2017 00:05	*CO_2/SO_2*	*56*	*0.82*	*H_2S/SO_2*	*0.33*	*0.92*	*0.80*	
03/05/2017 00:13	*CO_2/SO_2*	*54*	*0.84*	*H_2S/SO_2*	*0.50*	*0.88*	*0.92*	
03/05/2017 00:22	*CO_2/SO_2*	*34*	*0.82*	*H_2S/SO_2*	*0.44*	*0.96*	*1.09*	
03/05/2017 06:01	*CO_2/SO_2*	*50*	*0.67*	*H_2S/SO_2*	*0.37*	*0.86*	*0.80*	
03/05/2017 06:05	*CO_2/SO_2*	*60*	*0.64*	*H_2S/SO_2*	*0.37*	*0.89*	*0.75*	
03/05/2017 06:10	*CO_2/SO_2*	*56*	*0.70*	*H_2S/SO_2*	*0.43*	*0.82*	*0.68*	
03/05/2017 06:18	*CO_2/SO_2*	*72*	*0.63*	*H_2S/SO_2*	*0.34*	*0.79*	*0.76*	
04/05/2017 00:00	*CO_2/SO_2*	*26*	*0.65*	*H_2S/SO_2*	*0.42*	*0.86*	*0.70*	
04/05/2017 00:15	*CO_2/SO_2*	*37*	*0.82*	*H_2S/SO_2*	*0.64*	*0.93*	*0.77*	
04/05/2017 06:09	*CO_2/SO_2*	*22*	*0.67*	*H_2S/SO_2*	*0.42*	*0.93*	*1.00*	
04/05/2017 06:17	*CO_2/SO_2*	*38*	*0.63*	*H_2S/SO_2*	*0.53*	*0.91*	*0.76*	
04/05/2017 18:21	*CO_2/SO_2*	*38*	*0.87*	*H_2S/SO_2*	*0.52*	*0.91*	*1.10*	
04/05/2017 17:57	*CO_2/SO_2*	*19*	*0.63*	*H_2S/SO_2*	*0.46*	*0.88*	*1.25*	
05/05/2017 00:04	*CO_2/SO_2*	*14*	*0.60*	*H_2S/SO_2*	*0.62*	*0.89*	*0.50*	
05/05/2017 12:02	*CO_2/SO_2*	*3*	*0.74*	*H_2S/SO_2*	*0.56*	*0.97*	*1.20*	
05/05/2017 18:26	*CO_2/SO_2*	*4*	*0.90*	*H_2S/SO_2*	*0.52*	*0.98*	*1.20*	
08/05/2017 00:15	*CO_2/SO_2*	*6*	*0.80*	*H_2S/SO_2*	*0.64*	*0.97*	*1.41*	
08/05/2017 00:22	*CO_2/SO_2*	*17*	*0.76*	*H_2S/SO_2*	*0.27*	*0.52*	*1.01*	
08/05/2017 12:07	*CO_2/SO_2*	*68*	*0.61*	*H_2S/SO_2*	*0.35*	*0.83*	*0.80*	
08/05/2017 12:27	*CO_2/SO_2*	*116*	*0.62*	*H_2S/SO_2*	*0.35*	*0.71*	*0.76*	
08/05/2017 18:18	*CO_2/SO_2*	*38*	*0.77*	*H_2S/SO_2*	*0.49*	*0.92*	*1.26*	
08/05/2017 17:57	*CO_2/SO_2*	*127*	*0.69*	*H_2S/SO_2*	*0.54*	*0.92*	*0.69*	
09/05/2017 00:23	*CO_2/SO_2*	*67*	*0.65*	*H_2S/SO_2*	*0.41*	*0.81*	*1.20*	
09/05/2017 06:05	*CO_2/SO_2*	*86*	*0.60*	*H_2S/SO_2*	*0.44*	*0.67*	*0.40*	

Chapter 7

7 Along arc variation

CAVA extends from Guatemala to Costa Rica and comprises 40 major Quaternary-age volcanic centres because of subduction of Cocos plate under Carribean plate (*Carr et al., 1982*). Several studies (*Stoiber and Carr 1973; Carr 1984; Burkart and Self 1985; Case et al., 1990; Protti et al., 1995; DeMets, 2001; Shaw et al., 2003; Syracuse and Abers 2006; Mackenzie et al., 2008; LaFemina et al., 2009*) identified many geophysical difference along CAVA arc. Phisical variations, as the convergence rate, dip of Wadati-Benioff zone and crustal thickness, influence the thermal regime and both control the generation of the magmas (*Davies and Stevenson 1992*). In North-Western segment, with a pronounced slab dip, the crust is older and colder than Costa Rica (with shallow slab dip and younger and consequently warmer regime). Slab dip variations control the availability of fluids. General consensus is that slab-derived fluids play the most significant role in the generation of Nicaraguan magma while it decreases in El Salvador and Guatemala and Costa Rica. Here, shallow dip and metamorphic reactions favour fluids loss from the slab while Nicaraguan slab would not dehydrate until greater depths and fluid reaches the magma generation zone and consequently trigger melting (*Shaw et al., 2003*; *Zimmer et al.,2004*).

In the past years, researchers used different approach in order to investigate geochemical variations in Central American lavas and gases. Major and trace elements and isotopes are used as geochemical tracers in order to discriminate the contribution of slab, crust, and mantle wedge.

Isotope N studies in geothermal fluids indicate lower slab fluid contributions in Costa Rica than Guatemala and Nicaragua (*Fischer et al., 2002*). Chlorine isotope variations demonstrated mantle-like Cl signatures in the northernmost (Guatemala and El Salvador) and southernmost (Costa Rica) ends of the front, and sediment and/or serpentinite-derived signature in Nicaragua (*Barnes et al*., (2009). Similar results come from He and C isotopes (*Shaw et al., 2003; Leeuw et al., 2007; Di Piazza et al., 2015; Robidoux et al., 2017; Battaglia et al., 2018*). A great contribution of C-rich sediments is present beneath Nicaragua, and a minimal slab contribution in the volcanic output in Costa Rica. Large geochemical variations also exist in Central American lavas (*Carr et al., 1990; Morris et al., 1990*, *Leeman et al.,* 1994). Ba/La, B/La, $^{10}Be/^{9}Be$ ratios are highest in Nicaragua and decrease to the northwest and southeast. More advances come from [Deep sea Drilling Program (DSDP)] and Ocean Drilling Program (ODP). Analysis of sampled sediments on the subducting Cocos Plate adjacent to the Middle American Trench showed the presence of carbonate (~200 m) and hemipelagic rocks (~200 m with high organic matter) in the sedimentary sequence (*Patino et al., 2000*). The

stratigraphic units of the Cocos Plate have significantly different geochemical features that allow tracing their input into the magma generation process along the CAVA. Large differences exist in incompatible elements between the two sedimentary units. Carbonate unit exhibit low concentration of most incompatible elements. The hemipelagic section exhibit strong gradient with an increase of Ba, La, Y and Pb with depth and U decrease (*Patino et al., 2000*). Slab flux variation then create the along-arc variation in trace elements ratios as Ba/La and U/Th. On basis of all these observations, very consistent results come from *Aiuppa et al.,* 2014, who explored the along-arc variations in volcanic gas CO_2/S_t ratios in the Costa Rica-Nicaragua arc segment. Combining trace elements ratios and C/S systematic, they showed the correlation between CO_2-rich nature of Nicaraguan volcanoes and high slab flux signal. They highlighted that CO_2-richer composition of Nicaraguan gas is consistent with (i) high CO_2 contents recorded in MIs (*Wade et al., 2006; Benjamin et al., 2007 and Wehrmann et al., 2011*), (ii) the more-positive (e.g., sedimentary) isotopic signatures of N_2 and CO_2 in gas manifestations (*Zimmer et al., 2004; Elkins et al., 2006*), and (iii) high values of trace-element proxies for slab-derived fluids in magmas (e.g., high Ba/La, U/Th, and B contents in volcanic rocks).

Another contribute in order to understand the role of slab and mantle wedge comes from the study of helium isotopes. Noble gases are excellent tracers of both the origin of fluids and magma processes occurring in either the mantle or the crust. Several chemical dataset of fumaroles and geothermal manifestations exist (*Leeuw et al., 2007; Snyder et al., 2003; Snyder et al., 2001; Elkins et al., 2006; Shaw et al., 2003; Poreda and Craig, 1989; Oppenheimer et al., 2014 and references therein*). These studies have shown that the helium throughout the region is predominantly of mantle origin. Lower ratios produced by radiogenic helium (^{4}He from U and Th decay) are restricted to the region behind the volcanic front as in Berlin geothermal field where the lower ratios are possibly related to a crustal thickening of ~10 km (Case and MacDonald, 1990). While these studies covered most of CAVA segments, more authors (*Battaglia et al., 2018, this work; Fisher et al., 2010; Shaw et al., 2006; Fisher et al., 2005; Di Piazza et al. 2015; Poreda and Craig, 1989; Robidoux et al, 2017*) investigated the helium isotopes in the fluid inclusions (FI) in olivine and pyroxene crystals from tephra and lavas. These minerals can trap mantle volatiles as fluid or melt inclusions during crystallization within a magma chamber. In the majority of CAVA volcanoes studied so far (*Fischer et al.* 2005*; Shaw et al.* 2006*; Di Piazza et al.* 2015*; Robidoux et al.* 2017), the ^{3}He/^{4}He ratios in olivine-hosted fluid inclusions are typically higher than in (or at the upper range of) volcanic gases from the same volcanic system. FIs should thus be prioritized as more reliable indicators of the magmatic/mantle signature, where available. Unfortunately,

data of helium ratios from FI are missing for the northwest part of CAVA (e.g. Guatemala and El Salvador). During my PhD, I worked in order to improve dataset in this part of the volcanic arc. Part of this work performed at Pacaya volcano in Guatemala was presented in the chapter 5. In this chapter, I present the other part of work carried out in El Salvador. In particular, I collected rocks from Santa Ana, Ilopango and San Miguel volcano in order to investigate the possible variations from north to south El Salvador. Methodology for fluid inclusion and helium isotope analysis are the same of the chapter 4 (also discussed in the method section).

7.1 El Salvador segment

El Salvador is the smallest country of Central America with a surface of just 21040 Km^2 (*Canora et al., 2010*). It is located in the northern part of CAVA that extend along the active Pacific margin from Guatemala to Costa Rica and it is highly seismically active country. At least 11 major earthquakes have caused more than 3000 victims in the past 100 years (*Martínez-Díaz et al., 2004*). Three set of faults exist that strike NW, NE and E. The main active faults constitute the El Salvador Fault Zone (ESFZ, also called Jalpatogua Fault Zone, JFZ), a complex array of dextral strike-slip faults with dominant E-W strike and a right-lateral kinematics. ESFZ, part of major lineaments of Central America and analogous to Nicaragua depression, are delimited from two major strike slip faults (North and South) (*Carr and Stoiberg 1977*) and it are associated with extensional deformation and large volume silicic calderas. Indeed, production of ryolitic body tend to develop in zone with crustal thinning and graben formation (*Burkart and Self 2004*), as well showed also in Guatemala. Active volcanic front in El Salvador are formed in the ESFZ and consists of nine large volcanic centers: Alpaneca, Santa Ana-Izalco, Boqueron, Ilopango, San Vincente, Tecapa, San Miguel, Conchague and Fonseca from North to South. Circular to oval-shaped large Bouguer anomaly exist under Santa Ana, Ilopango, San Vincente and Conchague (*Carr 1981*). Recently, *Saxby et al.*, (2016) confirm the presence of large gravity anomaly under Ilopango probably associated with the upper portions

of an evolved silicic magma reservoir. Lavas from the Volcanic Front in El Salvador are basalt, basaltic andesite and andesites (*Carr 1881*).

Figure 7.1 Principal tectonic lineaments and volcanic centers of El Salvador country. Modified from Saxby et al. 2016.

7.2 Santa Ana volcano

Santa Ana volcano (also known as Ilamatepec volcano) (13°51' 11" N - 89° 37' 48") is the highest volcano in El Salvador (2381 masl) and it forms a part of Central American volcanic chain. It is located in the North part of the country, about 40 km west of San Salvador city at the intersection of a NW-SE system of regional faults (ESFZ). In these tectonic settings, Santa Ana volcano is part of a volcanic complex that comprises Coatepeque collapse caldera (6.5 x 10.5 km), Izalco volcano and numerous cinder cones (*Carr and Pontier 1981; Hernandez et al., 2007*) as Cerro Verde, San Marcelino, Chino, El Astillero and Conejal. The summit area of volcano (radius 1.5 km) is the result of four coalescent craters. The youngest formed after the 1904 eruption (*Carr and Pointer, 1981*) hosts an acid lake with a diameter of about 200 meter. The presence of high temperature fumarole in the western inner portion of the crater indicate the presence of a hydrothermal system located at low depth (*Bernard et al., 2004*). Twelve historical eruptions has been recorded since the years 1500; the last eruption occurred in 1904 (*Mooser et al., 1958*). The activity during the last few thousand years was characterized by phreato-phreatomagmatic activity at the central summit vent (*Pullinger, 1998*). The eruptive products range between olivine basalts and basaltic andesite to andesites typical for a calcalkaline series (*Carr et al., 1981; Carr et al., 1990*). Different lava flows shown more silicic composition: andesite

to dacite and trachy-andesite (*Carr and Pointer, 1981*). The chemical compositions of juvenile clasts from the major eruption of 1904 and 2005 (scoriae and lithics) have andesitic and trachy-andesitic compositions. (*Carr et al., 1981; Pullinger, 1998; Scolamacchia et al., 2005*). During second year of my Phd I collected rocks from the inner wall of crater of Santa Ana volcano. The samples have andesitic composition. I performed analysis in order to investigate helium content and his isotopes in fluid inclusions hosted in olivine crystals.

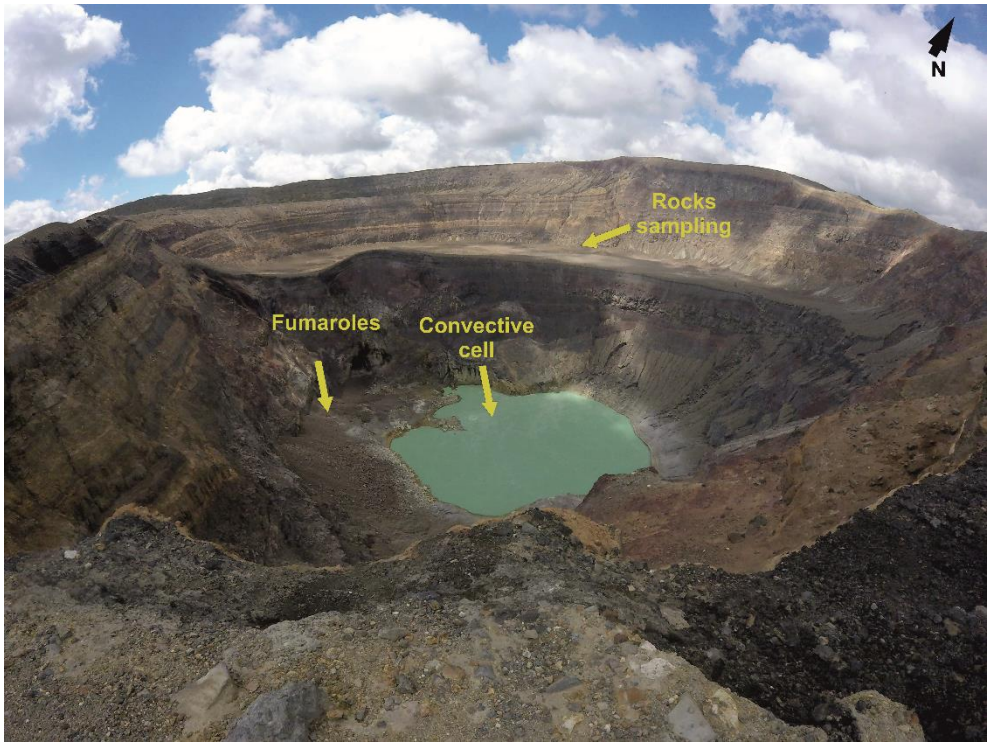

Figure 7.2 Santa Ana active crater. Rocks sampling location are indicated.

7.3 Ilopango volcano

Ilopango caldera (13° 40' 12.00" N - 89° 02' 60.00" W) is located in the Central El Salvador and it is bounded to the E-SE by San Vincente volcano and to the W-NW by San Salvador volcano, both of which with andesitic composition (*Richer et al., 2004*). His formation, as other Centro American large-volume silicic lava, is related with regional faulting and ESFZ structure. The caldera, an elongated depression (8 x 11 km), is partly filled by Ilopango lake, the second largest lake of the country, which has a depth of ~ 300 m (*Saxby et al., 2016*). A big eruption in the A.D. 429 (*Dull 2001*) is responsible for the migration of the Mayan people from El Salvador and produced Terra Blanca Joven (TBJ) tephra, a vast and extensive volcanic deposit. The last vigorous eruption in the 1879–1880 has formed the Isla Quemadas domes at the center of the lake. Ilopango caldera is still considered an important geological hazard due his proximity to San Salvador city that is located less than 10 km from the lake. Furthermore, more than 200,000 inhabitants live in

his drainage basin (*Lopez et al., 2009*). Volcanic products related with caldera range between andesitic to dacitic composition. The Isla Quemadas dome have a dacitic composition (68.4 wt% SiO_2). The dacitic dome have two type of inclusion: salt and peppers inclusions (1-2 % of volume) and dark-gray mafic inclusions (2-3 % of volume and size between <0.1 to 10 cm (*Richer et al., 2004*). These mafic inclusions (basaltic andesite with 53.9 wt% SiO_2) represent an important opportunity in order to characterize the helium signature of mafic source and then to extend measurement of helium isotope ratio in FI in the northern part of CAVA. Investigating the origin of mafic inclusions could allow understanding the magmas mixing processes and extend knowledge about along arc variations. *Richer et al.,* (2004) conducted an important petrographic - mineralogical study and concluded that the mafic intrusion could triggered the eruption because increased the volume of the magma body. Decompression of the dacite during convection induced rapid vesiculation and gas pressure, and/or the crystallization of the mafic magma may itself have liberated volatiles. During my Phd I sampled dacitic rocks from Isla Quemadas dome and I extracted mafic inclusions from dacitic matrix. I found and separated several mafic inclusions (dark-grey in fig.7.3). I perform geochemical study of helium isotopes in fluid inclusions hosted in olivine crystals (from mafic inclusions).

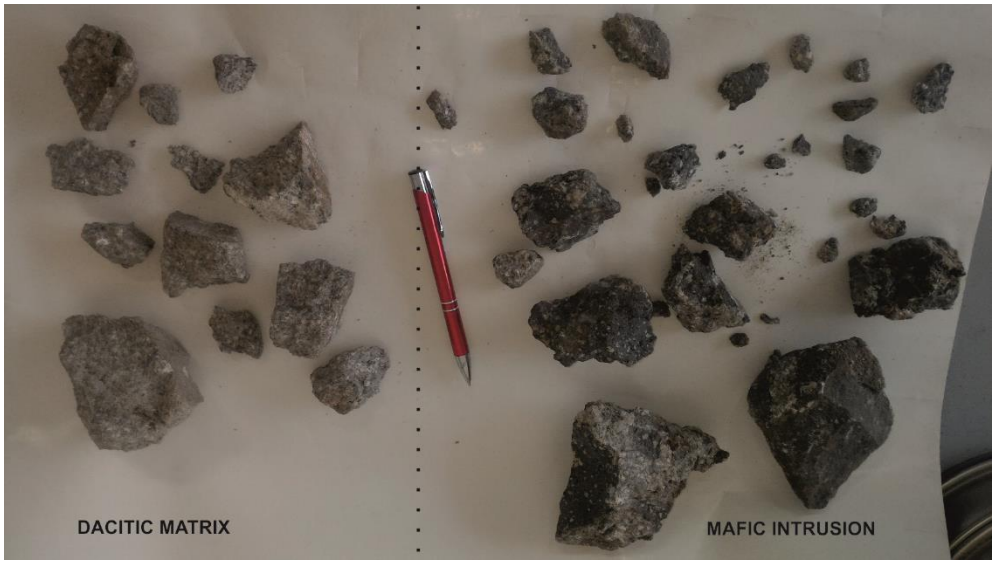

Figure 7.3 Mafic inclusion (dark gray) sepatared from dacitic rocks of Isla Quemadas dome (Ilopango, El Salvador).

7.4 San Miguel volcano

The San Miguel volcano (13.43143 N - 88.271468 W), part of the Central American Volcanic Front, is a symmetrical stratovolcano, which a maximum

altitude of 2130 above sea level. Its summit crater measures 800 m in diameter and 340 m in depth. It is located in the eastern part of El Salvador. Geologically, it belongs to the quaternary period and is mainly made up of basaltic and andesitic rocks but the stratigraphy of the volcano is intercalated with Plinian acid deposits (dacite and rhyodacite) of the close El Pacayal volcano. Tectonically, the volcano is located in the eastern segment of the El Salvador fault zone (ESFZ) and it is crossed by local faults with a predominant NW–SE direction (*Bonforte et al., 2016*). San Miguel volcano, also known as Chaparrastique volcano, is considered one of the most active volcanoes in El Salvador. In the last 1500 years, it produced at least 25 small eruptions. Since 1867, there have been at least 15 explosive eruptions through the central crater (*MARN, 2014*). This volcano show high seismic activity and the surface activity consists of pulsating gas emissions that ascend to maximum heights of ~200 m (*Scarlato et al., 2017*). After 12 years of inactivity, a vigorous eruption occurred on December 29, 2013, during witch more than ~5000 people living in ~3 km radius around the volcano have been evacuated (*Martinez-Hackert et al., 2015*). This vulcanian-type eruption was classified as VEI 2 and produced an ash plume with a maximum height of ~9 km (*Martinez-Hackert et al., 2015*). During second year of my Phd I collected lava and scoriae sample from the inner wall of crater of San Miguel volcano.

7.5 Results

This section presents results from new $^{3}He/^{4}He$ measurements in FI(s) hosted in olivine crystals collected in three El Salvador volcanoes described above. These new data together with those measured on Pacaya volcano are listed in tab. 7.1 and showed in figure 7.3.

Mafic inclusions hosted in dacitic rocks from Isla Quemadas have a basaltic andesite composition with (53.9% of SiO_2, *Richer et al., 2004*). Unfortunately, it was not possible to analyse the bulk rock chemistry from Santa Ana and San Miguel samples. However, petrography and modal observations together with microscopic evaluations of phenocrysts assemblage indicate an evolved composition toward andesite rocks. Frequently, magma mixing and more silicic composition were observed in El Salvador volcanic systems.

Ilopango dome olivine phenocrysts have euhedral to sub-hedral habitus while Santa Ana and San Miguel olivine phenocrysts have an irregular surface with reaction rims that suggest the presence of a possible mixing process, however of a more complex history.

The ^{4}He content in olivine crystals in El Salvador samples ranges between 6.54×10^{-14} and 2.87×10^{-13} mol/g, ^{20}Ne varies from 1.39×10^{-15} to 1.21×10^{-14} mol/g, while ^{40}Ar between 1.57×10^{-12} and 6.70×10^{-12} mol/g. The

$^{4}He/^{20}Ne$ ratio is an indicator of atmospheric contamination and ranges between 16.7 and 318.5, which is higher than the typical atmospheric ratio ($^{4}He/^{20}Ne$ = 0.318) (Fig. 7.3). The $^{40}Ar/^{36}Ar$ varies from 296 to 462.5, which is slightly higher than atmospheric ($^{40}Ar/^{36}Ar$ = 295.5). Both $^{4}He/^{20}Ne$ and $^{40}Ar/^{36}Ar$ ratios are lower than those typical of fluids from the upper mantle ($^{4}He/^{20}Ne$>1000 and $^{40}Ar/^{36}Ar$>40000; *Ozima and Podosek,* (1983)), but fall within the range of subduction-related volcanism worldwide and in CAVA (*Hilton et al.,* 2002*; Fischer et al.,* 2005*; Di Piazza et al.,* 2015*, Rizzo et al.,* 2015*; Robidoux et al.,* 2017). This indicates that gases released from FIs contain an atmospheric-derived component, perhaps related to the recycling of noble gases in the subducting slab. In fact, in Fig. 7.3 data from Guatemala and El Salvador plot along mixing paths between AIR and local magmatic terms.

We calculated the air-corrected ^{40}Ar content assuming that all the measured ^{36}Ar is atmospheric in origin:

$$^{40}Ar^{*}=^{40}Ar_{m}-((^{40}Ar/^{36}Ar)_{air}\times^{36}Ar_{m}) \qquad (7.1)$$

In equation (7.1), $^{40}Ar^{*}$ is the air-corrected ^{40}Ar, and the "m" subscript indicates "measured". The recalculated $^{4}He/^{40}Ar^{*}$ is 8.58, 0.84, 0.62 for IL, SA and SM respectively. SA and SM show values a little below the typical production ratio of the mantle ($^{4}He/^{40}Ar^{*}$=1–5; (*Ozima and Podosek,* 1983*; Marty*, 2012)), while IL have a higher ratio. Considering that He is around 10 times more soluble than Ar in silicate melts, magmatic degassing would lead to an increase of especially in the late stages of degassing (e.g., *Iacono-Marziano et al*., 2010). This could explain the highest ratio of IL. Instead, $^{4}He/^{40}Ar^{*}$ lower than 1-5 could indicate a slight extent of diffusive fractionation of He and Ar from fluid inclusions (e.g., Burnard, 2004). This process could significantly modify the pristine isotope signature.

The $^{3}He/^{4}He$ ratios corrected for atmospheric contamination are 5.73, 7.59 and 5.17 Ra for S. Ana (SA), Ilopango (IL) and San Miguel (SM) respectively (tab.7.1). Ilopango Rc/Ra is within the MORB-like range (R/Ra = 8.0 ± 1; *Graham*, (2002)). As mentioned above, this sample comes from mafic inclusions with basaltic andesite composition and 53.9 wt% SiO_2. This mafic magma mingled with the more shallow dacitic one and was reasonable responsible of the eruption of these rocks (*Richer et al., 2004*). For that reason and considering the $^{4}He/^{40}Ar^{*}$ slightly higher than the typical production ratio of the mantle, we argue that a $^{3}He/^{4}He$ of 7.6 Ra can be considered representative of the local magmatic source at least at the eruption time.

Instead, $^{3}He/^{4}He$ measured in SA and SM fluid inclusions are sensibly lower than expected ratios, suggesting the occurrence of secondary processes that acted in modifying the pristine magmatic signature. A possible process is the

diffusive fractionation of He from fluid inclusions, as supposed above to justify the low $^{4}He/^{40}Ar^{*}$. However, we have no constraints on this hypothesis and we cannot exclude the occurrence of a very shallow crustal contamination. Irrespective of the process that caused the lowering of He isotopic ratio, we argue that these ratios are not representative of SA and SM magmatic sources and will not considered for the following discussion on along-arc variations. In fact, $^{3}He/^{4}He$ measured in local geothermal fluids are higher than those in fluid inclusions. The reported $^{3}He/^{4}He$ ratios in the geothermal gases collected in the 2002 (*Leeuw et. al. 2007*), vary between 7.37 and 7.56 Ra.

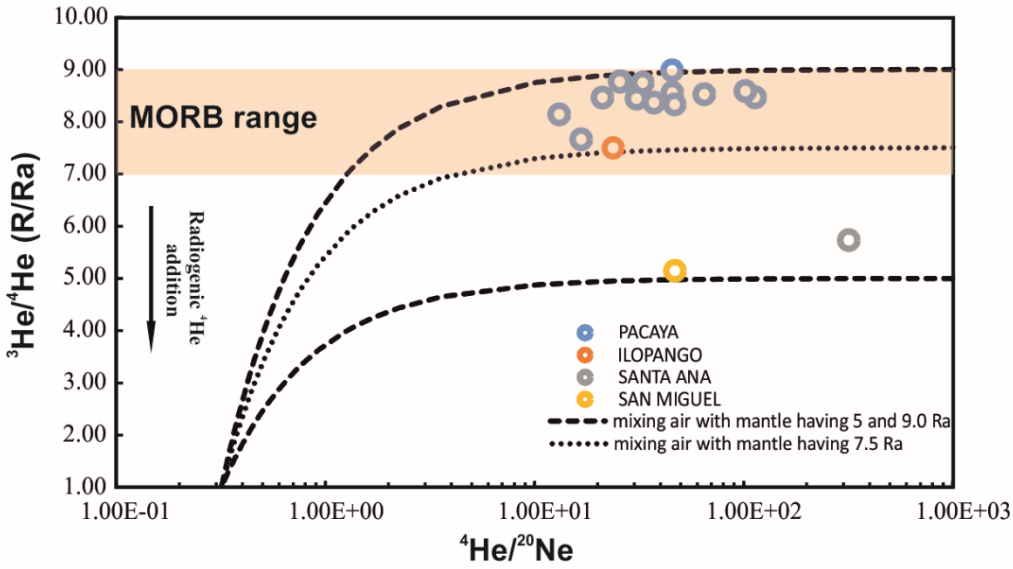

Figura 7.3 $^{3}He/^{4}He$ (expressed as R/Ra) vs. $^{4}He/^{20}Ne$ for Pacaya, Santa Ana, Ilopango and San Miguel olivine-hosted FIs. The black lines reproduce the mixing curves between air and mantle with 5, 7.5 and 9.0 Ra. The MORB range is also indicated.

Table 7.1

Volcano	Sample	Mineral	Weight of loaded minerals (g)	Crystal size fraction (mm)	(^{4}He) (mol/g)	(^{20}Ne) (mol/g)	^{40}Ar (mol/g)	^{36}Ar (mol/g)	^{40}Ar/^{36}Ar	Error on (^{40}Ar/^{36}Ar) (%)	^{38}Ar/^{36}Ar	Error on (^{38}Ar/^{36}Ar) (%)	R/Ra	^{4}He/^{20}Ne	Rc/Ra	Error +/-
Pacaya	P 2010	Ol	0.2313	1	1.37E-13	5.31E-15	2.17E-13	7.29E-16	298.45	0.91	0.218	0.22	8.77	25.82	8.87	0.21
Pacaya	P 1961	Ol	0.19088	1	2.21E-13	4.84E-15	2.72E-12	9.02E-15	302.50	0.14	0.188	0.19	8.55	45.68	8.61	0.18
Pacaya	P 2010	Ol	0.48897	1	1.89E-13	7.42E-15	6.68E-13	2.04E-15	328.49	0.28	0.191	0.19	8.76	25.53	8.87	0.14
Pacaya	P 2010	Ol	0.74272	0.5	1.34E-13	1.18E-15	6.90E-13	2.21E-15	313.65	0.13	0.189	0.19	8.46	113.47	8.48	0.13
Pacaya	P 1975	Ol	0.41451	0.5	2.06E-13	3.18E-15	1.56E-12	5.00E-15	313.39	0.15	0.187	0.19	8.52	64.76	8.56	0.14
Pacaya	P 1961	Ol	0.45078	0.5	1.03E-13	2.20E-15	1.08E-12	3.57E-15	303.92	0.14	0.187	0.19	8.33	46.84	8.38	0.17
Pacaya	P 1961	Ol	0.47792	0.5	1.11E-13	3.57E-15	1.62E-12	5.41E-15	300.11	0.10	0.186	0.19	8.58	31.02	8.67	0.22
Pacaya	P pre 1961	Ol	0.45588	0.5	1.16E-13	3.10E-15	5.25E-13	1.71E-15	309.28	0.25	0.193	0.19	8.36	37.24	8.43	0.18
Pacaya	P 2010	Ol	0.67055	0.5	1.23E-13	2.71E-15	1.19E-12	3.94E-15	303.36	0.08	0.187	0.19	8.98	45.54	9.04	0.15
Pacaya	P 1975	Ol	0.41887	0.5	7.77E-14	3.68E-15	7.06E-13	2.35E-15	301.96	0.17	0.187	0.19	8.46	21.11	8.58	0.22
Pacaya	P 1975	Ol	0.41702	1	2.71E-13	8.23E-15	1.49E-12	3.25E-15			0.187	0.19	8.74	32.90	8.82	0.17
Pacaya	P 1975	Ol	0.5308	1	1.56E-13	1.53E-15	9.84E-13	3.20E-15	308.71	0.10	0.189	0.19	8.58	101.97	8.61	0.16
Pacaya	P pre 1961	Ol	0.50041	0.5	9.41E-14	3.06E-15	5.28E-13	1.74E-15	305.32	0.20	0.191	0.19	8.44	30.71	8.52	0.21
Pacaya	P 2014	Ol	0.81927	0.5	2.00E-13	1.52E-14	3.12E-12	1.04E-14	299.02	0.05	0.186	0.18	8.14	13.13	8.32	0.12
Pacaya	P 2017	Ol	1.00511	0.5	1.56E-13	9.31E-15	3.65E-12	1.23E-14	297.34	0.05	0.186	0.18	7.66	16.72	7.80	0.12
Ilopango	IL	Ol	1.03436	0.5	2.87E-13	1.21E-14	6.70E-12	2.26E-14	296.98	0.06	0.186	0.18	7.50	23.77	7.59	0.11
Santa Ana	SA	Ol	0.5126	0.5	5.57E-13	1.75E-15	1.85E-12	3.99E-15	462.51	0.09	0.187	0.19	5.73	318.48	5.73	0.07
San Miguel	SM	Ol	0.56653	0.5	6.54E-14	1.39E-15	1.57E-12	4.95E-15	316.70	0.08	0.186	0.19	5.14	46.91	5.17	0.17

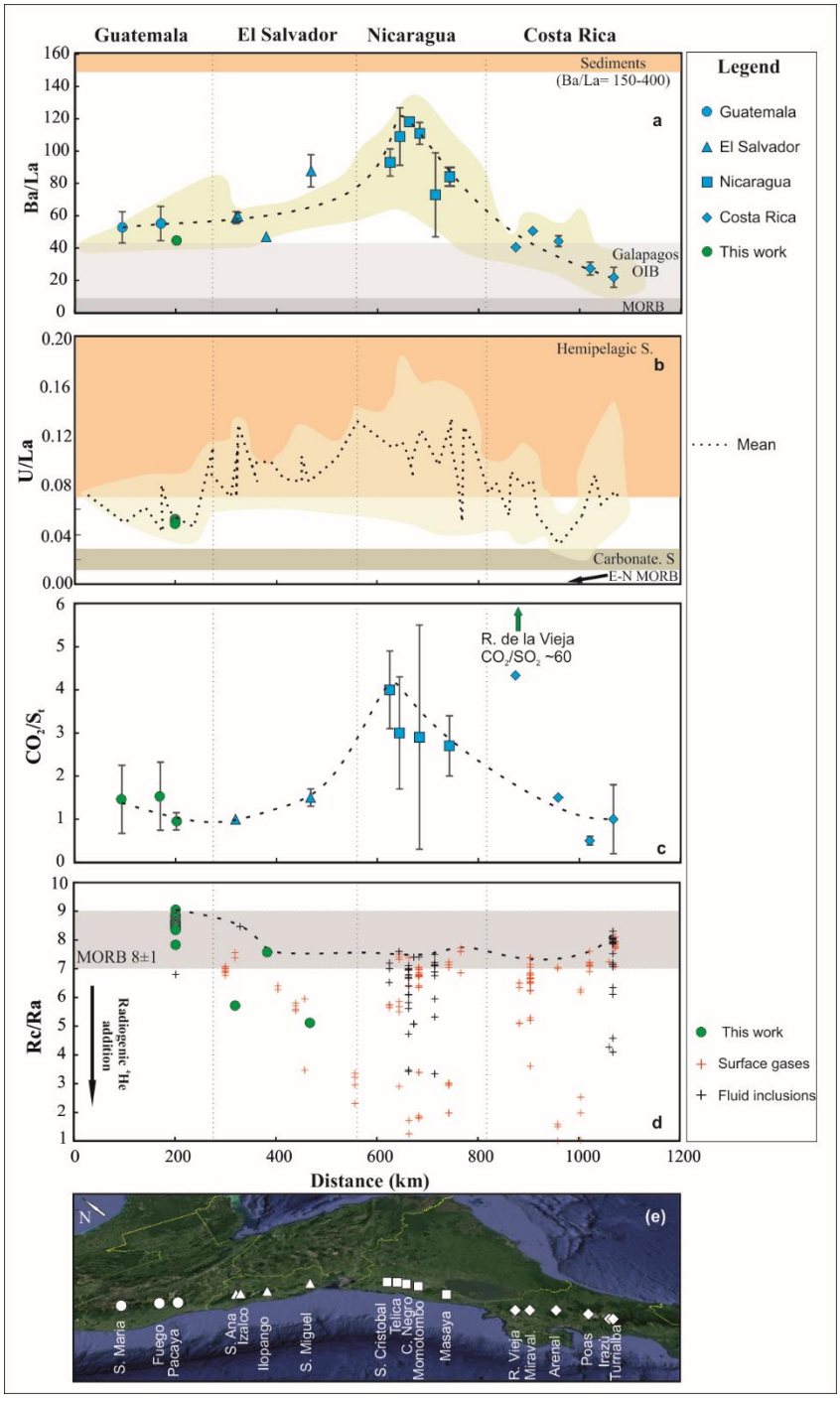

Figure 7.4 (a) Ba/La plot. The mean of Ba/La ratios were calculated averaging published whole-rock analyses (extracted from the earthchem portal; http://www.earthchem.org/portal). Value for Ilopango indicates the Ba/La measured in mafic inclusion from Isla Quemadas dome (see text). The error bars show one standard deviation. The yellow compositional field represent all dataset showed in Carr et. al. 2003. Black dotted line indicate the trend of Ba/La. (b) U/La plot. The yellow compositional field represent all dataset showed in Carr et. al. 2003. Dotted line represents the mean of U/La ratios for each volcanic system. U/La compositional field for hemipelagic and carbonate sediments from Carr et al., 2003. E-MORB and N-MORB U/La ratios from Sun and McDonough 1989. (c) CO_2/S_{tot} for

each volcano, the mean gas CO_2/S_t ratio is plotted, taken from this study (chapter 4) or from Aiuppa et al., (2014, 2017). CO_2/S_t ratios for Fuego and Santiaguito are derived from equation (4.3) using available Ba/La information (from earthchem portal). (d) Rc/Ra ratios vs distance along the arc. Red crosses represent the Rc/Ra measured in gases from Snyder et al. (2003), Elkins et al. (2006), Fischer et al. 2005 and de Leeuw et al. (2007), while those from FI (black crosses) are from this study, di Piazza et al. 2015, Poreda and Craig (1989), Shaw et al. (2006), Fisher et al. 2010. Black dotted line indicate the trend of helium isotopes signature (the highest Rc/Ra ratios measured in FI(s). Open symbols in all plots are from this PhD study.

7.6 Discussion

In order to deepen the evaluation of $^3He/^4He$ variations along CAVA in relation to other geochemical tracers (e.g., CO_2/S_t, Ba/La, Rc/Ra), in Fig. 7.4 we report all the available $^3He/^4He$ data including either fluid inclusions or surface gases. We considered the highest $^3He/^4He$ as the most suitable to be representative of the mantle; however, this approach does not exclude that low ratios could resemble shallow processes of contamination occurring within the crust, as suggested by *Battaglia et al.* (2018).

Before *Battaglia et al*. (2018), publication carried out during my PhD, the highest $^3He/^4He$ values along CAVA had been measured at Turrialba (Costa Rica), with values up to 8.1 Ra in fumarole gases (*Shaw et al.,* 2003*; Tassi et al.,* 2004*; Hilton et al.,* 2010*; Vaselli et al.,* 2010*; Di Piazza et al.,* 2015) and up to 8.3 Ra in fluid inclusions of olivine crystals (*Fischer et al.,* 2005*; Shaw et al.,* 2006*; Di Piazza et al.,* 2015). In addition, at Izalco volcano in El Salvador $^3He/^4He$~8.5 Ra were measured (*Fischer et al., 2005*). Slightly lower ratios (up to 7.6 Ra; *Poreda and Craig,* (1989)*; Shaw et al.,* (2003)*; Hilton et al.,* (2010)*; Fischer et al.,* (2015)) have also been measured in crater fumaroles from Póas volcano in Costa Rica (*Sano and Williams,* 1996*; Shaw et al.,* 2003*; Hilton et al.,* 2010*; Fischer et al.,* 2015). These high ratios have widely been interpreted as representative of the signature of the mantle wedge beneath this segment of CAVA, with no (or very limited) contribution from the subducting Cocos plate lithosphere. The MORB affinity of southern Costa Rican and northern CAVA volcanism is supported by several independent geochemical indicators, such as the low Ba/La, Ba/Th, and U/Th ratios in the erupted rocks (*Patino et al.,* 2000*; Sadofsky et al.,* 2008). *Battaglia et al*. (2018) have inferred a similar consideration for southern Guatemalan volcanos such as Pacaya, which showed the highest $^3He/^4He$ of the entire CAVA (up to 9 Ra), strongly indicating the lack of any contamination of the local mantle by radiogenic ^4He produced by subducting sediments.

Based on Ba/La and other geochemical tracers, the gradual increased sediment input from the subducting slab starts beneath El Salvador to the north and beneath north Costa Rica to the south, and increases even more beneath Nicaraguan segment of CAVA. If we assume that subducting sediments bearing U and Th are responsible of the contamination of $^3He/^4He$

in the mantle wedge by radiogenic ^{4}He addition, then we should expect to find the lowest ratios in correspondence of sediments with the highest content of U and Th, as those hemipelagic (Fig. 1.3). Effectively, the most contaminated segment of CAVA is found in Nicaragua, where the ^{3}He/^{4}He ratios range from 7.2 Ra at San Cristobal (*Robidoux et al.,* 2017) to 7.6 at Mombacho (*Shaw et al., 2003*), and never reach the values measured in Guatemala and Costa Rica. Therefore, a range of values between 7.2 and 7.6 Ra could resemble the lowest ^{3}He/^{4}He signature i.e. the most contaminated composition of mantle wedge expected for CAVA. The few measurements carried out in El Salvador at Santa Ana volcano have a ^{3}He/^{4}He up to 7.6 Ra (*de Leeuw et al.,* 2007). However, Izalco that is next and south to Santa Ana showed ^{3}He/^{4}He~8.5 Ra (*Fischer et al., 2005*), strongly indicating that beneath this segment of CAVA we should expect a mantle composition similar to that beneath southern Guatemala and Costa Rica (Fig. 7.3). Therefore, the ^{3}He/^{4}He measured in surface gases from Santa Ana should not be representative of the mantle source. Unfortunately, our fluid inclusions measurements yielded very low ^{3}He/^{4}He, suggesting for new investigations on other more mafic eruptions.

Based on the above considerations, we argue that the ^{3}He/^{4}He along CAVA shows a regional trend as observed for other geochemical tracers (e.g., Ba/La, C/S; Fig. 7.4). We exclude that ^{3}He/^{4}He varies in response of crustal contamination because we must expect a relation with crustal thickness that is not present. In fact, Fig. 1.2 shows that the lowest crustal thickness is found in the central part of CAVA, which is opposite of what expected. A more reasonable explanation in support of the existence of this regional trend comes from the slab thickness and subducting angle (Fig. 1.2), which point for important differences along the arc. In detail, beneath Nicaragua, the angle is higher than in other segments, favouring the reach of high depths, and couldenhance the release of supercritical fluids bearing radiogenic ^{4}He coming from the decay of U and Th hosted in subducted sediments.

We conclude that more studies of ^{3}He/^{4}He in fluid inclusions are necessary to better detail those portion of CAVA where data are still missing or not reliable.

8 Conclusion

Degassing represents the most evident expression of active volcanism. All gas emissions, volcanic plumes, fumaroles, geothermal gas etc. allow us to understand processes that happen in the Earth subsurface. Magmatic gases are responsible for ascending magma from the Earth's depths and their study is fundamental to monitoring and forecast volcanic eruptions. CO_2 and SO_2 are among the most abundant gases in volcanic plumes. Thanks its different solubilities and behaviour in the magma phase their study allow to characterize single volcanic systems, understand sub-surface processes and represent a powerful tool to monitoring and forecast volcanic eruptions. In nature, every volcanic system shows singular features due to different magma source, geology, lithology, hydrology, tectonic setting that are reflected in a volcanic activity, volcanic rocks and gas emissions. In arc settings, part of gases, in particular CO_2 comes from recycling of slab-fluids and magma-sediment interactions. *Aiuppa et al., (2017*), based upon hundreds of high-temperature (>450 °C) volcanic gas measurements, estimates the mean of CO_2/S_t ratios in arc settings worldwide as ~2.5. Howerer, in some part of the arcs, as in the Nicaraguan segment in Central America, the greater efficiency of fluids recycling can generate higher ratios as documented by CO_2/S_t in volcanic gas (*Aiuppa et al., 2014*), higher CO_2 contents in glass inclusions (*Wehrmann et al., 2011*), N_2 and CO_2 and He isotopic signatures (*Fischer et al., 2002; 2007, Robidoux et al., 2016*) and other geochemical tracers (e.g. Ba/La, U/La). High CO_2/S_t values are systematically observed in hydrotermal gases (<250 °C) and in mixed gases (magmatic and hydrothermal gases) in which scrubbing of magmatic S occur (*Aiuppa et al., 2017; Symond et al. 2001*). Moreover, studies of volcanic gas and fluxes budget allow to understand the impact of natural emission in climate change. In spite of all the efforts, several volcanic systems are poor studied and more insights are needed. In the last years attention has been increasingly focused also in the fluids-recycling efficiency in the non-arc setting (forearc and backarc) where significative amount of gases may be released. Progress of technology, (increase of remote instruments with highest spatially and temporal resolutions) allows to refining gas budget worldwide.

In this study, I measured volcanic gas emissions from three important volcanic systems in Central America contributing to the chemical characterization of volcanic plumes and gas fluxes in order to investigate along arc difference and to improve flux budget in CAVA an finally at global scale. Geochemical features along CAVA are related with physical parameters variations and tectonic segmentation that control the thermal regime, magma production and slab-fluid addiction. Clear evidences about mantle source affinity in some segment of the arc and crustal and/or slab-fluid

contamination in other segments come from many geochemical tracers. I investigated helium isotopes in fluid inclusions hosted in olivine minerals along the arc in order to explore and discovered if helium follows the other geochemical tracers. In Guatemala, I characterized the gas composition of plume of Pacaya volcano during a period of relatively mild intra-crateric strombolian activity and I estimated the Total Volatile Flux budget for one of the most active CAVA volcanoes. By combining the measured Pacaya CO_2 flux with inferred CO_2 fluxes from Fuego and Santiaguito using multidisciplinary approach (CAVA CO_2/S_t ratio vs. Ba/La ratio association), we tentatively assess the total volcanic CO_2 flux from Guatemalan segment of CAVA. Our plume compositional data suggest a limited slab-fluid contribution (at least compared to other volcanoes/arc segments; *Aiuppa et al.* 2017), and a dominant mantle-wedge derivation of the emitted volatiles. The $^3He/^4He$ ratios are within the MORB range (8±1Ra) and among the highest values in CAVA volcanism. This strongly supports that the mantle source beneath Pacaya lacks of any contamination of radiogenic ^4He from the slab or the crust, as observed in Costa Rica segment of CAVA.

The continuous gas monitoring at Masaya volcano in Nicaragua allowed to observe gas plume compositional change toward more CO_2-rich compositions before the appearance of the lava lake in December 2015 and toward SO_2-rich (and ~40% SO_2 flux increase) after the appearance of the lava lake due the shallow-level, faster than normal (4.4 vs. ~3 $m^3 \cdot s^{-1}$) magma circulation. This interpretation is consistent with a measured (late 2015-early 2016) inflation, having an inferred deformation source at ~ 2.3-3.8 km depth km beneath the surface. These results emphsize the importance of a extensive and permanent geochemical monitoring network in active volcanic systems worldwide, wich would allow to refine gases budget and in particular reducing volcanic risks for the most exposed populations near the volcanoes.

The measurements at Rincón de la Vieja allowed us to observe variations in gas chemical composition during the phreatic-phreatomagmatic eruptions for the first time. Thanks of this observations I investigated the interactions between volcanic and hydrothermal system and volcanic lake. These insights, in tandem with previous gas-change observations in volcanic systems with extensive volcanic lake (e.g. Poás volcano, *de Moor et al., 2016, Fisher et al., 2015*) lays the foundations for a development of a automatic continuous monitoring useful to observe geochemical precursors and so potentially forecast new eruptive events in active volcanoes characterized by volcanic lake.

I explored the helium isotope ratio in Guatemala and El Salvador volcanic systems contributing to expand helium data (in FIs) in the north part of CAVA. These new dataset allows to formulate more robust hypothesis about helium isotope variations along the Central America Volcanic Arc. As

discussed in the previous paragraph, the helium isotope variations along CAVA seem to remark the other principal geochemical tracers. However, many other helium measurements in rocks are needed.

9 Reference list

- Aiuppa, A., de Moor, J. M., Arellano, S., Coppola, D., Francofonte, V., Galle, et al. (2018). Tracking formation of a lava lake from ground and space: Masaya volcano (Nicaragua), 2014–2017. *Geochemistry, Geophysics, Geosystems*, 19, 496–515.https://doi.org/10.1002/2017GC007227
- Aiuppa, A., et al. (2017), A CO_2-gas precursor to the March 2015 Villarrica volcano eruption, *Geochemistry, Geophysics, Geosystems*, 18, doi:10.1002/2017GC006892.
- Aiuppa, A., T. P., Fischer, T., Plank, P., Robidoux, R., Di Napoli, (2017), Along-arc, inter-arc and arc-to-arc variations in volcanic gas CO_2/ST ratios reveal dual source of carbon in arc volcanism. *Earth-Science Reviews* 168, 24–47, http://dx.doi.org/10.1016/j.earscirev.2017.03.005
- Aiuppa A., E. Lo Coco, M. Liuzzo, G. Giudice, G. Giuffrida and R. Moretti, (2016), Terminal Strombolian activity at Etna's central craters during summer 2012: The most CO_2-rich volcanic gas ever recorded at Mount Etna, *Geochemical Journal*, 50 (2), 123-138.
- Aiuppa, A., P. Bani, Y. Moussallam, R. Di Napoli, P. Allard, H. Gunawan, M. Hendrasto, and G. Tamburello, (2015), First determination of magma-derived gas emissions from Bromo volcano, eastern Java (Indonesia). *J. Volcanol. Geotherm. Res.*, 304, 206–213.
- Aiuppa, A., P. Robidoux, G. Tamburello, V. Conde, B. Galle, G. Avard, E. Bagnato, J.M. De Moor, M. Martínez, and A. Muñóz (2014), Gas measurements from the Costa Rica-Nicaragua volcanic segment suggest possible along-arc variations in volcanic gas chemistry. *Earth Planet. Sci. Lett.*, 407, 134-147.
- Aiuppa, A., H. Shinohara, G. Tamburello, G. Giudice, M. Liuzzo, and R. Moretti, (2011). Hydrogen in the gas plume of an open-vent volcano, Mount Etna, Italy, *J. Geophys. Res. Solid Earth*, vol. 116, no. 10, pp. 1–8.
- Aiuppa, A., A. Bertagnini, N. Métrich, R. Moretti, A. Di Muro, M. Liuzzo, et al., (2010) A model of degassing for Stromboli volcano, *Earth Planet. Sci. Lett.*, vol. 295, no. 1–2, pp. 195–204.
- Aiuppa, A., R. Moretti, C. Federico, G. Giudice, S. Gurrieri, M. Liuzzo, P. Papale, H. Shinohara, and M. Valenza (2007), Forecasting Etna eruptions by real-time observation of volcanic gas composition, *Geology*, 35 (12), 1115-1118.
- Aiuppa, A., C. Federico, G. Giudice, S. Gurrieri, M. Liuzzo, H. Shinohara, et al. (2006), Rates of carbon dioxide plume degassing

from Mount Etna volcano, *J. Geophys. Res. Solid Earth*, vol. 111, no. 9, pp. 1–8.

- Aiuppa, A., Federico, C., Giudice, G., Gurrieri, S., (2005). Chemical mapping of a fumarolic field: La Fossa Crater, Vulcano Island (Aeolian Islands, Italy). *Geophysical Research Letters* 32(13), L13309. http://dx.doi.org/10.1029/2005GL023207.
- Allard, P., A. Aiuppa, P. Bani, N. Métrich, A. Bertagnini, P. J. Gauthier, H. Shinohara, G. Sawyer, F. Parello, E. Bagnato, B. Pelletier, and E. Garaebiti, (2015), Prodigious emission rates and magma degassing budget of major, trace and radioactive volatile species from Ambrym basaltic volcano, Vanuatu island Arc, *J. Volcanol. Geoth. Res*., 304, 378-402.
- Allard, P., (1983). The origin of hydrogen, carbon, sulfur, nitrogen, and rare gases in volcanic exhalations: evidence from isotope geochemistry. In: Tazieff, H., Sabroux, J.-C. (Eds.), Forecasting Volcanic Events. Elsevier, Amsterdam, 337–386.
- Alvarado G. E., D. Mele, P. Dellino, J. M. de Moor, and G. Avard, (2016). Are the ashes from the latest eruptions (2010–2016) at Turrialba volcano (Costa Rica) related to phreatic or phreatomagmatic events? *J. Volcanol. Geotherm. Res*. http://dx.doi.org/10.1016/j.jvolgeores.2016.09.003
- Alvarado, G.E., Kussmaul, S., Chiesa, S., Gillot, P.Y., Appel, H., Worner, G., et al. (1992). Resumen cronoestratigrafico de las rocas igneas de Costa Rica basado en dataciones radiometricas. J. South Am. Earth Sci. 6/3, 151– 168.
- Andres, R. J., and A. D., Kasgnoc (1998), A time-averaged inventory of subaerial volcanic sulfur emissions, *J. Geophys. Res*., 103, 25, 251–25, 261.
- Andres, R., W. Rose, R. Stoiber, S. Williams, O. Matuas, and R. Morales, (1993), A Summary of Sulfur dioxide emission rate measurements from Guatemalan volcanoes. *Bull. Volcanol*., 1(55), 379–388.
- Arámbula-Mendoza, R., Lesage, P., Valdés-González, C., Varley, N., Reyes-Dávila, G., Navarro, C., (2011) Seismic activity that accompanied the effusive and explosive eruptions during the 2004–2005 period at Volcán de Colima, Mexico. *J. Volcanol. Geotherm. Res.*, 205, 30-46.
- Atlas, Z. D. & Dixon, J. E. (2006). Interconnected magmatic conduit systems as recorded by melt inclusions from Masaya and Apoyo Calderas, Nicaragua, *Eos Trans. AGU* 87(52), Fall Meet. Suppl., AbstractV13D-06.

- Barckhausen, U., C. R. Ranero, R. von Huene, S. C. Cande, and H. A. Roeser, Revised tectonic boundaries in the Cocos Plate offCosta Rica: Implications for the segmentation of the convergent margin and for plate tectonic models (2001), J. Geophys. Res., 106, 19,207–19,220.
- Bardintzeff J.M. and C. Daniel, (1992), Magmatic evolution of Pacaya and cerro Chiquito volcanological complex, Guatemala. *Bull. Volcanol*., 54, 267-283.
- Barnes, J. D., Z. D. Sharp, T. P. Fischer, D. R. Hilton, and M. J. Carr, (2009), Chlorine isotope variations along the Central American volcanic front and back arc, *Geochemistry, Geophysics, Geosystems*, 10(11).
- Barnie, T.D., C. Oppenheimer, C. Pagli, (2016), Does the lava lake of Erta 'Ale volcano respond to regional magmatic and tectonic events? An investigation using Earth Observation data, *Geological Society Special Publication*, 420 (1), 181-208.
- Barquero, J. & Segura, J., (1983). La actividad del volcán Rincón de la Vieja. - *Bol. de Vulcanología*, 13: 5- 10, Heredia.
- Benjamin, E.R. et al., (2007). High water contents in basaltic magmas from Irazu Volcano, Costa Rica. *Journal of Volcanology and Geothermal Research*, 168, 68–92.
- Bernard, A., Escobar, C. D., Mazot, A. and Gutierrez, R.E. (2004), The acid volcani lake of Santa Ana volcano, El Salvador, *Geological Society of America*, Special paper 375:121-133.
- Bice, D.C., (1985), Quaternary volcanic stratigraphy of Managua, Nicaragua: correlation and source assignment for multiple overlapping plinian deposits, *Geol. Soc. Amer. Bull.*, 96, 553–566
- Bluth, G. J. S., J. M. Shannon, I. M. Watson, a. J. Prata, and V. J. Realmuto, (2007), Development of an ultra-violet digital camera for volcanic SO2 imaging. *J. Volcanol. Geotherm. Res.*, 161(1–2), 47–56.
- Boatwright J (1980). A spectral theory for circular seismic sources: Simple estimates of source dimension, dynamic stress drop, and radiated seismic energy. *Bulletin of the Seismological Society of America* 70: 1–27.
- Bodnar RJ (2003) Introduction to fluid inclusions. In I. Samson, A. Anderson, & D. Marshall, eds. Fluid Inclusions: Analysis and Interpretation. *Mineral. Assoc*. Canada, Short Course 32, 1-8.
- Bonforte A., D. A. Hernandez, E. Gutiérrez, L. Handal, C. Polío, S. Rapisarda, and P. Scarlato, "The unrest of the San Miguel volcano (El Salvador, Central America): Installation of the monitoring network

and observed volcano-tectonic ground deformation," Nat. *Hazards Earth Syst. Sci.*, vol. 16, no. 8, pp. 1755–1769, 2016.

- Boudoire G., A.L. Rizzo, A. Di Muro, F. Grassa, M. Liuzzo, (2018) Extensive CO_2 degassing in the upper mantle beneath oceanic basaltic volcanoes: First insights from Piton de la Fournaise volcano (La Réunion Island), *Geochimica et Cosmochimica Acta*, Volume 235, Pages 376-401, ISSN 0016-7037, https://doi.org/10.1016/j.gca.2018.06.004.
- Boudon, G., Rancon, J.P., Kieffer, G., Soto, G.J., Traineau, H., Rossignol, J.C., (1996). Les eruptions de 1966–1970 et 1991– 1992 du volcan Rincón de la Vieja, Costa Rica: exemple d'activité recurrente d'un systéme hydromagmatique. *C.R. Acad. Sci*. Paris 322-IIa, 101–108.
- Brandes, C., Astorga, A., Back, S., Littke, R., Winsemann, J., (2007). Deformation style and basin-fill architecture of the offshore Limón back-arc basin (Costa Rica), *Marine and Petroleum Geology*, Volume 24, Issue 5, 277-287, ISSN 0264-8172, https://doi.org/10.1016/j.marpetgeo.2007.03.002.
- Brantley, S.L., Koepenick, K.W., (1995). Measured carbon dioxide emissions from Oldoinyo Lengai and the skewed distribution of passive volcanic fluxes. Geology 23, 933–936.
- Browne, P.R.L., Lawless, J.V., (2001). Characteristics of hydrothermal eruptions, with examples from New Zealand and elsewhere. *Earth Sci. Rev*. 52, 299–331.
- Bruhn, A., Weickert, J. & Schörr, C., 2005. Lucas / Kanade Meets Horn / Schunck : Combining Local and Global Optic Flow Methods. International Journal of Computer Vision, 61(3), pp.211–231.
- Buck, A.L., (1981), New equations for computing vapor pressure and enhancement factor, *J Appl Meteorol.,* 20, 1527–1532.
- Burgi, P.Y., T.H. Darrah, D. Tedesco, W.K. Eymold, (2014), Dynamics of the Mount Nyiragongo lava lake, *J. Volcanol. Geoth. Res*., 119(5), 4016–4122
- Burkart, B., S. Self, (1985), Extension and rotation of crustal blocks in northern Central America and effect on the volcanic arc. *Geology* 13, 22–26
- Burton, M. R., G.M., Sawyer, D., Granieri, (2013), deep Carbon Emission from Volcanoes. Rev. in *Mineral & Geochem*. 75, 323-354, DOI: 10.2138/rmg.2013.75.11
- Burton, M. R., C. Oppenheimer, L. A. Horrocks, and P.W. Francis (2000), Remote sensing of CO_2 and H_2O emission rates from Masaya volcano, Nicaragua. *Geology*, 28, 915– 918.

- Cameron, B. I., J. a. Walker, M. J. Carr, L. C. Patino, O. Matías, and M. D. Feigenson, (2003), Flux versus decompression melting at stratovolcanoes in southeastern Guatemala. *J. Volcanol. Geotherm. Res*., 119(1–4), 21–50.
- Canora C., Josè J. Martinez Diaz, P. Villamor, K. Berryman, José A. Álvarez-Gómez, C. Pullinger, and R. Capote, (2010) Geological and Seismological Analysis of the 13 February 2001 Mw 6.6 El Salvador Earthquake: Evidence for Surface Rupture and Implications for Seismic Hazard. *Bulletin of Seismological Society of America* Vol. 100, No. 6, pp. 2873-2890, December 2010, doi: 10.1785/0120090377
- Carmichael, I. S. E., and M. S. Ghiorso (1986), Oxidation-reduction relations in basic magma: A case for homogeneous equilibria, Earth Planet. Sci. Lett., 78, 200–210, doi:10.1016/0012-821X(86)90061-0.
- Carr M. J., M. D. Feigenson, L. C. Patino, and J. a Walker, Volcanism and Geochemistry in Central America: Progress and Problems, (2003) Insid. Subduction Factory, *Geophys. Monogr. Ser*., vol. 138, no. January 2003, pp. 153–174.
- Carr, M. J., Feigenson, M. D., (1990) and E. A. Bennett, Incompatible element and isotopic evidence for tectonic control of source mixing and melt extraction along the Central American arc. *Contrib. to Mineral. Petrol*., 105(4), 369–380.
- Carr, M.J., (1984). Symmetrical and segmented variation of physical and geochemical characteristics of the Central American volcanic front. *J. Volcanol. Geotherm. Res*., 20, 231–252.
- Carr, M.J., Pointer, N.K., 1981. Evolution of a young parasitic cone toward a mature central vent; Izalco and Santa Ana volcanoes in El Salvador, Central America. *J. Volcanol. Geotherm. Res*. 11, 277–292.
- Carr, M.J., and Stoiber, R.E., 1977, Geologic setting of some destructive earthquakes in Central America: Geological *Society of America Bulletin*, v. 88, p. 151–156, doi: 10.1130/0016-7606(1977)88<151:GSOSDE>2.0.CO;2.
- Carr, M. J., (1976). Underthrusting and Quaternary faulting in northern Central America, Geol. Soc. Am. Bull., 87, 825-829,.
- Case, J.E., MacDonald, W.D., Fox, P.J., (1990), Caribbean crustal provinces; seismic and gravity evidence. In: Dengo, G., Case, J.E. Ž. Eds. , The Caribbean Region, The Geology of North America, Vol. H, *Geol. Soc. Am., Boulder*, CO, 15–36.
- Chan, L. H., Leeman, W. P., & You, C. F. (2002), Lithium isotopic composition of Central American volcanic arc lavas: Implications for modification of subarc mantle by slab-derived fluids: Correction.

Chemical Geology, *182*(2–4), 293–300. https://doi.org/10.1016/S0009-2541(01)00298-4

- Chiodini, G., Marini, L., (1998), Hydrothermal gas equilibria: the H2O-H2-CO2-CO-CH4 system. *Geochim. Cosmochim. Acta* 62, 2673–2687.
- Christenson BW, Tassi F (2015). Gases in volcanic lake environments, In: Rouwet D, Christenson BW, Tassi F, Vandemeulebrouck J (eds) Volcanic Lakes. *Springer*, Heidelberg.
- Christenson BW, Reyes AG, Young R, et al. (2010). Cyclic processes and factors leading to phreatic eruption events: Insights from the 25 September 2007 eruption through Ruapehu Crater Lake, New Zealand. *Journal of Volcanology and Geothermal Research* 191: 15–32.
- Conde, V., Robidoux, P., Avard, G., Galle, B., Aiuppa, A., Muñoz, A., Giudice, G., (2014), Measurements of volcanic SO_2 and CO_2 fluxes by combined DOAS, Multi-GAS and FTIR observations: a case study from Turrialba and Telica volcanoes. Int. *J. Earth Sci.* 103(8), 2335–2347.
- Conde, V., Bredemeyer, S., Duarte, E., Pacheco, J., Miranda, S., Galle, B., & Hansteen, T. H. (2013). SO2 degassing from Turrialba Volcano linked to seismic signatures during the period 2008–2012. *International Journal of Earth Science*, 103(7), 1983–1998. https://doi.org/10. 1007/s00531-00013-00958-00535
- Conway, F. M., J. F. Diehl, and O. Matias, (1992), Paleomagnetic constraints on eruption patterns at the Pacaya composite volcano, Guatemala. *Bull. Volcanol*., 55(1–2), 25–32
- Coppola, D., M. Ripepe, M. Laiolo, C. Cigolini (2017a), Modelling satellite-derived magma discharge to explain caldera collapse, *Geology*, 45 (6), pp. 523-526
- Coppola, D., D. Piscopo, M. Laiolo, C. Cigolini, D. Delle Donne, M. Ripepe, (2012), Radiative heat power at Stromboli volcano during 2000-2011: Twelve years of MODIS observations, *J. Volcanol. Geoth. Res*., 215-216, 48-60.
- Coppola, D., et al., (2017b), Shallow system rejuvenation and magma discharge trends at Piton de la Fournaise volcano (La Réunion Island), *Earth Planet. Sci. Lett*., 463, 13-24
- Coppola, D., Laiolo, M., Piscopo, D., Cigolini, C. (2013), Rheological control on the radiant density of active lava flows and domes, *J. Volcanol. Geoth. Res*., 249, 39-48.

- Coppola, D., R. Campion, M. Laiolo, E. Cuoco, C. Balagizi, M. Ripepe, C. Cigolini, D. Tedesco, (2016a), Birth of a lava lake: Nyamulagira volcano 2011–2015, *Bull. Volcanol*., 78 (3), 1-13.
- Coppola, D., M. Laiolo, C. Cigolini, D. Delle Donne, M. Ripepe (2016b), Enhanced volcanic hot-spot detection using MODIS IR data: Results from the MIROVA system, *Geological Society Special Publication*, 426 (1), 181-205
- Coppola, D., M., Laiolo, L.E. Lara, C. Cigolini, G. Orozco, (2016c), The 2008 "silent" eruption of Nevados de Chillán (Chile) detected from space: Effusive rates and trends from the MIROVA system, *J. Volcanol. Geotherm. Res*., 327, 322-329
- Coppola, D., et al., (2015), Magma extrusion during the Ubinas 2013-2014 eruptive crisis based on satellite thermal imaging (MIROVA) and ground-based monitoring, *J. Volcanol. Geoth. Res*., 302, 199-210
- Coppola, D., M. Laiolo, D. Delle Donne, M. Ripepe, C. Cigolini, (2014) Hot-spot detection and characterization of strombolian activity from MODIS infrared data International, *J. Remote Sensing*, 35 (9), 3403-3426.
- Correale, A., A. Paonita, A. Rizzo, F. Grassa, and M. Martelli (2015), The carbon-isotope signature of ultramafic xenoliths from the Hyblean Plateau (southeast Sicily, Italy): Evidence of mantle heterogeneity, *Geochemistry, Geophys. Geosystems*, 16, doi:10.1002/2014GC005656
- D'Aleo, R., M., Bitetto, D., Delle Donne, G., Tamburello, A., Battaglia, Coltelli, D., Patanè, M., Prestifilippo, M., Sciotto, and A., Aiuppa (2016), Spatially resolved SO_2 flux emission from Mt Etna, *Geophysical Research Letters*, 43, 7511-7519, doi: 10.1002/2016GL069938.
- Dalton, M. P., G. P. Waite, I. M. Watson, and P. a. Nadeau, (2010), Multiparameter quantification of gas release during weak Strombolian eruptions at Pacaya Volcano, Guatemala. *Geophysical Research Letters*, 37(9).
- Dasgupta, R., (2013), Ingassing, storage, and outgassing of terrestrial carbon through geologic time. *Rev. Mineral. Geochem*. 75 (1), 183-229.
- Davies JH, Stevenson DJ (1992) Physical model of source region of subduction zone volcanics. *J Geophys Res*. 97: 2037-2070
- De la Cruz-Reyna, S., Reyes-Davila, G.A., (2001). A model to describe precursory material-failure phenomena: applications to

short-term forecasting at Colima volcano, Mexico. *Bull. Volcanol*. 63, 297-308

- De Leeuw, G. A. M., D. R. Hilton, T. P. Fischer, and J. A. Walker, (2007). The He – CO2 isotope and relative abundance characteristics of geothermal fluids in El Salvador and Honduras: New constraints on volatile mass balance of the Central American Volcanic Arc. *Earth and Planetary Science Letters* vol. 258, 132–146.
- de Moor J. M., C. Kern, G. Avard, C. Muller, A. Aiuppa, A. Saballos, et al. (2017). A New Sulfur and Carbon Degassing Inventory for the Southern Central American Volcanic Arc: The Importance of Accurate Time-Series Data Sets and Possible Tectonic Processes Responsible for Temporal Variations in Arc-Scale Volatile Emissions, *Geochemistry, Geophysics, Geosystems*, pp. 4437–4468.
- de Moor J. M., A. Aiuppa, J. Pacheco, G. Avard, C. Kern, M. Liuzzo, et al. (2016a). Short-period volcanic gas precursors to phreatic eruptions: Insights from Poás Volcano, Costa Rica, *Earth* Planet. Sci. Lett., vol. 442, pp. 218–227.
- de Moor, J. M., A. Aiuppa, G. Avard, H. Wehrmann, N. Dunbar, C. Muller, G. Tamburello, G. Giudice, M. Liuzzo, R. Moretti, V. Conde, and B. Galle, (2016), Turmoil at Turrialba Volcano (Costa Rica): Degassing and eruptive processes inferred from high-frequency gas monitoring. *Journal of Geophysical Research: Solid Earth*, pp. 1–15.
- de Moor, J. M., A. Aiuppa, G. Avard, H. Wehrmann, N. Dunbar, C. Muller, et al. (2016b). Turmoil at Turrialba Volcano (Costa Rica): Degassing and eruptive processes inferred from high-frequency gas monitoring, *Journal of Geophysical Research Solid Earth*, vol. 121, no. 8, pp. 5761–5775.
- de Moor, J.M., et al., (2013), Sulfur degassing at Erta Ale (Ethiopia) and Masaya (Nicaragua) volcanoes: Implications for degassing processes and oxygen fugacities of basaltic systems, *Journal of Geophysical Research*, 14 (10), pp. 4076-4108
- Dee, D. P., Uppala, S. M., Simmons, A. J., Berrisford, P., Poli, P., Kobayashi, S., Andrae, U., Balmaseda, M. A., Balsamo, G., Bauer, P., Bechtold, P., Beljaars, A. C. M., van de Berg, L., Bidlot, J., Bormann, N., Delsol, C., Dragani, R., Fuentes, M., Geer, A. J., Haimberger, L., Healy, S. B., Hersbach, H., Hólm, E. V., Isaksen, L., Kållberg, P., Köhler, M., Matricardi, M., McNally, A. P., Monge-Sanz, B. M., Morcrette, J.-J., Park, B.-K., Peubey, C., de Rosnay, P., Tavolato, C., Thépaut, J.-N. and Vitart, F. (2011), The ERA-Interim reanalysis: configuration and performance of the data assimilation system, *Q.J.R. Meteorol. Soc.*, 137: 553–597. doi:10.1002/qj.828.

- Deines, P., (2002), The carbon isotope geochemistry of mantle xenoliths. *Earth-Science Reviews*, 58, 3–4, October 2002, 247-278 https://doi.org/10.1016/S0012-8252(02)00064-8
- Delmelle P., Bernard A., (2015). The remarkable chemistry of sulfur in volcanic acid crater lakes: a scientific tribute to Bokuichiro Takano and Minoru Kusakabe. In: Rouwet D, Tassi F, Vandemeulebrouck J, Christenson B (eds) Volcanic Lakes. *Springer*, Berlin. doi: 10.1007/978-3-642-36833-2_10
- Delmelle, P., Stix, J., Baxter, P., Garcia-Alvarez, J., Barquero, J. (2002), Atmospheric dispersion, environmental effects and potential health hazard associated with the low-altitude gas plume of Masaya volcano, Nicaragua, *Bull. Volcanol*., 64 (6), 423-434.
- Delmelle, P., P. Baxter, A. Beaulieu, M. Burton, P. Francis, J. Garcia-Alvarez, L. Horrocks, M. Navarro, C. Oppenheimer, D. Rothery, H. Rymer, K. St. Amand, J. Stix, W. Strauch, G. Williams-Jones, (1999), Origin, effects of Masaya volcano's continued unrest probed in Nicaragua, *Eos*, 80 (48), 575-581
- DeMets, C., Gordon, R.G. and Argus, D.F. (2010). Geologically Current Plate Motions. *Geophysical Journal International*, 181, 1-80. http://dx.doi.org/10.1111/j.1365-246X.2009.04491.
- DeMets C., (2001), A new estimate for present- day Cocos-Caribbean plate motion: Implication for slip along the Central American volcanic arc. *Geophysical Research Letters* 28(21): 4043-4047
- Di Napoli, R., C. Federico, A. Aiuppa, M. D'Antonio M. Valenza, (2013). Quantitative models of hydrothermal fluid–mineral reaction: The Ischia case, *Geochimica et Cosmochimica Acta,* Volume 105, Pages 108-129, ISSN 0016-7037, https://doi.org/10.1016/j.gca.2012.11.039
- Di Piazza, A., A. L. Rizzo, F. Barberi, M. L. Carapezza, G. De Astis, C. Romano, and F. Sortino, (2015), Geochemistry of the mantle source and magma feeding system beneath Turrialba volcano, Costa Rica. *Lithos*, 232, 319–335,.
- Duffell, H.J., C. Oppenheimer, D.M. Pyle, B. Galle, A.J.S. McGonigle, M.R. Burton, (2003), Changes in gas composition prior to a minor explosive eruption at Masaya volcano, Nicaragua, *J. Volcanol. Geotherm. Res*., 126 (3-4), 327-339
- Duffell H., Oppenheimer C., and Burton M. (2001) Volcanic gas emission rates measured by solar occultation spec- troscopy. *Geophys. Res. Lett*. 28, 3131–3134.

- Dull, R.A., Southon, J.R., Sheets, P., 2001. Volcanism, ecology and culture: a reassessment of the Volcán Ilopango TBJ eruption in the Southern Maya Realm. Latin Am. Antiq. 12 (1), 25–44.
- Eggers A. A. (1971), The geology and petrology of the Amatitlán quadrangle, Guatemala. Ph. D. Dissertation. Dartmouth College, Hanover, *New Hampshire*. 221p.
- Elkins, L.J., Fischer, T.P., Hilton, D.R., Sharp, Z.D., McKnight, S., Walker, J., (2006). Tracing ni- trogen in volcanic and geothermal volatiles from the Nicaraguan volcanic front. *Geochimica et Cosmochimica Acta* 70 (20), 5215–5235.
- Feigenson Mark D., Michael J. Carr; Positively correlated Nd and Sr isotope ratios of lavas from the Central American volcanic front (1986). *Geology*, 14 (1): 79–82. doi: https://doi.org/10.1130/0091-7613Fischer, T. P and G. Chiodini, (2015), Volcanic, Magmatic and Hydrothermal Gases. *The Encyclopedia of Volcanoes (Second Edition),* no. May, 2015, DOI: 10.1016/B978-0-12-385938-9.00045-6.
- Fischer, T. P., C. Ramírez, R. A. Mora-Amador, D. R. Hilton, J. D. Barnes, Z. D. Sharp, M. Le Brun, J. M. de Moor, P. H. Barry, E. Füri, and A. M. Shaw, (2015), Temporal variations in fumarole gas chemistry at Poás volcano, Costa Rica. *J. Volcanol. Geotherm. Res*., 294, 56–70.
- Fischer, T.P., A.M. Shaw, D.R. Hilton (2007), Gas geochemistry of volcanic and hydrothermal fluids of Central America. In *Central America: Geology, Resources and Hazards* (eds. Bundschuh, J. and Alvarado, G.E.), Taylor and Francis, Leiden, The Netherlands, 2, 839-867.
- Fischer T. P., and B. Marty, (2005), Volatile abundances in the sub-arc mantle: Insights from volcanic and hydrothermal gas discharges. *J. Volcanol. Geotherm. Res*., 140(1–3), 205–216.
- Fischer, T. P., N. Takahata, Y. Sano, H. Sumino, and D. R. Hilton, (2005), Nitrogen isotopes of the mantle: Insights from mineral separates. *Geophysical Research Letters*, 32(11), 1–5.
- Fortin, M-A., Riddle, J., Desjardins-Langlais, Y., Baker, D.R., (2015), The effect of water on the sulfur concentration at sulfide saturation (SCSS) in natural melts, *Geochimica et Cosmochimica Acta*, 160, 100-116.
- Fischer, T. P., Hilton, D. R., Zimmer, M. M., Shaw, A. M., Sharp, Z. D., and J. A. Walker, (2002), Subduction and Recycling of Nitrogen Along the Central American Margin. *Science* (80), 297, (5584), 1154–1157.

- Freundt, A., I.,Grevemeyer, W. Rabbel, C., Hensen, H., Wehrmann, S., Kutterolf, T.H., Hansteen, R., Halama, M., Frische (2014), Volatile (H_2O, CO_2, Cl, S) budget of the Central American subduction zone. *International Journal of Earth Sciences* 103(7), DOI: 10.1007/s00531-014-1001-1.
- Frischbutter A., Structure of the Managua graben, Nicaragua, from remote sensing images, (2002) Geofis. Int., vol. 41, no. 2, pp. 87–102.
- Frost, B. R. (1991), Introduction to oxygen fugacity and its petrologic importance, in Oxide Minerals : Petrologic and Magnetic Significance, edited by D. H. Lindsley, 1-9, *Mineralogical Society of America*.
- Galle, B., M. Johansson, C. Rivera, Y. Zhang, M. Kihlman, C. Kern, T. Lehmann, U. Platt, S. Arellano, and S. Hidalgo (2010), Network for Observation of Volcanic and Atmospheric Change (NOVAC)—A global network for volcanic gas monitoring: Network layout and instrument description, *J. Geophys. Res.*, 115.
- Gennaro, M. E., F. Grassa, M. Martelli, A. Renzulli, and A. L. Rizzo, (2017), Carbon isotope composition of CO_2-rich inclusions in cumulate-forming mantle minerals from Stromboli volcano (Italy). *J. Volcanol. Geotherm. Res.*, 1–9 (in press), http://dx.doi.org/10.1016/j.jvolgeores.2017.04.001
- Gherardi, F., C. Panichi, A. Yock, and J. Gerardo-Abaya, (2002). Geochemistry of the surface and deep fluids of the Miravalles volcano geothermal system (Costa Rica), *Geothermics* vol. 31, no. 1.
- Giggenbach, W. F. (1996). Chemical composition of volcanic gas, in IAVCEI-UNESCO: Monitoring and Mitigation of Volcanic Hazards, edited by R. Tilling, pp. 221–256, *Springer*, Berlin.
- Giggenbach, W.F. and R.S. Correales (1992a). Isotopic and chemical composition of water and steam discharges from volcanic-magmatic-hydrothermal systems of the Guanacaste geothermal province, Costa Rica, *Appl. Geochem.*, 7, 309-332.
- Giggenbach, W.F., (1987). Redox processes governing the chemistry of fumarolic gas discharges fromWhite Island, New Zealand. *Appl. Geochem*. 2, 141–161.
- Global Volcanism Program, 2017. Report on Rincón de la Vieja (Costa Rica). In: Venzke, E (ed.), *Bulletin of the Global Volcanism Network*, 42:8. Smithsonian Institution.
- Global Volcanism Program, (2016), Report on Masaya (Nicaragua). In: Venzke, E (ed.), *Bulletin of the Global Volcanism Network*, 41:8. Smithsonian Institution.

- Global Volcanism Program, (2013), Masaya (344100) in Volcanoes of the World, v. 4.5.5. Venzke, E (ed.), Smithsonian Institution. http://volcano.si.edu/volcano.cfm?vn=344100). http://dx.doi.org/10.5479/si.GVP.VOTW4-2013
- Global Volcanism Program, 2002. Report on Pacaya (Guatemala). In: Wunderman, R (ed.), *Bulletin of the Global Volcanism Network*, 27:7. Smithsonian Institution. http://dx.doi.org/10.5479/si.GVP.BGVN200207-342110
- Goff, F., McMurtry, G.M., Counce, D., Simac, J.A., Roldan-Manzo, A.R., Hilton, D.R., (2000), Contrasting hydrothermal activity at Sierra Negra and Alcedo volcanoes, Galapagos Archipelago, Ecuador. *Bull. Volcanol.* 62, 34–52.
- Graham DW (2002) Noble Gas Isotope Geochemistry of Mid-Ocean Ridge and Ocean Island Basalts: Characterisation of Mantle Source Reservoirs. In: Porcelli D, Ballentine CJ, Wieler R (eds) Noble Gases in *Geochemistry and Cosmochemistry*, vol 47. pp 245- 317
- Granieri, D., G. Salerno, M. Liuzzo, A. La Spina, G. Giuffrida, T. Caltabiano, G. Giudice, E. Gutierrez, and F. Montalvo, M. R., Burton, P., Papale, (2015), Emission of gas and atmospheric dispersion of SO_2 during the December 2013 eruption at San Miguel volcano (El Salvador, Central America), *Geophysical Research Letters* 42(14), 5847-5854.
- Gunawan, H., C. Caudron, J. Pallister, S. Primulyana, B. Christenson, W. McCausland, et al. (2016). New insights into KawahIjen's volcanic system from the wet volcano workshop experiment, *Geol. Soc. London, Spec. Publ.*, vol. 437.
- Harris, A.J.L., (2009), The pit-craters and pit-crater-filling lavas of Masaya volcano, *Bull. Volcanol*., 71 (5), 541-558
- Harris, A.J.L., and S.M. Baloga, (2009), Lava discharge rates from satellite-measured heat flux *Geophys. Res. Lett*., 36 (19), art. no. L19302
- Hasselle, N., Rouwet, D., Aiuppa, A., Jácome-Paz, M. P., Pfeffer, M., Taran, Y., et al. (2018). Sulfur degassing from steam-heated crater lakes: El Chichón (Chiapas, Mexico) and Víti (Iceland). *Geophysical Research Letters*, *45*. https://doi.org/10.1029/2018GL079012
- Heydolph, K., K. Hoernle, F. Hauff, P. Van Den Bogaard, M. Portnyagin, I. Bindeman, and D. Garbe-Schönberg, (2012), Along and across arc geochemical variations in NW Central America: Evidence for involvement of lithospheric pyroxenite. *Geochim. Cosmochim. Acta*, 84, 459–491.

- Hernández P. A., N. M. Pérez, J. C. Varekamp, B. Henriquez, A. Hernández, J. Barrancos, E. Padrón, D. Calvo, and G. Melián, (2007), Crater lake temperature changes of the 2005 eruption of Santa Ana volcano, El Salvador, Central America," *Pure Appl. Geophys.*, vol. 164, no. 12, pp. 2507–2522,.
- Hilton, D. R., C. J. Ramírez, R. Mora-Amador, T. P. Fischer, E. Füri, P. H. Barry, and A. M. Shaw, (2010) Monitoring of temporal and spatial variations in fumarole helium and carbon dioxide characteristics at Poás and Turrialba Volcanoes, Costa Rica (2001-2009). *Geochem. J.*, 44(5), 431–440.
- Hilton, D. R., T. P. Fischer, and B. Marty, (2002), Noble Gases and Volatile Recycling at Subduction Zones. *Rev. Mineral. Geochemistry*, 47(1), 319–370.
- Horrocks, L.A. (2001), Infrared Spectroscopy of Volcanic Gases at Masaya, Nicaragua, The Open Univ., Milton Keynes.
- Hurst, A.W., Bibby, H.M., Scott, B.J., McGuiness, M.J., (1991). The heat source of Ruapehu Crater Lake; deductions from the energy and mass balances. *Journal ofVolcanology and Geothermal Research* 46, 1–11.
- Iacono-Marziano G., A. Paonita, A., L., Rizzo, B. Scaillet, F., Gaillard, Noble gas solubilities in silicate melts: New experimental results and a comprehensive model of the effects of liquid composition, temperature and pressure. *Chemical Geology*, Volume 279, Issues 3–4, 2010, Pages 145-157, ISSN 0009-2541, https://doi.org/10.1016/j.chemgeo.2010.10.017.
- Janik, C. J., F. Goff, L. Fahlquist, A. I. Adams, A. Roldan, S. J. Chipera, P. E. Trujillo, and D. Counce, (1992), Hydrogeo- chemical exploration of geothermal prospects in the Tecuamburro Volcano region, Guatemala. *Geothermics*, 21, 447–481.
- Jaupart C., and S. Vergniolle, (1989), The generation and collapse of a foam layer at the roof of a basaltic magma chamber, *J. Fluid. Mech*., 203, 347-380.
- Javoy, M., Pineau, F., (1991), The volatiles record of a popping rock from the Mid-Atlantic ridge at 148N: chemical and isotopic composition of a gas trapped in the vesicles, *Earth Planet Sci. Lett* 107:598-611
- Javoy, M., Pineau, F. and Iiyama, I., (1978) Experimental determination of the isotopic fractionation between gaseous CO_2 and carbon dissolved in tholeiitic magma: a preliminary study. *Contrib. Mineral. Petrol*., 67, 35-39.

- Kantzas, E. P., A. J. S. McGonigle, G. Tamburello, A. Aiuppa, and R. G. Bryant, (2010), Protocols for UV camera volcanic SO2 measurements. *J. Volcanol. Geotherm. Res*., 194(1–3), 55–60.
- Kazahaya, K., H. Shinohara, G. Saito, (1994), Excessive degassing of Izu-Oshima volcano: magma convection in a conduit, *Bull. Volcanol*., 56 (3), 207–216. http://dx.doi.org/10.1007/BF00279605.
- Kelemen PB, Manning CE (2015) Reevaluating carbon fluxes in subduction zones, what goes down, mostly comes up. *PNAS* doi/10.1073/pnas.1507889112
- Kempter K. A., and G. L. Rowe, (2000). Leakage of Active Crater lake brine through the north flank at Rincón de la Vieja volcano, northwest Costa Rica, and implications for crater collapse, *Journal ofVolcanology and Geothermal Research* vol. 97, pp. 143–159.
- Kempter, K., (1997). Geologic evolution of the Rincón de la Vieja volcanic complex, northwestern Costa Rica - 159 págs., Univ. of Texas, Austin (Thesis Ph. D.).

  Kusakabe M., Y. Komoda, B. Takano, and T. Abiko, (2000). Sulfur isotopic effects in the disproportionation reaction of sulfur dioxide in hydrothermal fluids: Implications for the δ34S variations of dissolved bisulfate and elemental sulfur from active crater lakes,*J. Volcanol. Geotherm. Res.*, vol. 97, no. 1–4, pp. 287–307.
- Kutterolf, S., A. Freundt, and W. Peréz, (2008), The Pacific offshore record of Plinian arc volcanism in Central America: 2. Tephra volumes and erupted masses, *Geochemistry, Geophysics, Geosystems*, 9. doi:10.1029/2007GC001791.
- Kutterolf, S., A. Freundt, W. Pérez, H. Wehrmann, H.-U. Schmincke, (2007), Late Pleistocene to Holocene temporal succession and magnitudes of highly-explosive volcanic eruptions in west-central Nicaragua, *J. Volcanol. Geotherm. Res*., 163, 55–82.
- LaFemina, P., T. H. Dixon, R. Govers, E. Norabuena, H. Turner, A. Saballos, G. Mattioli, M. Protti, and W. Strauch (2009). Fore-arc motion and Cocos Ridge collision in Central America, *Geochemistry, Geophysics, Geosystems*, Vol. 10, Q05S14, p. 1 – 21
- Laiolo, M., D.Coppola, F. Barahona, J.E. Benítez, C. Cigolini, D. Escobar, R. Funes, E, Gutierrez, B. Henriquez, A. Hernandez, F. Montalvo, R. Olmos, M. Ripepe, A. Finizola (2017), Evidences of volcanic unrest on high-temperature fumaroles by satellite thermal monitoring: The case of Santa Ana volcano, El Salvador. *J. Volcanol. Geotherm. Res.*, 340, 170-179, http://dx.doi.org/10.1016/j.jvolgeores.2017.04.013.

- Leeman, W. P., M. J. Carr, and J. D. Morris, (1994), Boron geochemistry of the Central American Volcanic Arc: Constraints on the genesis of subduction-related magmas. *Geochim. Cosmochim. Acta*, 58(1), 149–168.
- Lesne, P., S.C. Kohn, J. Blundy, F. Whitham, R.E. Botcharnikov, and H. Behrens (2011), Experimental simulation of closed-system degassing in the system basalt-H_2O-CO_2-S-Cl, *J. Petrol.*, 32, 1737-1762.

  Lewicki J. L., P.J. Kelly, D. Bergfeld, R.G. Vaughan, J.B. Lowenstern, (2017). Monitoring gas and heat emissions at Norris Geyser Basin, Yellowstone National Park, USA based on a combined eddy covariance and Multi-GAS approach, *Journal of Volcanology and Geothermal Research*, vol. 347, pp. 312-326,ISSN 0377-0273,https://doi.org/10.1016/j.jvolgeores.2017.10.001.
- Longpré, M.A., J. Stix, F. Costa, E. Espinoza, A. Muñoz (2014), Magmatic processes and associated timescales leading to the January 1835 eruption of Cosigüina volcano, Nicaragua, *J. Petrol*., 55 (6), 1173–1201.
- López D., Ramson, Monterrosa, T. Soriano, Barahona, and J. Bundschuh, (2009) *Volcanic arsenic and boron pollution of Ilopango lake, El Salvador*. DOI: 10.1201/b11334-17

- Lucic, G., J. Stix, B. Sherwood Lollar, G. Lacrampe-Couloume, A. Muñoz, and M. I. Carcache, (2014), The degassing character of a young volcanic center: Cerro Negro, Nicaragua. *Bull. Volcanol.*, 76(9), 1–23.
- McGonigle, A. J. S., C. Oppenheimer, B. Galle, T. A. Mather, and D. M. Pyle, Walking traverse and scanning DOAS measurements of volcanic gas emission rates, (2002) *Geophys. Res. Lett*., 29(20), 1985, doi:10.1029/2002GL015827.
- MacKenzie, L., G. A. Abers, K. M. Fisher, E. M. Syracuse, J. M. Protti, V. Gonzales, and W. Strauch (2008), Crustal structure along the southern Central American volcanic front, *Geochemistry, Geophysics, Geosystems*, 9, Q08S09, doi:10.1029/ 2008GC001991.
- Macpherson, C. G., and D. P. Mattey (1994), Carbon isotope variations of CO_2 in LauBasin basalts and ferro basalts. *Earth Planet. Sci. Lett*., 121, 263–276.
- Marshall, J. S., D. M. Fisher, and T. W. Gardner (2000), Central Costa Rica deformed belt: Kinematics of diffuse faulting across the western Panama Block, Tectonics, 19, 468–497, doi:10.1029/1999TC001136.

- Martin, R.S., G.M. Sawyer, L. Spampinato, G.G. Salerno, C. Ramirez, E. Ilyinskaya, M.L.I. Witt, T.A. Mather, I.M. Watson, J.C. Phillips, C. Oppenheimer (2010), A total volatile inventory for Masaya Volcano, Nicaragua, *J. Geophys. Res.*, Solid Earth, 115 (9), art. no. B09215.
- Martinez-Diaz, J., J. Alvarez-Gomez, B. Benito, and D. Hernandez (2004), Triggering of destructive earthquakes in El Salvador, *Geology*, 32(1), 65–68.
- Martinez-Hackert, B., Bajo, J., Escobar, D., Gutierrez, E., Mixco, L., Hernandez, W., (2015). Chaparrastique (San Mighel) Volcano Eruptions Since Dec. 29th, 2013, El Salvador, Abstract V23A-3087, Presented at 2015 Fall Meeting, AGU, San Francisco, Calif., 14– 18 Dec.
- Marty, B., (2012), The origins and concentrations of water, carbon, nitrogen and noble gases on earth. *Earth and Planetary Science Letters* 313–314, 56–66
- Marty, B. Neon and xenon isotopes in MORB: implications for the earth–atmosphere evolution (1989). *Earth Planet. Sci. Lett.* 94, 45–56.
- Marty B, Jambon A (1987), C/3He fluxes from the solid Earth: implications for carbon geodynamics. *Earth Planet. Sci. Lett*. 83, 16–26.
- Mastin, L.G., J.B. Witter, (2000). The hazards of eruptions through lakes and seawater, *Journal of Volcanology and Geothermal Research,* Volume 97, Issues 1–4, , Pages 195-214, ISSN 0377-0273, https://doi.org/10.1016/S0377-0273(99)00174-2.
- Mather, T.A., D.M. Pyle, V.I. Tsanev, A.J.S. McGonigle, C. Oppenheimer, A.G. Allen, (2006), A reassessment of current volcanic emissions from the Central American arc with specific examples from Nicaragua, J. *Volcanol. Geotherm. Res*., 149, 297–311.
- Matías Gómez, R. O., Rose,W. I., Palma, J. L., and Escobar-Wolf, R. (2012). Notes on a map of the 1961–2010 eruptions of Volcán de Pacaya, Guatemala. *Geol. Soc. Am.* Digit.Map Chart Ser. 10, 10. doi: 10.1130/2012.DMCH010
- Matías, Gómez R.O., W. I. Rose, J. L. Palma, and R. Escobar-wolf, (2012), Notes on a Map of the 1961 – 2010 Eruptions of Volcán de Pacaya , Guatemala ABSTRACT, *Geol. Soc. Am*., vol. Digital Ma, pp. 1–10,.
- Mattey, D. P., (1991), Carbon dioxide solubility and carbon isotope fractionation in basaltic melt, *Geochimica et Cosmochimica Acta*,

55,(11), 3467-3473, http://dx.doi.org/10.1016/0016-7037(91)90508-3.

- Mavrogenes, J.A., O'Neill, H. St. C., (1999) The relative effects of pressure, temperature and oxygen fugacity on the solubility of sulfide in mafic magmas. Geochimica et Cosmochimica Acta 63, 1173–1180.
- McBirney, A.R. (1956), The Nicaraguan volcano Masaya and its caldera, *Eos, Transactions American Geophysical Union*, 37 (1), 83-96.
- Molina, F., and J. Martí, (2016). The Borinquen geothermal system (Cañas Dulces caldera, Costa Rica), *Geothermics*, vol. 64, pp. 410–425.
- Molina, F., Martì J., Aguirre, G., Vega, E., Chavarria, L., (2014). Stratigraphy and structure of the Canas Dulces caldera (Costa Rica). *Geol. Soc. Am.* Bull. 110 (11), 1448-1466
- Moreira M., (2013), Noble gas constraints on the origin and evolution of Earth's volatiles, *Geochemical Perspect.*, vol. 2, no. 2, pp. 229–403.
- Moretti, R. Baker, D.R., (2008), Modeling the interplay of fO_2 and fS_2 along the FeS-silicate melt equilibrium, *Chemical Geology*, 256, 285-297
- Moretti, R. and P. Papale, (2004), On the oxidation state and volatile behaviour in multicomponent gas–melt equilibria, *Chem. Geol*., 213, 265-280, doi: 10.1016/j.chemgeo.2004.08.048.
- Moretti, R., P. Papale, and G. Ottonello, (2003), A model for the saturation of C-O-H-S fluids in silicate melts, in *Volcanic degassing*, Geological Society London, Special Publication, 213, 81-101.
- Morris, J. D.,W. P. Leeman, and F. Tera (1990), The subducted component in island arc lavas: Constraints from Be isotopes and B-Be systematics. *Nature*, 344, 31–36, doi:10.1038/ 344031a0.
- Mooser, F., Meyer-Abich, H., McBirney, A., (1958), Catalogue of the Active Volcanoes of the World. International Association of Volcanology, Part VI Central America: Naples. 34 pp.
- Moune, S., Gauthier, P.-J., Delmelle, P., (2010), Trace elements in the particulate phase of the plume of Masaya Volcano, Nicaragua, J. *Volcanol. Geotherm. Res*., 193 (3-4), 232-244.
- Moune, S, F. Holtz, and R.E. Botcharnikov, (2009), Sulphur solubility in andesitic to basaltic melts: Implications for Hekla volcano, Cotrib. Mineral. Petrol., 157, 691-707
- Moussallam Y., N. Peters, C. Ramírez, C. Oppenheimer, and A. Aiuppa, (2014), Characterization of the magmatic signature in gas

emissions from Turrialba volcano, Costa Rica. *Solid Earth*, 2293–2320.

- Nadeau, P.A., and G. Williams-Jones, (2009), Apparent downwind depletion of volcanic SO_2 flux - Lessons from Masaya Volcano, Nicaragua, *Bull. Volcanol*., 71 (4), 389-400.
- Noll Jr., P.D., Newsom, H.E., Leeman, W.P., Ryan, J.G., (1996). The role of hydrothermal fluids in the production of subduction zone magmas: evidence from siderophile and chalcophile trace elements and boron. *Geochim. Cosmochim. Acta* 60, 587–611.
- Ohmoto H. and A. C. Lasaga (1982). Kinetics of reactions between aqueous sulfates and sulfides in hydrothermal systems, *Geochim. Cosmochim. Acta*, vol. 46, no. 10, pp. 1727–1745.
- Oikawa T., M. Yoshimoto, S. Nakada, F. Maeno, J. Komori, and T. Shimano, (2016). Reconstruction of the 2014 eruption sequence of Ontake Volcano from recorded images and interviews," *Earth, Planets and space,* pp.68-79, DOI 10.1186/s40623-016-0458-5
- Oppenheimer, C., Fischer, T.P., Scaillet, B., (2014), Volcanic degassing: process and impact. In: Holland, H.D., Turekian, K.K. (Eds.), *Treatise on Geochemistry*, The Crust, second ed. 4. Elsevier, pp. 111–179.
- Oppenheimer, C., A.S. Lomakina, P.R. Kyle, N.G. Kingsbury, and M. Boichu, (2009), Pulsatory magma supply to a phonolite lava lake, *Earth Planet. Sci. Lett*., 284 (3-4), 392-398
- Oppenheimer, C., A.J.S. McGonigle, P. Allard, M.J. Wooster, V. Tsanev (2004), Sulfur, heat, and magma budget of Erta 'Ale lava lake, Ethiopia, *Geology*, 32 (6), 509-512.
- Oppenheimer, C., (1992). Sulphur eruptions at Volcan Poás, Costa Rica. *Journal ofVolcanology and Geothermal Research* 49, 1–21.
- OVSICORI (Observatorio Vulcanologico y Sismologico de Costa Rica), 1995. Actividad eruptiva del volcan Rincón de la Vieja durante los dias 6–13 de noviembre, 1995. *Open report, OVSI- CORI-UNA*, p. 42.
- Ozima, M., Podosek, F.A., (1983). Noble Gas Geochemistry. *Cambridge University Press* (340 pp.)
- Palma, J.L., E.S. Calder, D. Basualto, S. Blake, and D.A. Rothery, (2008), Correlations between SO2 flux, seismicity, and outgassing activity at the open vent of Villarrica Volcano, Chile, *J. Geophys. Res*., 113, B10201, doi:10.1029/2008JB005577.

- Pasternack G. B., J. C. Varekamp, (1997). Volcanic lake systematics I. Physical constraints. *Bull. Volcanol*, 58: 528-538
- Patino, L. C., M. J. Carr, and M. D. Feigenson, (2000), Local and regional variations in Central American arc lavas controlled by variations in subducted sediment input. *Contrib. to Mineral. Petrol*., 138(3), 265–283.
- Patrick, M.R., T. Orr, A.J. Sutton, E. Lev, D. Fee (2016), Shallowly driven fluctuations in lava lake outgassing, Kīlauea Volcano, Hawai'I, *Earth Planet. Sci. Lett*., 433, 326–338
- Patrick, M., T. Orr, A.J. Sutton, T. Elias, D. Swanson, (2013) The first five years of Kilauea's summit eruption in Halema'uma'u crater, 2008-2013. U.S. Geological Survey Fact Sheet 2013–3116. http://dx.doi.org/10.3133/fs20133116
- Pearson, S.C.P., Kiyosugi, K., Lehto, H.L., Saballos, J.A., Connor, C.B., Sanford, W.E., (2012), Integrated geophysical and hydrothermal models of flank degassing and fluid flow at Masaya volcano, Nicaragua, *Geochemistry, Geophysics, Geosystems*, 13 (5), art. no. Q05011.
- Peccerillo. A., S.R. Taylor, (1976), Rare earth elements in East Carpathian volcanic rocks, *Earth Planet. Sci. Lett.* 32(2), 121-126, doi: 10.1016/0012-821X(76)90050-9.
- Pérez, W., A. Freundt, S. Kutterolf, H.-U. Schmincke, (2009), The Masaya Triple Layer: A 2100 year old basaltic multi-episodic Plinian eruption from the Masaya Caldera Complex (Nicaragua), *J. Volcanol. Geotherm. Res.*, 179 (3-4), 191-205.
- Pérez, W., and A. Freundt (2006), The youngest highly explosive basaltic eruptions from Masaya Caldera (Nicaragua). In: Rose,W.I., Bluth, G.J.S., Carr, M.J., Ewert, J.W., Patino, L.C., Vallance, J.W. (Eds.), Volcanic Hazards in Central America, *Geol. Soc. Am. Spec. Pap*., 412, 189–207.
- Pering T. D., G. Tamburello, A. J. S. McGonigle, A. Aiuppa, A. Cannata, G. Giudice, and D. Patanè, (2014). High time resolution fluctuations in volcanic carbon dioxide degassing from Mount Etna, *J. Volcanol. Geotherm. Res.*, vol. 270, pp. 115–121.http://dx.doi.org/10.1016/j.jvolgeores.2013.11.014
- Peters, N. et al., 2015. Use of motion estimation algorithms for improved flux measurements using SO2 cameras. Journal of *Volcanology and Geothermal Research*, 300, pp.58–69. http://dx.doi.org/10.1016/j.jvolgeores.2014.08.031
- Platt, U., and Stutz, J. (2008), Differential Optical Absorption Spectroscopy: Principles and Applications, *Physics of Earth and*

Space Environments, Springer Berlin Heidelberg, doi: 10.1007/978-3-540-75776-4_2.

- Poreda, R.J., Craig, H., (1989). Helium isotope ratios in circum-Pacific volcanic arcs. *Nature* 338, 473–478
- Portnyagin, M. V., K. Hoernle, and N.L. Mironov, (2014), Contrasting compositional trends of rocks and olivine-hosted melt inclusions from Cerro Negro volcano (Central America): Implications for decompression-driven fractionation of hydrous magmas, *International Journal of earth Sciences*, 103 (7), 1963-1982
- Protti, M., McNally, K., Pacheco, J., González, V., Montero, C., Segura, J., Brenes, J., Barboza, V., Malavassi, E., Güendel, F., Simila, G., Rojas, D., Velasco, A., Mata, A., Schillinger, W., (1995). The March 25, 1990 (Mw= 7.0, M L= 6.8), earthquake at the entrance of the Nicoya Gulf, Costa Rica: its prior activity, foreshocks, aftershocks, and triggered seis- micity. *J. Geophys. Res*. 100:20345. http://dx.doi.org/10.1029/94jb03099
- Pullinger, C., (1998), Evolution of the Santa Ana volcanic complex, El Salvador [Master thesis]: Houghton, Michigan Technological University, 151 pp.
- Putirka, K. D. (2008), Thermometers and barometers for volcanic systems, in Minerals, Inclusions and Volcanic Processes, edited by K. D. Putirka and F. J. Tepley, pp. 61–120, *The Mineral. Soc. of Am*., Chantilly, Va.
- Richer M., C. P. Mann, and J. Stix, (2004), Mafic magma injection triggers eruption at Ilopango Caldera, El Salvador, Central America, *Spec*. Pap. 375 Nat. Hazards El Salvador, pp. 175–190.
- Rizzo, A. L., Caracausi, A., Chavagnac, V., Nomikou, P., Polymenakou, P. N., Mandalakis, M., … Lampridou, D. (2016a). Kolumbo submarine volcano (Greece): An active window into the Aegean subduction system. *Scientific Reports*, *6*(May), 1–9. https://doi.org/10.1038/srep28013
- Rizzo, A. L., Piazza, A. Di, Moor, J. M. De, & Alvarado, G. E. (2016b). *Geochemistry, Geophysics, Geosystems*, 1–17. https://doi.org/10.1002/2016GC006525.
- Rizzo, A. L., F. Barberi, M. L. Carapezza, A. Di. Piazza, L. Francalanci, F. Sortino, and W. D'Alessandro (2015a), New mafic magma refilling a quiescent volcano: Evidence from He-Ne-Ar isotopes during the 2011–2012 unrest at Santorini, Greece, *Geochemistry, Geophysics, Geosystems*, 16, 798–814, doi:10.1002/2014GC005653.

- Rizzo, A. L., Federico, C., Inguaggiato, S., Sollami, A., Tantillo, M., Vita, F., … Liuzzo, M. (2015b). The 2014 effusive eruption at Stromboli volcano (Italy): Inferences from soil CO2 flux and $^{3}He/^{4}He$ ratio in thermal waters. *Geophysical Research Letters*, *42*(7), 2235–2243. https://doi.org/10.1002/2014GL062955

- Robidoux, P., A. Aiuppa, S. Rotolo, A.L., Rizzo, and E.H. Hauri (2017a), The volatile content of mafic-to-intermediate magmas from San Cristóbal volcano, Nicaragua, *Lithos*, 272-273, 147-163
- Robidoux, P., S.G. Rotolo, A. Aiuppa, G. Lanzo, E.H. Hauri, (2017b), Geochemistry and volatile content of magmas feeding explosive eruptions at Telica volcano (Nicaragua), *J. Volcanol. Geotherm. Res*., 341, 131–148, dx.doi.org/10.1016/j.jvolgeores.2017.05.007
- Rodríguez, L., I. M. Watson, W. I. Rose, Y. K. Branan, G. J. S. Bluth, G. Chigna, O. Matías, D. Escobar, S. Carn, and T.P. Fischer, (2004), SO2 emissions to the atmosphere from active volcanoes in Guatemala and El Salvador, 1999-2002. *J. Volcanol. Geotherm. Res*., 138(3–4), 325–344.
- Roedder E. (1958) Technique for the extraction and partial chemical analysis of fluid-filled inclusions from minerals: *Econ.Geology*, Vol. 53, pp.235-269.
- Roedder E. (1963), Studies of fluid inclusions II: Freezing data and their interpretation, *Econ. Geology*, Vol. 58, pp.167-211.
- Roggensack, K., (2001a), Unraveling the 1974 eruption of Fuego volcano (Guatemala) with small crystals and their young melt inclusions. *Geology*, 29, 911-914, doi:10.1130/0091-7613(2001)029<0911:UTEOFV>2.0.CO2
- Roggensack, K., R.L. Hervig, S.B. McKnight, and S.N. Williams, (1997), Explosive basaltic volcanism from Cerro Negro: Influence of volatiles on eruptive style, *Science*, 277, 1639-1642
- Rose, W.I., Palma, J.L., Escobar Wolf, R., and Matías Gomez, R.O., (2013), A 50 yr eruption of a basaltic composite cone: Pacaya, Guatemala, in Rose, W.I., Palma, J.L., Delgado Granados, H., and Varley, N., eds., Understanding Open-Vent Volcanism and Related Hazards: *Geological Society of America* Special Paper 498, p. 1–21, doi:10.1130/2013.2498(01).
- Rose, W.I., Jr., Newhall, C.G., Bornhorst, T.J. and Self, S., (1987). Quaternary silicic pyroclastic deposits of Atitlan Caldera, Guatemala. In: S.N. Williams and M.J. Carr (Editors). Richard E. Stoiber 75th Birthday *Volume. J. Volcanol. Geotherm. Res*., 33: 57-80.

- Rothery, D.A., Coppola, D., Saunders, C. (2005), Analysis of volcanic activity patterns using MODIS thermal alerts, *Bull. Volcanol*., 67 (6), 539-556.
- Rouwet D, Morrissey MM., (2015). Mechanisms of crater lake breaching eruptions, In: Rouwet D, Christenson BW, Tassi F, Vandemeulebrouck J (eds) Volcanic lakes. *Springer,* Heidelberg.
- Rye, R. O. (2005). A review of the stable-isotope geochemistry of sulfate minerals in selected igneous environments and related hydrothermal systems, *Chem. Geol.*, vol. 215, no. 1–4 SPEC. ISS., pp. 5–36.
- Rymer, H., B. Van Wyk De Vries, J. Stix, and G. Williams-Jones, (1998), Pit crater structure and processes governing persistent activity at Masaya Volcano, Nicaragua, *Bull. Volcanol*., 59 (5), 345-355
- Saginor I., E. Gazel, M. J. Carr, C. C. Swisher, and B. Turrin, (2011), New Pliocene – Pleistocene volcanic record Ar / 39 Ar ages fi ll in temporal gaps in the Nicaraguan, *J. Volcanol. Geotherm. Res*., vol. 202, no. 1–2, pp. 143–152.
- Sadofsky, S. J., M. Portnyagin, K. Hoernle, and P. van den Bogaard, (2008), Subduction cycling of volatiles and trace elements through the Central American volcanic arc: Evidence from melt inclusions. *Contrib. to Mineral. Petrol*., 155(4), 433–456.
- Salters V. J. M., and A. Stracke, (2004) Composition of the depleted mantle, *Geochemistry, Geophysics, Geosystems*, 5(5).
- Sano Y., & Fischer T. (2013). The Analysis and Interpretation of Noble Gases in Modern Hydrothermal Systems. The Noble Gases as Geochemical Tracers. 249-317. 10.1007/978-3-642-28836-4_10.
- Sano, Y., and S. N. Williams, (1996), Fluxes of mantle and subducted carbon along convergent plate boundaries. *Geophys. Res. Lett*., 23(20), 2749–2752.
- Sano, Y., and B. Marty (1995), Origin of carbon in fumarolic gas from island arcs. *Chem. Geol*., 119, 265–274.
- Saxby J., J. Gottsmann, K. Cashman, and E. Gutiérrez, (2016), Magma storage in a strike-slip caldera, *Nat. Commun.*, vol. 7, p. 12295, Jul..
- Scarlato P., S. Mollo, E. Del Bello, A. von Quadt, R. J. Brown, E. Gutierrez, B. Martinez-Hackert, and P. Papale, (2017), The 2013 eruption of Chaparrastique volcano (El Salvador): Effects of magma storage, mixing, and decompression, Chem. Geol., vol. 448, pp. 110–122.
- Schaefer, L. N., T. Oommen, C. Corazzato, a. Tibaldi, and W. I. Rose, (2012), Numerical modeling of volcanic slope instability and related

hazards at Pacaya Volcano, Guatemala. 46th US Rock Mech. / *Geomech. Symp*. 2012, vol. 4, pp. 2844–2851.

- Shaw, A. M., D. R. Hilton, T. P. Fischer, J. a. Walker, and G. a M. de Leeuw, (2006), Helium isotope variations in mineral separates from Costa Rica and Nicaragua: Assessing crustal contributions, timescale variations and diffusion-related mechanisms. *Chem. Geol*., 230(1–2), 124–139.
- Scolamacchia, T., Macías, J.L., Sheridan, M.F., Hughes, S.R., (2005), Morphology of ash aggregates in wet pyroclastic surge deposits of the 1982 eruption of El Chichón volcano, Mexico. *Bull. Volcanol*. 68 (2), 171–200.
- Shaw, A. M., D. R. Hilton, T. P. Fischer, J. a. Walker, and G. E. Alvarado, (2003), Contrasting He-C relationships in Nicaragua and Costa Rica: Insights into C cycling through subduction zones. *Earth Planet. Sci. Lett*., 214, (3–4), 499–513.
- Shinohara H., Yoshikawa S., Miyabuchi Y. (2015) Degassing Activity of a Volcanic Crater Lake: Volcanic Plume Measurements at the Yudamari Crater Lake, Aso Volcano, Japan. In: Rouwet D., Christenson B., Tassi F., Vandemeulebrouck J. (eds) Volcanic Lakes. *Advances in Volcanology*. Springer, Berlin, Heidelberg
- Shinohara H., J. Hirabayashi, K. Nogami, and M. Iguchi, (2011). Evolution of volcanic gas composition during repeated culmination of volcanic activity at Kuchinoerabujima volcano, Japan, *J. Volcanol. Geotherm. Res.*, vol. 202, no. 1–2, pp. 107–116.
- Shinohara, H. (2008), Excess degassing from volcanoes and its role on eruptive and intrusive activity, *Reviews of Geophysics*, 46 (4), art. no. RG4005.
- Shinohara, H., A. Aiuppa, G. Giudice, S. Gurrieri, and M. Liuzzo (2008), Variation of H_2O/CO_2 and CO_2/SO_2 ratios of volcanic gases discharged by continuous degassing of Mount Etna volcano, Italy, *J. Geophys. Res*., 113, B09203, doi:10.1029/2007JB005185.
- Shinohara, H., (2005), A new technique to estimate volcanic gas composition: Plume measurements with a portable multi-sensor system. *J. Volcanol. Geotherm. Res*., 143(4), 319–333.
- Snyder, G., R. Poreda, A. G. Hunt, and U. Fehn. (2001). Regional variations in volatile composition: Isotopic evidence for carbonate recycling in the Central American volcanic arc,. *Geochemistry, Geophysics, Geosystems*, 2, 10.129/2001GC000163,.
- Snyder G, Poreda RJ, Fehn U, Hunt A. (2003) Sources of nitrogen and methane in Central American geothermal settings: noble gas and 129I evidence for crustal and magmatic volatile components.

Geochemistry, Geophysics, Geosystems, 4:9001. doi:10.1029/2002GC000363.

- Spampinato, L., G. Ganci, P.A. Hernández, D. Calvo, D. Tedesco, N.M. Pérez, S. Calvari, C. Del Negro, M.M. Yalire, (2013), Thermal insights into the dynamics of Nyiragongo lava lake from ground and satellite measurements, *J. Geophys. Res*., 118 (11), 5771-5784.
- Stephens, K., J. Biggs, S. Ebmeier, N. Young, C. Wauthier (2017), Uncovering the mysteries behind lava lake deformation source mechanisms: a case study of the ephemeral lava lake at Masaya volcano, Nicaragua, Proc. IAVCEI 2017 conference, Abstract #652, Portland, OR, August 2017.
- Stevenson, D.S., and S. Blake, (1998), Modelling the dynamics and thermodynamics of volcanic degassing, *Bull. Volcanol*., 60 (4), 307–317. http://dx.doi.org/10.1007/s004450050234.
- Stix, J., de Moor, J. M. (2018). Understanding and forecasting phreatic eruptions driven by magmatic degassing. *Earth, Planets and Space*, *70*(1), 83.
- Stix, J. (2007), Stability and instability of quiescently active volcanoes: the case of Masaya, Nicaragua, *Geology*, 35, 535–538.
- Stoiber, R.E., S.N. Williams, and B.J. Huebert (1986), Sulfur and halogen gases at Masaya caldera complex, Nicaragua: total flux and variations with time. *J. Geophys. Res.,* 91, 12,215-12,231.
- Stoiber, R. E., and M. J. Carr (1973), Quaternary vol-canic and tectonic segmentation of Central Ameri- ca, Bull. Volcanol., 37(3), 304–325.
- Symonds R. B., C. J. Janik, W. C. Evans, B. E. Ritchie, D. Counce, R. J. Poreda, et al. (2003). Scrubbing masks magmatic degassing during repose at Cascade-Range and Aleutian-Arc volcanoes, *US Geol. Surv. Open-File Rep.*, vol. 3, pp. 3–435.
- Symonds, R. B., T. M. Gerlach and M. H. Reed (2001). Magmatic gas scrubbing: implications for volcano monitoring. *J. Volcanol. Geotherm. Res*., 108, 303- 341.
- Symonds, R.B., Rose,W.I., Bluth, G.J.S., Gerlach, T.M., (1994), Volcanic-gas studies: methods, results and applications. *Rev. Mineral*. 30, 1–66.
- Syracuse, E. M., and G. A. Abers (2006), Global compilation of variations in slab depth beneath arc volcanoes and implications. *Geochemistry, Geophysics, Geosystems*, 7(5), Q05017, doi:10.1029/2005GC001045.
- Takano B., S. Ohsawa, R.B Glover, (1994). Surveillance of Ruapehu Crater Lake, New Zealand, by aqueous polythionates, *Journal of*

Volcanology and Geothermal Research Volume 60, Issue 1, Pages 29-57, ISSN 0377-0273, https://doi.org/10.1016/0377-0273(94)90096-5.

- Tamburello, G. (2015), Ratiocalc: Software for processing data from multicomponent volcanic gas analyzers, *Comp. Geosci*., 82, 63-67.
- Tamburello, G., Agusto, M., Caselli, A., Tassi, F., Vaselli, O., Calabrese, S., et al. (2015). Intense magmatic degassing through the lake of Copahue volcano, 2013–2014. *Journal of Geophysical Research Solid Earth*, 120, 6071–6084. https://doi.org/10.1002/2015JB012160
- Tamburello, G., Aiuppa, A., Kantzas, E.P., McGonigle, A.J.S., Ripepe, M., (2012). Passive vs. active degassing modes at an open-vent volcano (Stromboli, Italy). *Earth Planet. Sci. Lett*. 359–360, 106–116.
- Tamburello, G., E. P. Kantzas, A. J. S. McGonigle, A. Aiuppa, and G. Giudice, (2011), UV camera measurements of fumarole field degassing (La Fossa crater, Vulcano Island). *J. Volcanol. Geotherm. Res*., 199(1–2), 47–52.
- Tassi, F., O. Vaselli, B. Capaccioni, C. Giolito, E. Duarte, E. Fernandez, et al. (2005), The hydrothermal-volcanic system of Rincón de la Vieja volcano (Costa Rica): A combined (inorganic and organic) geochemical approach to understanding the origin of the fluid discharges and its possible application to volcanic surveillance, *Journal of Volcanology and Geothermal Research*, Volume 148, Issues 3–4, Pages 315-333.
- Tassi, F., O. Vaselli, E. Fernandez, E. Duarte, M. Martinez, A. Delgado et al. (2009) Morphological and geochemical features of crater lakes in Costa Rica: An overview," *J. Limnol.*, vol. 68, no. 2, pp. 193–205.
- Tassi, F., O. Vaselli, V. Barboza, E. Fernandez, and E. Duarte, (2004), Fluid geochemistry and seismic activity in the period 1998-2002 at Turrialba Volcano (Costa Rica). *Ann. Geophys*. 47, 1501-1511,.
- Trull, T., Nadeau, S., Pineau, F., Polve, M., Javoy, M., (1993), C–He systematics in hotspot xenoliths: implications for mantle carbon contents and carbon recycling. *Earth Planet. Sci. Lett*. 118, 43–64.
- Van Wyk de Vries, B., (1993), Tectonics and magma evolution of Nicaraguan volcanic systems. PhD thesis, Open University, Milton Keynes, UK

- Varekamp J. C and Rowe GL Jr. (eds.) (2000) Crater Lakes. *Journal of Volcanology and Geothermal Research* (Special Issue) 97: 508
- Vaselli, O., F. Tassi, E. Duarte, and E. Fernandez, (2010), Evolution of fluid geochemistry at the Turrialba volcano (Costa Rica) from 1998 to 2008. *Bull Volcanol.* 72, 397–410..
- Vergniolle, S., and E. Bouche (2016), Gas-driven lava lake fluctuations at Erta 'Ale volcano (Ethiopia) revealed by MODIS measurements, *Bull. Volcanol*., 78, 60, 1-28.
- Wade J. A., Plank T., Melson W. G., Soto G. J. and Hauri E. H. (2006) The volatile content of magmas from Arenal volcano, Costa Rica. J. *Volcanol. Geoth. Res*. 157, 94–120.
- Walker, J. A., A. P. Teipel, J. G. Ryan, and E. Syracuse (2009), Light elements and Li isotopes across the northern portion of the Central American subduction zone. *Geochemistry, Geophysics, Geosystems*, 10, Q06S16, doi:10.1029/2009GC002414.
- Walker, J. A, L. C. Patino, M. J. Carr and M. D. Feigenson, (2001), Slab control over HFSE depletions in central Nicaragua. *Earth Planet. Sci .Lett*., 192, 533-543.
- Walker, J. A., J. E. Mickelson, R. B. Thomas, L. C. Patino, B. Cameron, M. J. Carr, M. D. Feigenson, and R. L. Edwards (2007), U-series disequilibria in Guatemalan lavas, crustal contamination, and implications for magma genesis along the Central American subduction zone. *J. Geophys. Res*., 112, B06205, doi:10.1029/2006JB004589.
- Walker, J. A., K. Roggensack, L. C. Patino, B. I. Cameron, and O. Matías, (2003), The water and trace element contents of melt inclusions across an active subduction zone. *Contrib. to Mineral. Petrol*., 146(1), 62–77.
- Walker, J. A., S.N. Williams, R.I. Kalamarides, and M.D. Feigenson (1993), Shallow open-system evolution of basaltic magma beneath a subduction zone volcano—The Masaya Caldera Complex, Nicaragua, *J. Volcanol. Geotherm. Res*., 56, 379–400.
- Wallace, P.J., Plank, T., Edmonds, M., Hauri, E.H., (2015), Volatiles in magmas. In: Sigurdsson, H., Houghton, B., McNutt, S., Rymer, H., Stix, J. (Eds.), *The Encyclopedia of Volcanoes, second edition* Academic Press, Elsevier, pp. 163–183.
- Wallace, P. J., (2005), Volatiles in subduction zone magmas: Concentrations and fluxes based on melt inclusion and volcanic gas data. *J. Volcanol. Geotherm. Res*., 140(1–3), 217–240.

- Wardman, J.; Sword-Daniels, V.; Stewart, C. and Wilson, T. 2012. Impact assessment of the May 2010 eruption of Pacaya volcano, Guatemala, *GNS Science Report* 2012/09. 90 p.
- Wehrmann, H., K. Hoernle, M. Portnyagin, M. Wiedenbeck, and K. Heydolph, (2011), Volcanic CO_2 output at the Central American subduction zone inferred from melt inclusions in olivine crystals from mafic tephras. *Geochemistry, Geophysics, Geosystems*, 12(6), 1–16.
- Werner, C., C. Kern, D. Coppola, J.J. Lyons, P.J. Kelly, K.L. Wallace, D.J. Schneider, R.L. Wessels, (2017), Magmatic degassing, lava dome extrusion, and explosions from Mount Cleveland volcano, Alaska, 2011–2015: Insight into the continuous nature of volcanic activity over multi-year timescales *J. Volcanol. Geotherm. Res*., 337, 98-110.
- Werner, R., K. Hoernle, U. Barckhausen, and F. Hauff (2003), Geodynamic evolution of the Gala´pagos hot spot system (Central East Pacific) over the past 20 m. y.: Constraints from morphology, geochemistry, and magnetic anomalies, *Geochemistry, Geophysics, Geosystems*, 4(12), 1108, doi:10.1029/ 2003GC000576.
- Williams, S.N., 1983. Plinian airfall deposits of basaltic composition. *Geology* 11, 211–214
- Williams-Jones, G., H. Rymer, and D.A. Rothery, (2003), Gravity changes and passive SO_2 degassing at the Masaya caldera complex, Nicaragua, *J. Volcanol. Geoth. Res*., 123 (1-2), 137-160.
- Witt, M. L. I., Mather, T. A., Pyle, D. M., Aiuppa, A., Bagnato, E. & Tsanev, V. I. (2008). Mercury and halogen emissions from Masaya and Telica volcanoes, Nicaragua. *Journal of Geophysical Research*, 113, B06203
- Witter, J. B., C. Victor, P. Kress, J. Delmelle, and J. Stix (2004), Volatile degassing, petrology, and magma dynamics of the Villarrica Lava Lake, Southern Chile, *J. Volcanol. Geotherm. Res.*, 134, 303–337.
- Wooster, M.J., B. Zhukov, D. Oertel, (2003), Fire radiative energy for quantitative study of biomass burning: Derivation from the BIRD experimental satellite and comparison to MODIS fire products, *Remote Sensing of Environment*, 86 (1), 83-107
- Wright, R., H. Garbeil, and A.J.L. Harris (2008), Using infrared satellite data to drive a thermo-rheological/stochastic lava flow emplacement model: A method for near-real-time volcanic hazard assessment, *Geophysical Research Letters*, 35 (19), art. no. L19307

- Wright, R., L. Flynn, H. Garbeil, A.J.L. Harris, E. Pilger, (2002), Automated volcanic eruption detection using MODIS, *Remote Sensing of Environment*, 82 (1), 135-155
- Wright, R., L.P. Flynn, H. Garbeil, A.J.L. Harris, E. Pilger, (2004), MODVOLC: Near-real-time thermal monitoring of global volcanism, *J. Volcanol. Geoth. Res*., 135 (1-2), 29-49
- Wunderman, R.L. and Rose W.I. (1984) Amatitlán, an actively resurging caldera 10 km south of Guatemala City. *J. Geophys. Res*. 89: 8525-8539.
- Zimmer, M.M., Fischer, T.P., Hilton, D.R., Alvarado, G.E., Sharp, Z.D., Walker, J.A., (2004). Nitrogen systematics and gas fluxes of subduction zones: insights from Costa Rica arc volatiles. *Geochemistry Geophysics Geosystems* 5. doi:10.1029/2003GC000651.
- Zurek, J.M., (2016), Multidisciplinary Investigation of the Evolution of Persistently Active Basaltic Volcanoes, PhD thesis, Simon Fraser University, Canada

10 Acnowledgements

This research received funding from the Deep Carbon Observatory Deep Earth Carbon Degassing program and from the European Research Council (FP7/ERC grant agreement n. 305377). I wish to thank OVSICORI-UNA staff, and ICE (Costa Rica), INETER (Nicaragua), MARN and UES (El Salvador) and RIESCA project team for the logistic support during the periods abroad in Central America. I wish to thank the Deep Carbon Observatory's Biology Meets Subduction project team I wish to thank my tutor prof. Alessandro Aiuppa for the scientific support during my PhD, my co-tutor prof. Maarten de Moor for logistic and scientific support, Andrea Luca Rizzo and INGV staff (section of Palermo) for the scientific support and laboratory facilities.